

University of Nottingham
UK | CHINA | MALAYSIA

# Dynamics of Ring-based CVGs including Non-linear Geometrical Effects

**Violetta Di Napoli**

Supervised by Dr. Stewart McWilliam & Prof. Atanas A. Popov

A thesis submitted for the degree of Doctor of Philosophy

August 2020

*Alla mia Famiglia*

# Abstract

Micro-Electro-Mechanical System (MEMS) ring-based Coriolis Vibrating Gyroscopes (CVGs) are devices that use vibration of micro-engineered thin rings to sense the angular rate of moving objects. High performance ring-based CVGs used in inertial navigation applications need to ensure the achievement of high sensitivity and improved signal-to-noise ratio. To achieve improved signal-to-noise ratio, ring-based resonators are designed to ensure low damping and mode-matching between drive and sense modes of vibration, and sensor sensitivity is improved by exciting the drive mode into large amplitude vibration. Large amplitude drive responses can cause the resonator to operate in a regime where geometrical non-linearity effects (i.e. non-linear strain-displacement relations) arise which have potential to alter sensor performance compared to a linear resonator operating at small amplitudes of vibration.

This thesis investigates the effects of geometrical non-linearity on the performance of ring-based resonators supported by a generic number of identical supports uniformly spaced around the ring circumference. A mathematical model for the supported ring resonator is developed including ring non-linear flexural vibration and non-linear support stiffness. The equations of motion governing the dynamics of the drive and sense $n\theta$ modes of the resonator are developed and used to investigate the non-linear drive and sense responses at large drive amplitudes of vibration under practical operating conditions.

The rotational symmetry of supported ring resonators operating at large amplitudes of vibration is investigated. The numbers of supports that maintain the rotational symmetry of a pair of $n\theta$ modes of vibration used to sense rotation are considered. This work illustrates that 8 supports maintain the rotational symmetry of practical ring-based resonators operating in the $2\theta$ modes when the resonator operates in the linear regime, but break the symmetry when the ring is excited into large amplitudes. In contrast, 16 supports are shown to maintain the rotational symmetry regardless of the amplitude of vibration.

The performance of ring-based CVGs having 8 and 16 supports are compared to investigate the impact on sensor performance. The sense mode response is determined when the ring is driven into large amplitudes of vibration, and the occurrence of quadrature errors and non-linear zero-rate-output response are investigated. Comparisons are made with an equivalent linear resonator in which ring and support geometrical non-linearity is neglected, to investigate non-linear amplification effects. Results illustrate that if the rotational symmetry of the resonator is broken, quadrature errors and non-linear zero-rate-output arise, which can adversely affect sensor performance by degrading the quality of rate measurement and by reducing sensor sensitivity. This work demonstrates that use of 16 supports for ring resonators operating in the $2\theta$ modes mitigates non-linear effects and improves rate measurement. Support geometries that linearise the overall dynamic behaviour of the resonator are investigated and key results are validated against a non-linear Finite Element analysis.

# Acknowledgement

First, I want to sincerely say thank you to Dr. Stewart McWilliam who guided me over the past four years and always gave me precious advices. Thank you also to Prof. A. Atanas Popov for the supervision.

Thank you to my sponsor Atlantic Inertial Systems, this would not be possible without your financial support.

I want to say thank you to my parents, my brothers Leonardo and Raffaello, and my sister Ultra for having always believed in me.

Thank you also to my special friends and colleagues Sofia Catalucci and Zi (Sara) Wang, for having been a family for me here in Nottingham. And thank you to Giulia and Flavia for having always been so close to me even living in different countries. And thank you to Shaun for having supported me during the thesis pending period.

# Contents

**1 Research background and aims** **1**

1.1 Introduction to MEMS Coriolis Vibrating Gyroscopes . . . . . 1

1.2 Operating principle of a single proof mass CVG . . . . . 4

1.3 Ring-based Coriolis Vibrating Gyroscopes . . . . . 8

1.4 Effects of broken rotational symmetry on MEMS ring-based CVGs . . . . . 13

1.5 Ring and supports geometrical non-linearity . . . . . 16

1.5.1 Ring geometrical non-linearity effects on unsupported ring resonators 17

1.5.2 Ring and support geometrical non-linearity effects on supported ring resonators . . . . . 19

1.6 Research aims . . . . . 21

1.7 Thesis outline . . . . . 23

**2 Mathematical model for a supported ring-based CVG operating in the linear regime** **25**

2.1 Introduction . . . . . 25

2.2 Mathematical model and energy expressions for a perfect unsupported ring . 27

2.2.1 Unsupported ring model and linear deflection . . . . . 27

2.2.2 Kinetic energy for an unsupported ring . . . . . 29

2.2.3 Potential energy for an unsupported ring . . . . . 32

2.3 Mathematical model and energy expressions for linear supports . . . . . 32
2.3.1 Mathematical model for a linear support structure . . . . . 33
2.3.2 Kinetic energy for a single support . . . . . 35
2.3.3 Potential energy for a single support . . . . . 35
2.3.4 Energy expressions for p supports . . . . . 37
2.4 Drive and sense equations of motion for a symmetric linear supported ring resonator . . . . . 41
2.5 Supported ring resonator having a point mass imperfection . . . . . 43
2.5.1 Mathematical model and kinetic energy for a point mass imperfection 44
2.5.2 Drive and sense equations of motion . . . . . 44
2.5.3 Drive and sense responses . . . . . 46
2.6 Summary and conclusions . . . . . 49

**3 Governing equations for a supported ring-based CVG operating at large amplitudes 51**

3.1 Introduction . . . . . 51
3.2 Equations of motion for an unsupported ring exhibiting large amplitude vibration 53
3.2.1 Ring non-linear flexural deflections . . . . . 53
3.2.2 Kinetic and potential energies for an unsupported ring . . . . . 54
3.2.3 Drive and sense equations of motion for an unsupported ring . . . . . 55
3.3 Mathematical model and energy expressions for a non-linear support structure 56
3.3.1 Mathematical model for non-linear supports . . . . . 57
3.3.2 Kinetic energy of the support structure . . . . . 58
3.3.3 Potential energy of the support structure . . . . . 61
3.3.4 Numbers of supports that break rotational symmetry for large amplitude vibrations . . . . . 63
3.3.5 Summary and interpretation . . . . . 65

3.4 Equations of motion for supported ring resonators at large vibration amplitudes 66
3.4.1 *Case Study I*: governing equations for the $2\theta$ modes for CVG having 8 supports . . . 72
3.4.2 *Case Study II*: governing equations for the $2\theta$ modes for CVG having 16 supports . . . 76
3.4.3 Summary of *Case Study I* and *Case Study II*, comparison and interpretation . . . 78
3.5 Summary and conclusions . . . 79

**4 Investigating the drive response for CVGs operating at large amplitude 81**
4.1 Introduction . . . 81
4.2 The method of averaging . . . 83
4.3 Finite Element (FE) non-linear analysis to determine drive mode frequency response curve . . . 86
4.4 Drive response for a ring having 8 supports . . . 90
4.4.1 Drive response obtained using the averaging method . . . 90
4.4.2 Numerical results . . . 94
4.5 Drive response for a ring having 16 supports . . . 101
4.5.1 Numerical results . . . 102
4.6 Comparing mathematical and Finite Element results . . . 105
4.7 Summary and conclusions . . . 107

**5 Investigating the sense response for CVGs operating at large amplitude 109**
5.1 Introduction . . . 109
5.2 Definition and interpretation of in-phase and quadrature sense responses . . . 110
5.3 Sense response for a CVG having 8 supports . . . 111
5.3.1 Averaged sense response . . . 112
5.3.2 Numerical Results . . . 115

5.3.3 Ring resonators having 8 supports arranged in pairs . . . . . 128
5.3.4 8 Supports: Summary of findings and interpretation . . . . . 130
5.4 Sense response for a CVG having 16 supports . . . . . 131
5.4.1 Averaged sense response . . . . . 132
5.4.2 Numerical results . . . . . 134
5.4.3 16 supports: Summary of findings and interpretation . . . . . 138
5.5 Summary and conclusions . . . . . 139

**6 Improved support design for a CVG having 16 supports 141**
6.1 Introduction . . . . . 141
6.2 Support geometries . . . . . 142
6.3 Use of mathematical model to determine improved support geometries . . . . 144
6.4 Arched geometries . . . . . 145
6.5 Straight geometries . . . . . 149
6.5.1 FE validation of frequency shift reduction for selected support geometries 155
6.6 Summary and conclusions . . . . . 161

**7 Conclusions and further work 163**
7.1 Introduction . . . . . 163
7.2 Review of thesis aims and work done . . . . . 163
7.3 Conclusions . . . . . 166
7.4 Contributions . . . . . 169
7.5 Further work . . . . . 170

**Bibliography 172**

**A Geometrical data and FE model for the ring-based resonator A1**
A.1 Ring and nominal support dimensions . . . . . A2
A.2 Finite Element model for the supported ring resonator . . . . . A4

A.3 Determination of the mass and stiffness coefficients to model the support . . A6
A.4 Principal axes of stiffness for the support . . . . . A10

**B Potential energy for a non-linear support structure B1**

**C Equations of motion for supported ring resonators operating at large amplitudes C1**

C.1 Drive and sense mode governing equations . . . . . C2
C.2 Drive and sense equations for small sense response amplitudes . . . . . C11

**D Validation using Runge-Kutta method D1**

D.1 Runge-Kutta time-integration method to determine the drive and sense responses D2
D.2 Runge-Kutta method ad averaging method compared . . . . . D2

# Chapter 1

# Research background and aims

## 1.1 Introduction to MEMS Coriolis Vibrating Gyroscopes

Gyroscopes are devices for measuring the angular rate of a body around a fixed axis with respect to an inertial space. The term "gyroscope" was introduced in 1852 by Jean Leon Foucault. The rotation of the plane of swing of Foucault pendulum in Paris Pantheon is known as the first experimental demonstration of Earth's rotation about its axis. Earliest gyroscopes (or gyros) made use of a rotating momentum wheel attached to a gimbal structure to sense rotation. In the 1960s, Coriolis Vibrating Gyroscopes (CVGs, or simply vibrating gyroscopes) were developed to solve issues associated with traditional gyros such as friction in gimbal bearings, by replacing the spinning rotor with a vibrating structure and using the rotational-induced Coriolis effect to sense rotation. In operation, one of the vibration modes of the vibrating element is forced into vibration and is referred to as drive mode. As the gyroscope rotates with non-zero angular rate, the Coriolis force causes energy transfer from the drive mode to its orthogonal companion mode, the sense mode, whose vibration amplitude is measured to sense the angular rate [1–3].

CVGs are classified [2] based on the nature of the drive and sense motion of the vibrating el-

ement (oscillatory, rotatory and their combination) and the type of mechanical element used (lumped single mass, lumped multiple masses, continuous mechanical element). Tuning-Fork Gyroscopes (TFGs) exploit flexural vibration of two tines of a so-called fork and torsional vibration about the fork stem to detect the angular rate. Other CVGs are based on oscillatory vibration of rotationally symmetric structures. Hemispherical Rotating Gyroscopes (HRGs) use hemispheric or glass-wine shaped shells; other common symmetric structures used are thin cylinders, disks and rings.

Directly mounted on a vehicle, inertial gyroscopes are key sensors for inertial navigation systems. Due to their restrictive cost and size, in the early 1900s high performance rate sensors were mainly used in aeronautical and maritime military applications only [1, 3]. In the 1980s, development of Micro-Electro-Mechanical System (MEMS) technologies which combine electrical and mechanical systems at a micro-scale revolutionised the inertial sensors market. Thanks to micromachining fabrications, it became possible to miniaturise inertial rate sensors, so that their cost, size and weight have been dramatically reduced. MEMS inertial gyroscopes captured the market of high performance inertial navigation and guidance systems for sea, space, and air advanced vehicles, and made gyroscopes accessible to everyone by use of smartphones and other electronic gadgets. Since the development of the first MEMS gyroscopes, their applications have been constantly growing. MEMS inertial sensors are now used in the automotive industry for advanced control and safety systems and guidance of autonomous vehicles, and in consumer electronics industry (e.g. smartphones, tablets, digital cameras, mobile games) [1–3]. Medical engineering applications are also emerging, and MEMS gyros find use in surgical robots, Magnetic Resonance Imaging (MRI) devices, angiography equipment and more [4].

Vibrating elements have developed excellent potential for miniaturisation so most MEMS gyroscopes are Coriolis Vibrating Gyroscopes [1, 3]. The first MEMS CVG was developed in

1991 [1] and relied upon silicon bulk micromachining; this technology has developed significantly in the last decades and is now used to produce multiple sensors from a single silicon wafer [1, 3].

A fundamental requirement for high performance MEMS CVGs is the achievement high sensitivity to improve signal-to-noise ratio (SNR) and reliability. The sensitivity of a CVG is defined as the amplitude of the sense mode per unit angular rate [5] and is one of the most important parameters characterising vibrating gyros performance [1, 3]. For CVGs the SNR is defined as the ratio of sensor output containing noise to the desired output, and is proportional to the angular rate.

To ensure robust sensor output during operation (i.e. sense mode vibration at constant amplitude, phase and frequency), the drive mode is commonly driven into resonant vibration with constant amplitude using phase lock and automatic gain control loops [1, 6, 7]. Under these circumstances, matching the drive and sense modes resonance frequencies is fundamental to maximising the sensitivity of the device to rotation [1, 3, 8] and reducing the impact of noises (e.g. electrostatic, thermal) on angular rate detection [9]. If mode-matching is achieved, the Coriolis mechanical response is increased by reducing the damping [3, 10] and exciting the drive mode into large amplitude vibration [7, 11].

Damping in MEMS CVGs is typically defined by the quality factor (or Q-factor) i.e. the energy stored over the energy lost per oscillation cycle [12]. MEMS devices make use of vacuum packaging technologies to reduce fluid damping, and the main damping mechanism for micromachined resonators is thermo-elastic damping (caused by the interaction between mechanical strain and thermal effects in the resonator [13]). Another important energy loss is caused by vibration transmission from the resonator to the supporting structure [13]. Extensive research has been conducted to reduce damping in MEMS resonators, and state-of-the-art High Q-factor gyroscopes are designed to have extremely low energy dissipation [14].

Devices having reduced damping have reduced bandwidth and are susceptible to fabrication imperfections and changes in operating condition (e.g. temperature variations) which can induce frequency splits between the drive and sense modes [1]; for this reason, in gyroscope designs where high robustness is preferred to high sensitivity, the device is operated in split-mode, i.e. drive and sense resonance frequencies are intentionally designed to be slightly shifted relative to each other [3].

For high performance sensors used in inertial navigation applications, achieving the highest sensitivity is one of the main drivers. Low damping, mode-matching and excitation of the drive mode into large amplitude vibration are fundamental requirements to increase sensitivity to angular rate and improve SNR. Vibration of the drive mode into large amplitude can cause the resonator to operate in a regime where geometrical non-linearity effects (i.e. non-linear strain-displacement relations) arise [5,9]. The work described in this thesis focuses on the effects of geometric non-linearity on the performance of high performance sensors for inertial navigation applications. Details on the origin and effects of geometrical non-linearity will be provided in later sections.

## 1.2 Operating principle of a single proof mass CVG

This Section introduces the operating principle of the basic Coriolis Vibrating Gyroscope shown in Figure 1.1 having a single proof mass as its vibrating element. The proof mass $m$ is free to oscillate in the $x$-$y$ plane along the drive direction $x$ and the sense direction $y$.

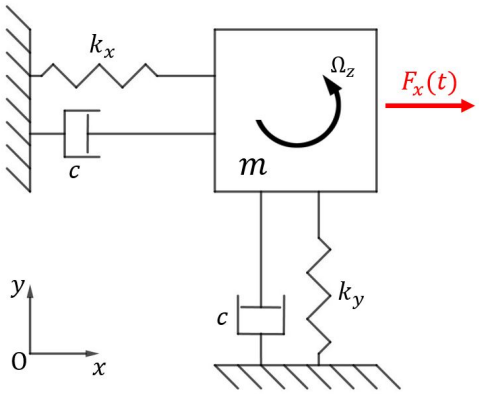



Figure 1.1: Schematic diagram for a single proof mass MEMS CVG.

The proof mass $m$ is supported by flexible linear suspensions and the dynamics of the resonator are modelled as a 2 degrees-of-freedom mass-spring-damper system [1, 3]. The stiffness of the linear suspensions along $x$ and $y$ are modelled as linear springs having stiffness coefficients $k_x$ and $k_y$, respectively. Coefficients $k_x$ and $k_y$ are assumed to be different from each other to allow for the case when the flexible suspensions have slightly different stiffnesses along $x$ and $y$. Typically, for MEMS CVGs, the damping in the drive and sense directions is approximately the same, so the damping is assumed to be equal along $x$ and $y$ and is indicated as damping coefficient $c$.

The gyroscope is considered to be attached to a body rotating with angular rate $\Omega_z$ about the OZ-axis, perpendicular to the $x$-$y$ plane. A harmonic force $F_x(t)$ is applied to the mass as shown in Figure 1.1; to ensure gyroscope sensitivity does not change during operation, the frequency of the applied force matches the drive mode resonance frequency $\omega_x = \sqrt{\frac{k_x}{m}}$ i.e. $F_x(t) = F_x \cos \omega_x t$ [1, 6]. The motion of the mass along the $x$-direction is referred to as primary motion or drive response. As the body rotates about the OZ-axis, the Coriolis force acts causing the mass to move along the $y$-direction. This motion is referred to as the secondary motion or sense response. Whilst the primary motion is caused by the external force, the secondary motion is purely caused by the Coriolis action and, for ideal gyroscopes, is zero in the absence of rotation.

Equations of motion for the proof mass motion along the $x$ and $y$ directions are [1, 3]:

$$\ddot{x} + \frac{\omega_x}{Q}\dot{x} + \omega_x^2 x = \frac{F_x(t)}{m} \tag{1.1}$$

$$\ddot{y} + \frac{\omega_y}{Q}\dot{y} + \omega_y^2 y = -2\Omega_z \dot{x} \tag{1.2}$$

where $\omega_x$ and $\omega_y$ respectively are the natural resonance frequencies of the drive and sense modes of the resonator, and $Q$ is the quality factor. Equations (1.1)-(1.2) are valid under the assumption that (i) the angular rate $\Omega_z$ is constant and much smaller than the natural frequencies of the resonator (so that $\dot{\Omega}_z = 0$ and $\Omega_z^2 = 0$) and (ii) the sense response amplitude is much smaller than the drive vibration amplitude (so that the Coriolis term in the drive mode equation, proportional to $\dot{y}$, is neglected).

These assumptions are acceptable for practical MEMS CVGs because their natural frequencies are typically in the range of 10 - 100 kHz, and the angular velocities detected are normally in the order of 1 $\frac{\text{rad}}{\text{s}}$ [12]. Moreover, the drive mode is directly excited into vibration whilst the sense mode is ideally only excited by the Coriolis force, so the drive response amplitude is normally orders of magnitude larger than the sense response [1, 5].

In [1] and [3] the steady-state drive and sense oscillations are respectively described as:

$$x(t) = A_x \sin \omega_x t \tag{1.3}$$

$$y(t) = A_y \sin\left(\omega_x t + \phi_y\right) \tag{1.4}$$

and drive and sense equations (1.1) and (1.2) are used to obtain the following expressions for the drive vibration amplitude $A_x$, sense response amplitude $A_y$, and sense response phase relative to the drive response $\phi_y$:

$$A_x = \frac{F_x}{k_x} Q \tag{1.5}$$

$$A_y = \frac{2A_x\omega_x\Omega_z}{\sqrt{(\omega_x^2 - \omega_y^2)^2 + \frac{\omega_x^2\omega_y^2}{Q^2}}} \tag{1.6}$$

$$\phi_y = \tan^{-1}\left(\frac{(\omega_y^2 - \omega_x^2)}{\omega_x\omega_y}Q\right) \tag{1.7}$$

Equation (1.6) indicates that the amplitude of the sense response is maximised by matching the drive and sense resonance frequencies i.e. $\omega_x = \omega_y$.

If $\omega_x = \omega_y = \omega_0$, sense mode response amplitude (1.6) becomes:

$$A_y = \frac{2A_xQ}{\omega_0}\Omega_z \tag{1.8}$$

This indicates that if drive and sense modes resonance frequencies are matched, the sense response amplitude is linearly proportional to $\Omega_z$ and is zero in the absence of rotation. The Coriolis coupling is weak [15] so the sense amplitude $A_x$ is typically small and mechanical amplification is required to increase sensor sensitivity and to reduce the effects of noise on the angular rate detection (i.e. to improve the SNR). If $\omega_x = \omega_y$, the sense response amplitude is (i) amplified by the quality factor $Q$ [3, 10], and (ii) increased by exciting the drive mode into large amplitude vibration [7, 11]. Moreover, it is noted that if $\omega_x = \omega_y$, then $\phi_y = 0$, so that the sense response is either in-phase or 180° out-of-phase relative to the drive response.

If drive and sense natural frequencies are split (i.e. $\omega_x \neq \omega_y$), then $\phi_y \neq 0$. In this case, the sense response consists of two components: an "in-phase response" which is in-phase or 180° out-of-phase relative to the drive response, and a so-called "quadrature response" which is 90° out-of-phase relative to the drive response. Whilst the amplitude of the in-phase response is used to measure the angular rate, the quadrature response causes occurrence of so-called quadrature errors that complicate the detection of the applied angular rate and have potential to degrade the quality of the rate measurement [6, 7, 9]. Quadrature response and

quadrature errors will be discussed in detail in later work.

## 1.3 Ring-based Coriolis Vibrating Gyroscopes

Extensive research has been conducted to design symmetric resonators providing mode matching and reduced sensitivity to temperature fluctuations. Hemispherical Rotating Gyroscopes (HRGs), firstly developed in the 1960s, use two degenerate modes of hemispheric shells to sense rotation. Other continuous and rotationally symmetric vibrating elements used are disks, thin cylinders and rings. Modes of vibrations of rotationally symmetric resonators occur in degenerate pairs having equal resonance frequencies, and are less susceptible to spurious environmental vibrations [16,17] and to temperature variations, because the degenerate modes are equally affected by temperature [11].

Thin rings are easier to miniaturise compared to other rotationally symmetric structures so that many MEMS CVGs use thin rings as their vibrating element. MEMS ring-based CVGs were firstly developed in 1994 and their performance improved incrementally since then. For modern silicon MEMS ring-based resonators, the thin ring resonator is supported by a number of identical supports uniformly spaced around the ring circumference. Figure 1.2 shows a modern ring-based MEMS CVG; a schematic diagram of its ring and supports (see red box in Figure 1.2) is illustrated in Figure 1.3.

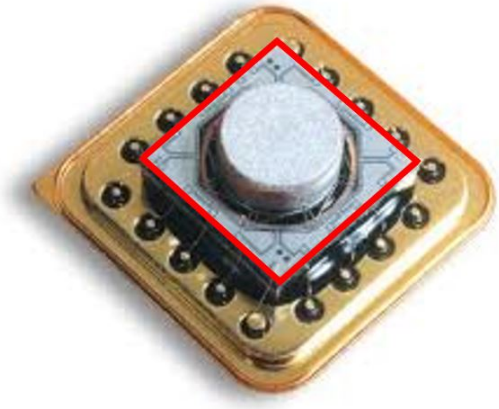


Figure 1.2: A MEMS ring-based Coriolis Vibrating Gyroscope [18].

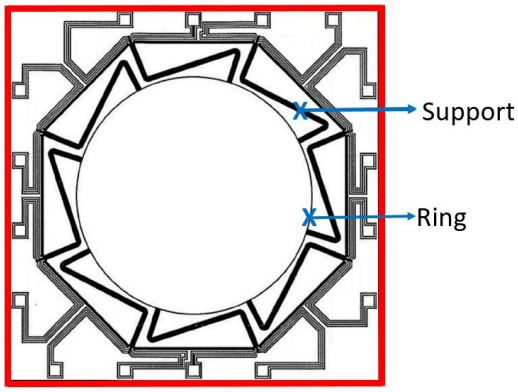



Figure 1.3: Diagram for a ring-based CVG where ring and supports are indicated [19].

Ring-based CVGs sense rotation using a pair of in-plane flexural modes of vibration of a thin ring, which occur in degenerate and spatially orthogonal pairs, having indeterminate angular position around the axis of symmetry [20, 21]. Figure 1.4 illustrates the first four in-plane modes of vibration of a perfect ring, where $n$ indicates the number of nodal diameters [22].

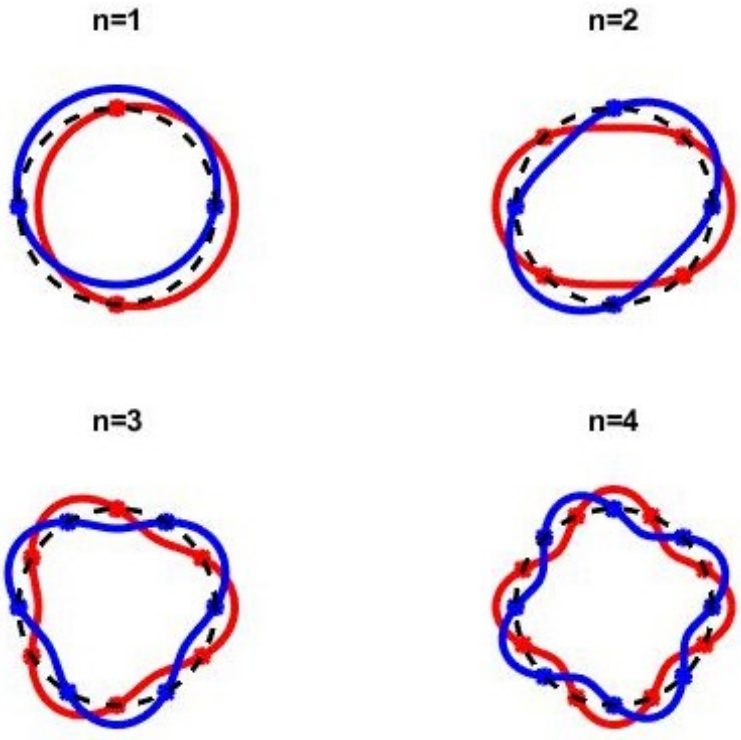



Figure 1.4: First four pairs of in-plane modes of vibration of a perfect thin ring.

For $n = 1$ the ring remains rigid whilst for $n \geq 2$ the ring deforms and flexes [23]. Ring-based CVGs normally operate using in-plane flexural modes, for this reason in what follows only modal numbers such that $n \geq 2$ will be considered. For each pair of degenerate modes, the nodes of the primary mode are at the anti-nodes of the secondary mode, and the mode shapes are identical except they are oriented $\frac{180}{2n}$ degrees relative to each other. Most ring-based CVGs operate using $n = 2$ in-plane flexural modes of the ring which are orientated 45 degrees relative to each other and are referred to as the $2\theta$ modes.

In what follows, linear deflection of rings undergoing $n\theta$ vibration is described to introduce the operating principle of a ring-based CVG. Timoshenko [24] analysed the linear in-plane flexural vibration of thin rings having uniform cross sections. Under the assumption that ring cross section dimensions are much smaller than ring radius, and that the elongation of

the ring mid-line remains constant during vibration, Timoshenko found that the radial $u$ and tangential $v$ displacements of the ring mid-line at circumferential coordinate $\theta$ can be expressed in the form:

$$u(\theta, t) = \sum_{n=1}^{\inf} [Q_{1n}(t) \cos n\theta + Q_{2n}(t) \sin n\theta] \tag{1.9}$$

$$v(\theta, t) = \sum_{n=1}^{\inf} \left[ -\frac{1}{n} Q_{1n}(t) \sin n\theta + \frac{1}{n} Q_{2n}(t) \cos n\theta \right] \tag{1.10}$$

Coefficients $Q_{1n}$ and $Q_{2n}$ vary with time and represent the generalised coordinates; $\cos n\theta$ and $\sin n\theta$ are the shapes of the $n\theta$ modes of vibration of the ring having $n$ nodal diameters. In CVG operation, harmonic forces having spatial $n\theta$ distribution and frequency equal to the natural frequency of the $n\theta$ modes are applied to the ring to excite one of the degenerate $n\theta$ modes into resonance. Commonly, $\cos n\theta$ is considered to be the ring mode excited to vibrate i.e. the drive mode. Under these circumstances, if the ring is perfect (i.e. in an ideal case) and the angular rate is zero, ring radial displacement (1.9) becomes:

$$u(\theta, t) = Q_1(t) \cos n(\theta - \alpha) \tag{1.11}$$

where $Q_1$ indicates the anti-node radial vibration amplitude of the drive mode at angle $\theta = \alpha$. For a perfect ring, the drive mode orientation around the ring circumference is arbitrary. Angle $\alpha$ in (1.11) is only used to specify the radial displacement at the drive axis location which aligns with the principal direction of the applied radial driving force.

Similar to that described for a proof mass CVG in Section 1.2, as the device rotates (i.e. when the gyroscope is attached to a body undergoing rotation), the Coriolis force excites the orthogonal companion mode $\sin n\theta$, i.e. the sense mode. At this point, the ring undergoes a combined $\cos n\theta$ and $\sin n\theta$ vibration and the radial displacement of the ring mid-line is:

$$u(\theta, t) = Q_1(t) \cos n(\theta - \alpha) + Q_2(t) \sin n(\theta - \alpha) \tag{1.12}$$

where $Q_2$ indicates the anti-node radial vibration amplitude of the sense mode at angle $\theta = \alpha + \frac{\pi}{2n}$. $Q_1$ and $Q_2$ are normally referred to as generalised coordinates. Figure 1.5 shows a schematic representation of ring-based CVGs in operation for $n = 2$: driving forces are applied to the ring to excite the drive $\cos 2\theta$ mode and rotation-induced Coriolis forces excite the sense $\sin 2\theta$ mode so that the ring undergoes combined vibration of drive and sense $2\theta$ modes.

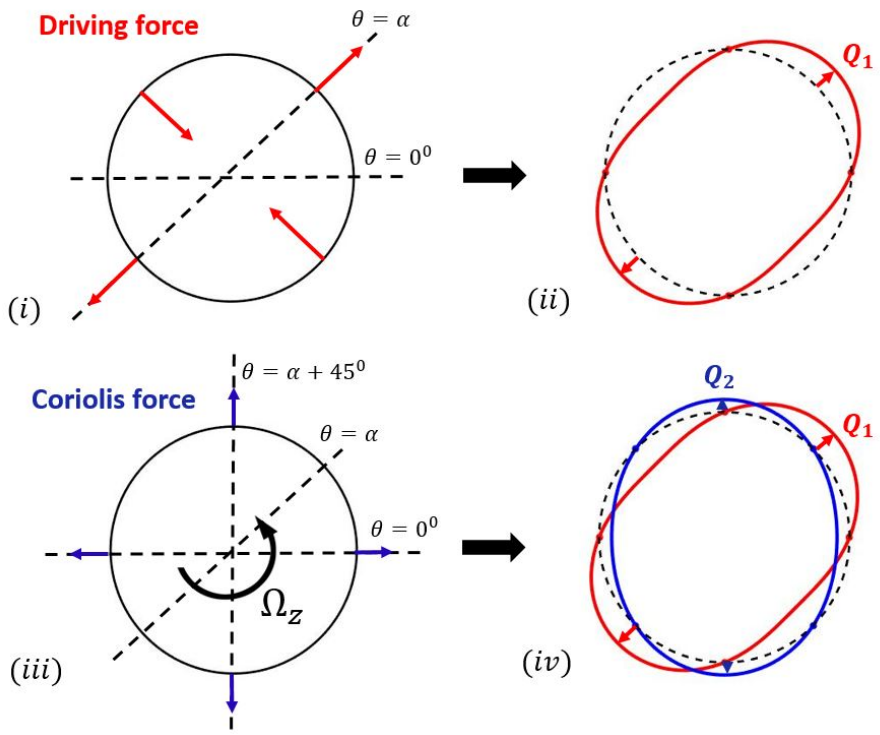



Figure 1.5: Schematic representation of a MEMS ring-based CVG in operation for $n = 2$. (i) Driving forces are applied to the ring to excite the drive $\cos 2\theta$ mode, (ii) the drive mode vibrates, (iii) rotation-induced Coriolis forces excite the sense $\sin 2\theta$ mode and (iv) the ring undergoes combined vibration of drive and sense $2\theta$ modes.

The described dynamics applies for ideal ring-based gyroscopes, where the ring is perfect and the resonator is rotationally symmetric. The drive mode maximum diameter aligns with the principal direction of the applied force and the sense response is caused by Coriolis action only. In practice, fabrication imperfections, material inhomogeneity and/or ring supports can

break the rotational symmetry of supported ring resonators causing performance to degrade.

## 1.4 Effects of broken rotational symmetry on MEMS ring-based CVGs

This Section describes known effects of broken rotational symmetry on the performance of a ring-based CVG operating in the linear regime. In practical devices, fabrication imperfections, structural irregularities, use of non-uniform or anisotropic materials and asymmetric ring support structures have potential to cause a non-uniform distribution of mass or stiffness around the ring circumference, and break the rotational symmetry of supported ring-based CVGs [9, 12, 25]. Imperfections fix the position of the primary and secondary $n\theta$ modes around the ring circumference, eliminating the positional indeterminacy. The modes are no longer degenerate and their resonance frequencies split [9, 20, 21, 23].

Many studies have been conducted to investigate the effect of imperfection on rings vibration. McWilliam *et al.* [20] considered frequency splits occurring for linear and perfect rings having (i) variable cross sections, (ii) single point mass imperfections and (iii) point mass imperfections uniformly spaced around the ring circumference, using a Rayleigh-Ritz approach. McWilliam *et al.* demonstrated that identical uniformly spaced point masses cause the $n\theta$ natural frequencies to split only if the number of masses $N_m$ is such that $\frac{2n}{N_m}$ is an integer.
Eley *et al.* [25] investigated the effects of material anisotropy on the frequency split for ring resonators made of crystalline silicon. Taking account of anisotropy effects in the strain energy formulation, Eley *et al.* found that frequency split occurs between pairs of modes that would be degenerate if the ring was made of isotropic material.
Bisegna *et al.* [23] investigated the dynamics of imperfect rings modelling imperfections as perturbations on the uniform density and bending stiffness of a perfect ring. Using a perturbation expansion and spectral representation, Bisegna *et al.* obtained closed expressions for

eigenfrequencies and mode shapes of the imperfect ring, and demonstrated that imperfections cause the eigenfrequencies to split and eigenmodes to deviate from sinusoidal shapes.

To eliminate the frequency split for slightly imperfect rings, Fox [21] estimated the trimming masses to be added or removed from a ring for a given pair of modes, using a Rayleigh-Ritz approach. For ring-based CVGs, El-Sayed *et al.* [17] and Ayazi *et al.* [11] pointed out the use of tuning electrodes located around the ring structure and electronic compensation to achieve the frequency match.

The effects of the support structure on the rotational symmetry of a ring resonator have also been considered. Weng *et al.* [26] observed that ring supports have potential to break the resonator rotational symmetry. Based on geometrical considerations, Weng *et al.* concluded that 8 identical supports uniformly spaced around the ring circumference maintain the frequency match between the $2\theta$ modes. This result was also obtained by Ayazi *et al.* [11] based on symmetry considerations.

Extensive research has been conducted to investigate imperfection effects on the sense response and hence sensor sensitivity. Wang *et al.* [6] investigated drive and sense modes dynamics of imperfect HRGs, by including inhomogeneous damping and frequency split between drive and sense modes. Hu *et al.* [7] analysed the effects of damping and stiffness imperfections on drive and sense dynamics of MEMS CVGs, developing drive and sense equations of motion for the resonator with inclusion of damping and elastic coupling terms between the equations. Nitzan *et al.* [9] studied imperfection effects on MEMS disk gyros, including stiffness coupling terms between drive and sense governing equations.

The above research findings are relevant to the work conducted here and are summarised below:

- *Imperfections reduce sensitivity to rotation and SNR.* The Coriolis coupling between drive and sense modes is generally weak and a large sense response is desirable to reduce the effect of sense detection noises and to increase sensitivity to rotation. In Section 1.2

for a proof mass gyro, it was shown that if drive and sense resonance frequencies are equal, the sense response amplitude can be amplified by increasing the Q-factor. Use of large quality factors reduces the drive and sense response bandwidths. If imperfections cause the drive and sense resonance frequencies to split, the sense response amplitude at the drive mode resonance frequency reduces and the sensor output is weak and hardly detectable from thermal or electrostatic noises.

- *Imperfections degrade the quality of the rate measurement.* As introduced in Section 1.2 for a proof mass gyro, the sense response can be demodulated as in-phase and quadrature responses, relative to the drive response. The in-phase component of the sense response is used to measure the angular rate $\Omega_z$. For an ideal gyro, the quadrature response is zero and the in-phase response amplitude is linearly proportional to the angular rate $\Omega_z$. Imperfections can cause occurrence of unwanted quadrature response and so-called quadrature errors which are sensing errors that complicate the detection of the angular rate from the sense response measurement. Moreover, imperfections can cause the sense response to be non-zero in the absence of rotation (i.e. for $\Omega_z = 0$). The in-phase response that is unrelated to the angular rate is commonly referred to as "zero-rate-output" (or ZRO) [5]. If the rotational symmetry is broken, sensing errors and ZRO have potential to degrade the quality of rate measurement.

In this work, the ring is assumed to be perfect and made of isotropic silicon, so that fabrication imperfections or material anisotropy will not be considered. The rotational symmetry of ring resonators operating in any pair of $n\theta$ in-plane ring flexural modes, and supported by a generic number of $p$ (identical and uniformly spaced) supports will be analysed. Although it is known that 8 identical and uniformly spaced supports maintain the $n = 2$ rotational symmetry for a ring resonator operating in the linear regime, the required number of supports to maintain frequency matching for a generic pair of $n\theta$ flexural modes (and why) has not been proposed yet. Moreover, geometrical non-linearity effects will be considered.

## 1.5 Ring and supports geometrical non-linearity

Previous sections highlighted that high performance CVGs used in inertial navigation applications require the excitation of the drive mode into large amplitude vibration to enhance gyro sensitivity to rotation and SNR. A consequence of this is that it is desirable to operate at large vibration amplitudes at which non-linearity effects are important and have potential to alter CVG performance compared to operating in the linear regime.

Non-linearity can arise from non-linear dissipative forces (i.e. damping non-linearity), non-linear stress-strain response of the material (i.e. material non-linearity) or non-linear strain-displacement relations (i.e. geometrical non-linearity). Another source of non-linearity relates to non-linear electrostatic forces acting on the ring structure for capacitive devices. Sieberer [27] investigated the shock-induced coupling between in-plane rigid and flexural modes of the ring caused by non-linear electrostatics, and demonstrated that the non-linear electrostatics causes the ring $n = 2$ modes to be excited by environmental shocks.

Electrostatic non-linearity is not considered in this work. Instead the work focuses on geometrical non-linearity only and is applicable to devices similar to that shown in Figure 1.2, for which the ring is driven into vibration using electromagnetic actuation, and the sense vibration is detected by induction [28].

The resonator is made of isotropic silicon which is linearly elastic until failure [29], so material non-linearity is not considered either. Analysis of non-linear damping effects is beyond the scope of this work. This thesis focuses on the effects of ring and support structures geometrical non-linearity on the performance of supported ring-based resonators.

This Section summarises and discusses relevant previous studies concerning the origins and effects of geometrical non-linearity on supported ring-based CVGs. Section 1.5.1 provides a literature review on ring non-linear vibration and its effect on unsupported ring-based resonators. Studies regarding supported ring resonators including ring and support geometrical

non-linearity are presented in Section 1.5.2.

### 1.5.1 Ring geometrical non-linearity effects on unsupported ring resonators

A detailed description of the historical development of research on rings non-linear vibration can be found in [30]. Reissner in the 1950s first dealt with non-linear vibration of shells. Neglecting in-plane inertia, Reissner restricted the analysis to non-linear flexural shell motion and developed a set of non-linear governing equations for shells.

In the 1960s, Evensen [31–33] adapted Reissner non-linear shell equations to thin circular rings, by considering (i) the radial and tangential displacements of the ring mid-line to be functions of circumferential coordinate and time only, (ii) the ring cross-section to be uniform around the ring, (iii) the ring radius $R$ to be much larger than ring radial thickness and (iv) longitudinal in-plane force and shearing force to be zero throughout the ring.

Evensen found that at large amplitude vibration, ring deflections proposed by Timoshenko [24] (i.e. equations (1.9)- (1.10)) involve elongation of the ring mid-line whilst in practice it remains constant during flexural motion. Limiting the discussion to vibrations involving the primary and secondary $n\theta$ modes only, Evensen suggested that a more realistic form for ring deflection is given by:

$$u(\theta,t) = Q_1 \cos n\theta + Q_2 \sin n\theta - \frac{\left(n^2-1\right)^2}{4Rn^2}\left(Q_1^2+Q_2^2\right) \tag{1.13}$$

$$\begin{aligned} v(\theta,t) = &-\frac{Q_1}{n}\sin n\theta + \frac{Q_2}{n}\cos n\theta + \\ &+\frac{\left(n^2-1\right)^2}{8Rn^3}\left[\left(Q_1^2-Q_2^2\right)\sin 2n\theta - 2Q_1Q_2\cos 2n\theta\right] \end{aligned} \tag{1.14}$$

where $Q_1$ and $Q_2$ are functions of time, and an antisymmetric mode of vibration ($n = 0$ mode or breathing mode [22]), consisting of a contraction of the ring (see Figure 1.6) is included to satisfy the inextensibility condition.

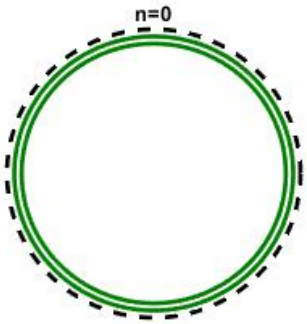



Figure 1.6: Breathing axisymmetric mode for a thin ring.

Equations (1.13)-(1.14) satisfy the continuity condition (i.e. the requirement that the circumferential displacement is single valued around the ring mid-line circumference), the inextensibility condition, and can be used as an approximate solution for the ring non-linear equations.

Using a Galerkin method, Evensen used displacements (1.13)-(1.14) to determine a non-linear differential equation for the vibration amplitude of the primary $n\theta$ mode, and approximated its solution using the averaging method. Results indicated that the breathing mode causes the primary mode to be resonant at smaller frequencies than the linear resonance frequency as the vibration amplitude increases i.e. rings have softening dynamic behaviour.

This shift of the drive resonance frequency from the linear regime will influence the dynamics of ring-based resonators which normally operate at the drive mode natural frequency. Evensen findings are known to researchers working on the high performance ring-based gyroscopes field and have been used to investigate ring resonators behaviour under large amplitude vibration. Polunin *et al.* [5] investigated the effects of geometrical and electrostatic non-linearity on the dynamic behaviour of drive and sense $2\theta$ modes of a perfect unsupported ring resonator. Using Evensen's non-linear expression for the radial displacement (1.13), Polunin *et al.* used Lagrange's method to obtain non-linear equations of motion in the drive and sense generalised coordinates. Equations were developed considering (i) drive mode ex-

cited by harmonic external force and (ii) ring undergoing constant rate rotation; action of non-linear electrostatic forces was also included. Polunin *et al.* found that geometrical and electrostatic non-linearity cause drive and sense equations to be parametrically coupled with each other by non-linear inertial, stiffness and electrostatic terms. Polunin *et al.* used the averaging method to determine the frequency backbone curve for the drive mode (which showed the known softening behaviour), and to obtain an analytical expression for the steady-state sense response amplitude. Frequency response curves for the sense mode were developed for a number of magnitudes of the applied driving forces. Results indicated that, due to the parametrical non-linear coupling, the sense response peak amplitude is larger compared to a linear resonator. Moreover, as the vibration amplitude increases, the frequency at which the sense amplitude peak occurs is shifted from the $2\theta$ natural frequencies.

The shift of the drive and sense peak amplitudes from the $2\theta$ natural frequencies, caused by ring geometrical non-linearity, is relevant for ring-based resonators. The amplitude of the sense response at the drive mode resonance frequency has potential to be significantly smaller than the peak value, so that sensor sensitivity is reduced. Studies in [5] do not indicate whether drive and sense non-linear peaks occur at the same frequency; moreover, the influence of the support structure was not considered.

### 1.5.2 Ring and support geometrical non-linearity effects on supported ring resonators

Sérandour [29,34] investigated the non-linear dynamic behaviour of perfect ring resonators operating in the $2\theta$ modes and supported by 8 identical supports uniformly spaced around the ring circumference. Sérandour developed a mathematical model for ring and supports, including ring non-linear vibration and non-linear strain-displacement relation for the supports. The model allowed any pair of $n$ flexural modes to be considered; however, the analysis was mainly restricted to the $n = 2$ modes. The model was based on the assumption that

the ring structure is dominant compared to the support structure (so that expressions for an unsupported ring non-linear deflection can still be used). The ring was modelled as a curved beam having uniform cross-section, and supports were modelled as mass-spring elements acting in the radial and tangential directions, having one extremity fully constrained to a rigid frame and the other attached to the ring. Different mass and stiffness coefficients were used for mass-spring elements in the radial and tangential directions. Sérandour took account of supports geometrical non-linearity by using cubic non-linear stiffness for the springs, and used ring non-linear radial and tangential displacements (1.13)-(1.14) (Evensen [31–33]) to take account of ring geometrical non-linearity. Lagrange's equation was used to obtain non-linear equations of motion in the drive and sense generalised coordinates, assuming that the drive mode is excited by applied external harmonic force.

The obtained drive and sense equations indicated that ring and support geometrical non-linearity causes the drive and sense modes to be parametrically coupled with each other by non-linear inertial, damping and stiffness terms (this result is similar to that in [5] for unsupported rings). Moreover, non-linear supports were found to cause the sense mode to be externally excited by inertia and stiffness non-linear terms associated with the drive response. Focusing the analysis on the dynamic behaviour of the drive mode, Sérandour simplified drive and sense non-linear equations under the assumption that the sense response amplitude is much smaller than the drive response, and then negligible (i.e. $Q_2 = 0$). Neglecting all terms involving the sense response in the drive equation, Sérandour used the averaging method to obtain an analytical expression for the drive mode frequency backbone curve.

By comparing drive frequency backbone curves for supported and unsupported ring resonators, Sérandour found that the dynamic behaviour of the drive mode is significantly influenced by the non-linear supports and cannot be described by the ring alone. Moreover, Sérandour demonstrated that supports behaviour depends on their geometry. In light of this, Sérandour suggested that the dependency of the drive mode resonance frequencies on the vibration amplitude could be eliminated by using hardening supports that neutralise the

softening behaviour of the ring.

Sérandour work demonstrated that support non-linearity needs to be considered to accurately analyse the dynamic behaviour of ring resonators. A relevant result of Sérandour research is that support geometrical non-linearity causes the sense mode to be excited by the drive response in the absence of rotation. For ring-based resonators, this has potential to give rise to the so-called zero-rate-output, introduced in Section 1.4 as a measured sense response that does not relate to the angular rate. Sérandour investigation focused on the drive response and did not provide a detailed analysis for the sense response. Moreover, only 8 supports were considered. Additional research is needed to investigate the effects of using a generic number of supports on the non-linear dynamics of ring-based resonators operating at small (but non-zero) sense response amplitudes.

## 1.6 Research aims

The literature review presented highlighted that several aspects on the dynamic behaviour of supported ring-based resonators are still open for research. The ultimate goal of this work is to provide an understanding of the dynamic behaviour (drive response, sense response) of supported ring-based CVGs undergoing large amplitude vibration. In particular, this work will focus on the impact of ring and support geometrical non-linearity on ring-based resonators performance. The proposed investigation is based on the mathematical model developed by Sérandour [29,34] described in Section 1.5.2, which will be extended to include a generic number $p$ of identical uniformly spaced supports. Key aims for the research are summarised below.

1. Determine the numbers of supports $p$ that maintain the rotational symmetry of ring-based resonators for any pair of $n\theta$ in-plane flexural modes in the linear regime.

2. Investigate the influence of ring and support geometrical non-linearity on the rotational

symmetry of supported ring-based resonators. Determine the numbers of supports $p$ that maintain the $n\theta$ rotational symmetry at large vibration amplitude, and compare against the numbers of support that maintain the symmetry in the linear regime.

3. Determine the equations governing the motion of drive and sense $n\theta$ modes of supported ring-based resonators operating at large amplitude vibration under practical operating conditions, including ring and support geometrical non-linearity. Non-linear equations need to allow any number of supports $p$ to be considered.

4. Investigate the influence of ring and support geometrical non-linearity on drive and sense equations of motion. For example, investigate potential occurrence of parametrical non-linear coupling between drive and sense modes.

5. For $n = 2$, investigate the steady-state drive response (amplitude, phase) for supported ring resonators operating at large amplitude vibration, under practical CVGs operating conditions. Compare against resonators operating in the linear regime to highlight ring and support geometrical non-linearity effects on the drive mode dynamics. Investigate the influence of non-linear support structure on the dynamic behaviour of the drive mode, compared to an unsupported ring.

6. For $n = 2$, investigate the steady-state sense response (in-phase response, quadrature response) for supported ring resonators undergoing large drive vibration amplitude. Compare against resonators in which geometrical non-linearity is neglected, to investigate potential non-linear amplification effects. Investigate the impact of geometrical non-linearity on sensor performance (i.e. investigate occurrence of sensing errors, zero-rate-output, impact on sensor sentitivity).

7. Investigate support designs (supports numbers and geometries) that linearise the dynamic behaviour of supported ring resonators operating at large amplitude of vibration.

Where possible, mathematical results obtained using the proposed mathematical model will be verified against results obtained using non-linear Finite Element analyses.

## 1.7 Thesis outline

This Section presents an outline of each of the thesis chapters.

**Chapter 2** The mathematical model for a supported ring-based CVG firstly developed by Sérandour [29, 34] is extended to allow a generic number $p$ of identical uniformly spaced supports to be included. Ring flexural vibration and support stiffness are considered to be linear. The model is used to determine analytical expressions for ring and support kinetic and potential energies for ring resonators operating in the $n\theta$ modes. The obtained energy expressions are used to investigate the numbers of supports that maintain the rotational symmetry in the linear regime. Drive and sense equations of motion are developed for linear, perfect and rotationally symmetric ring resonators, and a point mass imperfection is then added on the ring mid-line to investigate the impact of breaking the rotational symmetry on sensor performance.

**Chapter 3** Ring non-linear flexural vibration and support non-linear stiffness are included in the mathematical model developed for the supported ring resonator, to investigate CVGs operation at large amplitude of vibration. Analytical expressions for ring and support kinetic and potential energies are obtained and used to investigate the numbers of supports that maintain the rotational symmetry at large amplitudes. The equations of motion governing drive and sense $n\theta$ modes are developed for ring resonators having a generic number of supports $p$. The impact of geometrical non-linearity on the drive and sense governing equations is discussed for (i) rotationally asymmetric and (ii) rotationally symmetric ring resonators.

**Chapter 4** The mathematical model is used to investigate the $2\theta$ drive mode response for ring resonators operating at large amplitudes, using the method of averaging. The effects of ring and support geometrical non-linearity on the non-linear drive mode dynamics are discussed. The frequency backbone curve for the drive mode of supported and unsupported ring resonators are compared to investigate the influence of non-linear support. The impact of the breaking of rotational symmetry on the drive mode dynamics is investigated. Key results are verified against a non-linear Finite Element analysis.

**Chapter 5** The mathematical model is used to investigate the $2\theta$ in-phase and quadrature sense responses for ring resonators operating at large drive amplitudes, using the method of averaging. Comparisons are made against an equivalent ring resonator in which geometrical non-linearity is neglected, to investigate potential non-linear amplification caused by non-linearity. The effect of breaking the rotational symmetry on sensor performance is considered, and the impact of geometrical non-linearity is investigated. Key results are verified against a non-linear Finite Element analysis.

**Chapter 6** The mathematical model is used to investigate support designs that linearise the drive mode frequency backbone curve of supported ring resonators operating at large amplitudes. For selected improved support designs, the results obtained using the mathematical model are verified against a non-linear Finite Element analysis, and the accuracy of the mathematical results is discussed.

**Chapter 7** Main conclusions of this work are revised and suggestions for future work are proposed.

# Chapter 2

# Mathematical model for a supported ring-based CVG operating in the linear regime

## 2.1 Introduction

This Chapter deals with the dynamics of supported ring resonators operating in the linear regime, and lays the foundation for later work which relates to non-linearity. Chapter 1 introduced the importance of maintaining the rotational symmetry of ring resonators to achieve higher sensitivity to rotation and SNR, and to avoid sensing errors which have potential to degrade sensor performance. In this work, the ring is considered to be perfect and made of isotropic silicon, and it is shown that asymmetric support structures can break the rotational symmetry of the ring resonator. For rings undergoing linear vibration, references [11, 26] indicated that 8 identical supports uniformly spaced around the ring circumference maintain the rotational symmetry for $n = 2$.

In this Chapter, a mathematical model for a supported ring resonator based on the model introduced by Sérandour [29,34] is developed to include a generic number of supports $p$. The proposed model is used to investigate the numbers of supports that maintain the rotational symmetry in the linear regime, for any pair of $n\theta$ ring modes. The equation of motion of the drive and sense $n\theta$ modes are developed for rotationally symmetric supported ring resonators. A point mass imperfection is then added to the ring mid-line and expressions for the drive and sense responses are determined for the imperfect resonator. It will be shown that high sensitivity to rotation and good angular rate detection can be achieved only if the rotational symmetry of the supported ring resonator is maintained. In later work, ring and support geometrical non-linearity will be considered, and it will be shown that in some cases geometrical non-linearity effects on sensor performance are similar to those caused by a point mass imperfection.

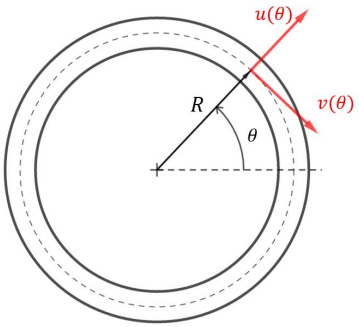
The structure of this Chapter is as follows. In Sections 2.2 and 2.3 a mathematical model is developed for a linear ring resonator (i.e. ring linear vibration and linear support stiffness) having a generic number of supports $p$. The model is used to determine kinetic and potential energy expressions for a supported ring resonator. The obtained energy expressions are used to investigate the numbers of supports that maintain the rotational symmetry in the linear regime. In Section 2.4, Lagrange's equation is used to determine the equations governing the $n\theta$ drive and sense modes motion for a rotationally symmetric supported ring resonator. In Section 2.5, a small point mass imperfection is added to the ring mid-line and breaks the rotational symmetry of the previously symmetric supported resonator. Equations of motion for the imperfect resonator are obtained and compared against those for a symmetric resonator. Analytical expressions for the drive and sense steady-state responses (amplitude and phase) are investigated based on the excitation of the drive mode into resonance; performance degradation caused by the breaking of rotational symmetry is demonstrated and discussed. Section 2.6 summarises the work done in this Chapter and reiterates key conclusions.

## 2.2 Mathematical model and energy expressions for a perfect unsupported ring

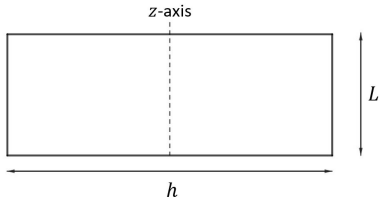
This Section illustrates the mathematical model developed for a perfect ring undergoing in-plane linear $n\theta$ vibration. The model is used to determine kinetic and potential energies expressions for the unsupported ring.

### 2.2.1 Unsupported ring model and linear deflection

Figure 2.1 shows a schematic diagram for a perfect ring having uniform rectangular cross-section, where $R$ is the ring mid-line radius, $h$ is the radial thickness and $L$ the axial length.




(a) In-plane ring.




(b) Ring cross-section.

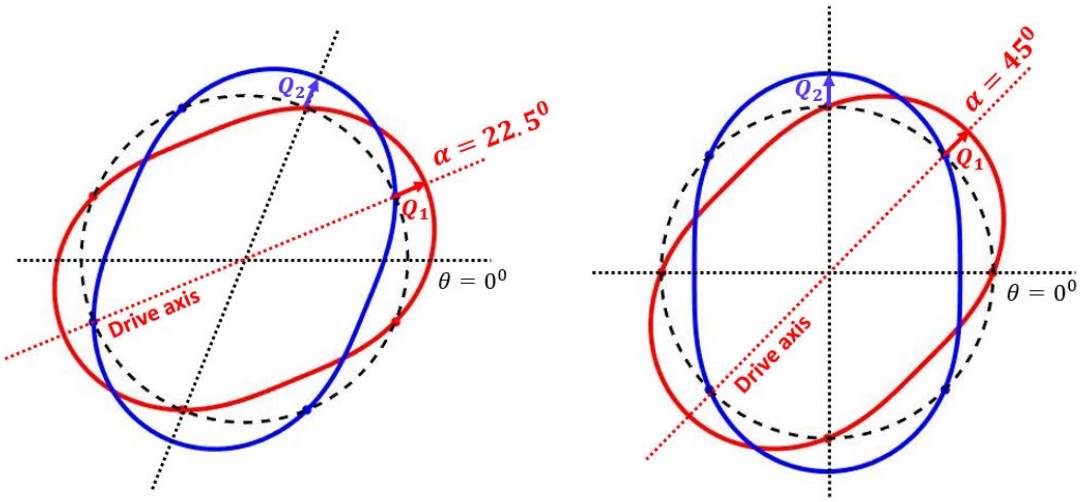
Figure 2.1: Diagram of the ring structure and in-plane displacements of the ring mid-line.

For a generic pair of in-plane flexural modes having $n$ nodal diameters, ring deflection can be described in terms of radial and tangential displacements $u(\theta, t)$ and $v(\theta, t)$, respectively, where $\theta$ defines the circumferential coordinate of the location considered. For ring vibration in the linear regime, radial and tangential deflections can be expressed as [24] (see equations (1.9)-(1.10)):

$$u(\theta, t) = Q_1(t) \cos n(\theta - \alpha) + Q_2(t) \sin n(\theta - \alpha) \tag{2.1}$$

$$v(\theta, t) = -\frac{Q_1(t)}{n} \sin n(\theta - \alpha) + \frac{Q_2(t)}{n} \cos n(\theta - \alpha) \tag{2.2}$$

where $Q_1(t)$ and $Q_2(t)$ vary with time and are generalised coordinates, and $\cos n\theta$ and $\sin n\theta$ are the shapes of the $n\theta$ modes of vibration, respectively indicated as drive mode and sense mode. Angle $\alpha$ in equations (2.1) and (2.2) is used to define the set of generalised coordinates considered. Figure 2.2 shows drive and sense $2\theta$ modes (i.e. $n = 2$) for $\alpha = 22.5°$ and $\alpha = 45°$, where reference circumferential coordinate $\theta = 0°$ is the horizontal.




(a) $\alpha = 22.5°$

(b) $\alpha = 45°$

Figure 2.2: Drive and sense $2\theta$ modes orientation for $\alpha = 22.5°$ and $\alpha = 45°$. Drive and sense generalised coordinates $Q_1$ and $Q_2$ are indicated. The drive axis location is defined by $\alpha$. Circumferential coordinate $\theta = 0°$ is the horizontal.

It is known that vibration modes of perfect rings have indeterminate position around the axis of symmetry [20,21]. In practice, harmonic radial forces having $\cos n\theta$ spatial distribution and frequency equal to the drive mode natural frequency are applied to the ring to excite the drive mode into resonance. In an ideal case, the drive axis will align with the principal direction of the applied force. Different directions of the force principal axis will imply different orientations of the drive axis around the ring circumference, and so a different $\alpha$ in equations (2.1) and (2.2). In what follows, a generic angle $\alpha$ is used in the displacements expressions.

### 2.2.2 Kinetic energy for an unsupported ring

This Section determines the kinetic energy for a ring vibrating under linear $n\theta$ deflection and rotating with constant angular rate $\Omega_z$ around the ring polar axis. To determine the kinetic energy stored in an infinitesimal ring mass element $dm$, centred at circumferential coordinate $\theta$, two frames of reference are defined: (i) a space-fixed frame of reference $x_F, y_F$ and (ii) a body-fixed frame of reference $x_R, y_R$ that rotates with angular rate $\Omega_z$, as illustrated in Figure 2.3.

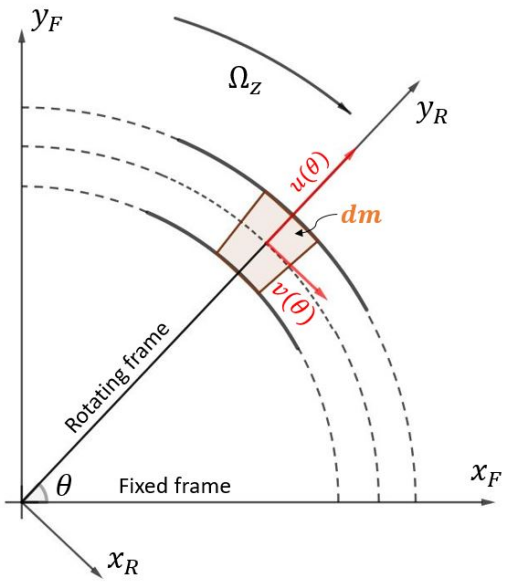



Figure 2.3: Diagram illustrating the space-fixed frame of reference $x_F, y_F$, the body-fixed frame of reference $x_R, y_R$ rotating with angular rate $\Omega_z$, and radial and tangential displacements of the infinitesimal ring mass element $dm$ at circumferential coordinate $\theta$.

The mass has mass $dm = \rho hLRd\theta$, where $\rho$ is the material density. By defining $\mathbf{r_0}$ to be the displacement vector of $dm$ in the inertial frame of reference, the infinitesimal kinetic energy $dT^L_{ring}$ is:

$$dT^L_{ring} = \frac{1}{2}\rho hLRd\theta \left(\frac{\partial \mathbf{r_0}}{\partial t}\right)^2 \tag{2.3}$$

The intention is to formulate the ring kinetic energy as function of radial and tangential ring

displacements $u(\theta)$ and $v(\theta)$ in equations (2.1)-(2.2). Therefore, vector $\frac{\partial \mathbf{r_0}}{\partial t}$ in equation (2.3) is expressed in terms of the displacement vector of $dm$ in the rotating frame of reference $\mathbf{r_{\Omega_{rot}}}$, and the angular velocity vector $\mathbf{\Omega_{rot}}$ using:

$$\frac{\partial \mathbf{r_0}}{\partial t} = \frac{\partial \mathbf{r_{\Omega_{rot}}}}{\partial t} + \mathbf{\Omega_{rot}} \times \mathbf{r_{\Omega_{rot}}} \tag{2.4}$$

Mass $dm$ moves in the plane of the ring, and the ring has angular velocity $\Omega_z$ about the $z$-axis, so vectors $\mathbf{r_{\Omega_{rot}}}$ and $\mathbf{\Omega_{rot}}$ respectively are:

$$\mathbf{r_{\Omega_{rot}}} = \begin{bmatrix} u(\theta) + R \\ v(\theta) \\ 0 \end{bmatrix} \tag{2.5}$$

$$\mathbf{\Omega_{rot}} = \begin{bmatrix} 0 \\ 0 \\ \Omega_z \end{bmatrix} \tag{2.6}$$

The kinetic energy of the ring is obtained by substituting (2.4)-(2.6) into (2.3) and integrating along the ring circumference. This gives:

$$T^L_{ring} = \frac{1}{2}\rho h L R \int_0^{2\pi} \left[\dot{u}^2 + \dot{v}^2 - 2\dot{u}v\Omega_z + 2\dot{v}(u+R)\Omega_z + (u+R)^2\Omega_z^2 + v^2\Omega_z^2\right] d\theta \tag{2.7}$$

The operation of ring-based resonators normally relies on the excitation of the $2\theta$ modes whose resonance frequencies are typically greater than 10 kHz, whilst the angular velocities detected are normally in the order of 1 $\frac{rad}{s}$ [12]. Under these circumstances, terms in $\Omega_z^2$ can be neglected from (2.7). Using expressions for $u(\theta)$ and $v(\theta)$ given by (2.1) and (2.2), and evaluating the integral in (2.7), the kinetic energy of the unsupported ring is:

$$T^L_{ring} = \frac{1}{2}\rho h L R \pi \left(\frac{n^2+1}{n^2}\right)\left(\dot{Q}_1^2 + \dot{Q}_2^2\right) + \frac{2}{n}\rho h L R \pi \Omega_z \left(-\dot{Q}_1 Q_2 + Q_1 \dot{Q}_2\right) \tag{2.8}$$

In this equation, the term involving $\Omega_z$ is associated with the Coriolis effect and the other term is independent of the angular rate and relates to the ring flexural vibration.

Kinetic energy expression (2.8) depends on the choice of generalised coordinates $Q_1$ and $Q_2$ which depend on $\alpha$ (see equations (2.1) and (2.2)). It can be shown that the form of $T^L_{ring}$ is unaltered when different sets of generalised coordinates are used. For example, one can use generalised coordinates $Q_{1\psi}$ and $Q_{2\psi}$, rotated by an angle $\psi$ from $Q_1$ and $Q_2$ as illustrated in Figure 2.4.

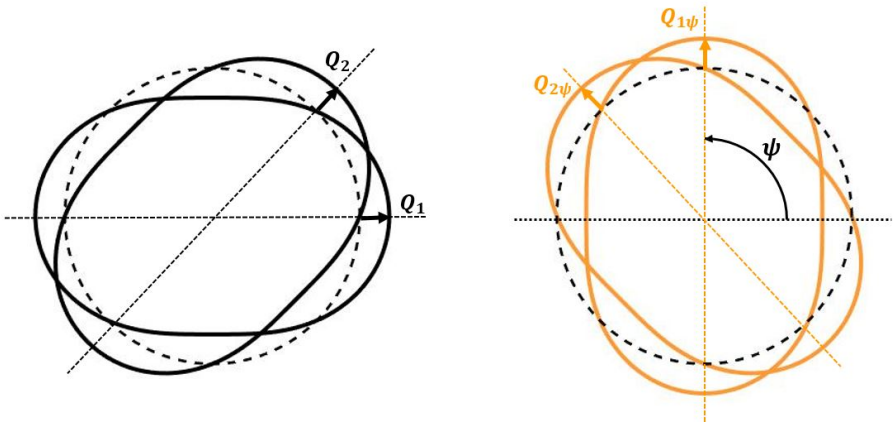



Figure 2.4: Generalised coordinates $Q_1$, $Q_2$ and $Q_{1\psi}$, $Q_{2\psi}$, rotated by an angle $\psi$ relative to each other.

It can be shown that:

$$Q_1 = Q_{1\psi}\cos\psi + Q_{2\psi}\sin\psi \tag{2.9}$$

$$Q_2 = -Q_{1\psi}\sin\psi + Q_{2\psi}\cos\psi \tag{2.10}$$

and

$$T^L_{ring}\big|_\psi = \frac{1}{2}\rho hLR\pi\left(\frac{n^2+1}{n^2}\right)\left(\dot{Q}^2_{1\psi}+\dot{Q}^2_{2\psi}\right) + \frac{2}{n}\rho hLR\pi\Omega_z\left(-\dot{Q}_{1\psi}Q_{2\psi}+Q_{1\psi}\dot{Q}_{2\psi}\right) \tag{2.11}$$

Comparing $T^L_{ring}\Big|_\psi$ in (2.11) to $T^L_{ring}$ in (2.8) it is clear that the kinetic energy is invariant to selected generalised coordinates: the expressions are identical except $Q_1$ and $Q_2$ are replaced

respectively by $Q_{1\psi}$ and $Q_{2\psi}$. This is because a perfect ring is rotationally symmetric.

### 2.2.3 Potential energy for an unsupported ring

The potential energy $V_{ring}^{L}$ for a perfect ring undergoing linear $n\theta$ vibration is given by [29]:

$$V_{ring}^{L} = \int_{0}^{2\pi} \frac{1}{2} \left( EI_{rs}\chi_{\theta}^{2} \right) Rd\theta \tag{2.12}$$

where $E$ is the Young's modulus, $I_{rs} = \frac{Lh^3}{12}$ is the second moment of area, and $\chi_\theta$ represents the change in the ring curvature from the undistorted to the distorted configuration caused by the ring in-plane flexural vibration, and can be approximated as [23, 29]:

$$\chi_{\theta} = \frac{1}{R^2} \left( \frac{\partial^2 u(\theta)}{\partial \theta^2} + u(\theta) \right) \tag{2.13}$$

By substituting (2.13) in (2.12) and evaluating the integral, it can be shown that the potential energy of the ring is:

$$V_{ring}^{L} = \frac{1}{24} \frac{ELh^3\pi}{R^3} \left( 1 + n^4 - 2n^2 \right) \left( Q_1^2 + Q_2^2 \right) \tag{2.14}$$

Similar to the kinetic energy, it can be shown that potential energy expression (2.14) is unaltered when a different set of generalised coordinates is used, because the ring is rotationally symmetric. Therefore, the sum of the kinetic and potential ring energies $\mathcal{E}_{ring}^{L} = T_{ring}^{L} + V_{ring}^{L}$ is rotationally symmetric.

## 2.3 Mathematical model and energy expressions for linear supports

This Section illustrates the mathematical model used for modelling the support structure and the assumptions made in its development. The support is considered to be attached to a

ring undergoing linear $n\theta$ vibration. Firstly, kinetic and potential energies are determined for a single support. The energy for a generic number of supports $p$ uniformly spaced around the ring circumference is then obtained by summing the kinetic and potential energies of a single support over $p$. Similar to that proposed in the previous Section for an unsupported ring, the obtained support energy expressions are analysed to investigate whether the supports maintain the rotational symmetry of the resonator.

### 2.3.1 Mathematical model for a linear support structure

Figure 2.5 shows a schematic representation of a support attached to the ring and anchored to the substrate (i.e. fixed frame). Figure 2.6 shows the mathematical model used to model the same support for resonators vibrating in the linear regime. This model was introduced and initially developed by Sérandour [29, 34]. The support inertia and stiffness are modelled by equivalent mass-spring elements acting in the radial and tangential directions. The inertia of the support in the radial and tangential directions are modelled by discrete masses $m_r$ and $m_t$, respectively, and the stiffness by linear springs having stiffness coefficients $k_{r_1}$ and $k_{t_1}$, respectively. Masses and stiffness coefficients for mass-spring elements in the radial and tangential directions are allowed to be different from each other as the mechanical properties of the supports are normally different along these directions.

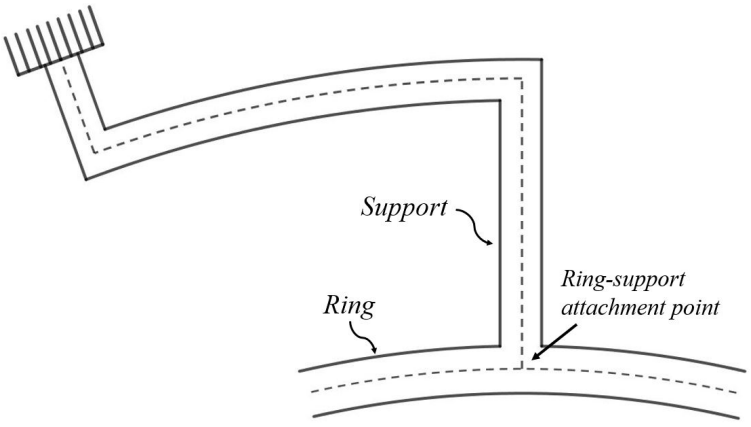



Figure 2.5: In-plane schematic representation of a support attached to the ring.

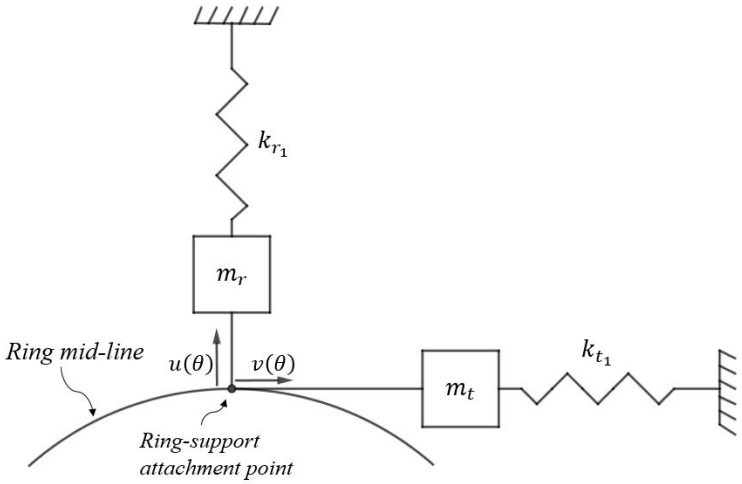



Figure 2.6: Diagram of the mathematical model proposed for representing the inertia and stiffness of a support along the radial and tangential directions.

The support model is developed by assuming that the $n\theta$ vibration of the ring is unaltered by the presence of the supports, so that the displacement of the ring-support attachment point can be expressed in terms of the radial and tangential linear ring displacements (i.e. equations (2.1) and (2.2)). Moreover, it is assumed that the local radial and tangential directions at the ring-support attachment point are principal axes of stiffness for the support.

Mass and stiffness coefficients ($m_r$, $m_t$, $k_{r_1}$, $k_{t_1}$) are determined using a Finite Element analysis of a single support. The linear radial and tangential stiffness coefficients are found by applying radial and tangential static forces at the support end that is attached to the ring, and performing static analyses to calculate the radial and tangential displacements caused by applied forces. Radial and tangential mass coefficients are obtained by applying radial and tangential harmonic forces at the same point, where the applied frequency matches the resonance frequency of the pair of $n\theta$ modes used in operation. Harmonic response analyses are performed to obtain amplitude and phase of the radial and tangential responses in steady-state. Under the assumption that the radial and tangential directions are principal axes of stiffness for the support, the tangential displacement caused by forces applied in

the radial direction is constrained to be zero; similarly, the radial displacement following the application of tangential forces is set to zero. Moreover, having assumed that the ring vibration is unaltered by the support, the rotation around the $z$-axis of the support end attached to the ring is constrained to be identical to rotation of the unsupported ring at the same point. Further details about the approach used to determine mass and stiffness coefficients are described in Appendix A, where mass and stiffness coefficients used to model practical ring-based MEMS CVGs supports are calculated and shown.

### 2.3.2 Kinetic energy for a single support

It is initially assumed that the support structure consists of one single support attached to the ring at angular position $\theta = \theta_S$. The kinetic energy of the support $T_S^L$ is given by:

$$T_S^L = \frac{1}{2} m_r \dot{u}^2(\theta_S) + \frac{1}{2} m_t \dot{v}^2(\theta_S) \tag{2.15}$$

where (under the assumption made of ring structure being dominant compared to the support structure) $u(\theta_S)$ and $v(\theta_S)$ coincide with ring deflections in (2.1) and (2.2) calculated for $\theta_S$. The proposed kinetic energy expression does not include rotational contribution from the applied angular rate. This simplification is made considering that typically the ring inertia is much larger than the support inertia.

### 2.3.3 Potential energy for a single support

The potential strain energy of a single support $V_S^L$ can be expressed as:

$$V_S^L = \frac{1}{2} \mathbf{u}^{\mathrm{T}} \mathbf{K_S^L} \mathbf{u} \tag{2.16}$$

where $\mathbf{u}$ is the displacements vector $\mathbf{u} = [u(\theta_S) \quad v(\theta_S)]^{\mathrm{T}}$ and $\mathbf{K_S^L}$ the support stiffness matrix. Under the assumption that the radial and tangential directions are principal axes of stiffness

for the support, $\mathbf{K_S^L}$ is the diagonal matrix below:

$$\mathbf{K_S^L} = \begin{bmatrix} k_{r_1} & 0 \\ 0 & k_{t_1} \end{bmatrix} \tag{2.17}$$

and potential strain energy (2.16) can be re-written in the following scalar notation:

$$V_S^L = \frac{1}{2} k_{r_1} u^2(\theta_S) + \frac{1}{2} k_{t_1} v^2(\theta_S) \tag{2.18}$$

If radial and tangential displacements are not principal axes of stiffness for the support, matrix $\mathbf{K_S^L}$ is symmetric with non-zero off-diagonal terms indicating coupling between the radial and tangential deflections. In this work, $\phi_{PA}$ defines the angle between the pair of orthogonal coordinates $x_{PA}$ and $y_{PA}$ representing the principal axes of stiffness of the support, and the radial and tangential directions. To determine $\phi_{PA}$, the full matrix $\mathbf{K_S^L}$ is calculated using a Finite Element analysis in a similar way to that proposed to determine $k_{r_1}$ and $k_{t_1}$, except the ring-support attachment point is free to move in both the radial and tangential directions when radial and tangential forces are applied. Full matrix $\mathbf{K_S^L}$ is used in the eigenvalue problem below:

$$\mathbf{K_S^L z_{PA}} = \mathbf{\Lambda_S^L z_{PA}} \tag{2.19}$$

Solving (2.19), angle $\phi_{PA}$ can be identified from the eigenvector matrix $\mathbf{z_{PA}}$, and support stiffness along the principal axes of stiffness are given by eigenvalue matrix $\mathbf{\Lambda_S^L}$. In later work, when the mathematical model is used to obtain numerical results for the drive and sense responses of practical supported ring-based CVGs geometries, angle $\phi_{PA}$ is calculated to quantify the accuracy of approximating the full stiffness matrix $\mathbf{K_S^L}$ with its simplified diagonal version in (2.17). Further details on the procedure used to determine $\phi_{PA}$ using a Finite Element analysis are provided in Appendix A.

### 2.3.4 Energy expressions for p supports

In previous sections, kinetic and potential energies have been calculated for a single support. Using (2.1) and (2.2) to describe $u(\theta_S)$ and $v(\theta_S)$ in kinetic and potential support energies (2.15) and (2.18), the total energy of a single support $\mathcal{E}_S^L = T_S^L + V_S^L$ can be expressed as:

$$\begin{aligned}\mathcal{E}_S^L = &\left(\frac{m_r}{4} + \frac{m_t}{4n^2}\right)\left(\dot{Q}_1^2 + \dot{Q}_2^2\right) + \left(\frac{k_{r_1}}{4} + \frac{k_{t_1}}{4n^2}\right)\left(Q_1^2 + Q_2^2\right) + \\ &+ \cos 2n\left(\theta_S - \alpha\right)\left[\left(\frac{m_r}{4} + \frac{m_t}{4n^2}\right)\left(\dot{Q}_1^2 - \dot{Q}_2^2\right) + \left(\frac{k_{r_1}}{4} + \frac{k_{t_1}}{4n^2}\right)\left(Q_1^2 - Q_2^2\right)\right] + \\ &+ \sin 2n\left(\theta_S - \alpha\right)\left[\left(\frac{m_r}{2} + \frac{m_t}{2n^2}\right)\dot{Q}_1\dot{Q}_2 + \left(\frac{k_{r_1}}{2} + \frac{k_{t_1}}{2n^2}\right)Q_1Q_2\right]\end{aligned} \tag{2.20}$$

Unlike the ring energy in Section 2.2 which was shown to be rotationally symmetric, it is clear from (2.20) that the single support energy expression is not rotationally symmetric, due to the presence of the $\alpha$ terms. This can be shown by expressing the support energy $\mathcal{E}_S^L$ in terms of generalised coordinates $Q_{1\psi}$ and $Q_{2\psi}$ rotated by a generic angle $\psi$ from $Q_1$ and $Q_2$ (see Figure 2.4). Using transformations (2.9) and (2.10), terms $\left(Q_1^2 - Q_2^2\right)$ and $Q_1Q_2$ are re-written as:

$$\left(Q_1^2 - Q_2^2\right)\big|_\psi = Q_{1\psi}^2\left(\cos^2\psi - \sin^2\psi\right) + Q_{2\psi}^2\left(\sin^2\psi - \cos^2\psi\right) + 4Q_{1\psi}Q_{2\psi}\cos\psi\sin\psi$$

$$Q_1Q_2\big|_\psi = \left(Q_{2\psi}^2 - Q_{1\psi}^2\right)\cos\psi\sin\psi + Q_{1\psi}Q_{2\psi}\left(\cos^2\psi - \sin^2\psi\right)$$

implying that energy $\mathcal{E}_S^L\big|_\psi$ in generalised coordinates $Q_{1\psi}$ and $Q_{2\psi}$ is different from $\mathcal{E}_S^L$ in (2.20). Thus, the use of one support breaks the rotational symmetry of the ring resonator.

For practical CVG resonators, multiple identical supports are uniformly spaced around the ring circumference i.e. if there are $p$ supports they are located at an angular distance of $\frac{360}{p}$ degrees from each other. In what follows it is assumed that one support is attached at the

reference circumferential coordinate $\theta = 0^0$ (i.e. the horizontal), as illustrated in Figure 2.7.

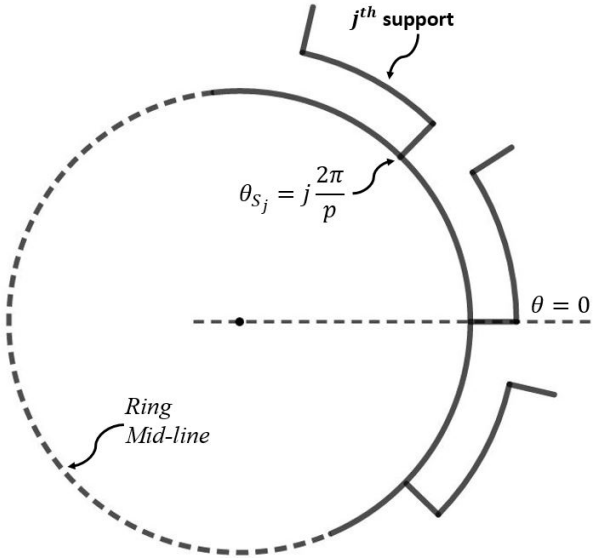



Figure 2.7: Schematic diagram for a ring having $p$ supports. One support is attached at the reference circumferential coordinate $\theta = 0^0$. The generic $j^{th}$ support is attached to the ring at $\theta_{S_j} = j\frac{2\pi}{p}$.

The energy of the $j^{th}$ support attached to the ring at $\theta_{S_j} = j\frac{2\pi}{p}$ is given in equation (2.20) with $\theta_S$ replaced by $\theta_{S_j}$. To calculate energy associated with $p$ supports, kinetic and potential energies (2.15) and (2.18) are summed over all supports to give:

$$T_S^L = \sum_{j=0}^{p-1}\left[\left(\frac{m_r}{4}+\frac{m_t}{4n^2}\right)\left(\dot{Q}_1^2+\dot{Q}_2^2\right)\right]+\sum_{j=0}^{p-1}\cos 2n\left(j\frac{2\pi}{p}-\alpha\right)\left[\left(\frac{m_r}{4}-\frac{m_t}{4n^2}\right)\left(\dot{Q}_1^2-\dot{Q}_2^2\right)\right]+ \\ +\sum_{j=0}^{p-1}\sin 2n\left(j\frac{2\pi}{p}-\alpha\right)\left[\left(\frac{m_r}{2}-\frac{m_t}{2n^2}\right)\dot{Q}_1\dot{Q}_2\right] \tag{2.21}$$

$$V_S^L = \sum_{j=0}^{p-1}\left[\left(\frac{k_{r_1}}{4}+\frac{k_{t_1}}{4n^2}\right)\left(Q_1^2+Q_2^2\right)\right]+\sum_{j=0}^{p-1}\cos 2n\left(j\frac{2\pi}{p}-\alpha\right)\left[\left(\frac{k_{r_1}}{4}-\frac{k_{t_1}}{4n^2}\right)\left(Q_1^2-Q_2^2\right)\right]+ \\ +\sum_{j=0}^{p-1}\sin 2n\left(j\frac{2\pi}{p}-\alpha\right)\left[\left(\frac{k_{r_1}}{2}-\frac{k_{t_1}}{2n^2}\right)Q_1Q_2\right] \tag{2.22}$$

Energies (2.21) and (2.22) consist of an invariant part (independent of $\alpha$) that is rotationally

symmetric, and another part that breaks the rotational symmetry of the supported ring resonator. Depending on the pair of flexural $n$ modes considered and the number of supports $p$, it can be shown that:

$$\sum_{j=0}^{p-1} \cos 2n\left(j\frac{2\pi}{p}-\alpha\right) = \begin{cases} 0 & \text{if } \frac{2n}{p} \text{ is not an integer} \\ p\cos 2n\alpha & \text{if } \frac{2n}{p} \text{ is an integer} \end{cases} \tag{2.23}$$

$$\sum_{j=0}^{p-1} \sin 2n\left(j\frac{2\pi}{p}-\alpha\right) = \begin{cases} 0 & \text{if } \frac{2n}{p} \text{ is not an integer} \\ p\sin 2n\alpha & \text{if } \frac{2n}{p} \text{ is an integer} \end{cases} \tag{2.24}$$

Hence, if the number of supports $p$ used is such that $\frac{2n}{p}$ is not an integer, all terms involving $\alpha$ that break the rotational symmetry of support kinetic and potential energies $T_S^L$ and $V_S^L$ are zero. In such cases, kinetic and potential energy expressions reduce to the invariant symmetric parts of equations (2.21) and (2.22).

The energy of the supported ring resonator $\mathcal{E}_R^L = \mathcal{E}_{ring}^L + \mathcal{E}_S^L$ is obtained by summing ring energies (2.8) and (2.14) and $p$ supports energies (2.21) and (2.22), and using relations (2.23) and (2.24). If the ratio $\frac{2n}{p}$ is not an integer, this gives:

$$\begin{aligned} \mathcal{E}_R^L =& \frac{1}{2}\rho hLR\pi\left(\frac{n^2+1}{n^2}\right)\left(\dot{Q}_1^2+\dot{Q}_2^2\right)+\frac{1}{24}\frac{ELh^3\pi}{R^3}\left(1+n^4-2n^2\right)\left(Q_1^2+Q_2^2\right)+ \\ &+p\left[\left(\frac{m_r}{4}+\frac{m_t}{4n^2}\right)\left(\dot{Q}_1^2+\dot{Q}_2^2\right)+\left(\frac{k_{r_1}}{4}+\frac{k_{t_1}}{4n^2}\right)\left(Q_1^2+Q_2^2\right)\right]+ \\ &+\frac{2}{n}\rho hLR\pi\Omega_z\left(-\dot{Q}_1Q_2+Q_1\dot{Q}_2\right) \end{aligned} \tag{2.25}$$

It can be shown that resonator energy $\mathcal{E}_R^L$ is symmetric and invariant to the choice of generalised coordinates $Q_1$ and $Q_2$. In later work, it will be shown that invariant supported ring resonator energies ensure drive and sense $n\theta$ modes have equal natural frequencies and are decoupled from each other. Therefore, numbers of supports $p$ such that $\frac{2n}{p}$ is not an integer ensure good performance for ring resonators operating in the linear regime.

The proposed approach used to determine the numbers of supports that maintain the rotational symmetry of supported ring resonators is useful when designing symmetric resonators operating in any $n\theta$ ring modes. Table 2.1 indicates some combinations of $n$ and $p$ that maintain ("SYM") or break ("ASY") the rotational symmetry of supported ring resonators, for CVGs operating in the linear regime.

| | Numbers of supports $p$ | | | | | | | | | | | |
|---|---|---|---|---|---|---|---|---|---|---|---|---|
| | 2 | 3 | 4 | 5 | 6 | 7 | 8 | 9 | 10 | 12 | 14 | 16 |
| $n = 2$ | ASY | SYM | ASY | SYM | SYM | SYM | SYM | SYM | SYM | SYM | SYM | SYM |
| $n = 3$ | ASY | ASY | SYM | SYM | ASY | SYM | SYM | SYM | SYM | SYM | SYM | SYM |
| $n = 4$ | ASY | SYM | ASY | SYM | SYM | SYM | ASY | SYM | SYM | SYM | SYM | SYM |

Table 2.1: Combinations of $n$ and $p$ that maintain ("SYM") or break ("ASY") the rotational symmetry of the supported ring resonator in the linear regime.

For a given modal number $n$, "SYM" in Table 2.1 indicates the numbers of supports $p$ that maintain the rotational symmetry in the linear regime (i.e. $\frac{2n}{p}$ is not an integer). Typically, ring-based CVGs operate based on the $2\theta$ modes excitation i.e. $n = 2$, and Table 2.1 indicates that ring resonators having 8, 12 or 16 (and others) supports maintain the rotational symmetry. For practical CVG devices, 8 and 16 supports are commonly used to maintain the rotational symmetry of resonators based on the $2\theta$ modes.

The combinations that break the rotational symmetry in the linear regime (indicated by "ASY") have no practical use as a CVG, so in what follows only numbers of supports that maintain the rotational symmetry in the linear regime are considered.

In the next Chapter, non-linear effects will be considered, and a similar approach to that shown in this Section will be used to determine the support numbers that maintain the rotational symmetry of a supported resonator operating at large vibration amplitude.

## 2.4 Drive and sense equations of motion for a symmetric linear supported ring resonator

In this Section, drive and sense governing equations are obtained for a symmetric ring resonator operating in any pair of $n\theta$ ring modes and having a number of supports $p$ such that $\frac{2n}{p}$ is not an integer. Drive and sense equations are determined using Lagrange's equation in generalised coordinates $Q_1$ and $Q_2$ as:

$$\frac{d}{dt}\frac{\partial T}{\partial \dot{Q}_k} - \frac{\partial T}{\partial Q_k} + \frac{\partial V}{\partial Q_k} + \frac{\partial D}{\partial \dot{Q}_k} = G_k \tag{2.26}$$

($k = 1$ for the drive, $k = 2$ for the sense) where $T = T^L_{ring} + T^L_S$ is the kinetic energy of ring and $p$ supports, respectively given by (2.8) and (2.21), and $V = V^L_{ring} + V^L_S$ is the potential energy of ring and $p$ supports, respectively given by (2.14) and (2.22). Equations are developed for a symmetric resonator, so that terms involving $\alpha$ in support energies (2.21) and (2.22) are zero (using relations (2.23), (2.24) for $\frac{2n}{p}$ not an integer). Term $D$ indicates the energy dissipation due to viscous friction; damping in drive and sense generalised coordinates is considered to be approximately the same, so in what follows it will be indicated by damping coefficient $c$. $G_k$ is the generalised force acting on generalised coordinate $Q_k$. The drive mode only is considered to be excited by modal harmonic driving force having magnitude $F_D$ and generic frequency $\Omega$. Under these circumstances, $G_2 = 0$ and generalised force $G_1$ is:

$$G_1 = F_D \cos \Omega t \tag{2.27}$$

Lagrange's equation for $Q_1$ and $Q_2$ gives the drive and sense equations of motion below:

$$M_{res}\ddot{Q}_1 + c\dot{Q}_1 + K_{res}Q_1 - \frac{4n}{(n^2+1)}M_{ring}\Omega_z\dot{Q}_2 = F_D \cos \Omega t \tag{2.28}$$

$$M_{res}\ddot{Q}_2 + c\dot{Q}_2 + K_{res}Q_2 + \frac{4n}{(n^2+1)}M_{ring}\Omega_z\dot{Q}_1 = 0 \tag{2.29}$$

where the modal mass $M_{res}$ and stiffness $K_{res}$ for the supported ring resonator are:

$$M_{res} = M_{ring} + pM_S \tag{2.30}$$

$$K_{res} = K_{ring} + pK_S \tag{2.31}$$

In these equations, $M_{ring}$ and $K_{ring}$ are the modal mass and stiffness of the unsupported ring, and $M_S$ and $K_S$ are the modal mass and stiffness for a single support, where:

$$M_{ring} = \left(\frac{n^2+1}{n^2}\right)\rho hLR\pi \tag{2.32}$$

$$K_{ring} = \frac{ELh^3\pi}{12R^3}\left(n^4 - 2n^2 + 1\right) \tag{2.33}$$

$$M_S = \frac{m_r}{2} + \frac{m_t}{2n^2} \tag{2.34}$$

$$K_S = \frac{k_{r_1}}{2} + \frac{k_{t_1}}{2n^2} \tag{2.35}$$

Dividing both drive and sense equations by $M_{res}$, (2.28) and (2.29) can be re-written as:

$$\ddot{Q}_1 + \frac{\omega_0}{Q}\dot{Q}_1 + \omega_0^2 Q_1 - \mathcal{B}\Omega_z\dot{Q}_2 = \frac{F_D}{M_{res}}\cos\Omega t \tag{2.36}$$

$$\ddot{Q}_2 + \frac{\omega_0}{Q}\dot{Q}_2 + \omega_0^2 Q_2 + \mathcal{B}\Omega_z\dot{Q}_1 = 0 \tag{2.37}$$

where $\omega_0$ is the natural frequency of the $n\theta$ modes, and the damping is expressed using quality factor $Q$ (it can be shown that $\frac{c}{M_{res}} = \frac{\omega_0}{Q}$). Coefficient $\mathcal{B}$ is the gyroscopic coupling factor (also known as Bryan factor [2]) and depends on the modal mass properties of the ring resonator; in practice, for a ring $\mathcal{B}$ is approximatively:

$$\mathcal{B} = \frac{4n}{(n^2+1)} \tag{2.38}$$

From equations (2.36) and (2.37) it is clear when the rotational symmetry is maintained there is no dependence on $\alpha$, and drive and sense natural frequencies $\omega_0$ are equal. In these equations, the Coriolis force only couples the drive and sense modes when angular rate is applied. In the next Section, a small point mass imperfection is added on the ring mid-line to investigate how the breaking of rotational symmetry affects drive and sense governing equations.

## 2.5 Supported ring resonator having a point mass imperfection

This Section describes the dynamics of drive and sense $n\theta$ modes for a ring resonator having a small point mass imperfection on the ring mid-line at circumferential coordinate $\theta_m$, as illustrated in Figure 2.8.

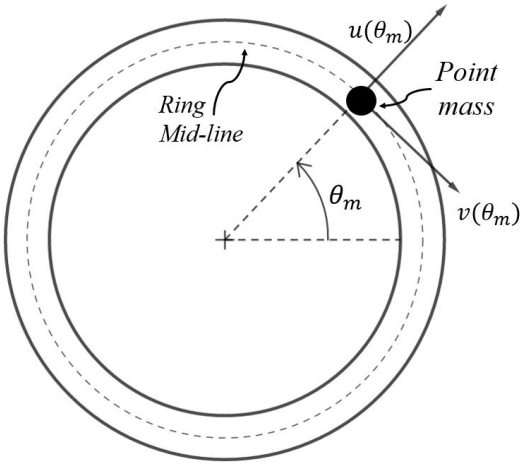



Figure 2.8: Diagram of in-plane ring having a point mass imperfection at circumferential coordinate $\theta_m$.

The ring is supported by $p$ supports that maintain the rotational symmetry in the linear regime (i.e. $\frac{2n}{p}$ is not an integer), so that the rotational symmetry is broken by the point mass.

### 2.5.1 Mathematical model and kinetic energy for a point mass imperfection

A simple mathematical model for a point mass imperfection is developed to obtain the point mass kinetic energy. Similar to the mathematical model described in Section 2.3.1 to model a single support inertia, Figure 2.9 shows the equal concentrated masses $m$ for modelling the inertia of a point mass imperfection in the radial and tangential directions.

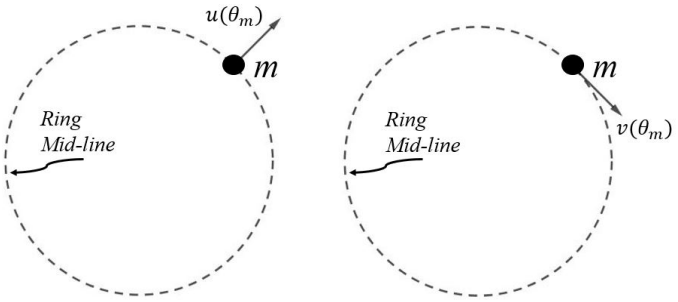



Figure 2.9: Model for representing a point mass imperfection.

The point mass is considered to be small so that ring $n\theta$ modes shapes are unchanged compared to a perfect ring. Under these circumstances, the kinetic energy $T_m$ for a small mass imperfection is:

$$T_m = \frac{1}{2}m\dot{u}^2(\theta_m) + \frac{1}{2}m\dot{v}^2(\theta_m) \tag{2.39}$$

where $u(\theta_m)$, $v(\theta_m)$ are the ring deflections. Using (2.1) and (2.2) for $\theta = \theta_m$ in (2.39), kinetic energy $T_m$ can be expressed in terms of drive and sense generalised coordinates $Q_1$ and $Q_2$. Similar to the single support energy given by equation (2.20), it can be shown that point mass energy $T_m$ is not invariant to the choice of generalised coordinates and involves terms in $(\theta_m - \alpha)$ which break the rotational symmetry of resonator energy expression.

### 2.5.2 Drive and sense equations of motion

The equations of motion governing drive and sense $n\theta$ modes are determined using Lagrange's equation as in Section 2.4. Kinetic energy $T_m$ in (2.39) is considered in Lagrange's

equation (2.26) to take account of the mass imperfection. Drive and sense equations of motion (2.28) and (2.29) become:

$$\left(M_{res} + \frac{m(n^2+1)}{2n^2} + \frac{m(n^2-1)}{2n^2}\cos 2n(\theta_m - \alpha)\right)\ddot{Q}_1 + \frac{m(n^2-1)}{2n^2}\sin 2n(\theta_m - \alpha)\ddot{Q}_2 + \\ + c\dot{Q}_1 + K_{res}Q_1 - \frac{4n}{(n^2+1)}M_{ring}\Omega_z\dot{Q}_2 = F_D\cos\Omega t \tag{2.40}$$

$$\left(M_{res} + \frac{m(n^2+1)}{2n^2} - \frac{m(n^2-1)}{2n^2}\cos 2n(\theta_m - \alpha)\right)\ddot{Q}_2 + \frac{m(n^2-1)}{2n^2}\sin 2n(\theta_m - \alpha)\ddot{Q}_1 + \\ + c\dot{Q}_2 + K_{res}Q_2 + \frac{4n}{(n^2+1)}M_{ring}\Omega_z\dot{Q}_1 = 0 \tag{2.41}$$

where $M_{res}$ and $K_{res}$ are given by (2.30) and (2.31), and $M_{ring}$ by (2.32). Obtained equations indicate that the point mass causes drive and sense modal masses to be different to each other, due to $\cos 2n(\theta_m - \alpha)$ term which has opposite sign in the drive and sense equations. This causes the resonance frequencies of drive and sense modes to split. Moreover, terms in $\sin 2n(\theta_m - \alpha)$ couple drive and sense equations, causing inertial backwards coupling (i.e. from the sense response to the drive response) in (2.40), and forwards coupling (i.e. from the drive to the sense) in (2.41) which do not relate to rotation. Both drive and sense equations involve $\alpha$ terms.

In practice, the drive mode response amplitude is typically orders of magnitude larger than the sense mode response [1, 5], because the drive mode is directly excited into vibration by harmonic driving force, whilst the sense mode is excited by the Coriolis force and the inertial coupling term in $\ddot{Q}_1$. It is then possible to approximate drive equation (2.40) by neglecting the backwards coupling terms involving $\ddot{Q}_2$ and $\dot{Q}_2$.

Dividing drive equation (2.40) by the resonator modal mass in the drive direction $M_D = M_{res} + \frac{m(n^2+1)}{2n^2} + \frac{m(n^2-1)}{2n^2}\cos 2n(\theta_m - \alpha)$, dividing sense equation (2.41) by the resonator modal mass in the sense direction $M_S = M_{res} + \frac{m(n^2+1)}{2n^2} - \frac{m(n^2-1)}{2n^2}\cos 2n(\theta_m - \alpha)$, and neglecting terms in $\ddot{Q}_2$ and $\dot{Q}_2$ from the drive equation, drive and sense equations can be

re-written as:

$$\ddot{Q}_1 + \frac{\omega_D}{Q}\dot{Q}_1 + \omega_D^2 Q_1 = \frac{F_D}{M_D}\cos\Omega t \tag{2.42}$$

$$\ddot{Q}_2 + \frac{\omega_S}{Q}\dot{Q}_2 + \omega_S^2 Q_2 + m_c\ddot{Q}_1 + \mathcal{B}\Omega_z\dot{Q}_1 = 0 \tag{2.43}$$

where $\omega_D$ and $\omega_S$ are the drive and sense resonance frequencies, respectively, and $m_c$ is the forward coupling term divided by $M_S$ i.e. $m_c = \frac{m(n^2-1)}{M_S 2n^2}\sin 2n(\theta_m - \alpha)$. Similar to the drive and sense equations for the symmetric resonator in Section 2.4, the damping is indicated using quality factor $Q$ and the gyroscopic coupling factor is approximated by coefficient $\mathcal{B}$ given by (2.38). Under the assumptions made, the drive response is independent of the sense motion, whilst the sense mode is externally excited by the Coriolis force and by term in $m_c$ involving the drive response.

### 2.5.3 Drive and sense responses

Drive and sense equations (2.42) and (2.43) are solved to determine the drive and sense responses (amplitude, phase) for the supported ring resonator having a point mass imperfection. For a practical CVG, the drive mode is excited into resonance so that the drive modal force has frequency $\Omega = \omega_D$ in (2.42). Under these circumstances, the steady-state drive response is 90° out-of-phase relative to applied excitation, and can be expressed as:

$$Q_1(t) = q_1 \sin\omega_D t \tag{2.44}$$

where $q_1$ is the drive response amplitude. Using (2.44) in drive equation (2.42) it can be shown that the amplitude of the drive response at resonance is:

$$q_1 = \frac{F_D}{M_D\omega_D^2}Q \tag{2.45}$$

and can be maximised by increasing the Q-factor and by increasing the magnitude of applied driving force, or reducing the modal mass.

The sense response in steady-state motion can be expressed as:

$$Q_2(t) = q_2 \sin(\omega_D t + \phi_{SD}) \tag{2.46}$$

where $q_2$ is the oscillation amplitude and $\phi_{SD}$ the phase of the sense response relative to the drive response. Sense response (2.46) can be demodulated into an in-phase response $q_{2I}$ (in-phase or 180° out-of-phase relative to the drive response) and quadrature response $q_{2Q}$ (90° out-of-phase relative to the drive response):

$$Q_2(t) = q_{2I} \sin \omega_D t + q_{2Q} \cos \omega_D t \tag{2.47}$$

where $q_{2I} = q_2 \cos \phi_{SD}$ and $q_{2Q} = q_2 \sin \phi_{SD}$. Chapter 1 stated that the in-phase response $q_{2I}$ is used to measure the angular rate whilst the quadrature response is zero for an ideal gyro. Using (2.44) and (2.47) in sense equation (2.43) and manipulating, one can obtain the following two equations governing the in-phase and quadrature sense responses:

$$(2\Delta\omega_0)q_{2Q} + \frac{\omega_D \omega_S}{Q} q_{2I} = -\mathcal{B}\Omega_z q_1 \omega_D \tag{2.48}$$

$$(2\Delta\omega_0)q_{2I} - \frac{\omega_D \omega_S}{Q} q_{2Q} = m_c q_1 \omega_D^2 \tag{2.49}$$

where $\Delta\omega_0 \approx \frac{(\omega_S^2 - \omega_D^2)}{2}$ is the frequency split between drive and sense resonance frequencies. From these equations, it is noted that inertial coupling term $m_c$ and frequency split $\Delta\omega_0$ give rise to non-zero quadrature response $q_{2Q}$; moreover, frequency split $\Delta\omega_0$ couples in-phase and quadrature responses. It can be shown that the amplitudes of the in-phase and quadrature responses respectively are:

$$q_{2I} = -\frac{\mathcal{B}\Omega_z q_1 \omega_D (\frac{\omega_D \omega_S}{Q}) + m_c q_1 \omega_D^2 (2\Delta\omega_0)}{4\Delta\omega_0^2 + \left(\frac{\omega_D \omega_S}{Q}\right)^2} \tag{2.50}$$

$$q_{2Q} = -\frac{\mathcal{B}\Omega_z q_1 \omega_D (2\Delta\omega_0) - m_c q_1 \omega_D^2 \frac{\omega_D \omega_S}{Q}}{4\Delta\omega_0^2 + \left(\frac{\omega_D \omega_S}{Q}\right)^2} \tag{2.51}$$

Inertial coupling and frequency split cause the in-phase response to be non-zero in the absence of rotation (i.e. $q_{2I} \neq 0$ for $\Omega_z = 0$), generating the so-called zero-rate-output (or ZRO) introduced in Section 1.4. When the in-phase response $q_{2I}$ is measured to detect the angular rate, terms in $\Delta\omega_0$ and $m_c$ in equation (2.50) complicate the determination of $\Omega_z$.

If the resonator is perfect and rotationally symmetric (i.e. $\Delta\omega_0 = 0$ so $\omega_D = \omega_S = \omega_0$, and $m_c = 0$ in equations (2.50) and (2.51)), the quadrature response is zero and the in-phase sense response has amplitude:

$$q_2 = \frac{\mathcal{B}\Omega_z q_1}{\omega_0} Q \tag{2.52}$$

In this case, angular rate $\Omega_z$ is easily detectable by measuring the sense response as $\Omega_z = \frac{q_2 \omega_0}{\mathcal{B} q_1 Q}$. If the same approach is repeated for the imperfect resonator using the in-phase amplitude $q_{2I}$ given by (2.50), the measured angular rate $\Omega_z$ would not be the same as the actual angular rate experienced by the device. This demonstrates how imperfections that break the rotational symmetry of the resonator cause sensing errors (i.e. quadrature errors) that have potential to degrade the quality of rate measurement.

In summary, the sense response in equation (2.52) applies to a perfect ring having a number of supports $p$ that maintain the rotational symmetry of the resonator (i.e. $\frac{2n}{p}$ is not an integer). Rotationally symmetric expressions for ring and support energies ensure the angular rate detection is not adversely affected by sensing errors, and the maximum sensitivity is achieved. Otherwise, if ring and support energies are asymmetric and depend on the choice of generalised coordinates, the drive and sense equations of motion are coupled by inertial (or elastic) terms and drive and sense resonance frequencies are split. Under these circumstances, the sense response amplitude reduces, and the rate measurement quality degrades.

## 2.6 Summary and conclusions

This Chapter developed a mathematical model for a supported ring resonator operating in a generic pair of $n\theta$ modes in the linear regime. The developed mathematical model for ring and $p$ supports was used to determine analytical expressions for the kinetic and potential energies of the resonator. It was noted that the ring energy is invariant to the choice of generalised coordinates and independent of drive angle $\alpha$ as perfect rings are rotationally symmetric. It was found that if the number of supports $p$ is such that $\frac{2n}{p}$ is an integer, support energy depends on the choice of generalised coordinates used and drive axis angle $\alpha$. In contrast, if $\frac{2n}{p}$ is not an integer, the support energy is rotationally symmetric, invariant to generalised coordinates used, and independent of $\alpha$. For the $2\theta$ modes, this study validated that 8 and 16 supports, commonly used for practical CVG devices, maintain the rotational symmetry.

Numbers of supports that break the rotational symmetry in the linear regime have no use, so drive and sense equations of motion were developed for a ring having a number of supports $p$ such that $\frac{2n}{p}$ is not an integer. It was demonstrated that if resonator energy is rotationally symmetric, drive and sense equations are only coupled by the Coriolis force in the presence of rotation, and drive and sense resonance frequencies are equal.

To investigate the impact of the breaking of rotational symmetry on supported ring resonators performance, a small point mass imperfection was added to the ring mid-line of a previously rotationally symmetric resonator. It was shown that the point mass makes the resonator energy expression asymmetric and causes inertial mode coupling and frequency split. Analytical expressions for the drive and sense responses in steady-state for the imperfect ring resonator were obtained, and it was found that frequency split and inertial coupling cause occurrence of non-zero quadrature response and zero-rate-output. It was concluded that only

when the rotational symmetry of the resonator is maintained, high sensitivity and SNR and good quality of the rate measurement are achieved.

In the next Chapter, the mathematical model for a linear resonator developed in this Chapter will be extended to include ring and support geometrical non-linearity. In later work, non-linear drive and sense dynamics will be investigated and it will be shown that, in some cases, the effects of non-linearity on supported ring resonators performance are similar to those caused by a point mass imperfection, investigated in this Chapter.

# Chapter 3

# Governing equations for a supported ring-based CVG operating at large amplitudes

## 3.1 Introduction

Previous chapters highlighted that high performance CVGs used in inertial navigation applications require high sensitivity and SNR, and discussed how this can be achieved by reducing the damping and by exciting the ring into large amplitude of vibration. The purpose of this Chapter is to develop an understanding of ring and support geometrical non-linearity effects on the performance of supported ring resonators operating at large amplitude vibration, and provide some insight how to design devices having improved performance.

The mathematical model for the linear supported ring resonator developed in Chapter 2 is extended to include ring non-linear flexural vibration and non-linear support stiffness. Following a similar investigation to that in Chapter 2, kinetic and potential energy expressions for ring and support are obtained for the non-linear resonator, and analysed to investigate

whether geometrical non-linearity influences the rotational symmetry of the resonator.

Ring and support energy expressions are used in Lagrange's equation to develop drive and sense equations of motion for supported ring resonator having $p$ supports and operating in the $n\theta$ modes. Resulting equations are discussed in detail for ring resonators operating in the $n = 2$ modes having 8 and 16 supports which, in Chapter 2, were found to maintain the rotational symmetry of the $2\theta$ modes in the linear regime. In later chapters, the equations of motion developed in this Chapter will be used to investigate the drive and sense responses in steady-state for practical CVGs operating at large amplitude vibration, to demonstrate non-linearity effects on supported ring resonators performance.

This Chapter is organised as follows. Section 3.2 develops the mathematical model for an unsupported ring including ring non-linear flexural deflection, and determines the equations of motion for the unsupported ring at large amplitude vibration. Section 3.3 develops the mathematical model for modelling non-linear supports. Similar to the investigation proposed in Chapter 2, support energy is obtained and analysed to investigate whether ring and support geometrical non-linearity have potential to break the rotational symmetry of supported ring resonators. In Section 3.4 ring and support energies are used in Lagrange's equation to determine the equations governing the drive and sense $n\theta$ modes motion for a ring resonator having $p$ supports. Drive and sense non-linear equations are discussed in details for ring resonators operating in the $2\theta$ modes and supported by 8 and 16 supports. Section 3.5 summarises the work done and key conclusions.

## 3.2 Equations of motion for an unsupported ring exhibiting large amplitude vibration

This Section develops the mathematical model for modelling an unsupported ring resonator when the ring is excited into large amplitude vibration. Kinetic and potential energies of the ring are obtained and used in Lagrange's equation to determine the equations of motion governing the drive and sense $n\theta$ modes for an unsupported ring.

### 3.2.1 Ring non-linear flexural deflections

A model similar to that presented in Section 2.2.1 for a linear ring is used to describe the deflection of a ring driven into large amplitude. Studies conducted by Evensen [31–33] and introduced in Section 1.5.1 suggest that to good approximation the ring mid-line remains inextensible when the ring vibrates. Expressions for radial and tangential displacements $u(\theta)$ and $v(\theta)$ in equations (2.1) and (2.2) do not satisfy the inextensibility condition when the ring undergoes large amplitude vibration, and are enhanced by including the non-linear breathing mode. The resulting radial $u(\theta)$ and tangential $v(\theta)$ displacements of the ring mid-line are:

$$u(\theta) = Q_1 \cos n(\theta - \alpha) + Q_2 \sin n(\theta - \alpha) - \gamma\left(Q_1^2 + Q_2^2\right) \tag{3.1}$$

$$\begin{aligned} v(\theta) = &-\frac{Q_1}{n}\sin n(\theta - \alpha) + \frac{Q_2}{n}\cos n(\theta - \alpha) + \\ &+ \frac{\gamma}{2n}\left[\left(Q_1^2 - Q_2^2\right)\sin 2n(\theta - \alpha) - 2Q_1Q_2\cos 2n(\theta - \alpha)\right] \end{aligned} \tag{3.2}$$

where

$$\gamma = \frac{\left(n^2 - 1\right)^2}{4Rn^2} \tag{3.3}$$

In the linear model, generalised coordinate $Q_1$ is the anti-node radial vibration amplitude of the drive mode at $\theta = \alpha$ i.e. $u(\alpha) = Q_1$, while generalised coordinate $Q_2$ is the anti-node radial vibration amplitude of the sense mode at $\theta = \alpha + \frac{\pi}{2n}$ i.e. $u(\alpha + \frac{\pi}{2n}) = Q_2$ (see radial

deflection in equation (2.1)). In the non-linear model, this is only approximatively true. Due to the breathing mode, the radial ring deflection at $\theta = \alpha$ is given by $u(\alpha) = Q_1 - \gamma\left(Q_1^2 + Q_2^2\right)$ and similarly, the radial deflection at $\theta = \alpha + \frac{\pi}{2n}$ is $u(\alpha + \frac{\pi}{2n}) = Q_2 - \gamma\left(Q_1^2 + Q_2^2\right)$. In later work it will be shown that generalised coordinate $Q_1$ can be obtained from the ring radial displacements at $\theta = \alpha$ and $\theta = \alpha + \frac{\pi}{n}$, while $Q_2$ can be obtained from $u(\alpha + \frac{\pi}{2n})$ and $u(\alpha + \frac{3\pi}{2n})$. It is noted that radial and tangential displacements are characterised by vibrations at twice the frequency of the dominant flexural vibration. If the steady-state vibration of the drive and sense modes has frequency $\omega$, the radial and tangential displacements will experience $2\omega$ frequency vibrations, arising from the $Q_1^2$, $Q_2^2$ and $Q_1 Q_2$ terms in equations (3.1) and (3.2). Furthermore, the radial displacement is reduced by the presence of the non-linear breathing mode term $\gamma(Q_1^2 + Q_2^2)$ which is independent of the circumferential coordinate $\theta$. The tangential displacement includes $2n(\theta - \alpha)$ terms, indicating that the tangential displacement is modified by non-linearity and includes a $2n\theta$ component.

The ring is assumed to be perfect, so that the $n\theta$ in-plane flexural modes have no preferred orientation, and a consequence of this is that angle $\alpha$ is arbitrary. Similar to the linear model described in Chapter 2, angle $\alpha$ is included in equations (3.1) and (3.2) to specify the radial displacement at the drive axis location which aligns with the principal direction of the applied radial force.

### 3.2.2 Kinetic and potential energies for an unsupported ring

The kinetic and potential energies of the ring are determined by substituting radial and tangential displacements (3.1) and (3.2) into (2.7) and (2.12) (via (2.13)) and calculating the integrals. The kinetic energy $T_{ring}$ and potential energy $V_{ring}$ for a ring undergoing large

amplitude vibrations can be expressed as:

$$\begin{aligned} T_{ring} =& \frac{1}{2}\rho hLR\pi \left[ \left( \dot{Q}_1^2 + \dot{Q}_2^2 \right) \left( \left( \frac{n^2+1}{n^2} \right) + \frac{\gamma^2}{n^2} \left( Q_1^2 + Q_2^2 \right) \right) + 8\gamma^2 \left( \dot{Q}_1 Q_1 + \dot{Q}_2 Q_2 \right)^2 \right] + \\ &+ \frac{2}{n}\rho hLR\pi\Omega_z \left( -\dot{Q}_1 Q_2 + Q_1 \dot{Q}_2 \right) \end{aligned} \tag{3.4}$$

$$V_{ring} = \frac{ELh^3\pi}{24R^3} \left( Q_1^2 + Q_2^2 \right) \left( 1 + n^4 - 2n^2 + 2\gamma^2 \left( Q_1^2 + Q_2^2 \right) \right) \tag{3.5}$$

The total energy of the ring $\mathcal{E}_{ring}$ is given by the sum of $T_{ring}$ and $V_{ring}$ and can be formulated as:

$$\begin{aligned} \mathcal{E}_{ring} =& T_{ring}^L + V_{ring}^L + \frac{\gamma^2}{2}\rho hLR\pi \left[ \frac{1}{n^2} \left( Q_1^2 + Q_2^2 \right) \left( \dot{Q}_1^2 + \dot{Q}_2^2 \right) + 8 \left( \dot{Q}_1 Q_1 + \dot{Q}_2 Q_2 \right)^2 \right] + \\ &+ \gamma^2 \frac{ELh^3\pi}{12R^3} \left( Q_1^2 + Q_2^2 \right)^2 \end{aligned} \tag{3.6}$$

where $T_{ring}^L$ and $V_{ring}^L$ are the kinetic and potential energy of the linear ring, respectively given by equations (2.8) and (2.14). Equation (3.6) highlights the influence of ring geometrical non-linearity on the energy expression. Using transformations (2.9) and (2.10) in Chapter 2, it can be shown that the ring energy expression $\mathcal{E}_{ring}$ is unaltered when generalised coordinates $Q_1$ and $Q_2$ are rotated by an arbitrary angle $\psi$ (as illustrated in Figure 2.4). This indicates that the rotational symmetry of the ring is maintained at large amplitude deflections and that ring geometrical non-linearity does not affect the rotational symmetry of the unsupported ring resonator.

### 3.2.3 Drive and sense equations of motion for an unsupported ring

Non-linear ring energies (3.4) and (3.5) are used in Lagrange's equation (2.26) to determine the equations of motion governing drive and sense $n\theta$ modes of the unsupported ring. The distribution of generalised radial forces applied to the ring to excite the $n\theta$ drive mode is assumed to be of the type $f_D(\theta, t) = F_D \cos n(\theta - \alpha) \cos \Omega t$. By expressing the damping in terms of the quality factor $Q$, and approximating the gyroscopic coupling factor as coefficient

$\mathcal{B}$ given by (2.38), it can be shown that the equations of motion for the drive and sense modes are:

$$\begin{aligned}
&\ddot{Q}_1\left[1+\left(Q_1^2+Q_2^2\right)\frac{\gamma^2}{(n^2+1)}\right]+\dot{Q}_1\left[\frac{\omega_0}{Q}+\left(\dot{Q}_1Q_1+\dot{Q}_2Q_2\right)\frac{2\gamma^2}{(n^2+1)}\right]+\\
&+Q_1\left[\omega_0^2\left(1+\left(Q_1^2+Q_2^2\right)\frac{4\gamma^2}{(n^4-2n^2+1)}\right)+\left(\dot{Q}_1^2+\dot{Q}_2^2\right)\frac{\left(8n^2-1\right)\gamma^2}{(n^2+1)}+\right.\\
&\left.+\left(\ddot{Q}_1Q_1+\ddot{Q}_2Q_2\right)\frac{8n^2\gamma^2}{(n^2+1)}\right]-\mathcal{B}\Omega_z\dot{Q}_2=\frac{F_D}{M_{ring}}\cos\Omega t
\end{aligned}\tag{3.7}$$

$$\begin{aligned}
&\ddot{Q}_2\left[1+\left(Q_1^2+Q_2^2\right)\frac{\gamma^2}{(n^2+1)}\right]+\dot{Q}_2\left[\frac{\omega_0}{Q}+\left(\dot{Q}_1Q_1+\dot{Q}_2Q_2\right)\frac{2\gamma^2}{(n^2+1)}\right]+\\
&+Q_2\left[\omega_0^2\left(1+\left(Q_1^2+Q_2^2\right)\frac{4\gamma^2}{(n^4-2n^2+1)}\right)+\left(\dot{Q}_1^2+\dot{Q}_2^2\right)\frac{\left(8n^2-1\right)\gamma^2}{(n^2+1)}+\right.\\
&\left.+\left(\ddot{Q}_1Q_1+\ddot{Q}_2Q_2\right)\frac{8n^2\gamma^2}{(n^2+1)}\right]+\mathcal{B}\Omega_z\dot{Q}_1=0
\end{aligned}\tag{3.8}$$

where $M_{ring}$ is given by (2.32) and $\omega_0$ is the natural frequency of the $n\theta$ modes of the unsupported ring. It is noted that ring geometrical non-linearity is governed by $\gamma$ and causes the drive and sense modal mass, damping and stiffness to depend upon non-linear terms in $Q_1$ and $Q_2$ (and time derivatives) and vary parametrically. Previous studies [5,29,31] introduced in Section 1.5 found that this parametric coupling causes the resonance frequency of the drive and sense modes to shift from the linear resonance frequency $\omega_0$ as the ring is excited into large amplitude vibration. This shift affects the performance of ring-based resonators which normally operate at the drive mode resonance frequency. The dependence of the drive mode resonance frequency on the drive response amplitude will be investigated in the next Chapter.

## 3.3 Mathematical model and energy expressions for a non-linear support structure

This Section develops the mathematical model introduced by Sérandour [29] for modelling the support structure including support non-linear stiffness. Ring geometrical non-linearity is considered using non-linear radial and tangential ring deflections (3.1) and (3.2) to describe

the displacements of ring-support attachment points. The model is used to determine kinetic and potential energy expressions for $p$ identical supports uniformly spaced around the ring circumference. A similar approach to that in Section 2.3 for a linear support is used to investigate the influence of ring and support geometrical non-linearity on the rotational symmetry of supported ring resonators when the ring is driven into large amplitudes.

### 3.3.1 Mathematical model for non-linear supports

Section 2.3 presented a model for $p$ linear identical supports uniformly spaced around the ring circumference. Figure 3.1 shows the mathematical model used for modelling a single support including support non-linear stiffness.

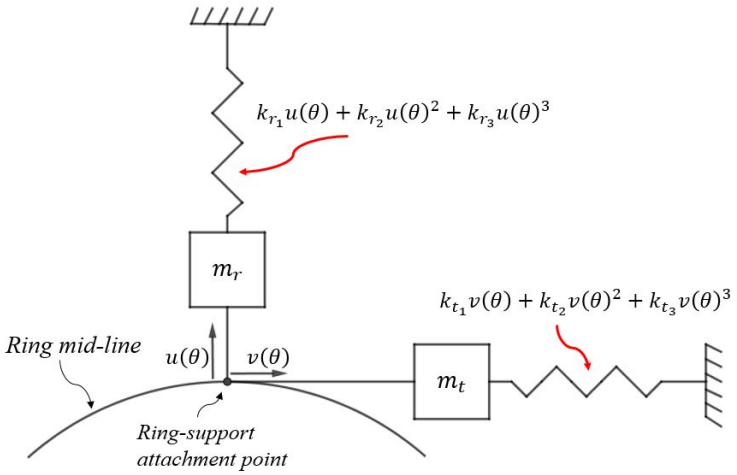



Figure 3.1: Diagram of the mathematical model proposed for representing the support inertia and non-linear stiffness in the radial and tangential directions.

Similar to the linear model shown in Figure 2.6, the inertia of the support in the radial and tangential directions are modelled by discrete masses $m_r$ and $m_t$. To take account of non-linearity, the stiffness in the radial and tangential directions are modelled by non-linear springs having cubic stiffness. The radial springs have linear, quadratic and cubic stiffness coefficients $k_{r_1}$, $k_{r_2}$ and $k_{r_3}$; and the tangential springs have linear, quadratic and cubic stiff-

ness coefficients $k_{t_1}$, $k_{t_2}$ and $k_{t_3}$.

These stiffness coefficients are calculated using a Finite Element analysis for a single support, in a similar way to that described in Section 2.3.1, used to determine coefficients $k_{r_1}$ and $k_{t_1}$ for a linear support. In summary, radial and tangential forces are applied to the support end that is attached to the ring mid-line, the radial and tangential directions are assumed to be principal axes of stiffness for the support, and the in-plane rotation of the ring-support attachment point is assumed to be the same as an unsupported ring undergoing linear vibration at that angular position. Large-deflection static analyses are performed to calculate the radial and tangential displacements caused by the applied forces, and the process is repeated by varying the magnitude of the applied forces to calculate the force-deflection curves in the radial and tangential directions. These curves are interpolated using cubic fitting functions and used to calculate the linear, quadratic and cubic stiffness coefficients. A more detailed description of the procedure used for the determination of the non-linear stiffness coefficients can be found in Appendix A, where the stiffness coefficients are calculated and shown for a practical ring-based CVGs support geometry.

### 3.3.2 Kinetic energy of the support structure

In Section 2.3.4, the kinetic energy of $p$ linear identical supports (uniformly spaced around the ring) was determined by summing the kinetic energy of a single support given by (2.15) over the total number of supports. A similar approach is followed here for the non-linear supports. To take account of ring geometrical non-linearity, non-linear radial and tangential ring displacements (3.1) and (3.2) are used to describe the displacement of support masses $m_r$ and $m_t$ respectively. Substituting (3.1) and (3.2) into (2.15) and summing over the total

number of supports, the kinetic energy $T_S$ of the support structure can be expressed as:

$$\begin{aligned}T_S =& T_S^i + \sum_{j=0}^{p-1} \cos n\left(j\frac{2\pi}{p} - \alpha\right) T_{C1} + \sum_{j=0}^{p-1} \sin n\left(j\frac{2\pi}{p} - \alpha\right) T_{S1} + \sum_{j=0}^{p-1} \cos 2n\left(j\frac{2\pi}{p} - \alpha\right) T_{C2} + \\ &+ \sum_{j=0}^{p-1} \sin 2n\left(j\frac{2\pi}{p} - \alpha\right) T_{S2} + \sum_{j=0}^{p-1} \cos 3n\left(j\frac{2\pi}{p} - \alpha\right) T_{C3} + \sum_{j=0}^{p-1} \sin 3n\left(j\frac{2\pi}{p} - \alpha\right) T_{S3} + \\ &+ \sum_{j=0}^{p-1} \cos 4n\left(j\frac{2\pi}{p} - \alpha\right) T_{C4} + \sum_{j=0}^{p-1} \sin 4n\left(j\frac{2\pi}{p} - \alpha\right) T_{S4}\end{aligned} \tag{3.9}$$

The invariant component of the kinetic energy $T_S^i$ and terms $T_{C1}, ..., T_{S4}$ are:

$$T_S^i = p\left[\left(\frac{m_r}{4} + \frac{m_t}{4n^2}\right)\left(\dot{Q}_1^2 + \dot{Q}_2^2\right) + \gamma^2\left(2m_r\left(\dot{Q}_1 Q_1 + \dot{Q}_2 Q_2\right)^2 + \frac{m_t}{4n^2}\left(\dot{Q}_1^2 + \dot{Q}_2^2\right)\left(Q_1^2 + Q_2^2\right)\right)\right] \tag{3.10}$$

$$T_{C1} = \gamma\left[-2m_r\dot{Q}_1\left(\dot{Q}_1 Q_1 + \dot{Q}_2 Q_2\right) - \frac{m_t}{2n^2} Q_1\left(\dot{Q}_1^2 + \dot{Q}_2^2\right)\right] \tag{3.11}$$

$$T_{S1} = \gamma\left[-2m_r\dot{Q}_2\left(\dot{Q}_1 Q_1 + \dot{Q}_2 Q_2\right) - \frac{m_t}{2n^2} Q_2\left(\dot{Q}_1^2 + \dot{Q}_2^2\right)\right] \tag{3.12}$$

$$T_{C2} = \left(\frac{m_r}{4} - \frac{m_t}{4n^2}\right)\left(\dot{Q}_1^2 - \dot{Q}_2^2\right) \tag{3.13}$$

$$T_{S2} = \left(\frac{m_r}{4} - \frac{m_t}{4n^2}\right) 2\dot{Q}_1\dot{Q}_2 \tag{3.14}$$

$$T_{C3} = \frac{m_t}{2n^2}\gamma\left[Q_1\left(\dot{Q}_1^2 - \dot{Q}_2^2\right) - Q_2\left(2\dot{Q}_1\dot{Q}_2\right)\right] \tag{3.15}$$

$$T_{S3} = \frac{m_t}{2n^2}\gamma\left[Q_2\left(\dot{Q}_1^2 - \dot{Q}_2^2\right) + Q_1\left(2\dot{Q}_1\dot{Q}_2\right)\right] \tag{3.16}$$

$$T_{C4} = \frac{m_t}{2n^2}\gamma^2\left[\frac{1}{2}\left(\dot{Q}_1^2 - \dot{Q}_2^2\right)\left(Q_2^2 - Q_1^2\right) + 2\dot{Q}_1\dot{Q}_2\left(Q_1 Q_2\right)\right] \tag{3.17}$$

$$T_{S4} = \frac{m_t}{2n^2}\gamma^2\left[\dot{Q}_1\dot{Q}_2\left(Q_2^2 - Q_1^2\right) + \left(\dot{Q}_2^2 - \dot{Q}_1^2\right)\left(Q_1 Q_2\right)\right] \tag{3.18}$$

In these equations, terms involving $\gamma$ are associated with ring geometrical non-linearity. By comparing $T_S$ in (3.9) against $T_S^L$ for $p$ linear supports given by equation (2.21), it is noted that ring geometrical non-linearity:

- Introduces multiple non-linear terms in $Q_1$ and $Q_2$ (including first time derivatives and combinations) to the invariant part of the kinetic energy $T_S^i$.

- Gives rise to coefficients $T_{Cm}$, $T_{Sm}$ with $m = 1, 3, 4$ which involve summations in $\cos mn\left(j\frac{2\pi}{p} - \alpha\right)$ and $\sin mn\left(j\frac{2\pi}{p} - \alpha\right)$ and have potential to break the rotational symmetry due to the dependence on $\alpha$.

Using transformations (2.9) and (2.10) it can be shown that expressing kinetic energy $T_S$ in (3.9) in terms of generalised coordinates $Q_{1\psi}$ and $Q_{2\psi}$ rotated by an angle $\psi$ relative to $Q_1$ and $Q_2$, the invariant component of the kinetic energy $T_S^i$ is unchanged whilst terms $T_{Cm}$, $T_{Sm}$ (for $m = 1, ..., 4$) vary. This indicates that $T_{Cm}$, $T_{Sm}$ terms break the rotational symmetry of the support kinetic energy expression.

By generalising (2.23) and (2.24), it can be shown that:

$$\sum_{j=0}^{p-1} \cos mn\left(j\frac{2\pi}{p} - \alpha\right) = \begin{cases} 0 & \text{if } \frac{mn}{p} \text{ is not an integer} \\ p\cos mn\alpha & \text{if } \frac{mn}{p} \text{ is an integer} \end{cases} \tag{3.19}$$

$$\sum_{j=0}^{p-1} \sin mn\left(j\frac{2\pi}{p} - \alpha\right) = \begin{cases} 0 & \text{if } \frac{mn}{p} \text{ is not an integer} \\ p\sin mn\alpha & \text{if } \frac{mn}{p} \text{ is an integer} \end{cases} \tag{3.20}$$

where $m$, $n$ and $p$ are integers. When investigating the linear regime, it was found in Section 2.3.4 that the rotational symmetry was broken for $p$ supports numbers when $\frac{2n}{p}$ is an integer. In contrast, this analysis indicates that ring geometrical non-linearity causes the rotational symmetry to break for numbers of support $p$ such that $\frac{n}{p}$, $\frac{3n}{p}$ and/or $\frac{4n}{p}$ are integers. Only if the ring is supported by $p$ supports such that $\frac{mn}{p}$ is not an integer (for $m = 1, ..., 4$) the rotational symmetry is maintained and all $\alpha$ terms in the support kinetic energy (3.9) are zero and $T_S$ reduces to the invariant part $T_S^i$ given in (3.10).

### 3.3.3 Potential energy of the support structure

In Section 2.3.4 the potential energy for $p$ linear supports was determined by summing the potential energy for a single support given in (2.18) over the total number of supports. To take account of support geometrical non-linearity, contributions from the quadratic and cubic radial and tangential stiffness are included in the potential energy expression for a single support (2.18). Summing over the total number of supports, the potential energy $V_S$ of the support structure can be expressed as:

$$\begin{aligned} V_S = &\sum_{j=0}^{p-1} \left[ \frac{1}{2} k_{r_1} u^2 \left( j\frac{2\pi}{p} \right) + \frac{1}{3} k_{r_2} u^3 \left( j\frac{2\pi}{p} \right) + \frac{1}{4} k_{r_3} u^4 \left( j\frac{2\pi}{p} \right) + \right. \\ &\left. + \frac{1}{2} k_{t_1} v^2 \left( j\frac{2\pi}{p} \right) + \frac{1}{3} k_{t_2} v^3 \left( j\frac{2\pi}{p} \right) + \frac{1}{4} k_{t_3} v^4 \left( j\frac{2\pi}{p} \right) \right] \end{aligned} \tag{3.21}$$

Substituting non-linear radial and tangential ring displacements (3.1) and (3.2) into (3.21) to determine the strain energy of the supports gives:

$$\begin{aligned} V_S = &V_S^i + \sum_{j=0}^{p-1} \left[ \cos n \left( j\frac{2\pi}{p} - \alpha \right) V_{C1} + \sin n \left( j\frac{2\pi}{p} - \alpha \right) V_{S1} + \cos 2n \left( j\frac{2\pi}{p} - \alpha \right) V_{C2} + \right. \\ &+ \sin 2n \left( j\frac{2\pi}{p} - \alpha \right) V_{S2} + \cos 3n \left( j\frac{2\pi}{p} - \alpha \right) V_{C3} + \sin 3n \left( j\frac{2\pi}{p} - \alpha \right) V_{S3} + \\ &+ \cos 4n \left( j\frac{2\pi}{p} - \alpha \right) V_{C4} + \sin 4n \left( j\frac{2\pi}{p} - \alpha \right) V_{S4} + \cos 5n \left( j\frac{2\pi}{p} - \alpha \right) V_{C5} + \\ &\left. + \sin 5n \left( j\frac{2\pi}{p} - \alpha \right) V_{S5} + \cos 6n \left( j\frac{2\pi}{p} - \alpha \right) V_{C6} + \sin 6n \left( j\frac{2\pi}{p} - \alpha \right) V_{S6} \right] \end{aligned} \tag{3.22}$$

where the invariant component of the potential energy of the supports $V_S^i$ is given by:

$$\begin{aligned} V_S^i = &p \left\{ \left( \frac{k_{r_1}}{4} + \frac{k_{t_1}}{4n^2} \right) \left( Q_1^2 + Q_2^2 \right) + \gamma^2 \left( \frac{k_{r_1}}{2} + \frac{k_{t_1}}{16n^2} \right) \left( Q_1^2 + Q_2^2 \right)^2 + \right. \\ &\left. + \left( Q_1^2 + Q_2^2 \right)^2 \left[ -\frac{k_{r_2}}{2}\gamma + \frac{3k_{r_3}}{32} \left( 1 + 8\gamma^2 \left( Q_1^2 + Q_2^2 \right) \right) + \frac{3k_{t_3}}{34n^4} \left( 1 + \gamma^2 \left( Q_1^2 + Q_2^2 \right) \right) \right] \right\} \end{aligned} \tag{3.23}$$

and coefficients $V_{C1}, ..., V_{S6}$ can be found in Appendix B in equations (B.1)-(B.12). Higher powers of $\gamma$ than the second order in potential energy expression (3.22) have been neglected as they are multiplied by terms involving $Q_1^6$, $Q_1^7$, $Q_2^6$ and/or $Q_2^7$. For the range of response amplitudes considered in this work, these terms are considered to be small and negligible.
By comparing $V_S$ against $V_S^L$ for $p$ linear supports given by (2.22), it is noted that ring and support geometrical non-linearity:

- Introduces non-linear terms into the invariant part of the potential energy $V_S^i$. In particular:
  - Ring geometrical non-linearity gives rise to terms in $\gamma$ multiplied by the linear stiffness coefficients of the supports $k_{r_1}$ and $k_{t_1}$.
  - The combined effect of the ring and support geometrical non-linearity introduces terms in the non-linear stiffness coefficients $k_{r_2}$, $k_{r_3}$, $k_{t_2}$ and $k_{t_3}$ which are multiplied by $\gamma$.
  - Support geometrical non-linearity introduces terms involving the non-linear stiffness coefficients which have no dependence on $\gamma$.
- Introduces non-linear terms into that part of potential energy multiplied by $\cos 2n\left(j\frac{2\pi}{p}-\alpha\right)$ and $\sin 2n\left(j\frac{2\pi}{p}-\alpha\right)$ (see expressions for $V_{C2}$ and $V_{S2}$ in (B.3) and (B.4)).
- Gives rise to coefficients $V_{Cm}$, $V_{Sm}$ with $m = 1, 3, ..., 6$ which involve summations in $\cos mn\left(j\frac{2\pi}{p}-\alpha\right)$ and $\sin mn\left(j\frac{2\pi}{p}-\alpha\right)$ and have potential to break the rotational symmetry due to the dependence on $\alpha$.

Using transformations (2.9) and (2.10) it can be shown the invariant part of the potential energy $V_S^i$ in (3.23) is unaltered when generalised coordinates are rotated by an arbitrary angle $\psi$. In contrast, energies $V_{Cm}$, $V_{Sm}$ ($m = 1, ..., 6$) respectively multiplied by $\cos mn\left(j\frac{2\pi}{p}-\alpha\right)$ and $\sin mn\left(j\frac{2\pi}{p}-\alpha\right)$ depend on the choice of generalised coordinates used and break the rotational symmetry of the supported ring resonator.

Using (3.19) and (3.20), it can be shown that if the ring is supported by $p$ supports such that $\frac{mn}{p}$ is not an integer ($m = 1, ..., 6$) all $\alpha$ terms in the support potential energy (3.22) are zero, and $V_S$ reduces to the invariant part $V_S^i$ given by (3.23).

### 3.3.4 Numbers of supports that break rotational symmetry for large amplitude vibrations

Section 2.3.4 for a linear resonator concluded that if the number of supports $p$ ensures $\frac{2n}{p}$ is an integer, the rotational symmetry of the $n\theta$ modes breaks in the linear regime. For resonators operating at large amplitude of vibration, it was found that:

- Ring geometrical non-linearity introduces rotational asymmetry in support kinetic energy expression $T_S$ in (3.9) for numbers of supports $p$ when $\frac{n}{p}$, $\frac{3n}{p}$ and/or $\frac{4n}{p}$ is an integer.

- Ring and support geometrical non-linearity causes support potential energy expression $V_S$ in (3.22) to be rotationally asymmetric for numbers of supports $p$ when $\frac{n}{p}$, $\frac{2n}{p}$, $\frac{3n}{p}$, $\frac{4n}{p}$, $\frac{5n}{p}$ and/or $\frac{6n}{p}$ is an integer.

One can conclude that for a given mode number $n$, at large amplitudes the rotational symmetry is maintained only if the number of supports $p$ ensures $\frac{mn}{p}$ is not an integer for $m = 1, ..., 6$. Using relations (3.19) and (3.20), if $\frac{mn}{p}$ is not an integer (for $m = 1, ..., 6$), the kinetic energy of the support (3.9) and potential energy of the support (3.22) reduce to the invariant parts $T_S^i$ and $V_S^i$ respectively given by (3.10) and (3.23). The supported ring resonator energy is:

$$\mathcal{E}_R = T_{ring} + V_{ring} + T_S^i + V_S^i \tag{3.24}$$

where $T_{ring}$ and $V_{ring}$ are respectively given by (3.4) and (3.5). It can be shown that energy $\mathcal{E}_R$ in (3.24) is independent of $\alpha$ and is invariant to the choice of generalised coordinates used.

Table 3.1 summarises these results and indicates the combinations of mode number $n$ and number of regularly spaced supports $p$ that maintain the rotational symmetry of the supported ring resonator ("SYM") or not ("ASY") as the ring is driven into large amplitudes vibration.

| | Numbers of supports $p$ | | | | | | | | | | | |
|---|---|---|---|---|---|---|---|---|---|---|---|---|
| | 2 | 3 | 4 | 5 | 6 | 7 | 8 | 9 | 10 | 12 | 14 | 16 |
| $n = 2$ | ASY | ASY | ASY | ASY | ASY | SYM | ASY | SYM | ASY | ASY | SYM | SYM |
| $n = 3$ | ASY | ASY | ASY | ASY | ASY | SYM | SYM | ASY | SYM | ASY | SYM | SYM |
| $n = 4$ | ASY | ASY | ASY | ASY | ASY | SYM | ASY | SYM | ASY | ASY | SYM | ASY |

Table 3.1: Combinations of $n$ and $p$ that maintain ("SYM") or break ("ASY") the rotational symmetry of the supported ring resonator as the ring is driven into large amplitudes vibration.

For a given modal number $n$, Table 3.1 indicates with "SYM" the support numbers $p$ that maintain the resonator rotational symmetry when the ring is excited into large amplitude vibration, and with "ASY" the support numbers that break the rotational symmetry when the ring is excited into large amplitude vibration.

It is interesting to compare Table 3.1 with Table 2.1 which was developed in Section 2.3.4 for supported ring resonators operating in the linear regime; the result is shown in Table 3.2. Combinations of $n$ and $p$ indicated with "X" in Table 3.2 break the rotational symmetry in the linear regime and have no practical use as a CVG, whilst all other combinations maintain the rotational symmetry in the linear regime. Combinations indicated with "ASY" break the rotational symmetry at large amplitude vibration, whilst combinations indicated with "SYM" maintain the rotational symmetry when the ring undergoes large amplitude deflections.

| | Numbers of supports $p$ | | | | | | | | | | | |
|---|---|---|---|---|---|---|---|---|---|---|---|---|
| | 2 | 3 | 4 | 5 | 6 | 7 | 8 | 9 | 10 | 12 | 14 | 16 |
| $n = 2$ | X | ASY | X | ASY | ASY | SYM | ASY | SYM | ASY | ASY | SYM | SYM |
| $n = 3$ | X | X | ASY | ASY | X | SYM | SYM | ASY | SYM | ASY | SYM | SYM |
| $n = 4$ | X | ASY | X | ASY | ASY | SYM | X | SYM | ASY | ASY | SYM | ASY |

Table 3.2: Combinations of $n$ and $p$ that (i) break the rotational symmetry in the linear regime ("X"), (ii) maintain the rotational symmetry in the linear regime and break it at large amplitude vibration ("ASY"), (iii) maintain the rotational symmetry in the linear regime and at large amplitude vibration ("SYM").

Results in Table 3.2 indicate that for a given modal number $n$, some numbers of supports $p$ indicated by "ASY" maintain the rotational symmetry when the ring resonator operates in the linear regime, and break it when the ring is excited into large amplitude vibration. Other supports numbers, indicated by "SYM", maintain the rotational symmetry of supported ring resonators regardless of the vibration amplitude. It is interesting to note that for CVGs operating in the $2\theta$ modes (i.e. $n = 2$), Table 3.2 indicates that 8 supports maintain the rotational symmetry when the device operates in the linear regime, and break it at large amplitude vibration due to ring and support geometrical non-linearity. In contrast, 16 supports maintain the rotational symmetry in the linear regime and for large amplitudes vibration.

### 3.3.5 Summary and interpretation

Chapter 2 for a linear resonator indicated that if the rotational symmetry is broken, frequency split and mode coupling occur and cause the sense response amplitude in operation to reduce and the quality of rate measurement to degrade. Practical high performance CVGs used for inertial navigation applications typically rely on the excitation of the $2\theta$ modes of the ring, and are often supported by 8 or 16 supports so the actuation and sensing mechanisms can be placed between supports. The non-linear results presented in this Section indicated that 8 supports maintain the rotational symmetry of the $2\theta$ modes in the linear regime

and break it when the ring undergoes large amplitude vibration. This suggests that as the amplitude of vibration is increased, the presence of geometric non-linearity degrades sensor performance for ring resonators having 8 supports. In contrast, 16 supports are shown to maintain the rotational symmetry at large amplitudes, so sensor performance are expected to be maintained when 16 supports are used.

## 3.4 Equations of motion for supported ring resonators at large vibration amplitudes

This Section develops the equations governing drive and sense $n\theta$ modes motion for a resonantor having a generic number of supports $p$, using Lagrange's method. Non-linear kinetic and potential energies expressions for the ring (i.e. $T_{ring}$ (3.4), $V_{ring}$ (3.5)) and for the support (i.e. $T_S$ (3.9), $V_S$ (3.22)) are used in Lagrange's equation (2.26). As in Section 2.4 for a linear resonator, it is assumed that the drive mode is excited by applied harmonic modal forces having frequency $\Omega$ and magnitude $F_D$. The damping is expressed in terms of the quality factor $Q$, and the gyroscopic coupling factor is approximated by coefficient $\mathcal{B}$ given by (2.38). The obtained drive and sense equations are quite long and complex and are given by (C.1) and (C.2) in Appendix C, respectively.

For practical CVGs, the governing equations of motion are simplified by noting that the amplitude of the drive response is normally orders of magnitude larger than the amplitude of the sense response [1, 5]. Under these circumstances, all non-linear terms in $Q_2$, $\dot{Q}_2$, $\ddot{Q}_2$ (including combinations) in the drive and sense equations are considered to be small and negligible. Neglecting non-linear terms in $Q_2$, drive and sense equations (C.1) and (C.2)

respectively reduce to:

$$\ddot{Q}_1\left(1+Q_1^2\gamma_1\right)+\dot{Q}_1\left(\frac{\omega_0}{Q}+\dot{Q}_1Q_1\gamma_2\right)+Q_1\left(\omega_0^2+\dot{Q}_1^2\gamma_3+\ddot{Q}_1Q_1\gamma_4+Q_1^2\gamma_5+Q_1^4\gamma_6\right)+$$
$$+\frac{1}{M_{res}}\sum_{j=0}^{p-1}\left[C_1^D\cos n\left(j\frac{2\pi}{p}-\alpha\right)+S_1^D\sin n\left(j\frac{2\pi}{p}-\alpha\right)+C_2^D\cos 2n\left(j\frac{2\pi}{p}-\alpha\right)+\right.$$
$$+S_2^D\sin 2n\left(j\frac{2\pi}{p}-\alpha\right)+C_3^D\cos 3n\left(j\frac{2\pi}{p}-\alpha\right)+S_3^D\sin 3n\left(j\frac{2\pi}{p}-\alpha\right)+$$
$$+C_4^D\cos 4n\left(j\frac{2\pi}{p}-\alpha\right)+S_4^D\sin 4n\left(j\frac{2\pi}{p}-\alpha\right)+C_5^D\cos 5n\left(j\frac{2\pi}{p}-\alpha\right)+$$
$$\left.+\ S_5^D\sin 5n\left(j\frac{2\pi}{p}-\alpha\right)+C_6^D\cos 6n\left(j\frac{2\pi}{p}-\alpha\right)+S_6^D\sin 6n\left(j\frac{2\pi}{p}-\alpha\right)\right]=$$
$$=\mathcal{B}\Omega_z\dot{Q}_2+\frac{F_D}{M_{res}}\cos\Omega t \tag{3.25}$$

$$\ddot{Q}_2\left(1+Q_1^2\gamma_1\right)+\dot{Q}_2\left(\frac{\omega_0}{Q}+\dot{Q}_1Q_1\gamma_2\right)+Q_2\left(\omega_0^2+\dot{Q}_1^2\gamma_3+\ddot{Q}_1Q_1\gamma_4+Q_1^2\gamma_5+Q_1^4\gamma_6\right)+$$
$$+\frac{1}{M_{res}}\sum_{j=0}^{p-1}\left[C_1^S\cos n\left(j\frac{2\pi}{p}-\alpha\right)+S_1^S\sin n\left(j\frac{2\pi}{p}-\alpha\right)+C_2^S\cos 2n\left(j\frac{2\pi}{p}-\alpha\right)+\right.$$
$$+S_2^S\sin 2n\left(j\frac{2\pi}{p}-\alpha\right)+C_3^S\cos 3n\left(j\frac{2\pi}{p}-\alpha\right)+S_3^S\sin 3n\left(j\frac{2\pi}{p}-\alpha\right)+$$
$$+C_4^S\cos 4n\left(j\frac{2\pi}{p}-\alpha\right)+S_4^S\sin 4n\left(j\frac{2\pi}{p}-\alpha\right)+C_5^S\cos 5n\left(j\frac{2\pi}{p}-\alpha\right)+$$
$$\left.+\ S_5^S\sin 5n\left(j\frac{2\pi}{p}-\alpha\right)+C_6^S\cos 6n\left(j\frac{2\pi}{p}-\alpha\right)+S_6^S\sin 6n\left(j\frac{2\pi}{p}-\alpha\right)\right]=$$
$$=-\mathcal{B}\Omega_z\dot{Q}_1 \tag{3.26}$$

where $M_{res}$ is the invariant component of the drive and sense modal mass, given in (2.30) and $\omega_0$ is the natural resonance frequency of the $n\theta$ modes of the supported ring resonator. Terms $C_m^D$ and $S_m^D$ in drive equation (3.25) and $C_m^S$ and $S_m^S$ in sense equation (3.26) ($m = 1, ..., 6$), multiplied by $\cos mn\left(j\frac{2\pi}{p}-\alpha\right)$ and $\sin mn\left(j\frac{2\pi}{p}-\alpha\right)$, arise from ring and support geometrical non-linearity. These terms are quite complex and can be found in equations (C.29)-(C.40) and (C.41)-(C.52) in Appendix C.

Non-linear terms in the ring energy expression and in the invariant support energies $T_S^i$ and

$V_S^i$ produce a part of the drive and sense equations of motion which is symmetrical in terms of generalised coordinates $Q_1$ and $Q_2$ and involves coefficients $\gamma_1, ..., \gamma_6$, where:

$$\gamma_1 = \frac{\gamma^2}{M_{res}} \left( \frac{M_{ring}}{(n^2+1)} + \frac{pm_t}{2n^2} \right) \tag{3.27}$$

$$\gamma_2 = 2\gamma_1 \tag{3.28}$$

$$\gamma_3 = \frac{\gamma^2}{M_{res}} \left( \frac{(8n^2-1)}{(n^2+1)} M_{ring} + p\left(4m_r - \frac{m_t}{2n^2}\right) \right) \tag{3.29}$$

$$\gamma_4 = \gamma_1 + \gamma_3 \tag{3.30}$$

$$\gamma_5 = \frac{1}{M_{res}} \left( \frac{4K_{ring}\gamma^2}{(n^4-2n^2+1)} + p\left(2k_{r_1}\gamma^2 - 2k_{r_2}\gamma + \frac{3k_{r_3}}{8} + \frac{k_{t_1}}{4n^2}\gamma^2 + \frac{3k_{t_3}}{8n^4}\right)\right) \tag{3.31}$$

$$\gamma_6 = \frac{p\gamma^2}{M_{res}} \left( \frac{9k_{t_3}}{16n^4} + \frac{9k_{r_3}}{2} \right) \tag{3.32}$$

Inertial coefficients $\gamma_1, ..., \gamma_4$ relate to ring geometrical non-linearity, and stiffness coefficients $\gamma_5$ and $\gamma_6$ relate to ring geometrical non-linearity, support geometrical non-linearity and their combination.

From drive and sense equations (3.25) and (3.26) it is noted that ring and support geometrical non-linearity cause the drive and sense modal mass, damping and stiffness to be non-linear in generalised coordinates $Q_1$ and $Q_2$. For an unsupported ring undergoing non-linear flexural vibration a similar behaviour was found in Section 3.2 and it was said that, based on previous studies [5,29,31], this parametric coupling has a potential to cause the resonance frequencies of the drive and sense modes to shift from the linear resonance frequency $\omega_0$ as the ring is excited into large amplitude vibration.

It can be shown that $\gamma_1, ..., \gamma_6$ coefficients arising from ring energy and invariant support energies $T_S^i$ and $V_S^i$ ensure the system parts of the drive and sense equations are equal to each

other. In contrast, terms $C_m^D$, $S_m^D$ and $C_m^S$, $S_m^S$ $(m = 1, ..., 6)$ involving $\cos mn\left(j\frac{2\pi}{p} - \alpha\right)$ and $\sin mn\left(j\frac{2\pi}{p} - \alpha\right)$ have potential to cause asymmetry between the drive and sense equations and to cause inertial, damping and elastic parametric coupling.

Terms $\cos mn\left(j\frac{2\pi}{p} - \alpha\right)$ and $\sin mn\left(j\frac{2\pi}{p} - \alpha\right)$ cause the drive and sense equations of motion to depend on $\alpha$ and so on the drive axis location around the ring circumference. For a perfect ring, the drive axis location aligns with the principal direction of the generalised forces applied to excite the drive mode. For $n = 2$, the distribution of generalised radial forces applied to excite the drive mode is of the type $f_D(\theta, t) = F_D \cos 2(\theta - \alpha) \cos \Omega t$. If $\alpha = 0°$, the distribution of applied forces is shown in Figure 3.2 and the drive mode axis aligns at $\theta = 0°$. If $\alpha = 22.5°$, the distribution of applied forces is shown in Figure 3.3 and the drive mode axis aligns at $\theta = 22.5°$.

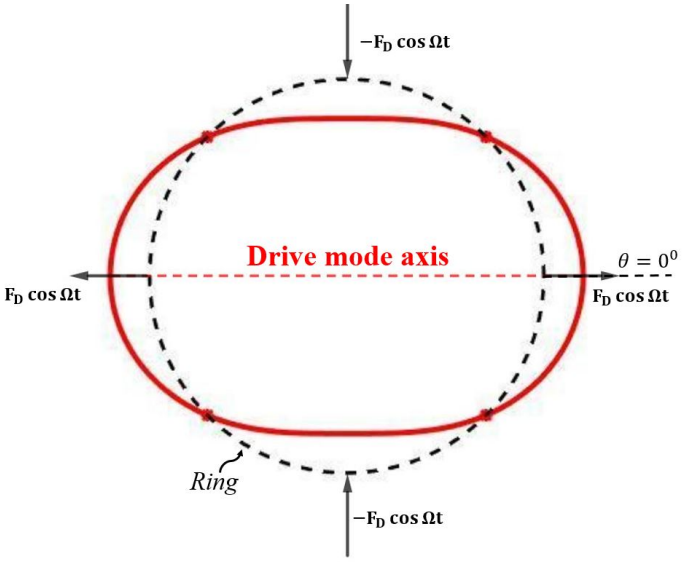



Figure 3.2: Schematic representation of the distribution of generalised forces applied to excite the $n = 2$ drive mode. For $\alpha = 0°$ then $f_D(\theta, t) = F_D \cos 2\theta \cos \Omega t$ and the drive axis aligns at $\theta = 0°$. The reference circumferential coordinate $\theta = 0°$ is the horizontal.

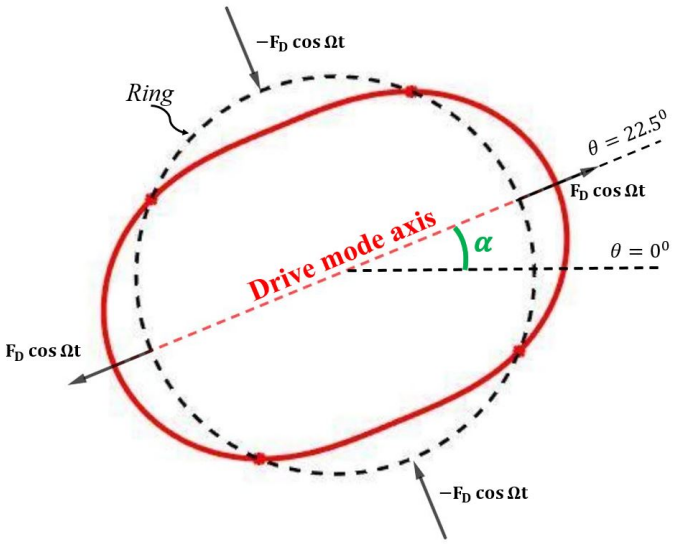



Figure 3.3: Schematic representation of the distribution of generalised forces applied to excite the $n = 2$ drive mode. For $\alpha = 22.5°$ then $f_D(\theta, t) = F_D \cos 2\left(\theta - \frac{\pi}{8}\right) \cos \Omega t$ and the drive axis aligns at $\theta = 22.5°$. The reference circumferential coordinate $\theta = 0°$ is the horizontal.

For supported ring resonators, the dependence of the drive and sense equations of motion on the drive axis location around the ring circumference implies that drive and sense equations depend on the orientation of the drive axis relative to the supports location. When the mathematical model for a linear support was developed in Section 2.3 it was said that one support is attached to the ring at $\theta = 0°$ (as shown in Figure 2.7). If $\alpha = 0°$ the drive mode axis aligns at $\theta = 0°$ and so aligns with one support as shown in Figure 3.4. If one support is attached to the ring at $\theta = 0°$ and the adjacent support is attached to the ring at $\theta = 45°$ (depending on the number of supports $p$), use of $\alpha = 22.5°$ aligns the drive mode axis mid-way between two supports, as shown in Figure 3.5. Therefore, non-linear terms $C_m^D$, $S_m^D$ and $C_m^S$, $S_m^S$ involving $\alpha$ in drive and sense equations (3.25) and (3.26) cause the dynamics of the drive and sense modes to depend upon the orientation of the drive axis relative to the supports.

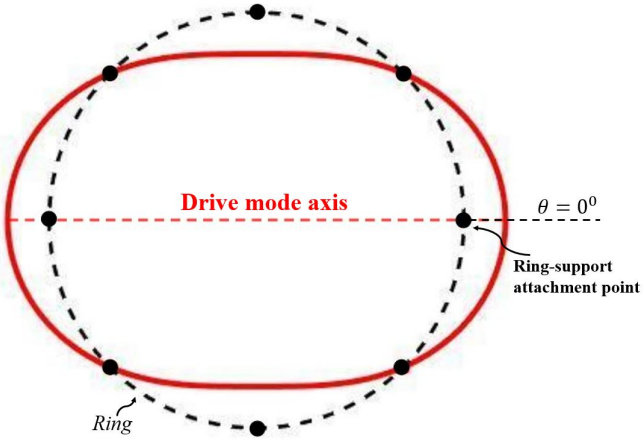



Figure 3.4: One support is attached to the ring at $\theta = 0°$. Use of $\alpha = 0°$ produces the alignment of the drive axis with a support.

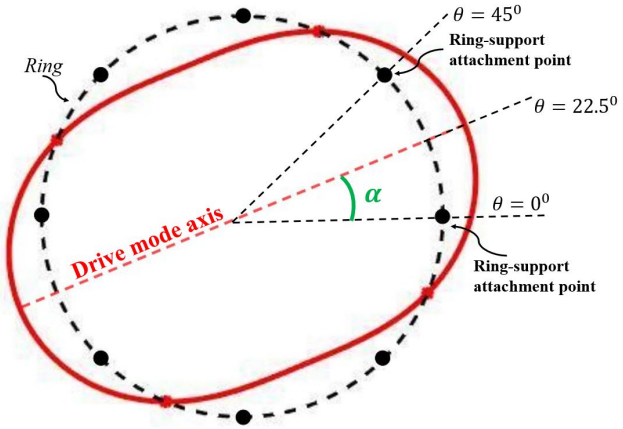



Figure 3.5: If one support is attached to the ring at $\theta = 0°$ and the adjacent support is attached to the ring at $\theta = 45°$ (depending on the number of supports), use of $\alpha = 22.5°$ produces the alignment of the drive axis mid-way between two supports.

In what follows the drive and sense non-linear equations of motion are developed for two case studies, both of which are representative of practical CVG devices. *Case Study I* considers a ring resonator based on $n = 2$ having $p = 8$ supports, while *Case Study II* considers a ring resonator based on $n = 2$ having $p = 16$ supports. For *Case Study I*, using relations (3.19) and (3.20) most of the $C_m^D$, $S_m^D$ and $C_m^S$, $S_m^S$ terms in drive and sense equations (3.25) and (3.26) are zero except for $C_4^D$, $S_4^D$ and $C_4^S$, $S_4^S$ because the ratio $\frac{mn}{p}$ is an integer

for $n = 2$, $p = 8$ and $m = 4$. In contrast, for *Case Study II*, all terms $C_m^D$, $S_m^D$ and $C_m^S$, $S_m^S$ are zero because $\frac{mn}{p}$ is not an integer for $m = 1, ..., 6$ and all terms involving $\alpha$ in the drive and sense equations of motion are zero.

### 3.4.1 *Case Study I*: governing equations for the $2\theta$ modes for CVG having 8 supports

This Section develops the governing equations of drive and sense $2\theta$ modes for a ring resonator having 8 supports such as that shown in Figure 3.6.

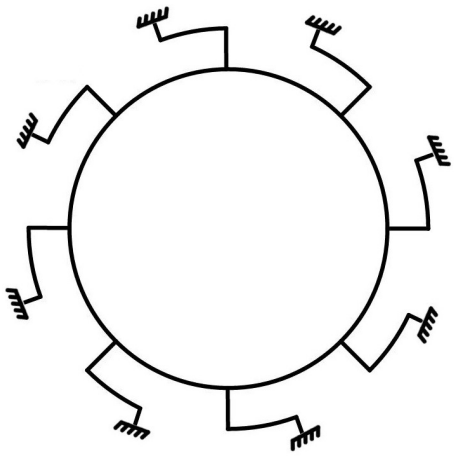


Figure 3.6: Schematic diagram of a ring-based resonator having 8 supports.

The equations are determined from (3.25) and (3.26) by selecting $n = 2$ and $p = 8$. The drive and sense governing equations of motion respectively are:

$$\ddot{Q}_1\left(1+Q_1^2\gamma_1\right)+\dot{Q}_1\left(\frac{\omega_0}{Q}+\dot{Q}_1Q_1\gamma_2\right)+Q_1\left(\omega_0^2+\dot{Q}_1^2\gamma_3+\ddot{Q}_1Q_1\gamma_4+Q_1^2\gamma_5+Q_1^4\gamma_6\right)+$$
$$+C_4^D\cos 8\alpha+S_4^D\sin 8\alpha=\mathcal{B}\Omega_z\dot{Q}_2+\frac{F_D}{M_{res}}\cos\Omega t \tag{3.33}$$

$$\ddot{Q}_2\left(1+Q_1^2\gamma_1\right)+\dot{Q}_2\left(\frac{\omega_0}{Q}+\dot{Q}_1Q_1\gamma_2\right)+Q_2\left(\omega_0^2+\dot{Q}_1^2\gamma_3+\ddot{Q}_1Q_1\gamma_4+Q_1^2\gamma_5+Q_1^4\gamma_6\right)+$$
$$+C_4^S\cos 8\alpha+S_4^S\sin 8\alpha=-\mathcal{B}\Omega_z\dot{Q}_1 \tag{3.34}$$

where inertial and stiffness coefficients $\gamma_1, ..., \gamma_6$ are given in (3.27)-(3.32) and

$$C_4^D = -\ddot{Q}_1 Q_1 I_1 + Q_1 \left(-\dot{Q}_1^2 I_1 + Q_1^2 S_1 + 6Q_1^4 S_3\right) + 3Q_2 Q_1^2 S_2 \tag{3.35}$$

$$S_4^D = -Q_1^3 S_2 - \ddot{Q}_2 Q_1^2 I_1 - 2\dot{Q}_2 \dot{Q}_1 Q_1 I_1 + Q_2 \left(-2\ddot{Q}_1 Q_1 I_1 - \dot{Q}_1^2 I_1 + 3Q_1^2 S_1 + 20Q_1^4 S_3\right) \tag{3.36}$$

$$C_4^S = \ddot{Q}_2 Q_1^2 I_1 + 2\dot{Q}_2 \dot{Q}_1 Q_1 I_1 + Q_2 \left(\dot{Q}_1^2 I_1 + 2\ddot{Q}_1 Q_1 I_1 - 3Q_1^2 S_1 - 10Q_1^4 S_3\right) + Q_1^3 S_2 \tag{3.37}$$

$$S_4^S = 3Q_2 Q_1^2 S_2 - \ddot{Q}_1 Q_1^2 I_1 + Q_1 \left(-\dot{Q}_1^2 I_1 + Q_1^2 S_1 + 4Q_1^4 S_3\right) \tag{3.38}$$

In these equations, coefficients $I_1$, $S_1$, $S_2$ and $S_3$ relate to the inertia (I) and stiffness (S) of the supports and are:

$$I_1 = \frac{1}{M_{res}} m_t \gamma^2 \tag{3.39}$$

$$S_1 = \frac{1}{M_{res}} \left(k_{r_3} - \frac{k_{t_1}}{2}\gamma^2 + \frac{k_{t_3}}{16}\right) \tag{3.40}$$

$$S_2 = \frac{1}{M_{res}} \frac{k_{t_2}}{2} \gamma \tag{3.41}$$

$$S_3 = -\frac{1}{M_{res}} \frac{3k_{t_3}}{64} \gamma^2 \tag{3.42}$$

Inertial coefficient $I_1$ relates to the tangential support inertia and ring geometrical non-linearity. Stiffness coefficient $S_1$ relates to the non-linear cubic radial and tangential stiffness of the support and ring geometrical non-linearity through $k_{t_1}$ which is multiplied by $\gamma$. Coefficients $S_2$ and $S_3$ are respectively related to the non-linear quadratic and cubic tangential stiffness of the support and ring geometrical non-linearity.

By substituting terms (3.35)-(3.38) in drive and sense equations (3.33), (3.34) and rearranging, the drive and sense equations of motion for a ring resonator having 8 supports can be

expressed as:

$$\begin{aligned}
&\ddot{Q}_1\left[1+Q_1^2\left(\gamma_1-I_1\cos 8\alpha\right)\right]+\dot{Q}_1\left(\frac{\omega_0}{Q}+\dot{Q}_1Q_1\gamma_2\right)+Q_1\left[\omega_0^2+\dot{Q}_1^2\left(\gamma_3-I_1\cos 8\alpha\right)+\right.\\
&\left.+\ddot{Q}_1Q_1\gamma_4+Q_1^2\left(\gamma_5+S_1\cos 8\alpha-S_2\sin 8\alpha\right)+Q_1^4\left(\gamma_6+6S_3\cos 8\alpha\right)\right]-\ddot{Q}_2Q_1^2\left(I_1\sin 8\alpha\right)-\\
&-\dot{Q}_2\dot{Q}_1Q_1\left(2I_1\sin 8\alpha\right)+Q_2\left[\ddot{Q}_1Q_1\left(-2I_1\sin 8\alpha\right)+\dot{Q}_1^2\left(-I_1\sin 8\alpha\right)+\right.\\
&\left.+Q_1^2\left(3S_1\sin 8\alpha+3S_2\cos 8\alpha\right)+Q_1^4\left(20S_3\sin 8\alpha\right)\right]=\mathcal{B}\Omega_z\dot{Q}_2+\frac{F_D}{M_{res}}\cos\Omega t
\end{aligned}\tag{3.43}$$

$$\begin{aligned}
&\ddot{Q}_2\left[1+Q_1^2\left(\gamma_1+I_1\cos 8\alpha\right)\right]+\dot{Q}_2\left[\frac{\omega_0}{Q}+\dot{Q}_1Q_1\left(\gamma_2+2I_1\cos 8\alpha\right)\right]+Q_2\left[\omega_0^2+\right.\\
&\left.+\dot{Q}_1^2\left(\gamma_3+I_1\cos 8\alpha\right)+\ddot{Q}_1Q_1\left(\gamma_4+2I_1\cos 8\alpha\right)+Q_1^2\left(\gamma_5-3S_1\cos 8\alpha+3S_2\sin 8\alpha\right)+\right.\\
&\left.+Q_1^4\left(\gamma_6-10S_3\cos 8\alpha\right)\right]-\ddot{Q}_1Q_1^2\left(I_1\sin 8\alpha\right)+Q_1\left[\dot{Q}_1^2\left(-I_1\sin 8\alpha\right)+\right.\\
&\left.+Q_1^2\left(S_1\sin 8\alpha+S_2\cos 8\alpha\right)+Q_1^4\left(4S_3\sin 8\alpha\right)\right]=-\mathcal{B}\Omega_z\dot{Q}_1
\end{aligned}\tag{3.44}$$

It is noted that terms $I_1$, $S_1$, $S_2$ and $S_3$ are all multiplied by either $\cos 8\alpha$ or $\sin 8\alpha$ and break the symmetry between the system parts of the drive and sense equations of motion. Due to the presence of $\alpha$, the drive and sense mode non-linear equations depend on the orientation of the drive axis relative to the supports. From equation (3.43) it is noted that $I_1$, $S_1$, $S_2$ and $S_3$ terms cause the drive equation to parametrically depend on linear terms in $Q_2$ producing backwards coupling from the sense response to the drive response. From equation (3.44) one can see that terms $I_1$, $S_1$, $S_2$ and $S_3$ cause the sense equation to have non-linear terms involving the drive response which couple the sense motion to the drive response in the absence of rotation.

For a linear resonator in Chapter 2 it was demonstrated that frequency split and mode coupling in the absence of rotation cause sensing errors and reduce sensor sensitivity to rotation and SNR. One can deduce that terms $I_1$, $S_1$, $S_2$ and $S_3$ cause a similar behaviour for non-linear resonators having 8 supports. It is worth noting that whilst it is not feasible to eliminate the tangential support inertial term $I_1$, actions can be taken to mitigate against this

coupling by reducing (ideally eliminating) stiffness coefficients $S_1$, $S_2$ and/or $S_3$. Stiffness coefficient $S_1$ can be eliminated by designing supports ensuring $-8k_{t_1}\gamma^2 + k_{t_3} + 16k_{r_3} = 0$. Similarly, $S_2$ is eliminated when $k_{t_2} = 0$ and $S_3 = 0$ when $k_{t_3} = 0$. In later work, a support design having $k_{t_2} = 0$ will be proposed.

Drive and sense equations (3.43) and (3.44) were developed under the assumption that $Q_2 << Q_1$ so that all non-linear terms in $Q_2$ in drive and sense equations were neglected. In practice, if the sense response amplitude in operation is much smaller than the drive response, linear terms involving $Q_2$ in the drive equation can also be neglected. Moreover, for the range of drive response amplitudes considered in this work, higher powers of $Q_1$ than the cubic are considered to be small and negligible. Under these circumstances, the backwards coupling from the sense response to the drive response is neglected, and drive and sense equations (3.43) and (3.44) become:

$$\begin{aligned}&\ddot{Q}_1\left[1+Q_1^2\left(\gamma_1 - I_1\cos 8\alpha\right)\right] + \dot{Q}_1\left(\frac{\omega_0}{Q} + \dot{Q}_1 Q_1\gamma_2\right) + Q_1\left[\omega_0^2 + \dot{Q}_1^2\left(\gamma_3 - I_1\cos 8\alpha\right) + \right.\\ &\left. + \ddot{Q}_1 Q_1\gamma_4 + Q_1^2\left(\gamma_5 + S_1\cos 8\alpha - S_2\sin 8\alpha\right)\right] = \frac{F_D}{M_{res}}\cos\Omega t\end{aligned} \tag{3.45}$$

$$\begin{aligned}&\ddot{Q}_2\left[1+Q_1^2\left(\gamma_1 + I_1\cos 8\alpha\right)\right] + \dot{Q}_2\left[\frac{\omega_0}{Q} + \dot{Q}_1 Q_1\left(\gamma_2 + 2I_1\cos 8\alpha\right)\right] + \\ &+Q_2\left[\omega_0^2 + \dot{Q}_1^2\left(\gamma_3 + I_1\cos 8\alpha\right) + \ddot{Q}_1 Q_1\left(\gamma_4 + 2I_1\cos 8\alpha\right) + \right.\\ &\left. + Q_1^2\left(\gamma_5 - 3S_1\cos 8\alpha + 3S_2\sin 8\alpha\right)\right] - \ddot{Q}_1 Q_1^2\left(I_1\sin 8\alpha\right) - Q_1\dot{Q}_1^2\left(I_1\sin 8\alpha\right) + \\ &+Q_1^3\left(S_1\sin 8\alpha + S_2\cos 8\alpha\right) = -\mathcal{B}\Omega_z\dot{Q}_1\end{aligned} \tag{3.46}$$

In later work, simplified equations (3.45) and (3.46) will be used to investigate the drive and sense responses for ring resonators based on the $2\theta$ modes having 8 supports, for practical CVGs operation. The influence of higher powers of $Q_1$ than the cubic and of the backwards coupling on the drive and sense responses will be investigated to justify the assumptions made. Furthermore, the drive response will be determined for drive axes aligned at the

supports (i.e. $\alpha = 0°$) and mid-way between supports (i.e. $\alpha = 22.5°$) to evaluate the effect of using a different angle $\alpha$ on the drive mode dynamics.

### 3.4.2 *Case Study II*: governing equations for the $2\theta$ modes for CVG having 16 supports

This Section develops the equations of motion governing the dynamics of drive and sense $2\theta$ modes for a ring resonator having 16 supports such as that shown in Figure 3.7.

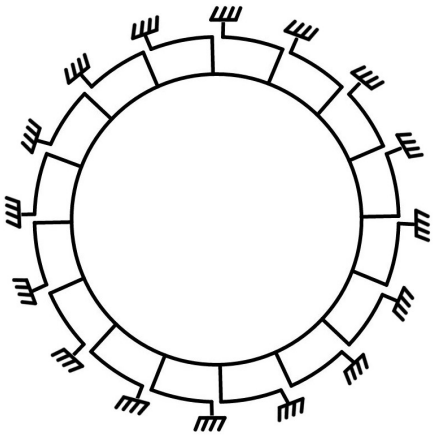


Figure 3.7: Schematic diagram of a ring-based resonator having 16 supports.

The equations of motion are determined from (3.25) and (3.26) for $n = 2$ and $p = 16$. In this case, all terms in $C_m^D$, $S_m^D$ and $C_m^S$ and $S_m^S$ (for $m = 1, ..., 6$) are zero because $\frac{mn}{p}$ is not an integer for $m = 1, ..., 6$. The drive and sense equations of motion respectively are:

$$\ddot{Q}_1\left(1+Q_1^2\gamma_1\right)+\dot{Q}_1\left(\frac{\omega_0}{Q}+\dot{Q}_1Q_1\gamma_2\right)+Q_1\left(\omega_0^2+\dot{Q}_1^2\gamma_3+\ddot{Q}_1Q_1\gamma_4+Q_1^2\gamma_5+Q_1^4\gamma_6\right)= \\ =\mathcal{B}\Omega_z\dot{Q}_2+\frac{F_D}{M_{res}}\cos\Omega t \tag{3.47}$$

$$\ddot{Q}_2\left(1+Q_1^2\gamma_1\right)+\dot{Q}_2\left(\frac{\omega_0}{Q}+\dot{Q}_1Q_1\gamma_2\right)+Q_2\left(\omega_0^2+\dot{Q}_1^2\gamma_3+\ddot{Q}_1Q_1\gamma_4+Q_1^2\gamma_5+Q_1^4\gamma_6\right)= \\ =-\mathcal{B}\Omega_z\dot{Q}_1 \tag{3.48}$$

where $\gamma_1, ..., \gamma_6$ are given by (3.27)-(3.32). It is noted that when the rotational symmetry is maintained, the system parts of the drive and sense equations are identical and the equations are independent of the location of the drive axis relative to the supports. Similar to the 8 support case (*Case Study I*), ring and support geometrical non-linearity causes the drive and sense modal mass, stiffness and damping to be parametrically coupled to non-linear terms in $Q_1$. However, when the rotational symmetry is maintained, drive and sense responses are only parametrically coupled with each other, and the sense equation is externally excited by the Coriolis force only in the presence of angular rate. For a linear resonator in Chapter 2 it was demonstrated that if drive and sense resonance frequencies are matched and modes are only coupled by the Coriolis action in the presence of rotation, sensor performance are enhanced. Based on those results, similar good performance may be expected for a ring resonator having 16 supports operating at large amplitude vibration.

Similar to the 8 support case, for the range of drive response amplitudes considered in this work, higher powers of $Q_1$ than the cubic in drive and sense equations (3.47) and (3.48), and the Coriolis term in drive equation (3.47) are considered to be small and negligible. Under these circumstances, drive and sense equations reduce to:

$$\begin{aligned} &\ddot{Q}_1\left(1+Q_1^2\gamma_1\right)+\dot{Q}_1\left(\frac{\omega_0}{Q}+\dot{Q}_1Q_1\gamma_2\right)+Q_1\left(\omega_0^2+\dot{Q}_1^2\gamma_3+\ddot{Q}_1Q_1\gamma_4+Q_1^2\gamma_5\right)= \\ &=\frac{F_D}{M_{res}}\cos\Omega t \end{aligned} \tag{3.49}$$

$$\begin{aligned} &\ddot{Q}_2\left(1+Q_1^2\gamma_1\right)+\dot{Q}_2\left(\frac{\omega_0}{Q}+\dot{Q}_1Q_1\gamma_2\right)+Q_2\left(\omega_0^2+\dot{Q}_1^2\gamma_3+\ddot{Q}_1Q_1\gamma_4+Q_1^2\gamma_5\right)= \\ &=-\mathcal{B}\Omega_z\dot{Q}_1 \end{aligned} \tag{3.50}$$

In later work, equations (3.49) and (3.50) will be used to investigate the drive and sense responses for ring resonators based on the $2\theta$ modes having 16 supports, for practical CVGs operation. The independence of the drive response on angle $\alpha$ will be verified against a

non-linear Finite Element analysis by investigating the drive response for different $\alpha$ angles.

### 3.4.3 Summary of *Case Study I* and *Case Study II*, comparison and interpretation

Section 3.3 indicated that for practical ring resonators based on the $2\theta$ modes 8 supports break the rotational symmetry when the resonator is excited into large amplitude vibration; in contrast, 16 supports maintain the symmetry. The equations governing the drive and sense $2\theta$ modes for ring resonators having 8 and 16 supports were developed in Sections 3.4.1 and 3.4.2, respectively. It was found that:

- For ring resonators having 8 regularly spaced supports, ring and support non-linearity causes the drive and sense modal mass, damping and stiffness to be different from each other and to depend on the orientation of the drive axis relative to the supports. Terms involving drive angle $\alpha$ couple the drive and sense equations in the absence of rotation. Chapter 2 for a linear resonator demonstrated that frequency split and mode coupling in the absence of rotation cause sensing errors and reduce sensor sensitivity. Based on those results, 8 supports are expected to degrade sensor performance when the resonator operates at large amplitudes.

- For ring resonators having 16 supports, the modal mass, damping and stiffness of the drive and sense modes are identical to each other. The $2\theta$ drive and sense modes are only coupled by the Coriolis force in the presence of angular rate. In Chapter 2 for a linear resonator, it was shown that if drive and sense resonance frequencies are equal, and modes are coupled by the rotation-induced Coriolis force only, the angular rate can be accurately detected by measuring the in-phase sense response. Therefore, 16 supports are expected to provide accurate sensor performance compared to 8 supports when the ring is driven into large amplitude vibration.

## 3.5 Summary and conclusions

This Chapter developed a mathematical model for modelling ring resonators having $p$ supports, operating in any pair of $n\theta$ modes at large vibration amplitudes. The mathematical model included ring and support geometrical non-linearity, and was used to determine analytical expressions for the kinetic and potential energies of non-linear ring and support structures. It was found that whilst $p$ supports maintain the $n\theta$ rotational symmetry in the linear regime when $\frac{2n}{p}$ is not an integer, ring and support geometrical non-linearity causes the rotational symmetry to break for supports numbers $p$ which ensure $\frac{mn}{p}$ is an integer, for $m = 1, ..., 6$. Therefore, some numbers of supports which maintain the rotational symmetry in the linear regime, break the symmetry when the ring is driven into large amplitude vibration. For practical CVGs based on the $2\theta$ modes, 8 supports were found to break the rotational symmetry at large amplitudes, whilst 16 supports were found to maintain the symmetry.

The equations of motion governing the drive and sense $n\theta$ modes were developed for ring resonators having $p$ supports. Under the assumption that the drive response amplitude is much larger than the sense response, all non-linear terms in $Q_2$ were neglected from the equations. The impact of the breaking of rotational symmetry was investigated by comparing the equations of motion of the $2\theta$ modes obtained for resonators having 8 and 16 supports.
It was found that for 8 supports, ring and support non-linearity causes the drive and sense modal mass, damping and stiffness to be different from each other. Drive and sense equations depend on the orientation of the drive axis relative to the supports, and the $2\theta$ modes are coupled in the absence of rotation. Based on the results obtained for a linear resonator having a point mass imperfection in Chapter 2, performance of resonators having 8 supports are expected to degrade when the ring operates at large amplitudes.
In contrast, for 16 supports it was found that system parts of the drive and sense equations are identical to each other. Drive and sense equations are coupled only by the rotation-

induced Coriolis force in the presence of rotation. It was concluded that 16 supports which maintain the rotational symmetry are expected to enhance sensor performance compared to 8 supports that break the symmetry, when the ring is driven into large amplitude vibration.

# Chapter 4

# Investigating the drive response for CVGs operating at large amplitude

## 4.1 Introduction

This Chapter investigates the drive $2\theta$ response for a ring that is driven into large vibration amplitude, for ring resonators having 8 and 16 supports. In Chapter 3, drive and sense equations of motion were developed, and it was found that ring and support geometrical non-linearity causes the governing equation of the drive mode to parametrically depend on non-linear terms in drive generalised coordinate $Q_1$. Previous studies [5, 29, 31] indicated that non-linear $Q_1$ terms in the modal mass, damping and stiffness equations of the drive mode have a potential to cause the drive mode resonance frequency to shift from the linear resonance frequency for large drive amplitudes. This non-linear behaviour of the drive mode is investigated in this Chapter. The averaging method is used to investigate the amplitude and phase of the drive response in steady-state when the ring is driven into large amplitude vibration. The drive mode frequency response curves are compared against those for a linear resonator, to highlight the effect of ring and support geometrical non-linearity. The frequency backbone curve for the drive mode is determined based on a drive response having

phase of 90 degrees relative to the applied driving force. The frequency backbone curve for the supported and unsupported ring resonators are compared to investigate the influence of the support structure on the non-linear drive mode behaviour, for two different support geometries. In later work, the influence of the support structure on the drive mode dynamic behaviour investigated in this Chapter will be used to design improved support geometries which mitigate non-linearity effects on the drive response.

In Chapter 3 it was found that 8 and 16 supports, respectively, break and maintain the $n = 2$ rotational symmetry when the ring is driven into large amplitude vibration. It was found that for the 8 support structure, the drive mode equation involves terms in drive angle $\alpha$ causing the drive mode dynamics to depend upon the orientation of the drive axis relative to the supports. In contrast, for the 16 support structure, the drive mode equation is independent of $\alpha$. In this Chapter, the dependence of the drive mode dynamics on the location of the drive axis is investigated by calculating the drive mode frequency backbone curve for two $\alpha$ angles, i.e. two different drive excitations. Finite Element non-linear transient analyses are used to verify the results obtained using the averaging method.

This Chapter is structured as follows. Section 4.2 introduces the method of averaging, as applied herewith, and describes in general terms how the method is used to determine the steady-state amplitude and phase of the drive response when subjected to harmonic excitation. Section 4.3 describes how a non-linear transient Finite Element (FE) analysis is used to determine the frequency response curve for the drive mode, for the purpose of comparison against the results obtained using the method of averaging. Sections 4.4 and 4.5 show results obtained using the averaging method and a FE non-linear transient analysis for ring resonators having 8 and 16 supports, respectively. Section 4.6 discusses the comparison between mathematical and Finite Element results, and Section 4.7 summarises the work done in this Chapter and reiterates key conclusions.

## 4.2 The method of averaging

In this work, the averaging method is used to determine the steady-state response of the drive mode (amplitude and phase) when the drive mode is subjected to harmonic excitation and driven into large amplitude. In this Section, the averaging method [35–37] is introduced to determine the steady-state solution of a non-linear oscillator subjected to external harmonic excitation. Consider the forced harmonic oscillation of a mass connected to a non-linear spring, described by the damped Duffing's equation below:

$$\ddot{x} + \delta\dot{x} + \omega_0^2 x + \epsilon x^3 = F\cos\omega t \tag{4.1}$$

where $\delta$ is the damping coefficient, $\omega_0$ the natural resonance frequency of the oscillator, and $\epsilon$ the stiffness coefficient of the cubic non-linear spring. One can assume that initial conditions are $x(0) = 0$ and $\dot{x}(0) = 0$. For the equivalent linear system (i.e. $\epsilon = 0$), the solution is given by $x(t) = A\cos(\omega t + \phi)$ where $A$ is the oscillation amplitude and $\phi$ the phase of the mass response relative to the applied harmonic force. For a linear system, amplitude $A$ and $\phi$ phase are constants. For the non-linear system (i.e. $\epsilon \neq 0$), solution of the non-linear equation (4.1) can be searched in the form:

$$x(t) = A(t)\cos\chi(t) \tag{4.2}$$

where $\chi = \omega t + \phi(t)$ and amplitude $A(t)$ and phase $\phi(t)$ are unknown functions of time. Using the Krylov-Bogoliubov technique [35–37], solution (4.2) is subject to condition:

$$\dot{x}(t) = -\omega A(t)\sin\chi(t) \tag{4.3}$$

implying that the velocity has the same form as $\epsilon = 0$. Differentiating (4.2) with respect to time, gives:

$$\dot{x}(t) = \dot{A}\cos\chi - A\omega\sin\chi - A\dot{\phi}\sin\chi \tag{4.4}$$

Comparing (4.3) and (4.4) it is noted that amplitude $A$ and phase $\phi$ satisfy the condition:

$$\dot{A}\cos\chi - A\dot{\phi}\sin\chi = 0 \tag{4.5}$$

Differentiating (4.3) with respect to time gives:

$$\ddot{x}(t) = -\omega\dot{A}\sin\chi - \omega^2 A\cos\chi - \omega A\dot{\phi}\cos\chi \tag{4.6}$$

Equations for $x(t)$, $\dot{x}(t)$ and $\ddot{x}(t)$ respectively given by (4.2), (4.3) and (4.6) are used in Duffing's equation (4.1). This gives:

$$-\omega\dot{A}\sin\chi - \omega^2 A\cos\chi - \omega A\dot{\phi}\cos\chi - \delta\omega A\sin\chi + \omega_0^2 A\cos\chi + \epsilon A^3\cos^3\chi = F\cos\omega t \tag{4.7}$$

Equations (4.5) and (4.7) are solved for $\dot{A}$ and $\dot{\phi}$, giving:

$$\omega A\dot{\phi} = \left(-\omega^2 A\cos\chi + \omega_0^2 A\cos\chi - \delta\omega A\sin\chi + \epsilon A^3\cos^3\chi - F\cos\omega t\right)\cos\chi \tag{4.8}$$

$$\omega\dot{A} = \left(-\omega^2 A\cos\chi + \omega_0^2 A\cos\chi - \delta\omega A\sin\chi + \epsilon A^3\cos^3\chi - F\cos\omega t\right)\sin\chi \tag{4.9}$$

These first order equations for the amplitude $A$ and phase $\phi$ are equivalent to the non-linear second order differential equation (4.1) for $x(t)$. An approximation is now introduced by noting that right-hand sides of equations (4.8) and (4.9) are periodic with respect to $\chi$ and have period of oscillation $T = \frac{2\pi}{\omega}$. It is assumed that amplitude $A$ and phase $\phi$ remain approximatively constant during the oscillation period $T$. Equations (4.8) and (4.9) are averaged over the period $T$, considering $\dot{A}$, $\dot{\phi}$, $A$ and $\phi$ constant while performing the

averaging. For steady-state solution (i.e. $\dot{A} = \dot{\phi} = 0$), this gives:

$$A\left(\omega_0^2 - \omega^2\right) + \frac{3}{4}\epsilon A^3 = F\cos\phi \tag{4.10}$$

$$\delta\omega A = -F\sin\phi \tag{4.11}$$

In these equations, $A$ and $\phi$ indicate the averaged quantities. Equations (4.10) and (4.11) can be solved in $A$ and $\phi$ to approximate the amplitude and phase of the steady-state solution for the non-linear oscillator. It can be shown that equations (4.10) and (4.11) can also be obtained by multiplying equation (4.7) by (i) $\cos\chi$ and (ii) $\sin\chi$, and averaging the obtained equations over the oscillation period, under equivalent assumptions, i.e. $A$ and $\phi$ slowly vary in $T$ and are constant during the averaging.

In Sections 4.4 and 4.5, the averaging method is applied to determine the averaged amplitude and phase of the drive response in steady-state when the drive mode is subjected to harmonic excitation. The drive response $Q_1(t)$ is expressed as:

$$Q_1(t) = q_1(t)\cos\chi \tag{4.12}$$

where $q_1(t)$ is the oscillation amplitude and

$$\chi = \Omega t + \phi_D(t) \tag{4.13}$$

In this equation, $\Omega$ is the frequency of the applied harmonic force and $\phi_D$ is the phase of the drive response relative to the applied force. Solution (4.12) is subject to the condition:

$$\dot{Q}_1(t) = -\Omega q_1(t)\sin\chi \tag{4.14}$$

Differentiating (4.14) with respect to time, gives:

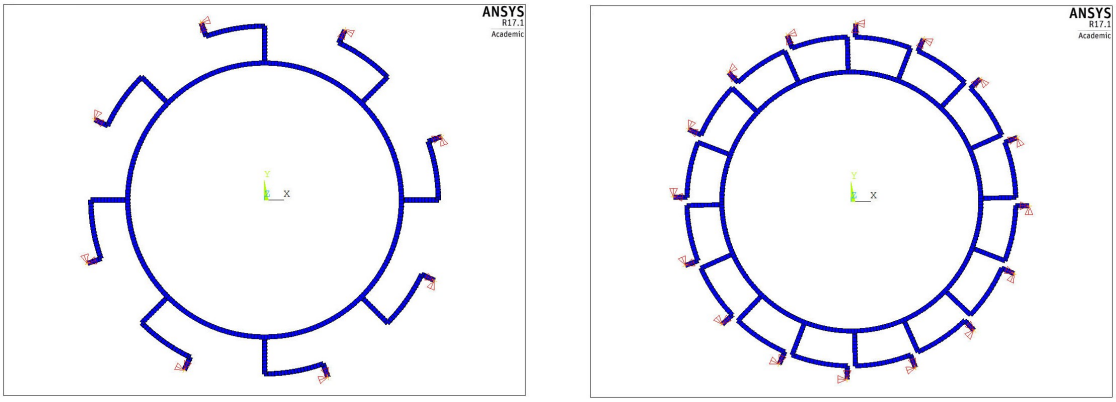
$$\ddot{Q}_1(t) = -\Omega \dot{q_1} \sin\chi - \Omega^2 q_1 \cos\chi - \Omega q_1 \dot{\phi_D} \cos\chi \tag{4.15}$$

Equations (4.12), (4.14) and (4.15) are respectively substituted to $Q_1$, $\dot{Q}_1$ and $\ddot{Q}_1$ in the non-linear drive equation. The drive equation is then multiplied by (i) $\cos\chi$, and (ii) $\sin\chi$. The obtained two equations in $\dot{A}(t)$, $\dot{\phi_D}(t)$, $A(t)$ and $\phi_D(t)$ are averaged over the time period $\frac{2\pi}{\Omega}$. Amplitude $q_1(t)$ and phase $\phi_D(t)$ of the drive response vary little over the oscillation period and can be substituted by their averaged values $q_1$ and $\phi_D$. The obtained equations in averaged quantities $q_1$ and $\phi_D$ are solved to approximate the steady-state response of the drive mode.

## 4.3 Finite Element (FE) non-linear analysis to determine drive mode frequency response curve

Finite Element (FE) analyses are used in Sections 4.4 and 4.5 to verify results obtained using the averaging method for ring resonators having 8 and 16 supports, respectively. This Section describes how the frequency backbone curve for the drive mode is determined using a FE non-linear transient analysis (or time history analysis). The commercial software package used is *ANSYS Parametric Design Language* (APDL). Appendix A describes the Finite Element models developed for practical supported ring resonators having 8 and 16 supports. In summary, ring and support structures have been modelled using uni-axial beam elements BEAM3. Each element translates in the ring plane and rotates around the ring polar axis. Each support is attached to the ring by one end and the other end is fully clamped. Figures 4.1a and 4.1b show Finite Element models developed for ring resonators having respectively 8 and 16 arched supports, where the ring structure and supports geometry are the same for the 8 and 16 support structure. Geometrical data for the ring and support structures shown

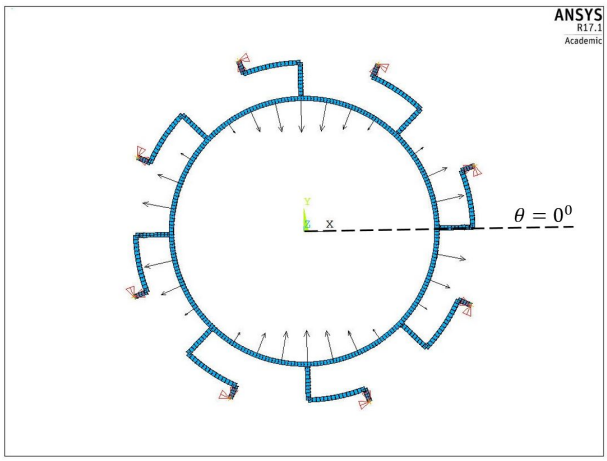
in Figures 4.1a and 4.1b are provided in Section A.1 in Appendix A. In what follows, arched supports such as those in Figure 4.1 will be referred to as nominal supports.



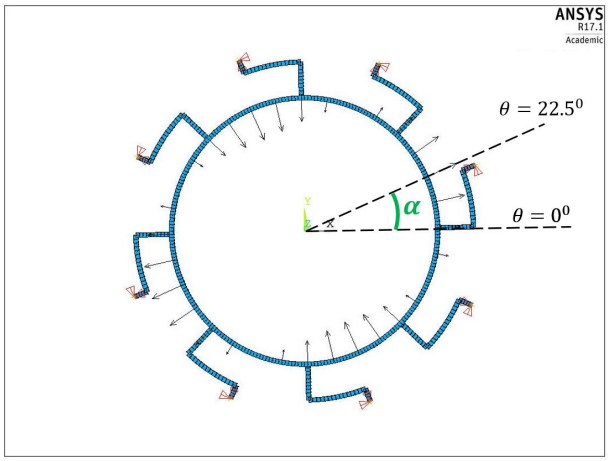

(a) $p = 8$ (b) $p = 16$

Figure 4.1: Finite Element models developed for practical ring-based CVGs having 8 and 16 nominal supports. Supports geometry and ring structure are equal for $p = 8$ and $p = 16$.

The drive mode frequency backbone curve is investigated performing Finite Element structural non-linear transient analyses which calculate the dynamic response of a structure under the action of time-varying loads, using the Newmark time-integration method [38]. The ring is excited in a pure $2\theta$ mode by applying circumferential radial harmonic forces. For the ring resonator having 8 nominal supports, Figures 4.2a and 4.2b illustrate the applied forces distributed around the ring circumference to generate a $2\theta$ force distribution aligned with the supports (i.e. $\alpha = 0^0$) and aligned mid-way between two supports (i.e. $\alpha = 22.5^0$), respectively.




(a) $\alpha = 0^0$




(b) $\alpha = 22.5^0$

Figure 4.2: Radial applied forces distributed around the ring circumference to generate a $2\theta$ force distribution aligned with the supports (i.e. $\alpha = 0^0$) and aligned mid-way between two supports (i.e. $\alpha = 22.5^0$) for a ring resonator having 8 supports. The circumferential reference coordinate $\theta = 0^0$ is the horizontal.

A structural transient analysis is performed to obtain time histories of the radial displacements of the ring nodes caused by applied harmonic forces, and ring and support geometric non-linearity is considered by including large-deflections effects. The integration time step and duration of the simulation are selected as to ensure the non-linear transient analysis captures the dynamics accurately. The structural damping coefficient is defined by selecting the multiplication coefficient of the mass matrix, given by $\omega_0 Q^{-1}$, where the value of the linear

natural frequency $\omega_0$ is calculated using a FE modal analysis. For a Q-factor of 1000, a time step of about $\frac{1}{70f_0}$ seconds (where $f_0 = \frac{\omega_0}{2\pi}$) was found to provide an accurate time response for the radial oscillation. As $f_0$ for the resonators considered is approximately 15 kHz, the time step used for the simulations is $10^{-6}$ seconds. To determine if the time response is in steady-state, the peak amplitudes are detected for each cycle, and the response is considered to be in steady-state when the difference between the peak values of two consecutive cycles is within 0.05%. Using a Q-factor of 1000, the steady-state condition is verified after about 0.20 seconds of simulation. Due to the high computational cost, all the FE simulations have been performed for a Q-factor of 1000, and only key results obtained analytically have been verified against FE simulations.

Steady-state radial displacements of ring nodes at $\alpha$ and $\alpha + 90^0$ calculated using the FE non-linear transient analysis are used to obtain the steady-state radial anti-node response $Q_1$. Based on non-linear equation (3.1), the radial displacements of the ring at $\theta = \alpha$ and $\theta = \alpha + 90^0$ are:

$$u(\alpha) = Q_1 - \gamma\left(Q_1^2 + Q_2^2\right) \tag{4.16}$$

$$u\left(\alpha + 90^0\right) = -Q_1 - \gamma\left(Q_1^2 + Q_2^2\right) \tag{4.17}$$

Using these equations it can be shown easily that generalised coordinate $Q_1$ is:

$$Q_1(t) = \frac{1}{2}\left[u(\alpha) - u\left(\alpha + 90^0\right)\right] \tag{4.18}$$

The steady-state response $Q_1$ is post-processed to obtain the amplitude $q_1$ and phase $\phi_D$ of the drive response relative to the applied driving forces. The frequency backbone curve for the drive mode is obtained by varying the frequency of the harmonic forces to identify the frequency at which the drive response is 90° out-of-phase relative to applied force. This is repeated for different levels of force magnitude. The dependency of the drive mode non-linear dynamics on the position of the drive axis relative to the supports is investigated by

calculating the drive mode frequency backbone curve for different $\alpha$ angles, applying forces as shown in Figures 4.2a and 4.2b for a ring resonator having 8 supports.

## 4.4 Drive response for a ring having 8 supports

In this Section, the drive $2\theta$ response is investigated for ring resonators having 8 supports. The averaging method is applied to the non-linear drive equation to investigate the averaged amplitude and phase of the drive response in steady-state, when the drive mode is subjected to external harmonic excitation. Drive mode frequency backbone curves obtained using the averaging method are verified against Finite Element simulations. Numerical results are shown for the practical ring resonator having 8 nominal supports, shown in Figure 4.1a.

### 4.4.1 Drive response obtained using the averaging method

The $2\theta$ drive mode equation of motion for ring resonators having 8 supports was developed in Section 3.4.1 in Chapter 3 by considering that, in practice, the response amplitude of the drive mode is much larger than the sense response amplitude, so that all non-linear terms in $Q_2$ in the drive equation were considered to be small and neglected. The resulting drive equation (3.43) had linear terms in $Q_2$ indicating backwards coupling from the sense to the drive mode, including the rotation-induced Coriolis force. For the range of drive response amplitudes condiered in this work, backwards coupling terms and powers of $Q_1$ higher than the cubic were considered to be small and neglected from equation (3.43) which reduced to equation (3.45) here repeated below:

$$\ddot{Q_1}\left[1+Q_1^2\left(\gamma_1-I_1\cos 8\alpha\right)\right]+\dot{Q_1}\left(\frac{\omega_0}{Q}+\dot{Q_1}Q_1\gamma_2\right)+Q_1\Big[\omega_0^2+\dot{Q_1}^2\left(\gamma_3-I_1\cos 8\alpha\right)+ \\ +\ddot{Q_1}Q_1\gamma_4+Q_1^2\left(\gamma_5+S_1\cos 8\alpha-S_2\sin 8\alpha\right)\Big]=\frac{F_D}{M_{res}}\cos\Omega t \tag{4.19}$$

where coefficients $\gamma_1, ..., \gamma_5$ are defined in (3.27)-(3.31) and $I_1$, $S_1$ and $S_2$, respectively, in (3.39), (3.40) and (3.41).

To investigate the steady-state response of the drive mode, the averaging method is applied as discussed in Section 4.2. The steady-state response of the drive mode (4.12) having amplitude $q_1(t)$ and phase $\phi_D(t)$ relative to the exciting force is used in drive equation (4.19). The drive equation is then multiplied by (i) $\cos\chi$ and (ii) $\sin\chi$, where $\chi = \Omega t + \phi_D(t)$. Averaging the obtained equations over the oscillation period $\frac{2\pi}{\Omega}$ gives the following equations in the averaged amplitude $q_1$ and averaged phase $\phi_D$ of the steady-state drive response:

$$\begin{aligned} q_1\left(\omega_0^2 - \Omega^2\right) + q_1^3\Bigg[-\Omega^2\left(\frac{3}{4}\gamma_1 - \frac{1}{4}\gamma_2 - \frac{1}{4}\gamma_3 + \frac{3}{4}\gamma_4 - \frac{1}{2}I_1\cos 8\alpha\right) + \\ + \frac{3}{4}\left(\gamma_5 + S_1\cos 8\alpha - S_2\sin 8\alpha\right)\Bigg] = \frac{F_D}{M_{res}}\cos\phi_D \end{aligned} \tag{4.20}$$

$$-\frac{q_1\omega_0\Omega}{Q} = \frac{F_D}{M_{res}}\sin\phi_D \tag{4.21}$$

These equations can be solved to determine $q_1$ and $\phi_D$. It can be shown that squaring and adding equations (4.20) and (4.21) gives:

$$c_6 q_1^6 + c_4 q_1^4 + c_2 q_1^2 = \left(\frac{F_D}{M_{res}}\right)^2 \tag{4.22}$$

where

$$c_2 = \left(\omega_0^2 - \Omega^2\right)^2 + \left(\frac{\omega_0}{Q}\Omega\right)^2 \tag{4.23}$$

$$\begin{aligned} c_4 =& 2\left(\omega_0^2 - \Omega^2\right)\Bigg[-\Omega^2\left(\frac{3}{4}\gamma_1 - \frac{1}{4}\gamma_2 - \frac{1}{4}\gamma_3 + \frac{3}{4}\gamma_4 - \frac{1}{2}I_1\cos 8\alpha\right) + \\ &+ \frac{3}{4}\left(\gamma_5 + S_1\cos 8\alpha - S_2\sin 8\alpha\right)\Bigg] \end{aligned} \tag{4.24}$$

$$c_6 = \left[\Omega^2\left(\frac{3}{4}\gamma_1 - \frac{1}{4}\gamma_2 - \frac{1}{4}\gamma_3 + \frac{3}{4}\gamma_4 - \frac{1}{2}I_1\cos 8\alpha\right) - \frac{3}{4}\left(\gamma_5 + S_1\cos 8\alpha - S_2\sin 8\alpha\right)\right]^2 \tag{4.25}$$

Real positive solutions of (4.22) give the amplitude $q_1$ of the drive response for a given external applied force.

Dividing (4.21) by (4.20) it can be shown that the phase $\phi_D$ of the drive response relative to the applied force is:

$$\phi_D = \tan^{-1} \frac{-\omega_0 \Omega Q^{-1}}{\left(\omega_0^2 - \Omega^2\right) - \Omega^2 q_1^2 \left(\frac{3}{4}\gamma_1 - \frac{1}{4}\gamma_2 - \frac{1}{4}\gamma_3 + \frac{3}{4}\gamma_4 - \frac{1}{2}I_1 \cos 8\alpha\right) + \\ + \frac{3}{4} q_1^2 \left(\gamma_5 + S_1 \cos 8\alpha - S_2 \sin 8\alpha\right)} \tag{4.26}$$

Equations (4.22) and (4.26) describe the steady-state averaged amplitude and phase of the drive response. It is clear from the equations that ring and support geometrical non-linearity causes the amplitude and phase of the drive response to vary with drive amplitude. The frequency of the external force causing the drive mode to respond in resonance with amplitude $q_1$ is obtained based on $\phi_D = -90^0$ in equation (4.26). This gives:

$$\Omega_D^2 \left(q_1\right) = \frac{\omega_0^2 + \frac{3}{4} q_1^2 \left(\gamma_5 + S_1 \cos 8\alpha - S_2 \sin 8\alpha\right)}{1 + q_1^2 \left(\frac{3}{4}\gamma_1 - \frac{1}{4}\gamma_2 - \frac{1}{4}\gamma_3 + \frac{3}{4}\gamma_4 - \frac{1}{2}I_1 \cos 8\alpha\right)} \tag{4.27}$$

This equation describes the frequency backbone curve for the drive mode for ring resonators having 8 supports, including ring and support geometrical non-linearity effect. For a given drive amplitude $q_1$, equation (4.27) gives the corresponding resonance frequency (or pseudo-resonance frequency) $\Omega_D$. At large vibration amplitudes, the effect of non-linear terms $\gamma_1, ..., \gamma_5$ and $I_1$, $S_1$ and $S_2$ is significant and causes the resonance frequency $\Omega_D$ to shift from natural frequency $\omega_0$. To highlight ring and support non-linear terms which cause the resonance frequency to shift, equation (4.27) can be re-written using (3.27)-(3.31) and

(3.39)-(3.41), as:

$$\begin{aligned}\Omega_D^2 - \omega_0^2 =& \frac{q_1^2}{M_{res}} \left[ -\Omega_D^2 \left( \frac{33}{10} M_{ring} + \frac{1}{2} m_t \left(1 - \cos 8\alpha\right) + 16 m_r \right) \gamma^2 + \right. \\ &+ \frac{1}{3} K_{ring} \gamma^2 + 12 k_{r_1} \gamma^2 + \frac{3}{8} k_{t_1} \gamma^2 \left(1 - \cos 8\alpha\right) - 12 k_{r_2} \gamma - \frac{3}{8} k_{t_2} \gamma \sin 8\alpha + \\ &\left. + \frac{3}{4} k_{r_3} \left(3 + \cos 8\alpha\right) + \frac{3}{64} k_{t_3} \left(3 + \cos 8\alpha\right) \right]\end{aligned} \tag{4.28}$$

In this equation, the left-hand term would be zero in the absence of frequency shift. Hence, right-hand terms can be thought as responsible of the frequency shift occurrence. It can be noticed that the frequency shift is caused by:

- Terms in $M_{ring}\gamma^2$ and $K_{ring}\gamma^2$ involving ring non-linear flexural vibration.
- Non-linear support stiffness coefficients $k_{r_3}$ and $k_{t_3}$.
- Terms in $m_t\gamma^2$, $m_r\gamma^2$, $k_{r_1}\gamma^2$ and $k_{t_1}\gamma^2$ arising due to ring non-linear flexural vibrations in the presence of the support structure.
- Terms in $k_{r_2}\gamma$ and $k_{t_2}\gamma$ due to the combined effect of ring and support geometrical non-linearity.

From equation (4.28) it is noted that if the right-hand side has a negative value, then $(\Omega_D^2 - \omega_0^2) < 0$, so for large amplitudes of vibration the drive resonance frequency $\Omega_D$ is smaller than the linear resonance frequency $\omega_0$ (i.e. softening behaviour). In contrast, if the right-hand side in equation (4.28) is positive, then $(\Omega_D^2 - \omega_0^2) > 0$ so for large amplitudes the drive mode is resonant at frequencies larger than the linear frequency $\omega_0$ (i.e. hardening behaviour). For unsupported rings, it can be shown that non-linear inertial term $M_{ring}\gamma^2$ multiplied by $\Omega_D^2$ in (4.28) is much larger than non-linear stiffness term $K_{ring}\gamma^2$. This causes the known softening behaviour characterising ring structures. For supported ring resonators, the dynamic behaviour of the drive mode is influenced by the support stiffness. The ring inertia is normally much larger than support inertia, so the dynamic behaviour of supported

ring resonators is softening or hardening essentially depending on the magnitude of the support stiffness terms in (4.28) compared to $M_{ring}\gamma^2\Omega_D^2$. In Chapter 6 this result will be used to investigate hardening support designs that neutralise the softening behaviour of the ring, in order to achieve a pseudo-linear frequency backbone curve for the drive mode.

It is noted that when the rotational symmetry is broken, the frequency backbone curve (equation (4.27)) depends on the position of the drive axis relative to the supports location defined by $\alpha$. This dependence is investigated in Section 4.4.2 and is mainly caused by terms $S_1 \cos 8\alpha$ and $S_2 \sin 8\alpha$ which relate to support stiffness coefficients $k_{t_1}$, $k_{t_2}$, $k_{t_3}$ and $k_{r_3}$. Intuitively, a support structure having negligible stiffness compared to the ring inertia has negligible influence on the dynamic behaviour of the drive mode, so that the dependence of the frequency backbone curve on $\alpha$ is expected to be small. In contrast, more hardening supports would cause less softening or even hardening dynamic behaviour for the drive mode and the dependence of the frequency backbone curve on the drive axis position is expected to be stronger.

### 4.4.2 Numerical results

This Section shows numerical results for the drive mode frequency response curves and frequency backbone curve obtained using the averaging method and FE non-linear transient analyses for the ring resonator having 8 nominal supports shown in Figure 4.1a. The material properties and geometrical data of ring and support structures are based on a real ring-based CVG design used for inertial navigation applications. The ring and supports are made of isotropic silicon, having Young's modulus $E$ equal to 170 GPa and density $\rho$ of 2330 kg/m$^3$. The ring radius is approximatively 3 mm, the axial thickness of ring and support structures is approx. 100 $\mu$m. The radial thickness of ring and supports are approx. 125 $\mu$m and 10 $\mu$m, respectively. A detailed description of ring and support dimensions and results for the mass and stiffness coefficients used for modelling the supports are provided in Appendix A.

**Frequency response curves and frequency backbone curve for a given angle $\alpha$**

The frequency response curves and the frequency backbone curve are firstly investigated for drive excitations such that $\alpha = 22.5^0$. For a given external harmonic force having magnitude $F_D$ and frequency $\Omega$, the drive amplitude $q_1$ is calculated by solving (4.22), and the phase $\phi_D$ relative to the applied force is calculated using (4.26). Figures 4.3 and 4.4 illustrate amplitude and phase plots of the drive mode frequency response curves for five levels of force magnitude $F_D$. The lowest magnitude causes a drive response in the linear regime, while the larger values cause the drive mode to respond in the non-linear regime. For each level of force magnitude, the excitation frequency $\Omega$ is varied in a range of $\pm 2$ Hz around the natural frequency $f_0 = \frac{\omega_0}{2\pi}$. In the plots, $\Delta f$ is the frequency variation from the natural frequency in Hertz (i.e. $\Delta f = f - f_0$ where $f = \frac{\Omega}{2\pi}$). The frequency response curves are compared against those for an equivalent linear resonator in which geometrical non-linearity is neglected, calculated using equation (4.22) for $q_1$ and equation (4.26) for $\phi_D$, with $\gamma_1, ..., \gamma_5$ equal to zero and $I_1 = S_1 = S_2 = 0$ as there is no non-linearity. The drive mode frequency backbone curve for the non-linear resonator is calculated using equation (4.27) and is indicated as "Drive FBC" in Figure 4.3.

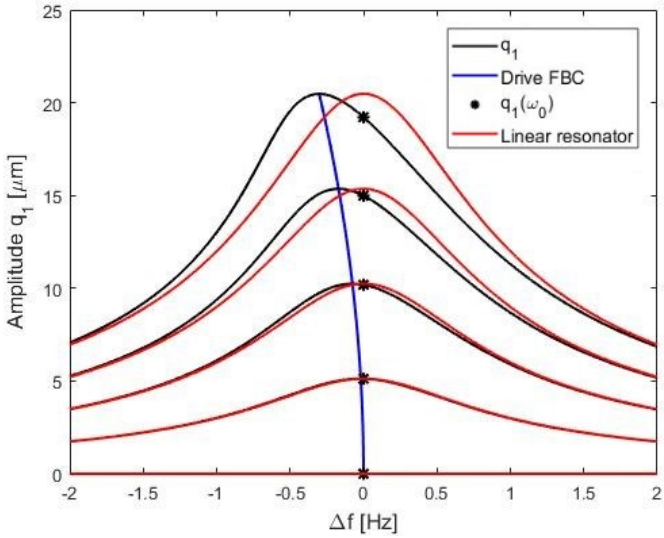



Figure 4.3: Frequency response curves and frequency backbone curve for the drive mode for a ring resonator having 8 nominal supports. Comparison against linear resonator. Q=10000. $\alpha = 22.5^0$.

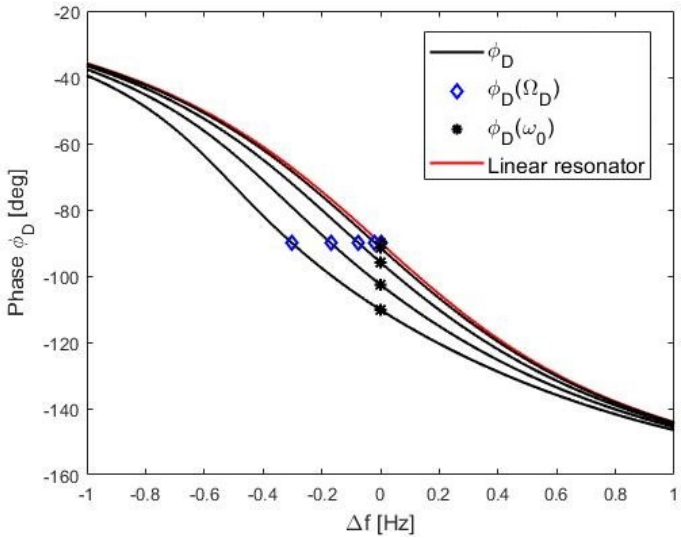



Figure 4.4: Phase plot for the drive mode response for a ring resonator having 8 nominal supports. Comparison against linear resonator. Q=10000. $\alpha = 22.5^0$.

Results show that, at large amplitudes, the drive mode responds in resonance at frequencies $\Omega_D$ smaller than the natural frequency $\omega_0$, indicating a non-linear softening dynamic behaviour. For larger magnitudes of the excitation, the amplitude of the drive response at frequency $\omega_0$ (see $q_1(\omega_0)$ in Figure 4.3) is smaller than the amplitude of the linear resonator at the same frequency, and the drive phase relative to the applied force (see $\phi_D(\omega_0)$ in Figure 4.4) is less than -90 degrees.

As stated in Chapter 1, practical CVGs normally operate at the drive mode resonance frequency. Control feedback loops are used to achieve a drive response having constant amplitude, frequency and phase as this ensures the amplitude, frequency and phase of the sense response do not vary in operation. The obtained frequency backbone curve for the practical supported ring resonator considered indicated a frequency shift of approx. -0.30 Hz from the linear resonance frequency when the drive amplitude is 20 $\mu$m, demonstrating that ring and support geometrical non-linearity causes the drive mode to be resonant at frequencies different from the designed resonance frequency. This implies that the frequency of the exciting force needs to be adjusted depending on the drive mode vibration amplitude in order to maintain the drive mode resonant, when the resonator operates at large amplitudes.

In Appendix D, the Runge-Kutta time-integration scheme is applied to drive equation (3.43) which includes backwards coupling from the sense response to the drive response and $Q_1^4$ terms. Amplitude and phase of the drive response in steady-state are obtained using the Runge-Kutta numerical method to develop the frequency response curves for the drive mode. Results obtained using the Runge-Kutta method are compared against the frequency response curves in Figures 4.3 and 4.4 obtained using the averaging method. Results obtained using the Runge-Kutta method and the averaging method are found to be in good agreement, and demonstrate that (for the range of drive response amplitudes considered) backwards coupling and $Q_1^4$ terms have a small influence on the drive mode dynamics and can be safely neglected.

**Dependency of the drive frequency backbone curve on drive angle $\alpha$**

In what follows, the drive mode frequency backbone curves obtained for $\alpha = 0^0$ and $\alpha = 22.5^0$ are compared to investigate the effect of using different drive angles $\alpha$ on the non-linear drive mode dynamics. For a ring resonator having 8 supports, $\alpha = 0^0$ and $\alpha = 22.5^0$, respectively, indicate alignment of the drive mode maximum diameter with the supports and mid-way between two supports.

Figure 4.5 shows the frequency backbone curves obtained using the averaging method and FE non-linear transient analyses, and the frequency backbone curve for the unsupported ring. Finite Element results are obtained as described in Section 4.3, by applying forces to the ring as shown in Figures 4.2a and 4.2b. Pseudo-resonance frequencies obtained using FE transient analyses have an accuracy of 0.001 Hz.

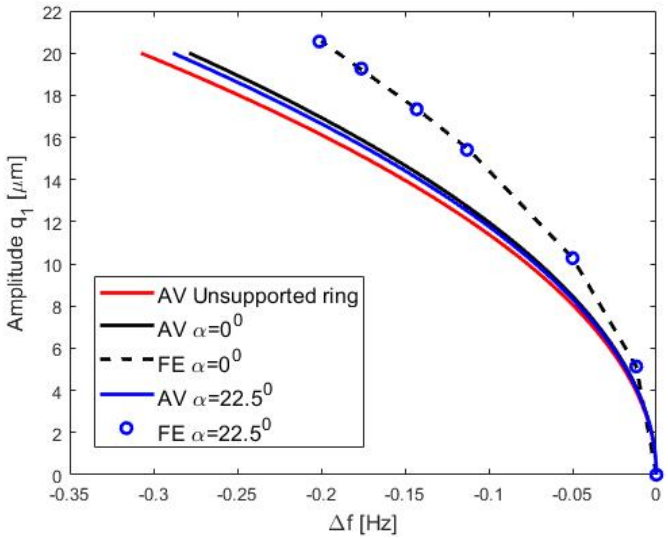



Figure 4.5: Frequency backbone curve for a ring resonator having 8 nominal supports for $\alpha = 0^0$ and $\alpha = 22.5^0$ and for the unsupported ring. Analytical (AV) and Finite Element (FE) results. Finite Element results for $\alpha = 0°$ and $\alpha = 22.5°$ are almost coincident. Q=1000.

The frequency backbone curves in Figure 4.5 show a softening non-linear dynamic behaviour for the supported ring resonator, just slightly less softening than the unsupported

ring. For a drive amplitude of 20 $\mu$m, the frequency shift obtained using the averaging method is -0.278 Hz and -0.288 Hz for $\alpha = 0^0$ and $\alpha = 22.5^0$, respectively. Therefore, results obtained using the averaging method for $\alpha = 0^0$ and $\alpha = 22.5^0$ are very similar to each other. This suggests that ring non-linearity is dominant compared to support non-linearity, and that terms involving $\alpha$ associated with support non-linearity in the drive frequency backbone curve equation (4.27) are much smaller than the terms associated with ring geometrical non-linearity.

Frequency backbone curves obtained using the FE analyses confirm the softening non-linear dynamics for the supported ring resonator and indicate that drive angle $\alpha$ has a small influence on the non-linear dynamics of the resonator: results obtained for $\alpha = 0^0$ and $\alpha = 22.5^0$ are almost identical (for a drive amplitude of 20 $\mu$m, the frequency shift obtained for $\alpha = 0^0$ and $\alpha = 22.5^0$ only differ by 0.001 Hz which is the accuracy used to develop the Finite Element frequency backbone curves). The frequency backbone curves obtained using the FE analyses are less softening than those obtained using the averaging method. For a drive amplitude of 20 $\mu$m, the frequency shift obtained using the FE analyses is smaller than that obtained using the mathematical model by 28% and 29% for $\alpha = 0^0$ and $\alpha = 22.5^0$, respectively. Section 4.6 summarises and discusses in detail the comparison between results obtained using the mathematical model and Finite Element method.

To further investigate the effect of drive excitation angle $\alpha$, the drive mode frequency backbone curves are investigated by increasing the thickness of the supports. Figure 4.6 illustrates the frequency backbone curves calculated for the same ring but with the radial thickness of the nominal supports increased from 10 $\mu$m to 30 $\mu$m.

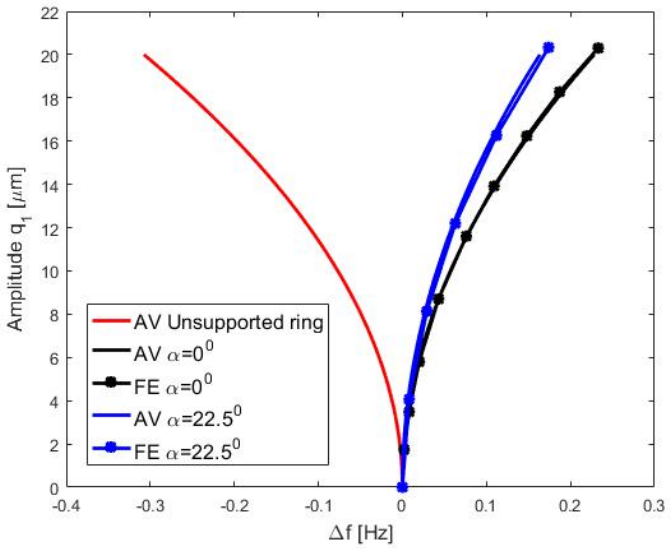



Figure 4.6: Frequency backbone curve for a ring resonator having 8 for nominal supports 30 $\mu$m thick, results for $\alpha = 0^0$ and $\alpha = 22.5^0$. Analytical (AV) and Finite Element (FE) results. Q=1000.

Whilst the nominal supports produced a frequency shift for the supported ring resonator which was essentially unaltered compared to the unsupported ring, the increase in support thickness causes the overall dynamic behaviour of the supported ring resonator to harden. The frequency shift for a drive amplitude of 20 $\mu$m is 0.228 Hz for $\alpha = 0^0$ and 0.163 Hz for $\alpha = 22.5^0$ using the averaging method. These results indicate that supports with increased thickness may be used to mitigate against non-linear drive dynamics. As thicker supports have a more significant influence on the drive mode dynamics compared to thin supports, the dependency on drive angle $\alpha$ is also more significant in Figure 4.6. This is explained by noting that terms involving $\alpha$ in frequency backbone curve equation (4.27) are multiplied by support stiffness coefficients $k_{t_1}$, $k_{t_2}$, $k_{t_3}$ and $k_{r_3}$. Such stiffness coefficients for the proposed thicker supports are orders of magnitude larger than those of the nominal supports.

The FE results in Figure 4.6 validate the hardening behaviour of the supported ring resonator and the stronger dependency of the frequency backbone curve on drive angle $\alpha$. The

frequency backbone curves obtained for $\alpha = 0^0$ and $\alpha = 22.5^0$ are different from each other, validating that when the rotational symmetry is broken, the drive mode dynamics depends on the drive axis location relative to the supports. The Finite Element results are in good agreement with those obtained using the averaging method, and validate that 8 supports break the $2\theta$ rotational symmetry of ring resonators for large amplitude vibrations.

## 4.5 Drive response for a ring having 16 supports

Following a similar approach as the 8 support case considered in Section 4.4, the drive response for a ring resonator having 16 supports is considered. The equation of motion governing the drive response for the 16 support case was developed in Section 3.4.2 and given by (3.47) were all non-linear terms in $Q_2$ were neglected. Unlike the 8 support case, drive equation (3.47) was coupled to the sense equation by the rotation-induced Coriolis force only. By neglecting the Coriolis force and higher powers of $Q_1$ than the cubic, drive equation (3.47) reduced to equation (3.49) here repeated below:

$$\ddot{Q_1}\left(1 + Q_1^2\gamma_1\right) + \dot{Q_1}\left(\frac{\omega_0}{Q} + \dot{Q_1}Q_1\gamma_2\right) + Q_1\left(\omega_0^2 + \dot{Q_1}^2\gamma_3 + \ddot{Q_1}Q_1\gamma_4 + Q_1^2\gamma_5\right) = \frac{F_D}{M_{res}}\cos\Omega t \tag{4.29}$$

Expressing the steady-state drive response using equation (4.12) and applying the averaging method, it can be shown that the averaged drive amplitude and the averaged drive phase relative to the applied force can be calculated by solving (4.22) and (4.26), respectively, with $I_1 = S_1 = S_2 = 0$. The equation for the drive mode frequency backbone curve is:

$$\Omega_D^2\left(q_1\right) = \frac{\omega_0^2 + \frac{3}{4}q_1^2\gamma_5}{1 + q_1^2\left(\frac{3}{4}\gamma_1 - \frac{1}{4}\gamma_2 - \frac{1}{4}\gamma_3 + \frac{3}{4}\gamma_4\right)} \tag{4.30}$$

Using (3.27)-(3.31), equation (4.30) can be re-written as:

$$\Omega_D^2(q_1) = \frac{\omega_0^2 + \frac{q_1^2}{M_{res}}\left(\frac{1}{3}K_{ring}\gamma^2 + 24k_{r_1}\gamma^2 + \frac{3}{4}k_{t_1}\gamma^2 - 24k_{r_2}\gamma + \frac{9}{2}k_{r_3} + \frac{9}{32}k_{t_3}\right)}{1 + \frac{q_1^2}{M_{res}}\left(\frac{33}{10}M_{ring}\gamma^2 + m_t\gamma^2 + 32m_r\gamma^2\right)} \tag{4.31}$$

Comparing (4.31) to (4.28) for the 8 supports case, it can be noted that the dependency of the frequency backbone curve on drive angle $\alpha$ and on quadratic tangential support stiffness coefficient $k_{t_2}$ is eliminated when 16 supports are used.

### 4.5.1 Numerical results

This Section shows the frequency backbone curves obtained for the practical ring resonator design having 16 nominal supports shown in Figure 4.1b. The geometrical data and results of mass and stiffness coefficients used to model the supports can be found in Appendix A. The frequency response curves (amplitude and phase plots) obtained using the averaging method are similar to those shown for the ring having 8 supports in Section 4.4.2 and comparisons against the linear resonator lead to identical findings and will not be repeated in this Section. Figure 4.7 illustrates the frequency backbone curves obtained using the averaging method (i.e. equation (4.30)) and FE non-linear transient analyses for $\alpha = 0^0$ and $\alpha = 11.25^0$ which respectively indicate alignment of the drive mode maximum diameter with the supports and mid-way between two supports.

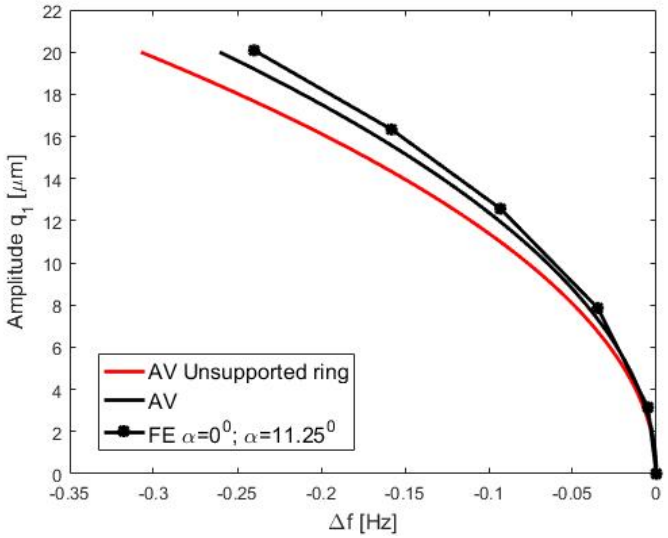



Figure 4.7: Frequency backbone curve for a ring resonator having 16 nominal supports for $\alpha = 0^0$ and $\alpha = 11.25^0$ and for the unsupported ring. Analytical (AV) and Finite Element (FE) results. Q=1000.

The frequency backbone curve for the supported ring resonator shows a dynamic behaviour slightly less softening than the unsupported ring. When the drive mode vibrates with an amplitude of 20 $\mu$m, the calculated frequency shift is -0.260 Hz using the averaging method. The Finite Element simulations verify the non-linear softening dynamic behaviour for the drive mode. For a drive amplitude of 20 $\mu$m the frequency shift obtained using the FE analyses is smaller by 8% with respect to that calculated using the averaging method. The frequency backbone curves calculated by the Finite Element simulations for $\alpha = 0^0$ and $\alpha = 11.25^0$ are identical to each other for 0.001 Hz accuracy.

Similar to the 8 support case, the dependence of the drive mode frequency backbone curve on $\alpha$ is further investigated by increasing the supports thickness. Figure 4.8 shows the frequency backbone curves obtained for the same ring by increasing the thickness of the nominal supports from 10 $\mu$m to 30 $\mu$m.

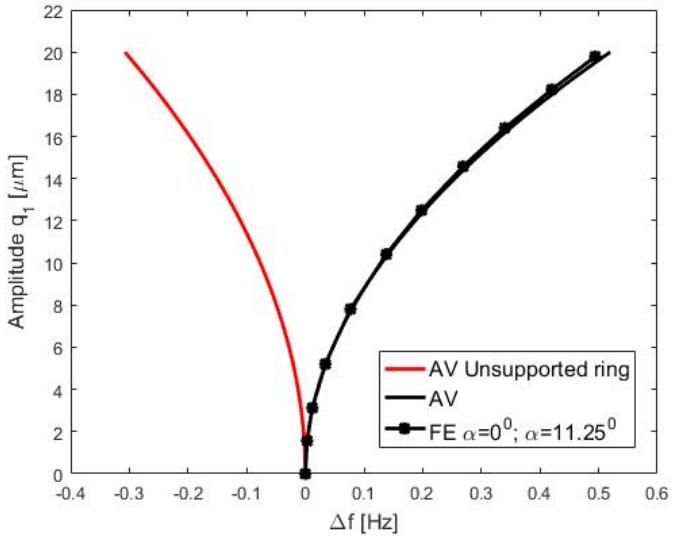



Figure 4.8: Frequency backbone curve for a ring resonator having 16 nominal supports 30 $\mu$m thick; results for $\alpha = 0^0$ and $\alpha = 11.25^0$. Analytical (AV) and Finite Element (FE) results. Q=1000.

Similar to that observed for the 8 support case, the increase in support thickness causes the dynamic behaviour of the supported ring resonator to be hardening. At 20 $\mu$m amplitude, the frequency shift calculated using equation (4.30) is 0.519 Hz, which is approx. 3% larger than that obtained using the Finite Element method. Unlike the 8 support structure, the FE results obtained for $\alpha = 0^0$ and $\alpha = 11.25^0$ are identical to each other (for 0.001 Hz accuracy). Therefore, the Finite Element simulations validate that when 16 supports are used, the drive mode dynamics is independent of the drive axis position relative to the supports. This demonstrates that the 16 support structure maintains the rotational symmetry of supported ring resonators when the ring is driven into large amplitude vibration. If the dependence of the drive mode resonance frequency on the vibration amplitude is eliminated by designing supports that neutralise the softening nature of the ring, use of 16 supports would ensure the drive dynamics is the same as a linear resonator, despite ring and support geometrical non-linearity effects. This will be investigated in detail in Chapter 6.

## 4.6 Comparing mathematical and Finite Element results

In Sections 4.4.2 and 4.5.1 the frequency backbone curves for the drive mode obtained using the mathematical model and non-linear Finite Element transient analyses were compared for ring resonators having 8 and 16 supports, respectively.
It was found that:

- For ring resonators having 8 supports:
  - When the support thickness is 10 $\mu$m (i.e. nominal supports), the frequency backbone curve obtained using the mathematical model is quite different to that obtained using the Finite Element method. However, the Finite Element results demonstrate that when the ring inertia is dominant compared to the support stiffness, the dependence of the drive frequency backbone curve on $\alpha$ is non-zero and small. Moreover, the frequency backbone curve obtained using both methods is softening.
  - For supports having 30 $\mu$m thickness, the drive mode frequency backbone curves obtained using the mathematical and Finite Element analyses are in good agreement (almost identical to each other). The frequency backbone curve calculated using both methods is hardening. The Finite Element results demonstrate that when 8 supports are used, the rotational symmetry is broken and the frequency backbone curve for the drive mode depends on drive angle $\alpha$.
- For ring resonators having 16 supports:
  - The frequency backbone curves for nominal supports having 10 $\mu$m thickness obtained using the mathematical model are quite different to those obtained using the Finite Element analyses. However, Finite Element results demonstrate that when 16 supports are used, the frequency backbone curve of the drive mode is independent of drive angle $\alpha$ as the rotational symmetry is maintained. The frequency

backbone curve obtained using both methods is softening.

- For 30 $\mu$m thick support, the drive mode frequency backbone curves obtained using mathematical and Finite Element analyses are hardening and approximately identical to each other. The Finite Element results demonstrate that 16 supports maintain the rotational symmetry of the ring resonator.

One can conclude that although the agreement between the mathematical model and Finite Element method is weak for the nominal support, the developed mathematical model still provides a good qualitative description of the dynamic behaviour of the drive mode. The computational time needed to obtain the frequency backbone curves using the mathematical model is orders of magnitude smaller than that required to perform multiple Finite Element non-linear transient analyses. Moreover, the developed mathematical model shows similar characteristics to the Finite Element method. For example, the dependency of the drive mode frequency backbone curve on the drive axis calculated using the Finite Element simulations can be explained using the mathematical model noticing that 8 supports break the rotational symmetry of the supported ring resonator.

Investigations have been conducted to understand the reasons for the discrepancies between the results obtained using the mathematical model and the Finite Element model. The discrepancies are believed to be associated with assumptions used to develop the mathematical model described in Chapters 2 and 3 as:

- The stiffness and mass coefficients used to model the supports in the mathematical model are calculated by assuming that the in-plane rotation of the ring-support attachment points is the same as an unsupported ring undergoing $2\theta$ linear vibration at the same angular position. This approximation may not be accurate (i) when the support structure influences the ring vibration and (ii) when the ring is driven into large amplitudes.

- The support model is developed under the assumption that the radial and tangential directions are principal axes of stiffness for the supports. As will be shown later in Chapter 6, the accuracy of the results obtained using the mathematical model degrades when the angle between the radial and tangential directions and the principal axes of stiffness of the support is significantly large.

- The non-linear support stiffness is modelled using cubic non-linear springs. More accurate results might be obtained using stiffness coefficients up to the fifth order to model the support stiffness. However, doing so, the drive and sense equations of motions would become significantly more complicated.

Investigations were also conducted to verify that, in the Finite Element simulations, forces distributions such as shown in Figures 4.2a and 4.2b only excite the $2\theta$ mode. The radial displacements of the ring in steady-state were post-processed and it was found that in steady-state the ring vibration has a $2\theta$ shape.
Additional investigation aimed to understand the reasons for the discrepancies between the results obtained using the mathematical model and Finite Element analysis is proposed as area of further work in Section 7.5.

## 4.7 Summary and conclusions

This Chapter investigated the effect of ring and support geometrical non-linearity on the $2\theta$ drive response when the drive mode is excited into large amplitude by harmonic external forces. The investigation focused on practical ring resonators having 8 and 16 supports.
The averaging method was used to develop the frequency response curves for the drive mode, and the drive mode frequency backbone curve was developed based on a drive response having phase of $90^\circ$ degrees relative to the applied excitation. Results showed that ring and support geometrical non-linearity causes the drive mode resonance frequency to shift from the linear resonance frequency when the drive amplitude becomes large. Whilst the dynamic behaviour

of the drive mode is softening for unsupported rings, it was found to depend on the support structure for supported ring resonators. If the support stiffness is small compared to the ring inertia, the ring non-linearity is dominant compared to the non-linearity of the support structure and the drive mode behaviour is softening. In contrast, more hardening supports cause the behaviour of the drive mode to be less softening or even hardening.

Results obtained for resonators having 8 and 16 supports were compared to investigate the impact of the breaking of rotational symmetry on the drive mode response. It was found that for the 8 support structure, the drive mode frequency backbone curve depends on the position of the drive axis relative to the supports location. The dependence of the drive mode dynamics on drive axis angle $\alpha$ was found to be stronger when the thickness of the support is increased, and the influence of the support structure on the resonator dynamics is more significant. In contrast, for the 16 support structure, it was found that the drive mode frequency backbone curve is independent of the drive excitation considered. Finite Element non-linear transient analyses verified the dependence of the drive mode dynamics on the drive axis for ring resonators having 8 supports, and verified that 16 supports maintain the rotational symmetry.

In Chapter 6, the analytical expression for the drive mode frequency backbone curve obtained in this Chapter will be used to investigate hardening support designs that linearise the drive mode frequency backbone curve of the resonator by neutralising the softening behaviour of the ring.

# Chapter 5

# Investigating the sense response for CVGs operating at large amplitude

## 5.1 Introduction

This Chapter investigates the $2\theta$ sense response for supported ring resonators driven into large drive amplitude vibration, to investigate the impact of ring and support geometrical non-linearity on sensor performance. The investigation of the sense response is presented for ring resonators having 8 and 16 supports. In Chapter 3 it was found that 8 supports cause the sense equation to be coupled to the drive response in the absence of angular rate. In contrast, when 16 supports are used, the equation of motion of the sense mode is coupled to the drive response only by the rotation-induced Coriolis force. In Chapter 2 for a linear resonator, it was found that mode coupling and frequency split cause the sense response amplitude in operation to reduce, and cause the occurrence of zero-rate-output and quadrature errors which degrade the rate measurement quality. In this Chapter, mode coupling effects on the sense response are investigated for ring resonators operating in the large amplitude non-linear regime.

In the proposed investigation, the ring is assumed to rotate around its polar axis with con-

stant angular rate $\Omega_z$ so that the sense mode is excited by the Coriolis force. External harmonic forces are applied to the ring to excite the drive mode. The sense response is investigated using the averaging method in a similar way to that proposed for the drive response in Chapter 4, using the non-linear equation of motion for the sense mode developed in Chapter 3. Comparisons are made between results obtained for 8 and 16 support structures, to understand if support structures which maintain the rotational symmetry are beneficial for sensor performance. Numerical results are shown for the same devices with 8 and 16 nominal supports considered in Chapter 4 for the drive response, and Finite Element non-linear transient analyses are used to verify key results obtained using the mathematical model.

The structure of this Chapter is as follows. Section 5.2 defines the in-phase and quadrature sense mode responses. Sections 5.3 and 5.4 investigate the sense response for ring resonators having 8 and 16 supports, respectively. Analytical expressions for the amplitudes of the in-phase and quadrature sense responses are obtained using the averaging method. Frequency response curves for the sense response are developed and compared against those for an equivalent linear resonator, to highlight ring and support geometrical non-linearity effects on the sense mode dynamics. Numerical parametric studies are presented to investigate the influence of the Q-factor on the sense response. Section 5.5 summarises the work done in this Chapter and highlights key conclusions.

## 5.2 Definition and interpretation of in-phase and quadrature sense responses

Similar to the drive response in Chapter 4, the sense response is expressed as:

$$Q_2(t) = q_2 \cos\left(\Omega t + \phi_D + \phi_{SD}\right) \tag{5.1}$$

where $q_2$ is the oscillation amplitude, $\phi_D$ is the phase of the drive response relative to the applied drive force at frequency $\Omega$, and $\phi_{SD}$ is the phase of the sense response relative to the drive response. Amplitude $q_2$ and phases $\phi_D$ and $\phi_{SD}$ in (5.1) vary with time.

Equation (5.1) can be re-written as:

$$Q_2(t) = \underbrace{[-A_{SC}\cos(\Omega t + \phi_D)]}_{\text{In-phase}} + \underbrace{[-A_{SS}\sin(\Omega t + \phi_D)]}_{\text{Quadrature}} \tag{5.2}$$

where $A_{SC}(t) = -q_2\cos\phi_{SD}$ and $A_{SS}(t) = q_2\sin\phi_{SD}$. Sense response (5.2) has two components which are $90^0$ out-of-phase with each other: (i) a component either in-phase or $180^0$ out-of-phase relative to the drive response having amplitude $A_{SC}$, and (ii) a component $\pm 90^0$ out-of-phase relative to the drive response having amplitude $A_{SS}$. In what follows, these components of the sense response will be referred to as "in-phase" and "quadrature" responses, respectively.

For a CVG having perfectly degenerate and mechanically decoupled modes of vibration, the sense response is only caused by the rotation-induced Coriolis force which is $90^0$ out-of-phase relative to the drive response. Since the modes are degenerate, when the drive mode is excited into resonance at natural frequency $\omega_0$, the sense response phase is $90^0$ out-of-phase relative to the Coriolis force so the quadrature response is zero. A consequence of this is that for ideal gyros, the in-phase component of the sense response is used to measure the angular rate while a non-zero quadrature response is normally interpreted as an indication of mode coupling and/or drive and sense responses which are not in resonance at the same frequency.

## 5.3 Sense response for a CVG having 8 supports

This Section investigates the sense response for a CVG having 8 supports when the drive axis acts midway between two supports i.e. $\alpha = 22.5^0$. Analytical expressions for the amplitude of the in-phase and quadrature sense responses are obtained using the averaging

method, and numerical results for the frequency response curves for the sense response are shown and discussed.

### 5.3.1 Averaged sense response

The equation of motion for the sense mode for a CVG having 8 supports was determined in Chapter 3 and given by equation (3.46), which is repeated below:

$$\begin{aligned}
&\ddot{Q}_2\left[1+Q_1^2\left(\gamma_1+I_1\cos 8\alpha\right)\right]+\dot{Q}_2\left[\frac{\omega_0}{Q}+\dot{Q}_1Q_1\left(\gamma_2+2I_1\cos 8\alpha\right)\right]+\\
&+Q_2\Big[\omega_0^2+\dot{Q}_1^2\left(\gamma_3+I_1\cos 8\alpha\right)+\ddot{Q}_1Q_1\left(\gamma_4+2I_1\cos 8\alpha\right)+\\
&+Q_1^2\left(\gamma_5-3S_1\cos 8\alpha+3S_2\sin 8\alpha\right)\Big]=\ddot{Q}_1Q_1^2\left(I_1\sin 8\alpha\right)+Q_1\dot{Q}_1^2\left(I_1\sin 8\alpha\right)-\\
&-Q_1^3\left(S_1\sin 8\alpha+S_2\cos 8\alpha\right)-\mathcal{B}\Omega_z\dot{Q}_1
\end{aligned}\tag{5.3}$$

This equation was developed under the assumption that the drive response amplitude is much larger than the sense response amplitude, so the non-linear terms in $Q_2$ were neglected. Moreover, higher powers of $Q_1$ than cubic were neglected as considered to be small for the range of response amplitudes considered in this work. As discussed in Section 3.4.1, for a CVG having 8 supports the sense mode is non-linearly parametrically coupled to the drive motion and is self-excited to vibrate by non-linear terms in $\ddot{Q}_1$, $\dot{Q}_1$ and $Q_1$ which are unrelated to angular rate $\Omega_z$.

The averaging method is used to investigate the steady-state amplitudes of the in-phase and quadrature components of the sense response, using a similar approach to that described for the drive response in Section 4.2. The sense response in equation (5.2) and the drive response in equation (4.12) are used in sense equation (5.3). The sense equation is then multiplied by $\sin\left(\Omega t+\phi_D\right)$ and $\cos\left(\Omega t+\phi_D\right)$ and averaged over one cycle to obtain the following equations for the averaged amplitudes of the in-phase component $A_{SC}$ and quadrature component $A_{SS}$

of the sense response in steady-state:

$$\begin{aligned} & A_{SC}\left[\Omega^2-\omega_0^2+q_1^2\Omega^2\left(\frac{3}{4}\gamma_1-\frac{1}{4}\gamma_2-\frac{1}{4}\gamma_3+\frac{3}{4}\gamma_4+\frac{3}{2}I_1\cos 8\alpha\right)-\right. \\ & \left.-\frac{3}{4}q_1^2\left(\gamma_5-3S_1\cos 8\alpha+3S_2\sin 8\alpha\right)\right]-\frac{\omega_0\Omega}{Q}A_{SS}= \\ & =-\frac{1}{2}\Omega^2q_1^3I_1\sin 8\alpha-\frac{3}{4}q_1^3\left(S_1\sin 8\alpha+S_2\cos 8\alpha\right) \end{aligned} \tag{5.4}$$

$$\begin{aligned} & A_{SS}\left[\Omega^2-\omega_0^2+q_1^2\Omega^2\left(\frac{1}{4}\gamma_1+\frac{1}{4}\gamma_2-\frac{3}{4}\gamma_3+\frac{1}{4}\gamma_4+\frac{1}{2}I_1\cos 8\alpha\right)-\right. \\ & \left.-\frac{1}{4}q_1^2\left(\gamma_5-3S_1\cos 8\alpha+3S_2\sin 8\alpha\right)\right]+\frac{\omega_0\Omega}{Q}A_{SC}=\mathcal{B}\Omega_z\Omega q_1 \end{aligned} \tag{5.5}$$

Setting $\alpha = 22.5^0$, equations (5.4) and (5.5) can be expressed as:

$$A_{SC}\frac{\left(\Omega^2-\Omega_{SC}^2\right)}{\mu_{SC}\Omega}-A_{SS}=f_S\frac{Q}{\Omega\omega_0} \tag{5.6}$$

$$A_{SS}\frac{\left(\Omega^2-\Omega_{SS}^2\right)}{\mu_{SS}\Omega}+A_{SC}=\mathcal{B}\Omega_z q_1\frac{Q}{\omega_0} \tag{5.7}$$

where

$$\Omega_{SC}^2=\frac{\omega_0^2+\frac{3}{4}q_1^2\left(\gamma_5+3S_1\right)}{1+q_1^2\left(\frac{3}{4}\gamma_1-\frac{1}{4}\gamma_2-\frac{1}{4}\gamma_3+\frac{3}{4}\gamma_4-\frac{3}{2}I_1\right)} \tag{5.8}$$

$$\mu_{SC}=\frac{\left(\frac{\omega_0}{Q}\right)}{1+q_1^2\left(\frac{3}{4}\gamma_1-\frac{1}{4}\gamma_2-\frac{1}{4}\gamma_3+\frac{3}{4}\gamma_4-\frac{3}{2}I_1\right)} \tag{5.9}$$

$$\Omega_{SS}^2=\frac{\omega_0^2+\frac{1}{4}q_1^2\left(\gamma_5+3S_1\right)}{1+q_1^2\left(\frac{1}{4}\gamma_1+\frac{1}{4}\gamma_2-\frac{3}{4}\gamma_3+\frac{1}{4}\gamma_4-\frac{1}{2}I_1\right)} \tag{5.10}$$

$$\mu_{SS}=\frac{\left(\frac{\omega_0}{Q}\right)}{1+q_1^2\left(\frac{1}{4}\gamma_1+\frac{1}{4}\gamma_2-\frac{3}{4}\gamma_3+\frac{1}{4}\gamma_4-\frac{1}{2}I_1\right)} \tag{5.11}$$

$$f_S=\frac{3}{4}q_1^3S_2 \tag{5.12}$$

Equations (5.6) and (5.7) indicate that the sense mode is self-excited to vibrate by non-linear terms proportional to $f_S$. This term is proportional to the non-linear tangential quadratic

stiffness coefficient of the support $k_{t_2}$ (see expression for $S_2$ (3.41)) and is zero only if $k_{t_2} = 0$. In later work, ring resonators having 8 supports arranged in-pairs will be considered as in that case $k_{t_2} = 0$ and $f_S = 0$ in equations (5.6) and (5.7).

The in-phase amplitude $A_{SC}$ and quadrature amplitude $A_{SS}$ are obtained from equations (5.6) and (5.7) and it can be shown that:

$$A_{SC} = \frac{\left(\frac{Q}{\Omega\omega_0}\right)\left[\mathcal{B}\Omega_z q_1 \Omega + f_S \frac{(\Omega^2 - \Omega_{SS}^2)}{\mu_{SS}\Omega}\right]}{\Delta} \tag{5.13}$$

$$A_{SS} = \frac{\left(\frac{Q}{\Omega\omega_0}\right)\left[\mathcal{B}\Omega_z q_1 \frac{(\Omega^2 - \Omega_{SC}^2)}{\mu_{SC}} - f_S\right]}{\Delta} \tag{5.14}$$

where $\Delta$ is:

$$\Delta = 1 + \frac{\left(\Omega_{SC}^2 - \Omega^2\right)\left(\Omega_{SS}^2 - \Omega^2\right)}{\mu_{SC}\mu_{SS}\Omega^2} \tag{5.15}$$

In Chapter 2 it was found that for perfect and rotationally symmetric resonators operating in the linear regime, when the drive mode is excited into resonance at frequency $\omega_0$ the sense response is in-phase relative to the drive response and has amplitude given by equation (2.52) here repeated below:

$$q_2 = \frac{\mathcal{B}\Omega_z Q}{\omega_0} q_1 \tag{5.16}$$

Sense response amplitude (5.16) is measured to detect $\Omega_z$. For the non-linear resonator having 8 supports, equations (5.13) and (5.14) indicate that when the drive mode is excited into resonance at large vibration amplitude at pseudo-resonance frequency $\Omega_D$ (given by equation (4.27) in Section 4.4.1), the sense response contains in-phase and quadrature components. Comparing expressions for the sense response for the linear resonator (i.e. (5.16)) and the non-linear resonator (i.e. (5.13) and (5.14) calculated for $\Omega = \Omega_D$), it is clear that ring and support geometrical non-linearity complicates the sense response amplitude expression

compared to the equivalent linear resonator. The in-phase response (5.13) and quadrature response (5.14) both include additional terms proportional to $f_S$ which indicate the occurrence of zero-rate-output response when $\Omega_z$ is zero. A similar result was found in Section 2.5 for a linear resonator having a point mass imperfection on the ring mid-line. This preliminary analysis suggests that ring and support geometrical non-linearity degrades the quality of the rate measurement for ring resonators having 8 supports compared to the equivalent linear resonator. In what follows, these effects will be investigated based on numerical examples.

### 5.3.2 Numerical Results

This Section presents numerical results for the practical device with 8 nominal supports shown in Figure 4.1a, which was considered in Section 4.4.2 for the investigation of the drive response. The numerical results and investigations are structured as follows:

- *Frequency response curves for the sense response.* The frequency response curves for the sense response amplitude are developed using equations (5.13) and (5.14). In-phase and quadrature components are shown to aid visualisation of the phase of the sense response.

- *Amplification of the sense response caused by non-linearity.* The frequency response curves for the sense response are compared against those for an equivalent linear ring resonator having 8 supports in which geometrical non-linearity is neglected.

- *Relationship between $q_2$ and $q_1$ in operation.* For linear rotationally symmetric resonators, the sense response amplitude in operation is linearly proportional to the drive response amplitude, and the angular rate $\Omega_z$ is detected based on linear relation (5.16). The relation between $q_2$ and $q_1$ is investigated for non-linear resonators when the drive mode is excited into resonance at large vibration amplitude.

- *Numerical parametric analysis for the Q-factor.* The effect of using different levels of damping on the sense response is investigated.

- *Finite Element verification of zero-rate-output.* The occurrence of zero-rate-output is verified using a Finite Element non-linear transient analysis.

To verify the results obtained using the averaging method (i.e. equations (5.13) and (5.14)), comparisons are made with results obtained using the Runge-Kutta time-integration scheme to solve sense equation (3.44) in Appendix D. Results obtained using averaging method and Runge-Kutta method are shown to be in good agreement.

**Frequency response curves for the sense response**

The frequency response characteristics of the sense response are investigated when the drive mode is excited by a harmonic force having magnitude $F_D$ and frequency $\Omega$ close to the natural frequency of the $2\theta$ modes $\omega_0$. The drive response for this applied external excitation was considered in Section 4.4, and it was found that the amplitude of the drive response $q_1$ can be calculated by solving (4.22). In this Section, drive response amplitude $q_1$ is considered to be known as previously calculated, and the sense response amplitude is calculated as $q_2 = \sqrt{A_{SC}^2 + A_{SS}^2}$ where $A_{SC}$ and $A_{SS}$ are given by (5.13) and (5.14), respectively.
Figure 5.1 shows the frequency response curves for drive and sense responses obtained for seven different levels of magnitude of the applied force. For each level of magnitude, the exciting frequency is varied in a range of $\pm 1$ Hz around the natural frequency $f_0 = \frac{\omega_0}{2\pi}$ of the drive and sense $2\theta$ modes. In the plot, $\Delta f$ is the frequency variation from $f_0$ in Hertz.

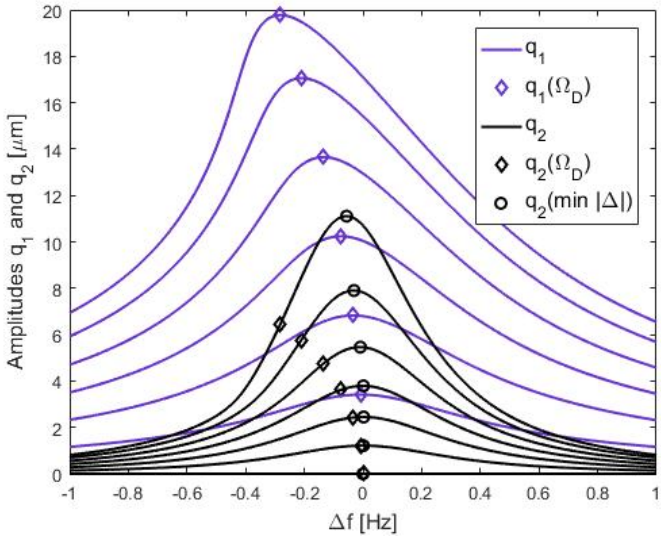



Figure 5.1: Frequency response curves for drive and sense modes for a CVG having 8 nominal supports. Q=20000.

In Figure 5.1, $q_1(\Omega_D)$ and $q_2(\Omega_D)$ indicate the amplitudes of the drive and sense responses at the drive mode pseudo-resonance frequencies, respectively. Results indicate that when the drive mode is excited into large amplitudes, the amplitude of the sense response at the drive mode non-linear resonance frequency is significantly smaller than the peak value. To identify the frequency at which the sense response reaches its largest amplitude, it is necessary to analyse equations (5.13) and (5.14) and notice that amplitudes $A_{SC}$ and $A_{SS}$ increase as $|\Delta|$ decreases towards zero. To a good approximation, the sense response reaches its maximum amplitude at that frequency corresponding to the minimum value of $|\Delta|$, indicated as $q_2\,(\min|\Delta|)$ in Figure 5.1.

It is worth repeating that having a large sense response amplitude is fundamental to maximising sensor sensitivity to rotation and signal-to-noise ratio. For this reason, it is interesting to investigate the frequencies which ensure $|\Delta|$ reaches its minimum. The value of $\Delta$ (see equation (5.15)) depends on frequencies $\Omega_{SC}$ and $\Omega_{SS}$ given by equations (5.8) and (5.10), respectively. Frequencies $\Omega_{SC}$ and $\Omega_{SS}$ depend on the inertia and stiffness characteristics of

ring and support structures. For the considered CVG having 8 nominal supports, $\Omega_{SC}$ and $\Omega_{SS}$ are calculated for a range of drive amplitudes from 0 to 20 $\mu$m and plotted in Figure 5.2, where they are compared against the non-linear resonance frequencies $\Omega_D$ for the drive mode.

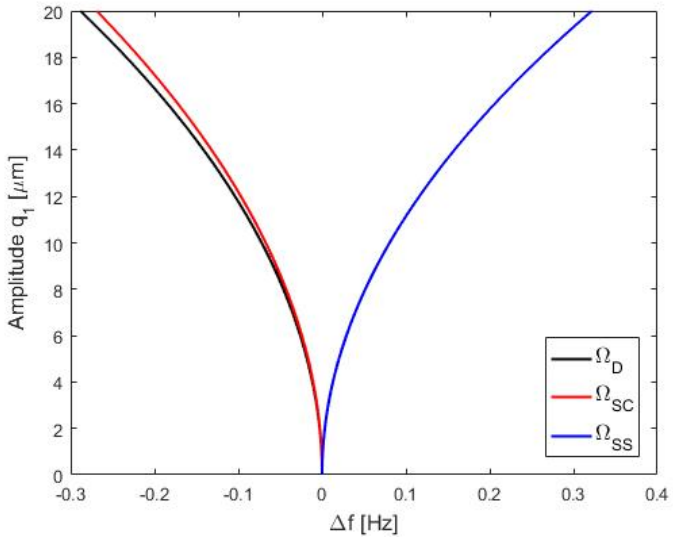



Figure 5.2: Frequencies $\Omega_D$, $\Omega_{SC}$ and $\Omega_{SS}$ for a CVG having 8 nominal supports.

Figure 5.2 indicates that for the supported ring resonator considered, frequencies $\Omega_{SS}$ are greater than $\Omega_{SC}$ for all amplitudes of the drive mode considered. Using this result in equation (5.15), one can conclude that the minimum value of $|\Delta|$ (and so the largest sense response) occurs at frequencies between $\Omega_{SC}$ and $\Omega_{SS}$ which ensure $|\Delta| < 1$. Figure 5.2 indicates that for the ring resonator considered, the pseudo-resonance frequency of the drive mode $\Omega_D$ is smaller than $\Omega_{SC}$ and so does not lie between $\Omega_{SC}$ and $\Omega_{SS}$. This explains why the sense response amplitude at the pseudo-resonance frequencies of the drive mode is significantly smaller than the peak value.

This analysis demonstrates that unlike the linear regime where the sense response amplitude reaches its peak at the drive mode resonance frequency, ring and support geometrical

non-linearity causes the sense response amplitude to be significantly smaller than the peak value when the resonator is excited into large drive amplitudes. Therefore, in the non-linear regime, sensor sensitivity is not maximised when the drive mode is excited into resonance.

To aid visualisation of the phase of the sense response, Figures 5.3 and 5.4 show the amplitude of the in-phase ($A_{SC}$) and quadrature ($A_{SS}$) sense responses, respectively.

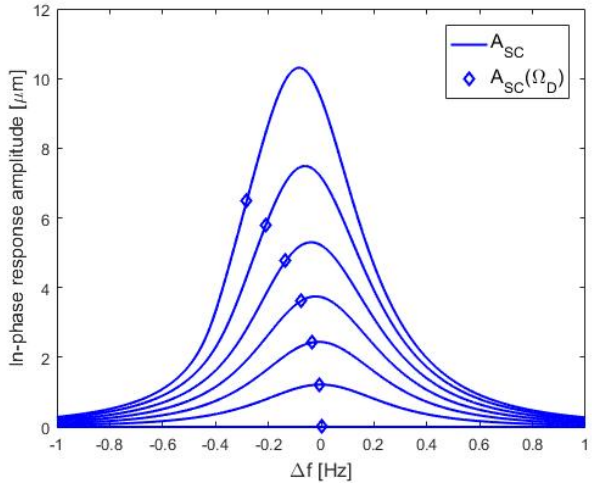



Figure 5.3: Amplitude of in-phase sense response $A_{SC}$ for a CVG having 8 nominal supports. Q=20000.

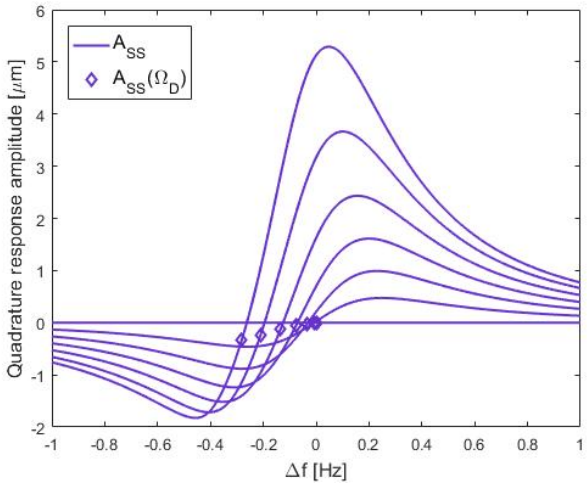



Figure 5.4: Amplitude of quadrature sense response $A_{SS}$ for a CVG having 8 nominal supports. Q=20000.

Figures 5.3 and 5.4 illustrate that for the largest magnitude of the applied external force, the amplitude of the quadrature response at $\Omega_D$ is about 0.3 $\mu$m which is significantly smaller than the amplitude of the in-phase response, which is approximatively 6 $\mu$m. Using results shown Figure 5.2, one can deduce that the quadrature response is small at $\Omega_D$ because $\Omega_D$ and $\Omega_{SC}$ are very close to each other and so term $(\Omega_D - \Omega_{SC})$ in equation (5.14) is very small.

**Amplification of the sense response caused by non-linearity**

In what follows, the frequency response curves of the sense response for the non-linear resonator are compared against the equivalent linear resonator having 8 nominal supports, for which ring and support geometrical non-linearity is neglected. The purpose of this investigation is to determine the effect of ring and support non-linearity on the sense response. Equation (5.16) describes the sense response amplitude for the linear resonator when the applied harmonic forces have frequency $\Omega = \omega_0$. It can be easily shown that the sense response amplitude for the linear resonator at the generic frequency $\Omega$ can be obtained from (5.13) and

(5.14) by noting that for a linear resonator $\Omega_{SC}$ and $\Omega_{SS}$ are equal to the natural frequencies of drive and sense modes $\omega_0$ (see (5.8) and (5.10)) and $\mu_{SC} = \mu_{SS} = \frac{\omega_0}{Q}$ (see (5.9) and (5.11)). Moreover, $f_S = 0$ because there is no non-linearity ($k_{t_2} = 0$). This gives the following analytical expression for the amplitude of the sense response for the linear resonator:

$$q_2^L = \frac{\mathcal{B}\Omega_z q_1 \Omega}{\left|\left(\Omega^2 - \omega_0^2\right)^2 + \left(\frac{\omega_0}{Q}\Omega\right)^2\right|}\sqrt{\left(\frac{\omega_0}{Q}\Omega\right)^2 + \left(\Omega^2 - \omega_0^2\right)^2} \tag{5.17}$$

Figure 5.5 shows the sense mode frequency response curves obtained for the non-linear and linear resonators for different force magnitudes and exciting frequencies in a range of ±1 Hz around the natural resonance frequency $f_0$. The sense response amplitude $q_2$ of the non-linear resonator is calculated from (5.13) and (5.14), and the amplitude of the linear resonator $q_2^L$ is calculated using (5.17).

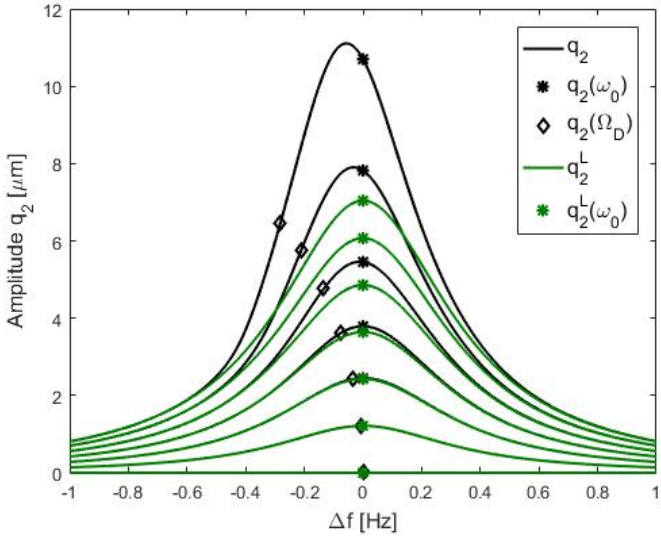



Figure 5.5: Sense mode frequency response curves for a linear and non-linear resonators having 8 nominal supports. Q=20000.

Frequency response curves in Figure 5.5 show that as the drive mode is driven into large amplitude vibration, the geometrical non-linearity of ring and support structures amplifies

the sense response amplitude. The sense response amplitude of the non-linear resonator at $\omega_0$ (i.e. $q_2(\omega_0)$) is much larger than the amplitude of the linear resonator at the same frequency (i.e. $q_2^L(\omega_0)$). Considering that a larger sense response amplitude increases sensor sensitivity to rotation and makes the sensor output more detectable from noise, the amplification of the sense response caused by ring and support geometrical non-linearity appears appealing. However, it is fundamental to bear in mind that traditional CVGs operate at the drive mode resonance frequency: phase lock control loops are used to constantly adjust the frequency of the applied driving forces in order to maintain a drive response having 90° phase lag. Chapter 4 demonstrated that when the ring is excited into large amplitudes, ring and support mechanical non-linearity cause the resonance frequency of the drive mode to shift from $\omega_0$. Therefore, whilst for a linear resonator the operating frequency is $\omega_0$, for a non-linear resonator vibrating at amplitude $q_1$, the operating frequency is $\Omega_D(q_1)$ given by equation (4.27). Results in Figure 5.5 indicate that the amplitude of the non-linear resonator in operation i.e. $q_2(\Omega_D)$ is smaller than the amplitude of the linear resonator in operation i.e. $q_2^L(\omega_0)$. A consequence of this is that although ring and support geometrical non-linearity do amplify the amplitude of the sense response compared to the equivalent linear resonator, the amplitude in operation is reduced. These results suggest that ring and support mechanical non-linearity do not improve sensor performance but rather they cause sensor sensitivity to rotation and SNR to be smaller compared to the equivalent linear resonator.

**Relationship between $q_2$ and $q_1$ in operation**

Traditional gyros detect the angular rate by measuring the amplitude of the sense response which, for a linear and rotationally symmetric resonator, is linearly proportional to the drive amplitude and given by (5.16). In what follows, the relationship between the sense response amplitude $q_2$ and the drive response amplitude $q_1$ is investigated when the ring is excited into large amplitude, and ring and support geometrical non-linearity is considered. Figure 5.6 shows the sense response amplitudes for non-linear and equivalent linear resonators obtained

by exciting the drive mode into resonance (i.e. at frequency $\Omega_D$ for the non-linear resonator and $\omega_0$ for the linear) for drive amplitudes in the range 0 to 20 $\mu$m.

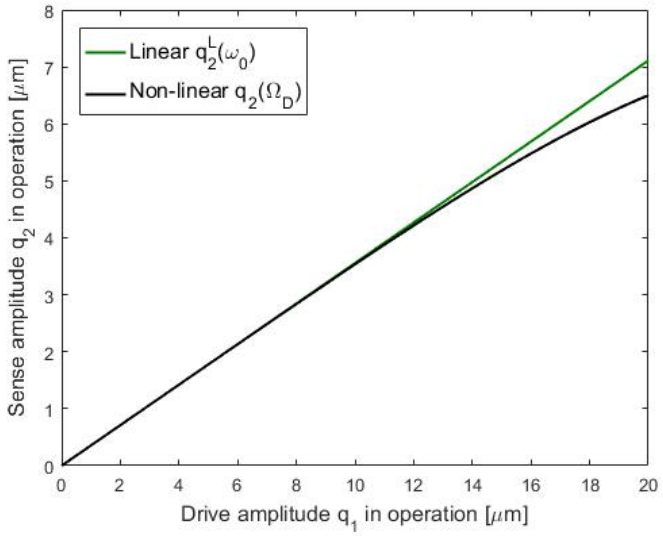
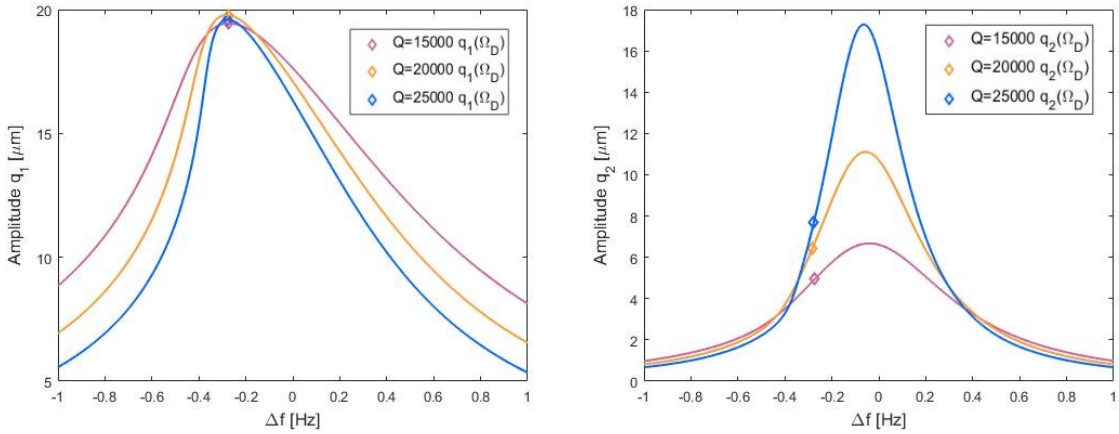



Figure 5.6: Sense response amplitude in operation for linear and non-linear resonators having 8 nominal supports. Q=20000.

It is noted that at small drive amplitudes, the non-linear resonator behaves as a linear resonator and the sense response amplitude is proportional to $q_1$. As the drive amplitude increases, geometrical non-linearity effects become more significant and the sense amplitude is reduced compared to the equivalent linear resonator. Referring back to equations (5.13) and (5.14) for $A_{SC}$ and $A_{SS}$, respectively, it can be seen that $\Omega_{SC}$, $\Omega_{SS}$, $\mu_{SC}$ and $\mu_{SS}$ vary non-linearly with $q_1$ and this causes the sense amplitude to non-linearly depend on $q_1$. This suggests that the linear relationship between $q_1$ and $q_2$ is not valid for ring resonators having 8 supports when the ring is excited into large amplitudes. If a standard $q_1$-$q_2$ linear relation is used to detect the angular rate, the measured angular rate would be inaccurate and affected by sensing errors.

**Numerical parametric analysis for the Q-factor**

Practical CVGs operate at large Q-factors to maximise the sense response amplitude and improve sensor sensitivity. It is then interesting to investigate the influence of the quality factor on the sense response. Figures 5.7a and 5.7b show the drive and sense frequency response curves, respectively, obtained for different levels of Q-factor i.e. 15000, 20000 and 25000. For each Q-factor considered, the drive mode is excited to vibrate so as to ensure its amplitude at resonance is approx. 20 $\mu$m.




(a) Drive mode.

(b) Sense mode.

Figure 5.7: Frequency response curves for drive and sense modes for a CVG having 8 nominal supports for Q=15000, Q=20000 and Q=25000.

It is noted that the difference between the amplitude of the sense response at the drive mode pseudo-resonance frequency and at the peak becomes larger as the Q-factor increases, because the sense amplitude at frequencies corresponding to the minimum value of $|\Delta|$ is much more amplified by the Q-factor than the sense amplitude at frequency $\Omega_D$. In fact, from $\Delta$ equation (5.15), it can be seen that for frequencies between $\Omega_{SC}$ and $\Omega_{SS}$ (for which $|\Delta| < 1$) larger values of the Q-factor reduce $|\Delta|$ so that sense amplitude $q_2$ significantly increases for frequencies in that range.

Figure 5.8 illustrates the drive and sense frequency response curves obtained for Q=30000.

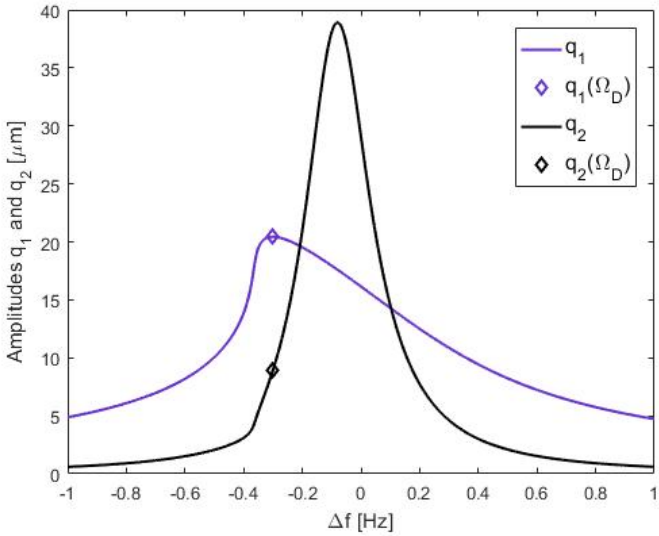



Figure 5.8: Frequency response curves for drive and sense modes for a CVG having 8 nominal supports for Q=30000.

Figure 5.8 shows that for Q=30000, when the drive mode is driven into large amplitude, the amplitude peak of the sense response becomes larger than the amplitude peak of the drive response. It can be shown that for even larger Q-factors the sense response is further amplified. The proposed mathematical model for a supported resonator is based on the assumption that the sense response amplitude is smaller than the drive amplitude (as it is in practical CVGs), so only Q-factors ensuring the sense amplitude is smaller than the drive are considered in this study.

Similar to Figure 5.6, Figure 5.9 illustrates the sense response amplitudes obtained for non-linear and linear resonators by exciting the drive mode into resonance (i.e. at frequency $\Omega_D$ for the non-linear resonator and $\omega_0$ for the linear) for Q-factor values equal to 15000, 20000 and 25000.

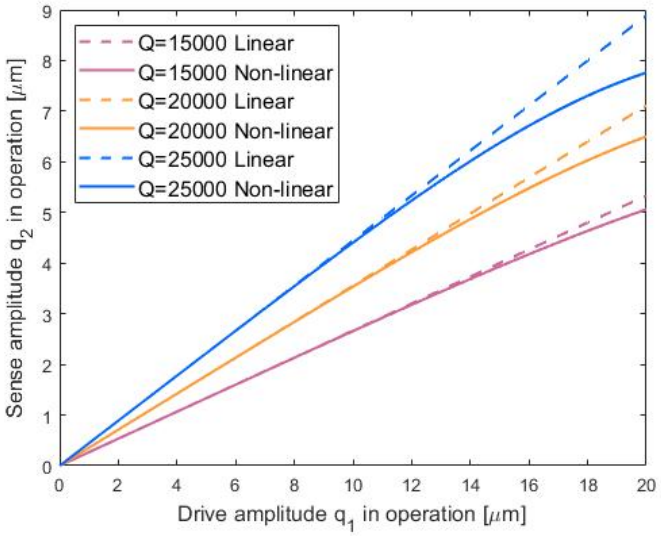



Figure 5.9: Sense response amplitude in operation for linear and non-linear resonators having 8 nominal supports for Q=15000, Q=20000 and Q=25000.

It can be noted that for larger Q-factors, the difference between the sense amplitude of linear and non-linear resonators at large vibration amplitude increases. These results suggest that when large values for the quality factor are used, the relationship between $q_2$ and $q_1$ becomes increasingly non-linear compared to the straight-line relationship for a linear resonator. Practical CVGs use large Q-factors to increase sensor sensitivity to rotation. Under these circumstances, the obtained results suggest that the measure of the angular rate is affected even more significantly by sensing errors compared to CVGs operating with low values of Q.

**Finite Element verification of zero-rate-output**

In what follows, the portion of the sense response caused by the non-linear mechanical coupling to the drive response and unrelated to angular rate $\Omega_z$ (i.e. zero-rate-output response) is quantified using equations (5.13) and (5.14), and verified using a Finite Element non-linear analysis. For Q=1000, when the drive mode is excited so as to ensure its amplitude

at resonance is 20 $\mu$m, the sense response amplitude obtained using the averaging method is:

- $q_2(\Omega_D) \approx 0.36$ $\mu$m in the presence of angular rate $\Omega_z$ in the range of 50-100 degrees per second.
- $q_2(\Omega_D) \approx 0.001$ $\mu$m for $\Omega_z = 0$.

The obtained amplitude of the sense response in the absence of rotation is small; however, it is fundamental to highlight again that what really adversely affects sensor performance is the occurrence of the zero-rate-output response itself, regardless of its amplitude. As introduced in previous sections, the zero-rate-output complicates the measurement of the angular rate. In operation, it is difficult to distinguish between the in-phase sense response amplitude which relates to $\Omega_z$ (the so-called "useful" sense response, used for rate detection) and that part of the in-phase sense response unrelated to $\Omega_z$.

The occurrence of the zero-rate-output is verified against a Finite Element non-linear transient analysis performed similar to that described in Section 4.3 for the drive response. In this case, the amplitude of the steady-state sense response is obtained from the steady-state radial displacements at $\alpha + 45^\circ$ and $\alpha + 135^\circ$, as:

$$Q_2(t) = \frac{1}{2}\left[u(\alpha + 45^\circ) - u(\alpha + 135^\circ)\right] \tag{5.18}$$

Figure 5.10 shows a time history of the the steady-state sense response obtained by applying harmonic drive forces to the ring as shown in Figure 4.2b to generate a resonant drive response having 20 $\mu$m amplitude using a non-linear Finite Element analysis.

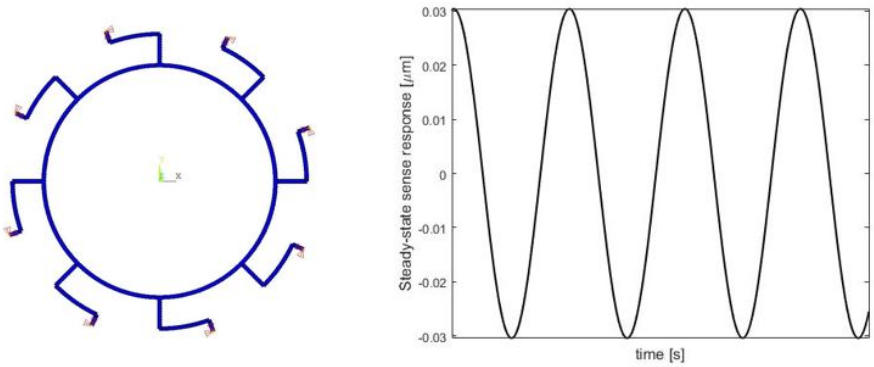



Figure 5.10: Steady-state sense response obtained using a FE non-linear transient analysis in absence of rotation for a CVG having 8 nominal supports. Q=1000.

Since rotation is not included in the Finite Element simulations, a non-zero response at the sense anti-nodes indicates the presence of zero-rate-output. The amplitude of the zero-rate-output is approx. 0.03 $\mu$m which is much larger than the 0.001 $\mu$m calculated by using the mathematical model and averaging method. As discussed in Chapter 4 in Section 4.6, possible explanations for the discrepancy between the results obtained using the mathematical model and the FE model may be associated with some of the approximations used to develop the mathematical model. Considering these limitations, in this Section the Finite Element simulations were used to validate the occurrence of zero-rate-output characterising ring resonators having 8 supports. Although qualitatively the amplitude of the sense response in the absence of rotation calculated using the mathematical model is not accurate, the Finite Element simulations validate the occurrence of ZRO for ring resonators when the rotational symmetry is broken.

### 5.3.3 Ring resonators having 8 supports arranged in pairs

Section 5.3.2 showed numerical results obtained for ring resonators having 8 single nominal supports uniformly spaced around the ring circumference. This Section investigates the sense response for a ring-based CVG having 8 nominal supports arranged in pairs around the ring

circumference similar to that shown in Figure 5.11.

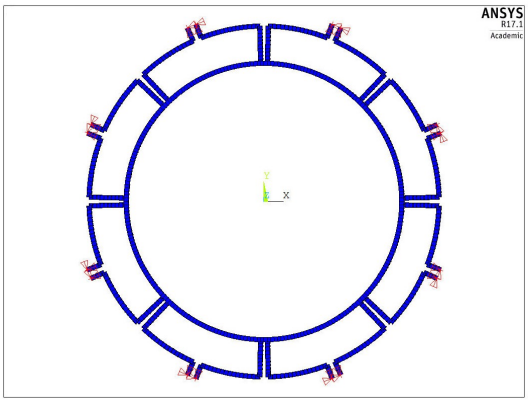



Figure 5.11: Finite Element model developed for a CVG having 8 nominal supports arranged in pairs.

Two supports making a pair are attached to the ring at approximatively the same circumferential coordinate. A consequence of this is that although the number of supports is 16, the CVG has features similar to those of a CVG having 8 supports. In the mathematical model, two supports making a pair are considered to share the same attachment point to the ring, and are subjected to equal radial and tangential ring displacements. Each pair of supports is modelled as one single support having doubled values of radial and tangential mass coefficients, radial stiffness coefficients and linear and cubic tangential stiffness coefficients, compared to a single support. The quadratic tangential stiffness coefficients of two supports making a pair are equal in absolute value and have opposite sign, so that the resultant quadratic tangential stiffness coefficient $k_{t_2}$ for a pair of supports is zero.

As discussed in Section 5.3.1, when $k_{t_2} = 0$ then $f_S = 0$ in (5.13) and (5.14) and it can be shown that the sense response amplitude is:

$$q_2 = \frac{\mathcal{B}\Omega_z q_1}{\left(\frac{\omega_0}{Q}\right)} \frac{\sqrt{\left(1 + \left(\frac{\Omega^2 - \Omega_{SC}^2}{\mu_{SC}\Omega}\right)^2\right)}}{|\Delta|} \tag{5.19}$$

where $\Delta$ is (5.15). This equation indicates that unlike the 8 single support structure, when $\Omega_z = 0$ sense response (5.19) is zero, therefore the benefit of arranging supports in pairs is that the zero-rate-output is zero. Similar to the 8 single supports in Section 5.3.2, this result is investigated against a non-linear FE analysis. Figure 5.12 shows the steady-state sense response obtained using a FE non-linear transient analysis for a CVG having 8 nominal supports arranged in pairs.

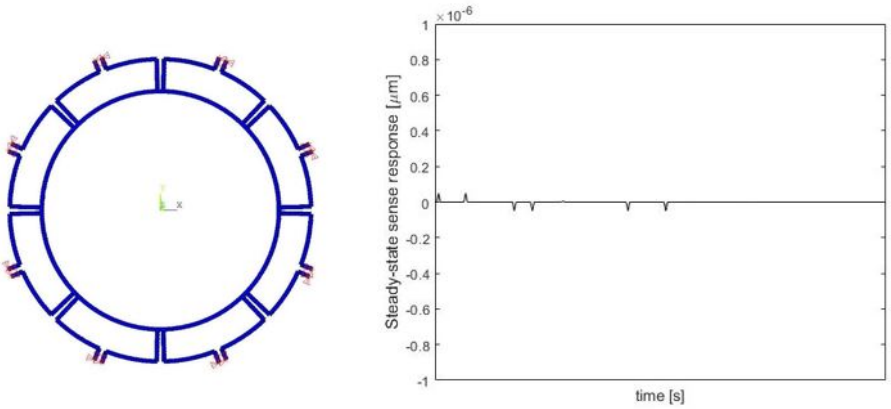



Figure 5.12: Steady-state sense response obtained using a FE non-linear transient analysis in absence of rotation for a CVG having 8 nominal supports arranged in pairs. Q=1000.

The Finite Element results indicate that in the absence of rotation the sense response is approx. zero (its amplitude is smaller than $1\times10^{-7}$ $\mu$m), and so confirm that arranging supports in pairs eliminates the zero-rate-output response.

It can be shown that the frequency response curves (amplitude, phase) of the sense mode for a ring having 8 supports in pairs are similar to those investigated in Section 5.3.2 for a ring having 8 single supports, and comparisons against the linear resonator lead to identical findings. For this reason, such analyses will not be repeated for this support configuration.

### 5.3.4 8 Supports: Summary of findings and interpretation

In what follows, main results of the investigation on the non-linear sense response for ring resonators having 8 single supports are summarised. Results refer to the excitation of the

drive mode into large amplitudes of vibration.

- When the drive response is excited in resonance ($\Omega = \Omega_D$), the sense response has a in-phase and quadrature components even when the ring is perfect.
- The sense response amplitude is not maximised when the drive mode is excited at its pseudo-resonance frequency $\Omega_D$, and the amplitude peak occurs at different frequencies.
- Geometrical non-linearity amplifies the sense response compared to the equivalent linear resonator. However, in operation at $\Omega = \Omega_D$, the sense response amplitude is smaller than that of the equivalent linear resonator at $\omega_0$.
- Using a standard linear model for the detection of $\Omega_z$ (i.e. based on a linear $q_2$-$q_1$ relation), the rate measurement is affected by quadrature errors and zero-rate-output.
- Geometrical non-linearity causes occurrence of zero-rate-output. Finite Element results verified the occurrence of non-zero sense response in the absence of rotation.
- For drive excitation $\alpha = 22.5°$, the ZRO can be eliminated by arranging the supports in 8 pairs, ensuring $k_{t_2} = 0$. Finite Element results confirmed that for this support configuration the amplitude of the ZRO is approximately zero.
- By increasing the Q-factor, the amplitude of the sense response at $\Omega_D$ reduces compared to the peak value. The amplification of the sense response amplitude caused by geometrical non-linearity becomes more significant, and the $q_2$-$q_1$ relation becomes significantly different compared to the equivalent linear resonator.

## 5.4 Sense response for a CVG having 16 supports

This Section investigates the sense response for a CVG having 16 supports. Similar to the 8 support structure in Section 5.3, analytical expressions for the in-phase and quadrature

sense responses are investigated using the averaging method, and numerical results for the frequency response curves for the sense response are presented.

### 5.4.1 Averaged sense response

The equation of motion for the sense mode for a CVG having 16 supports was determined in Chapter 3 and is given by equation (3.50), which is repeated below:

$$\ddot{Q}_2\left(1+Q_1^2\gamma_1\right)+\dot{Q}_2\left(\frac{\omega_0}{Q}+\dot{Q}_1Q_1\gamma_2\right)+Q_2\left(\omega_0^2+\dot{Q}_1^2\gamma_3+\ddot{Q}_1Q_1\gamma_4+Q_1^2\gamma_5\right)=-\mathcal{B}\Omega_z\dot{Q}_1 \tag{5.20}$$

In this equation, non-linear terms in $Q_2$ and higher powers of $Q_1$ than cubic are neglected. As discussed in Section 3.4.2, for 16 supports the sense mode equation is independent of drive angle $\alpha$ and is parametrically coupled to the drive response through non-linear terms in $\ddot{Q}_1$, $\dot{Q}_1$ and $Q_1$; the sense mode is excited by the Coriolis force only in the presence of angular rate. Using the same approach described for 8 supports in Section 5.3.1, the averaging method is used to determine the sense response. Averaged equations for $A_{SC}$ and $A_{SS}$ given by (5.4) and (5.5) for the 8 supports are valid for the 16 support case by setting $I_1 = S_1 = S_2 = 0$. This gives:

$$A_{SC}\left[\Omega^2-\omega_0^2+q_1^2\Omega^2\left(\frac{3}{4}\gamma_1-\frac{1}{4}\gamma_2-\frac{1}{4}\gamma_3+\frac{3}{4}\gamma_4\right)-\frac{3}{4}q_1^2\gamma_5\right]-\frac{\omega_0\Omega}{Q}A_{SS}=0 \tag{5.21}$$

$$A_{SS}\left[\Omega^2-\omega_0^2+q_1^2\Omega^2\left(\frac{1}{4}\gamma_1+\frac{1}{4}\gamma_2-\frac{3}{4}\gamma_3+\frac{1}{4}\gamma_4\right)-\frac{1}{4}q_1^2\gamma_5\right]+\frac{\omega_0\Omega}{Q}A_{SC}=\mathcal{B}\Omega_z\Omega q_1 \tag{5.22}$$

The in-phase and quadrature response amplitudes can be obtained from equations (5.21) and (5.22), and can be expressed in terms of $\Omega_{SC}$, $\Omega_{SS}$, $\mu_{SC}$ and $\mu_{SS}$ given by (5.8)-(5.11) with $I_1 = S_1 = S_2 = 0$. It is noted that for a given drive amplitude $q_1$, frequency $\Omega_{SC}$ is equal to the drive mode non-linear resonance frequency $\Omega_D$ (given by (4.30)). It can be shown that the amplitudes of the in-phase and quadrature sense responses for a CVG having 16 supports

are:

$$A_{SC} = \frac{\left(\frac{Q}{\Omega\omega_0}\right)(\mathcal{B}\Omega_z q_1 \Omega)}{\Delta} \tag{5.23}$$

$$A_{SS} = \frac{\left(\frac{Q}{\Omega\omega_0}\right)\left(\mathcal{B}\Omega_z q_1 \frac{(\Omega^2 - \Omega_D^2)}{\mu_{SC}}\right)}{\Delta} \tag{5.24}$$

where $\Delta$ is:

$$\Delta = 1 + \frac{\left(\Omega_D^2 - \Omega^2\right)\left(\Omega_{SS}^2 - \Omega^2\right)}{\mu_{SC}\mu_{SS}\Omega^2} \tag{5.25}$$

And the sense response amplitude is:

$$q_2 = \frac{\mathcal{B}\Omega_z q_1}{\left(\frac{\omega_0}{Q}\right)} \frac{\sqrt{\left(1 + \left(\frac{\Omega^2 - \Omega_D^2}{\mu_{SC}\Omega}\right)^2\right)}}{|\Delta|} \tag{5.26}$$

Unlike the 8 support structure, it is noted that for a ring having 16 supports there is no zero-rate-output response (i.e. $q_2 = 0$ when $\Omega_z = 0$) because $S_2 = 0$. Similar to the 8 support case, the largest sense response occurs when $|\Delta|$ is the smallest.

Equation (5.24) indicates that for $\Omega = \Omega_D$ the quadrature response is zero. This implies that when the drive mode is excited into resonance at frequency $\Omega_D$, the sense mode responds with a phase of 90° relative to the Coriolis force (which has also frequency $\Omega_D$). This implies that when 16 supports are used, drive and sense modes are resonant at the same frequency.

From equation (5.26) it can be easily shown that in operation at $\Omega = \Omega_D$ the sense response has amplitude:

$$q_2(\Omega_D) = q_1 \frac{\mathcal{B}\Omega_z Q}{\omega_0} \tag{5.27}$$

Comparing sense response amplitude (5.27) against that one for a linear and rotationally symmetric resonator in (5.16), it is noted that the amplitude of the sense response in operation

at large amplitude vibration is the same as the linear resonator. This result is important as it suggests that when 16 supports are used, the angular rate $\Omega_z$ can be detected based on the standard linear relation between $q_2$ and $q_1$ given by (5.16). Unlike the 8 supports, the measured angular rate detected based on a linear model is not affected by sensing errors such as zero-rate-output and quadrature errors. This suggests that numbers of supports that maintain the rotational symmetry in the non-linear regime dramatically improve the quality of the rate measurement when the ring undergoes large amplitude vibration.

### 5.4.2 Numerical results

This Section presents numerical results for the practical device with 16 nominal supports shown in Figure 4.1b, considered in Section 4.5.1 for the investigation of the drive response. Figure 5.13 illustrates the frequency response curves for drive and sense modes. The drive mode is excited by harmonic forces and its response amplitude, investigated in Section 4.5, is considered to be known. The sense response amplitude is calculated using equation (5.26). The frequency response curves are developed for seven magnitudes of applied external forces, and exciting frequencies in a range of $\pm 1$ Hz around the natural frequency of the $2\theta$ modes.

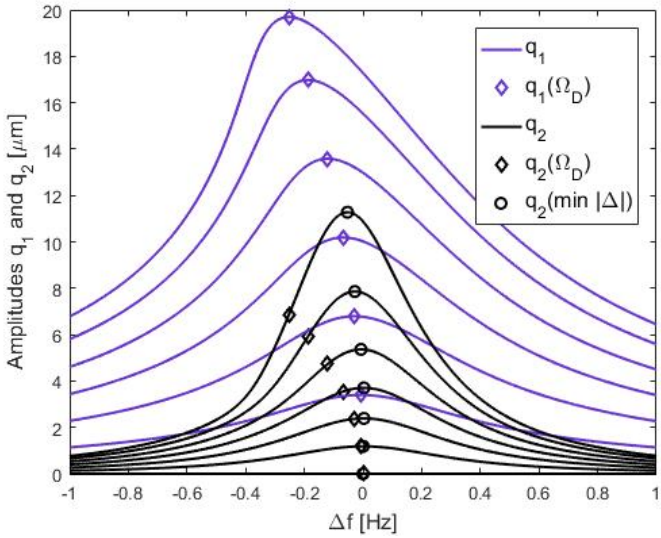



Figure 5.13: Frequency response curves for drive and sense modes for a CVG having 16 nominal supports. Q=20000.

Similar to the 8 support structure, results indicate that when the ring is excited into large amplitudes, the amplitude of the sense response at frequency $\Omega_D$ is significantly smaller than the peak value. To a good approximation, the sense response reaches its largest amplitude at that frequency corresponding to the minimum value of $|\Delta|$. It can be shown that for the device considered $\Omega_{SC} = \Omega_D$ and $\Omega_D$ is smaller than $\Omega_{SS}$, so that the frequency ensuring $|\Delta|$ reaches its minimum value is within frequencies $\Omega_D$ and $\Omega_{SS}$.

Figure 5.14 shows the frequency response curves for the sense mode obtained for the non-linear and linear resonators.

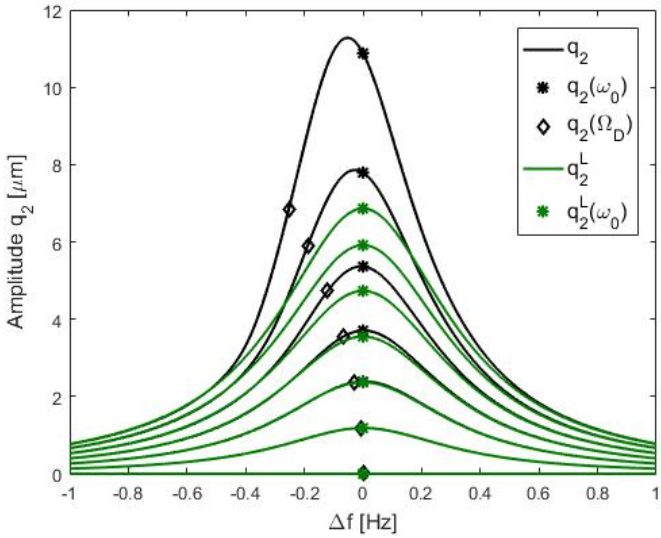



Figure 5.14: Sense mode frequency response curves for linear and non-linear resonators having 16 nominal supports. Q=20000.

These results indicate that as the drive mode is driven into large amplitude vibration, ring and support geometrical non-linearity amplifies the sense response amplitude. However, as introduced in Section 5.4.1, the sense response amplitude at the drive non-linear resonance frequency $\Omega_D$ (given by equation (5.27)) is equal to that of the equivalent linear resonator at $\omega_0$ (given that the damping is identical). Therefore, unlike the 8 support structure, geometrical non-linearity amplifies the response of the sense mode but maintains the same response amplitude in operation compared to a linear resonator.

Figure 5.15 shows the sense response amplitudes for non-linear and equivalent linear resonators obtained by exciting the drive mode into resonance (i.e. at frequency $\Omega_D$ for the non-linear resonator and $\omega_0$ for the linear) for drive amplitudes in the range 0 to 20 $\mu$m.

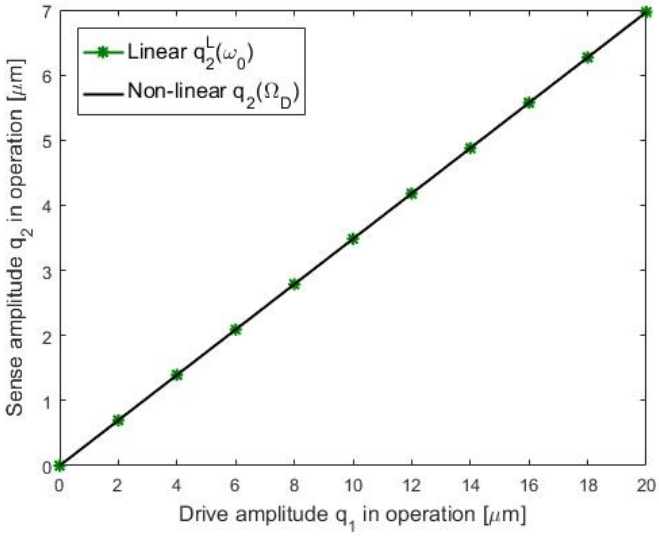



Figure 5.15: Sense response amplitude in operation for linear and non-linear resonators having 16 nominal supports. Q=20000.

It is noted that the non-linear resonator behaves as a linear resonator and the sense response amplitude is proportional to $q_1$. Unlike the 8 support structure, the angular rate can be detected based on the standard linear relationship between $q_2$ and $q_1$ in (5.16), even when the ring is excited into large amplitudes.

Similar to the 8 supports and the 8 supports in pairs, the zero-rate-output response is investigated using a FE analysis. Figure 5.16 illustrates the steady-state sense response obtained using a FE non-linear transient analysis for a CVG having 16 nominal supports.

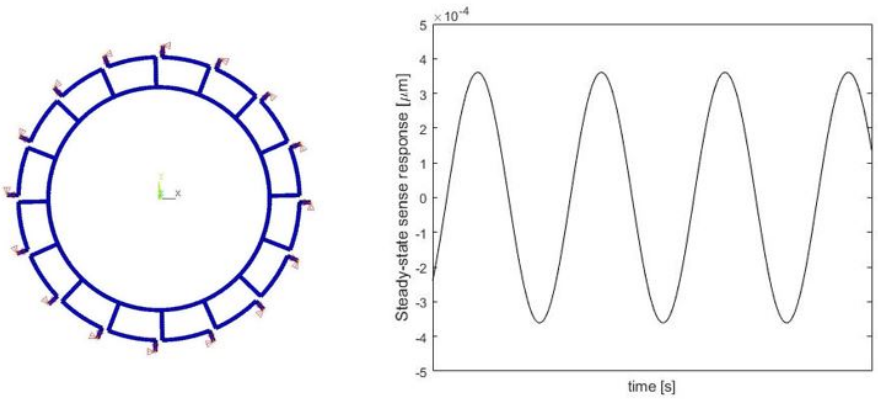



Figure 5.16: Steady-state sense response obtained using a FE non-linear transient analysis in absence of rotation for a CVG having 16 nominal supports. Q=1000.

The amplitude of the sense response in the absence of rotation obtained using Finite Element simulations is in the order of $1\times10^{-4}$ $\mu$m. Therefore, whilst the mathematical model predicts a zero sense response in the absence of angular rate, Finite Element simulations predict a very small sense response. Comparing Figure 5.16 to Figure 5.10 for a ring resonator having 8 supports, one can notice that when 16 supports are used, the sense response obtained using Finite Element simulations is two orders of magnitude smaller than that obtained for the 8 single support case. Therefore, this Finite Element investigation indicates that when the rotational symmetry is maintained (i.e. 16 supports), the ZRO can be considered to be negligible as predicted using the mathematical model.

Numerical parametric analyses for the Q-factor for a ring having 16 supports lead to similar findings to those shown for the ring having 8 supports i.e. larger Q-factors increase the difference between the sense response amplitude at $\Omega_D$ and at the peak.

### 5.4.3 16 supports: Summary of findings and interpretation

Main results obtained from the investigation on the sense response for ring resonators having 16 supports can be summarised as follows:

- When the drive mode is excited in resonance ($\Omega = \Omega_D$) at large amplitudes, the sense response is in-phase relative to the drive response. It implies that drive and sense modes respond with a phase lag of 90° to excitations having equal frequencies.

- The amplitude of the sense response is not maximised when the drive mode is excited at its pseudo-resonance frequency $\Omega_D$. The largest sense response occurs at frequencies different from $\Omega_D$.

- Ring and support geometrical non-linearity amplifies the sense response compared to the equivalent linear resonator. However, in operation at $\Omega = \Omega_D$, the sense response amplitude is the same as the equivalent linear resonator at $\omega_0$, and is defined by the damping used.

- When the drive mode is excited into resonance at large vibration amplitude, sense response amplitude $q_2$ is linearly proportional to drive amplitude $q_1$. The angular rate can be easily detected by using a standard linear $q_2$-$q_1$ relation, even when the resonator undergoes large drive amplitudes.

- In the absence of rotation, the mathematical model predicts that the sense response is zero so the zero-rate-output is zero. Finite Element results indicated that the sense response for $\Omega_z = 0$ is two orders of magnitude smaller than that obtained for the 8 supports, and can be considered to be negligible.

## 5.5 Summary and conclusions

This Chapter investigated the sense response for supported ring resonators when the ring is excited into large drive amplitudes. The effects of ring and support geometrical non-linearity on the sense response were investigated for ring resonators having 8 and 16 supports. Key results obtained using the mathematical model were verified qualitatively using a Finite Element analysis.

It was found that ring and support geometrical non-linearity causes the sense response amplitude to be smaller than the peak value when the drive mode is excited into its pseudo-resonance frequency, so that sensor sensitivity is not maximised in operation. Ring and support geometrical non-linearity was found to amplify the sense response compared to the equivalent linear resonator in which non-linearity is neglected. This amplification becomes more significant for larger values of Q-factor.

For ring resonators having 8 supports it was found that the sense response in operation at drive mode pseudo-resonance frequency $\Omega_D$ has in-phase and quadrature components relative to the drive response. The amplitude of the sense response in operation is not linearly proportional to the drive response amplitude, and zero-rate-output and quadrature errors were found to complicate the angular rate detection. Moreover, the sense response amplitude in operation was found to be smaller than that for the equivalent linear resonator, indicating that non-linearity reduces the signal-to-noise ratio.

For ring resonators having 16 supports it was found that the sense response in operation at $\Omega_D$ is in-phase relative to the drive response, so drive and sense modes are resonant at the same frequency. The sense response is negligible in the absence of angular rate, and the sense response amplitude in operation is the same as the equivalent linear resonator. A standard $q_2$-$q_1$ relation can be used to detect the angular rate even when the resonator undergoes large drive amplitudes.

This investigation demonstrated that using a number of supports that maintains the rotational symmetry in the non-linear regime is beneficial for sensor performance, and is strongly recommended in order to avoid sensing errors, and to allow sensor operation to be described by standard linear models, even when the ring experiences large vibration amplitudes.

# Chapter 6

# Improved support design for a CVG having 16 supports

## 6.1 Introduction

Previous investigations in Chapter 4 indicated that ring and support geometrical non-linearity causes the drive mode frequency backbone curve to be non-linear. The support structure was found to influence the non-linear dynamic behaviour of a supported CVG compared to an unsupported ring: whilst the ring behaviour is softening, supported ring resonators are hardening or softening depending on the support structure used.

In this Chapter, support geometry is modified whilst the ring remains unaltered to investigate hardening support designs that neutralise the softening behaviour of the ring, in order to achieve a pseudo-linear frequency backbone curve for the drive mode. Chapters 4 and 5 demonstrated that numbers of supports that maintain the rotational symmetry at large amplitude vibration improve the CVG performance, so the proposed design investigation is presented for ring resonators having 16 supports. A parametric analysis is conducted by varying the geometry of the supports, and the developed mathematical model is used to determine the shift of the drive mode resonance frequency at large amplitudes. The obtained

frequency shift is compared against that for a CVG having nominal support design. For selected support designs that significantly reduce the frequency shift compared to nominal supports, the drive mode frequency backbone curve is verified against a FE non-linear transient analysis.

This Chapter is structured as follows. Section 6.2 introduces the support geometries considered for the proposed design investigation. Two types of geometries are considered: arched geometries and straight geometries. Section 6.3 illustrates how the mathematical model is used to investigate support geometries that linearise the frequency backbone curve for the drive mode. In Sections 6.4 and 6.5 arched and straight geometries are analysed, respectively. Parametric analyses are conducted to investigate hardening supports, and the mathematical model is used to determine the drive mode frequency shift at large vibration amplitude. For selected supports that significantly reduce of the frequency shift compared to nominal supports, the drive mode frequency backbone curve is verified against a non-linear FE analysis. Section 6.6 summarises the work done in this Chapter and highlights key conclusions.

## 6.2 Support geometries

Figure 6.1 provides a schematic of the nominal support geometry.

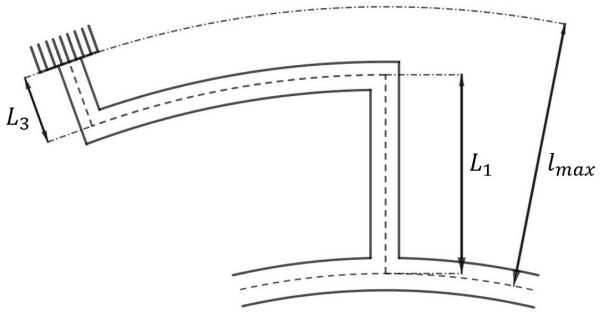
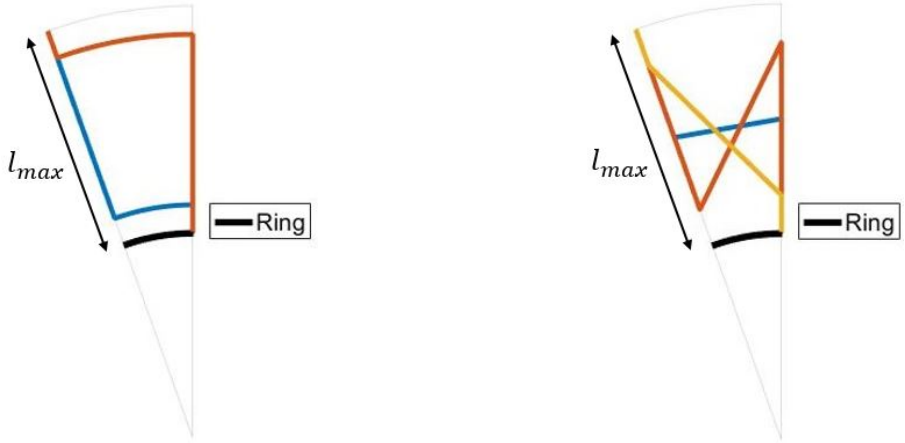



Figure 6.1: Schematic for nominal support geometry.

Each support has three segments. The segment attached to the ring has length $L_1 \approx 0.8$

mm and is orientated in the radial direction. The segment attached to the substrate has length $L_3$ ≈0.3 mm and is similarly orientated in the radial direction. $L_1$ and $L_3$ are joined by an arched middle segment parallel to the ring centre line. The radial distance between the ring mid-line and the substrate is $l_{max}$ ≈1.1 mm. In this study, two different types of supports are investigated: (i) arched segment supports and (ii) straight segment supports. For arched supports, the radial distance between the arched segment and the ring is varied as shown in Figure 6.2a. For straight geometries, the middle segment is replaced by a straight segment arbitrarily oriented with respect to $L_1$ and $L_3$ directions as shown in Figure 6.2b.




(a) Arched geometries. (b) Straight geometries.

Figure 6.2: Types of support geometries considered for the proposed design investigation.

For both arched and straight geometries, the radial distance between ring and substrate $l_{max}$ is maintained the same as the nominal geometry so that $L_1 < l_{max}$ and $L_3 < l_{max}$. The angle between directions associated with $L_1$ and $L_3$ is also maintained the same as the nominal geometry. For arched geometries, the middle segment is maintained parallel to the ring centre line and lengths $L_1$ and $L_3$ are designed so that $L_1 + L_3 = l_{max}$. A consequence of this is that when the length of $L_1$ is increased compared to the nominal geometry, the length of $L_3$ is reduced and vice versa. In contrast, for straight geometries $L_1$ and $L_3$ can be varied independently of each other.

## 6.3 Use of mathematical model to determine improved support geometries

The frequency backbone curve defining drive mode resonance for a CVG having 16 supports is given in equation (4.30), and can be expressed as:

$$\Omega_D^2 = \omega_0^2 + \frac{q_1^2}{M_{res}} \left( S_t - \Omega_D^2 I_n \right) \tag{6.1}$$

where inertial and stiffness terms $I_n$ and $S_t$ respectively are:

$$I_n = \frac{33}{10} M_{ring} \gamma^2 + m_t \gamma^2 + 32 m_r \gamma^2 \tag{6.2}$$

$$S_t = \frac{1}{3} K_{ring} \gamma^2 + \frac{3}{4} k_{t_1} \gamma^2 + 24 k_{r_1} \gamma^2 - 24 k_{r_2} \gamma + \frac{9}{2} k_{r_3} + \frac{9}{32} k_{t_3} \tag{6.3}$$

These coefficients relate to the modal mass and stiffness of the ring and the radial and tangential mass and stiffness of the support. For an unsupported ring it was shown in Section 4.4 that $\frac{1}{3} K_{ring} \gamma^2$ is smaller than $\Omega_D^2 \frac{33}{10} M_{ring} \gamma$, and for the device investigated it can be shown that support inertia is negligible compared to ring inertia. A consequence of this is that the dynamic behaviour of the drive mode is essentially defined by the ring inertia and support stiffness coefficients $k_{r_1}$, $k_{r_2}$, $k_{r_3}$, $k_{t_1}$ and $k_{t_3}$ which appear in equation (6.3) for $S_t$.
The frequency backbone curve for the drive mode is more hardening for supports having a larger $S_t$ (see (6.1)) i.e. for supports having larger stiffness coefficients $k_{r_1}$, $k_{r_3}$, $k_{t_1}$, $k_{t_3}$ (with a positive sign) and $k_{r_2}$ (with a negative sign). Linear stiffness coefficients $k_{r_1}$ and $k_{t_1}$ in (6.3) are multiplied by $\gamma^2$ and are involved in non-linear stiffness coefficient $S_t$ because of the non-linear flexural vibration of the ring.

In what follows, a parametric analysis is conduced for arched and straight geometries by varying lengths $L_1$ and $L_3$. Mass and stiffness coefficients to model the radial and tangential

inertia and stiffness of the supports are calculated using a FE analysis of a single support as introduced in Section 3.3 (more details are provided in Appendix A). The frequency shift is defined as $\Omega_D - \omega_0$ where $\Omega_D$ is calculated using (6.1). For nominal supports, the frequency shift for a drive amplitude of 20 $\mu$m was found to be -0.260 Hz (see Section 4.5.1). Support geometries producing a frequency shift significantly smaller than 0.260 Hz (in absolute value) are considered to be "improved supports" as they reduce the dependency of the drive mode resonance frequency on the amplitude vibration. For selected improved supports, the frequency backbone curve for the drive mode is verified against a FE non-linear transient analysis using the same approach described in Section 4.3. Due to high computational cost, only a limited number of improved supports are considered for FE verification.

## 6.4 Arched geometries

Figure 6.3 shows the nominal geometry and the arched geometries considered for the proposed support design investigation.

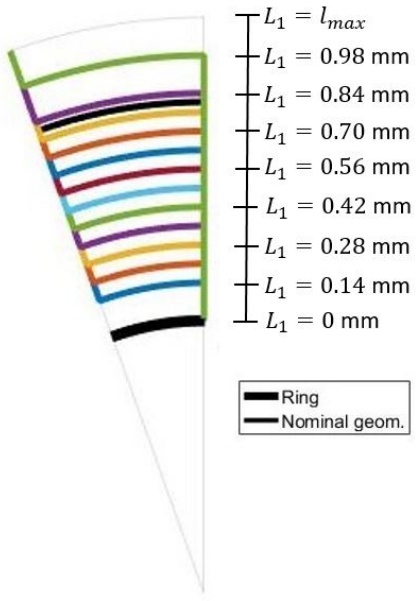



Figure 6.3: Arched geometries analysed.

Length $L_1$ is varied between $\frac{1}{8}l_{max}$ and $\frac{7}{8}l_{max}$. For all arched geometries considered, coefficients $I_n$ and $S_t$ are obtained using (6.2) and (6.3), respectively. Figure 6.4 shows how terms $\Omega_D^2 I_n$ and $S_t$ vary when the length $L_1$ is varied across the specified range.

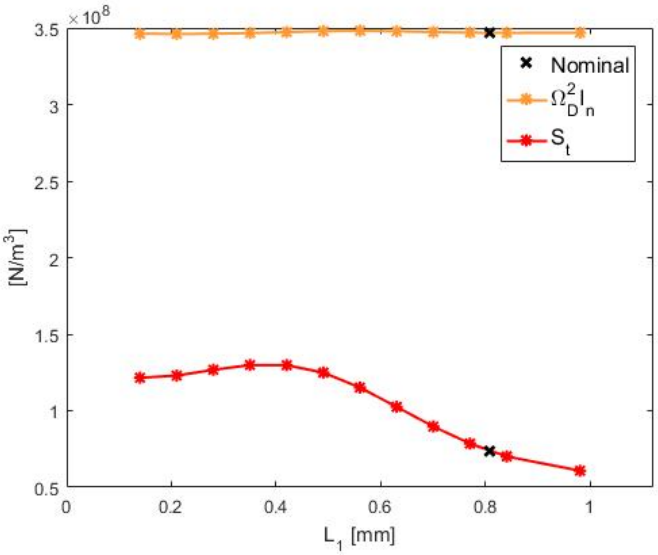



Figure 6.4: Value of terms $\Omega_D^2 I_n$ and $S_t$ for geometries investigated (see equations (6.1)-(6.3)). Frequencies $\Omega_D$ are calculated using (6.1) for $q_1$ equal to 20 $\mu$m.

Figure 6.4 illustrates that for all arched geometries considered, coefficient $I_n$ is approx. the same (as the ring inertia is much larger than support inertia), and $\Omega_D^2 I_n$ is larger than $S_t$. A consequence of this is that a CVG supported by any arched support has a softening frequency backbone curve for the drive mode (see equation (6.1)).

Arched supports having $L_1$ shorter than the nominal value have a larger stiffness coefficient $S_t$ (see "Nominal" value in Figure 6.4) so they have a more hardening dynamic behaviour than nominal supports. The largest value of $S_t$ is obtained for $L_1$ ≈0.4 mm. Figures 6.5 and 6.6 show the calculated radial and tangential stiffness coefficients, respectively, when $L_1$ is varied.

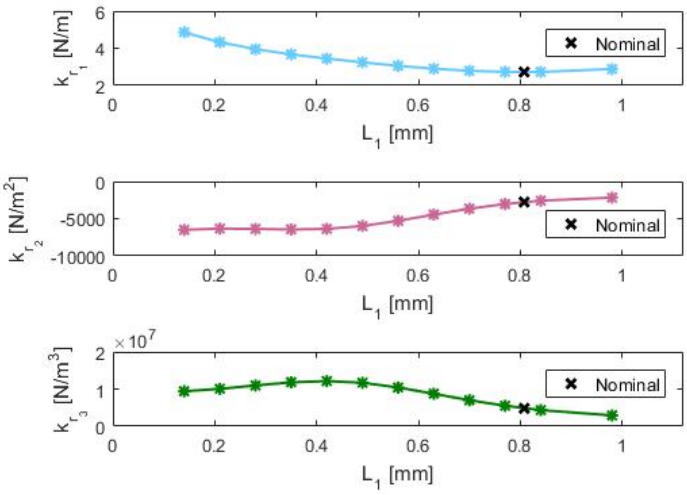



Figure 6.5: Radial linear, quadratic and cubic stiffness coefficients for geometries investigated.

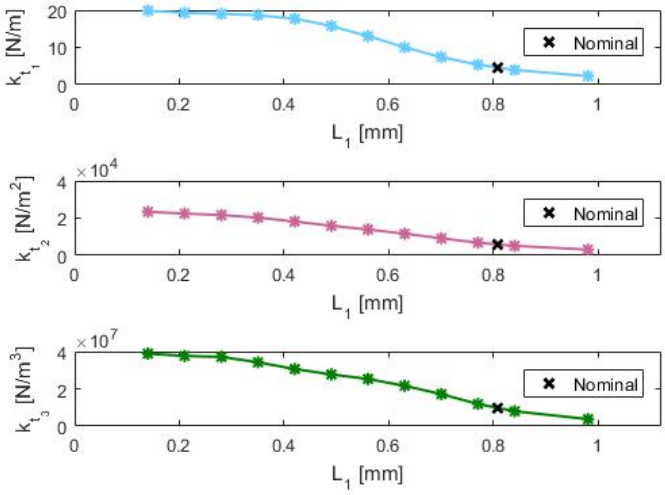



Figure 6.6: Tangential linear, quadratic and cubic stiffness coefficients for geometries investigated.

Coefficient $k_{r_1}$ is positive and decreases as length $L_1$ increases. Coefficient $k_{r_2}$ is negative and is approximatively equal for supports having $L_1$ between 0.14 mm and 0.4 mm. For longer $L_1$, its absolute value decreases. The largest coefficient $k_{r_3}$ is obtained for arched

supports having $L_1$ approx. 0.4 mm long. Coefficients $k_{t_1}$ and $k_{t_3}$ are approx. equal for supports having $L_1$ between 0.14 mm and 0.25 mm, and decrease for longer $L_1$. Stiffness coefficient $k_{t_2}$ does not appear in equation (6.1) hence does not contribute to the frequency shift and is of no interest here. Comparing $k_{r_3}$ in Figure 6.5 to $S_t$ in Figure 6.4, it is noted that coefficient $S_t$ is strongly influenced by the cubic radial stiffness coefficient of the support.

Figure 6.7 shows the frequency shift obtained for a drive amplitude of 20 $\mu$m for CVGs having the considered arched supports. The pseudo-resonance frequency $\Omega_D$ is obtained using (6.1), and the frequency shift is calculated as $\Omega_D - \omega_0$.

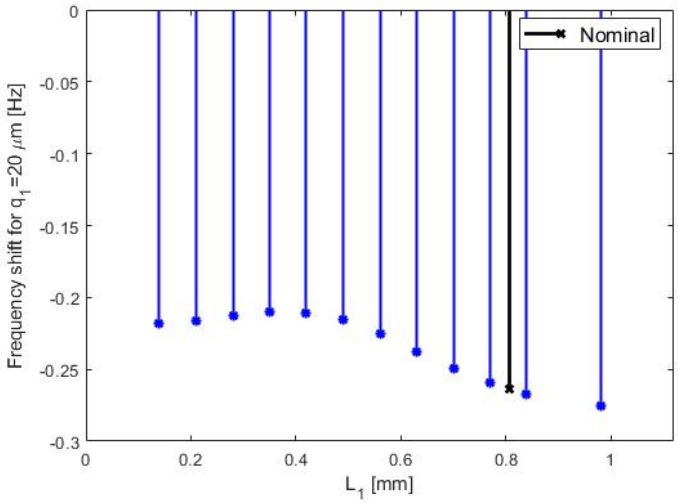



Figure 6.7: Frequency shift for a drive amplitude of 20 $\mu$m for arched geometries considered.

The frequency shift is negative for all arched geometries considered, indicating a softening drive mode frequency backbone curve. The smallest frequency shift obtained (in absolute value) is 0.210 Hz, which is a 20% reduction compared to nominal supports. This reduction is not considered to be significant, and this investigation concludes that support geometries having a middle arched segment parallel to the ring centre line do not linearise the drive mode frequency backbone curve for any practical length $L_1$ considered. Different support designs need to be investigated to linearise the frequency backbone curve for the drive mode.

## 6.5 Straight geometries

Figure 6.8 shows a schematic diagram for a support having straight geometry.

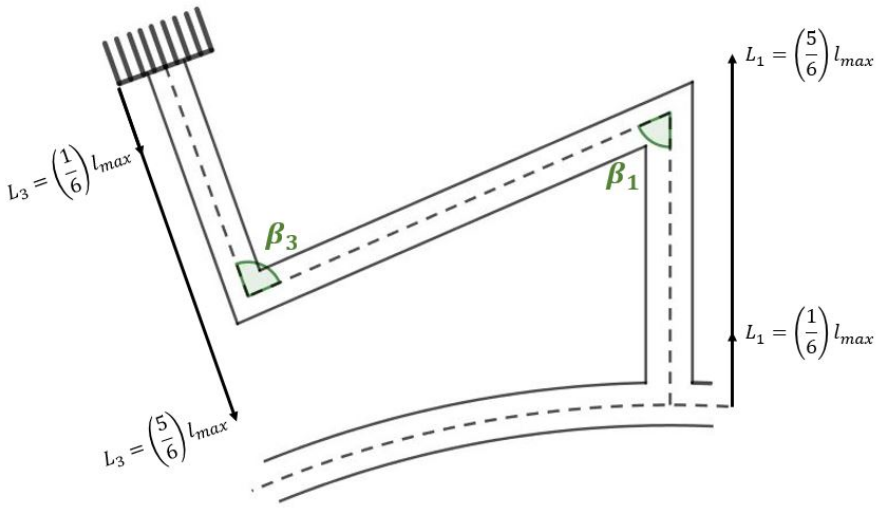



Figure 6.8: Schematic diagram for a straight support.

As introduced in Section 6.2, lengths $L_1$ and $L_3$ are arbitrary varied by changing angles $\beta_1$ and $\beta_3$. The only geometrical constraints considered are the radial distance between the ring mid-line and the substrate (i.e. $l_{max}$) and the angle between the directions associated with $L_1$ and $L_3$, which are maintained the same as the nominal geometry. The shortest and the longest lengths considered for both $L_1$ and $L_3$ respectively are $\frac{1}{6}l_{max}$ and $\frac{5}{6}l_{max}$.

Figure 6.9 shows how stiffness coefficient $S_t$ varies by varying $L_1$ and $L_3$.

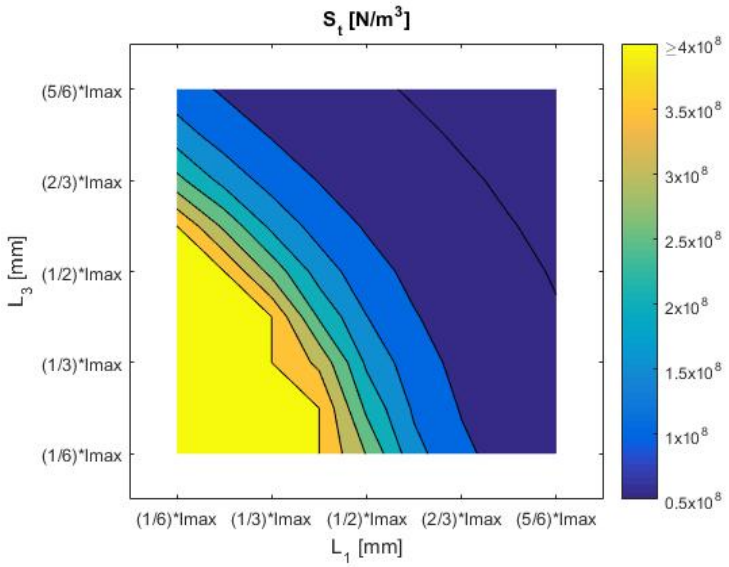
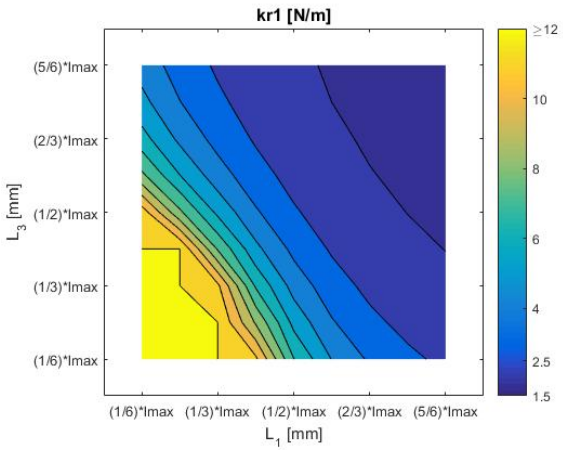


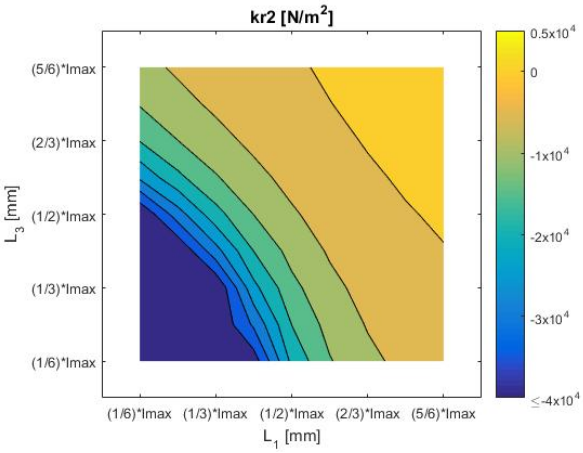

Figure 6.9: Coefficient $S_t$ for straight geometries considered.

The results indicate that stiffness coefficient $S_t$ for a straight support having $L_1 = \frac{1}{6}l_{max}$ and $L_3 = \frac{1}{6}l_{max}$ is significantly larger than that for a straight support having $L_1 = \frac{5}{6}l_{max}$ and $L_3 = \frac{5}{6}l_{max}$, so supports having shorter $L_1$ and/or $L_3$ are more hardening.

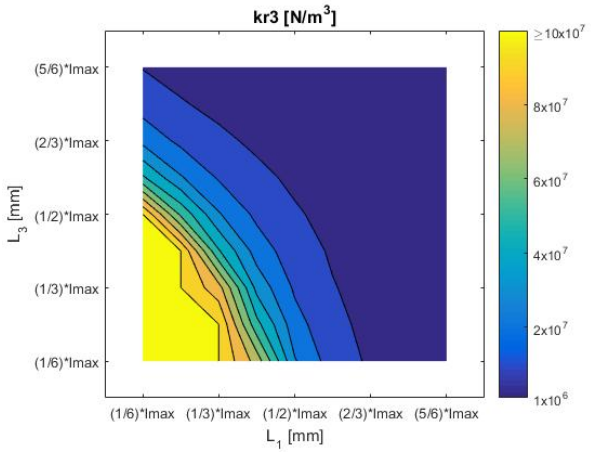
Figure 6.10 shows how radial linear, quadratic and cubic stiffness coefficients for a straight support vary as $L_1$ and $L_3$ are changed. Similarly, Figure 6.11 illustrates the tangential linear and cubic stiffness coefficients ($k_{t_2}$ is not illustrated as it is not of interest in this analysis).




(a) Stiffness coefficient $k_{r_1}$.

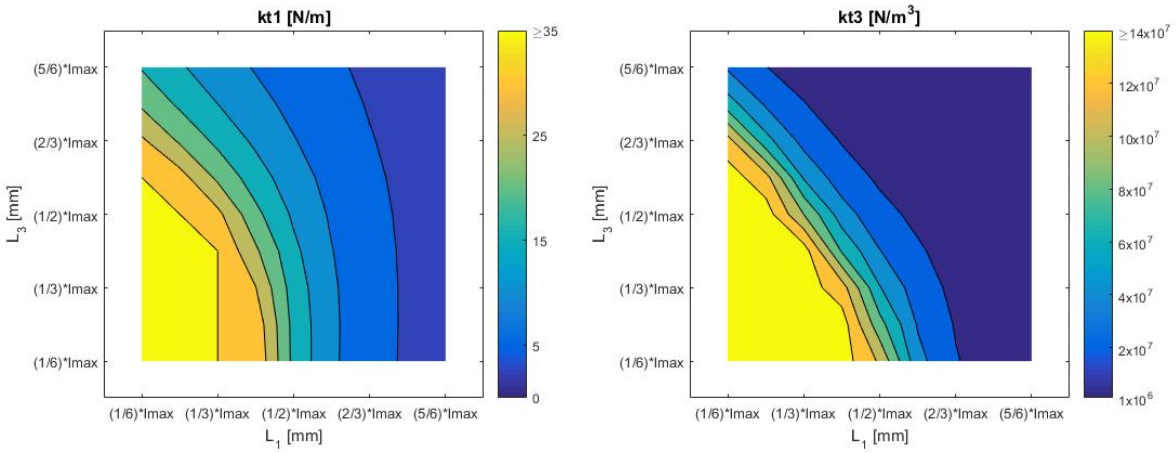



(b) Stiffness coefficient $k_{r_2}$.




(c) Stiffness coefficient $k_{r_3}$.

Figure 6.10: Radial linear, quadratic and cubic stiffness coefficients for straight geometries considered.




(a) Stiffness coefficient $k_{t_1}$.

(b) Stiffness coefficient $k_{t_3}$.

Figure 6.11: Tangential linear and cubic stiffness coefficients for straight geometries considered.

Figure 6.10 indicates that stiffness coefficients $k_{r_1}$, $k_{r_3}$ and $k_{t_3}$ are positive for all $L_1$ and $L_3$ lengths considered. Larger $k_{r_1}$, $k_{r_3}$ and $k_{t_3}$ values are obtained for supports having shorter $L_1$ and/or $L_3$. Quadratic radial stiffness coefficient $k_{r_2}$ is negative for most lengths of $L_1$ and $L_3$ considered, except for $L_1$ and $L_3$ both longer than approx. $\frac{2}{3}l_{max}$. In absolute value, a larger $k_{r_2}$ is obtained for shorter $L_1$ and/or $L_3$. Coefficient $k_{t_1}$ is positive and larger for supports having shorter $L_1$.

Comparing Figures 6.10c and 6.11b for $k_{r_3}$ and $k_{t_3}$, respectively, against Figure 6.9 for $S_t$, it can be noted that stiffness coefficient $S_t$ is essentially defined by the cubic radial and tangential stiffness coefficients of the support. Supports having shorter $L_1$ and/or $L_3$ are more hardening than supports having longer $L_1$ and/or $L_3$ because their $k_{r_3}$ and $k_{t_3}$ are significantly larger.

Equation (6.1) is used to determine the drive mode frequency backbone curve for CVGs having straight supports. Figure 6.12 illustrates the frequency shift obtained for a drive amplitude of 20 $\mu$m.

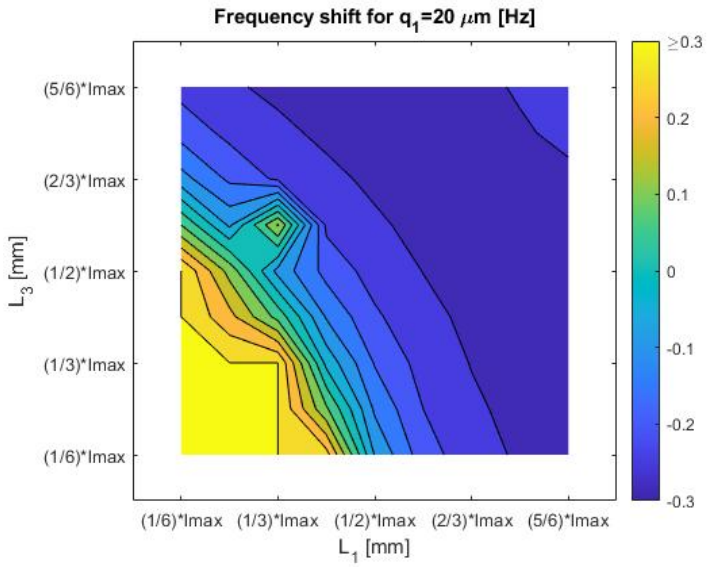



Figure 6.12: Frequency shift for a drive amplitude of 20 $\mu$m for straight geometries considered.

The noticeable change in frequency shift by varying $L_1$ and $L_3$ demonstrates that the performance of the resonator are significantly influenced by the support structure. For example, a positive frequency shift is obtained for straight supports having both $L_1$ and $L_3$ shorter than approx. $\frac{1}{3}l_{max}$, indicating that the frequency backbone curve for the drive mode is hardening. In contrast, supports having both $L_1$ and $L_3$ longer than approx. $\frac{2}{3}l_{max}$ cause the frequency shift to be negative and so the frequency backbone curve will be softening. Figure 6.13 illustrates the percentage reduction of the frequency shift (in absolute value) with respect to nominal supports.

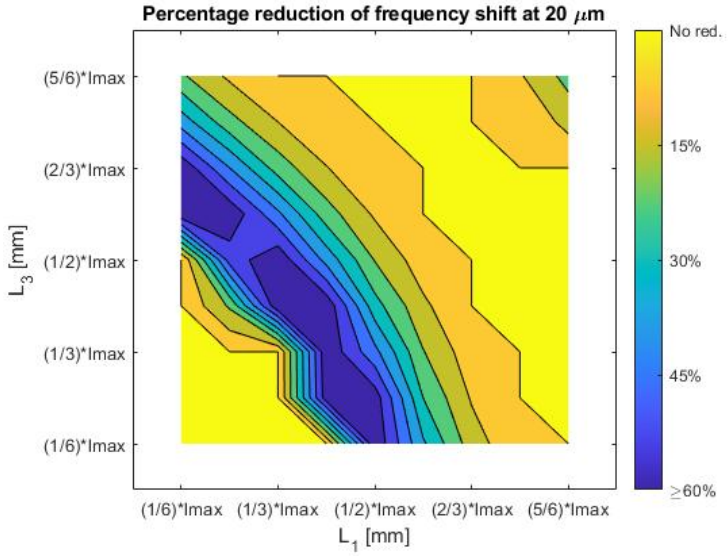



Figure 6.13: Reduction of the frequency shift in absolute value compared to that characterising nominal geometry supports, for a drive amplitude of 20 $\mu$m. "No red." indicates that supports do not reduce the frequency shift (i.e. the frequency shift is equal or larger compared to the nominal supports).

It is noted that straight supports having (i) both $L_1$ and $L_3$ shorter than approx. $\frac{1}{3}l_{max}$, (ii) $L_1 > \frac{2}{3}l_{max}$ and (iii) $L_1 > \frac{1}{3}l_{max}$ and $L_3 > \frac{1}{2}l_{max}$, cause the frequency shift to be equal or larger than that for nominal supports. For all other lengths $L_1$ and $L_3$, straight supports improve CVG performance as the frequency shift is reduced compared to that characterising nominal supports.

For some straight supports, the frequency shift is reduced by over 60% compared to nominal supports, demonstrating that support geometrical non-linearity can be used to linearise the frequency backbone curve for the drive mode.

In what follows, the drive mode frequency backbone curve is verified against a Finite Element analysis. As the computational time required to perform FE non-linear transient analyses is very high, the drive mode frequency backbone curve is validated against FE method for only three straight support geometries for which the mathematical model predicts a reduction of the frequency shift between 30% and 75%.

### 6.5.1 FE validation of frequency shift reduction for selected support geometries

#### Selected straight geometries considered for FE validation

Figure 6.14 shows the same plot as Figure 6.13 and indicates the straight geometries selected for FE verification.

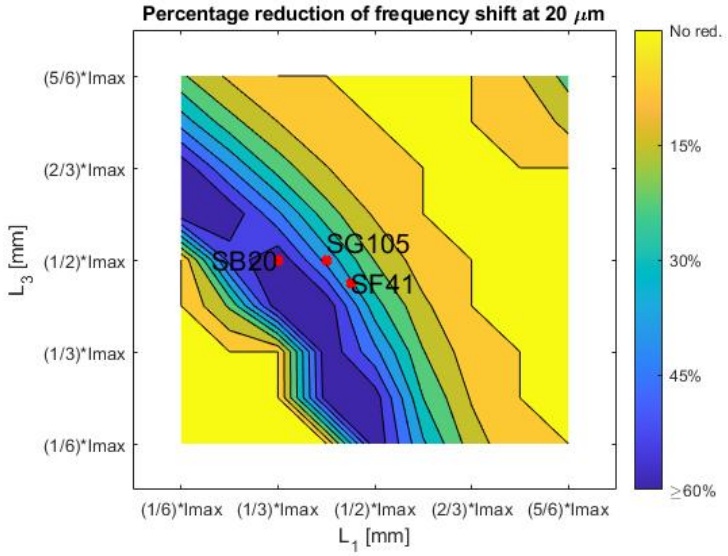



Figure 6.14: Straight support geometries selected for FE verification, indicated as SF 41, SG 105 and SB 20.

Figure 6.15 shows schematic diagrams for selected geometries and Figure 6.16 shows the Finite Element models developed to perform the non-linear transient analyses. Lengths $L_1$ and $L_3$ are provided in Table 6.1.

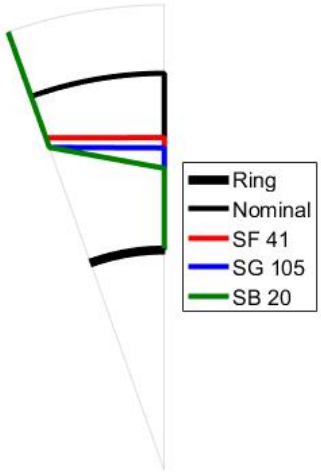
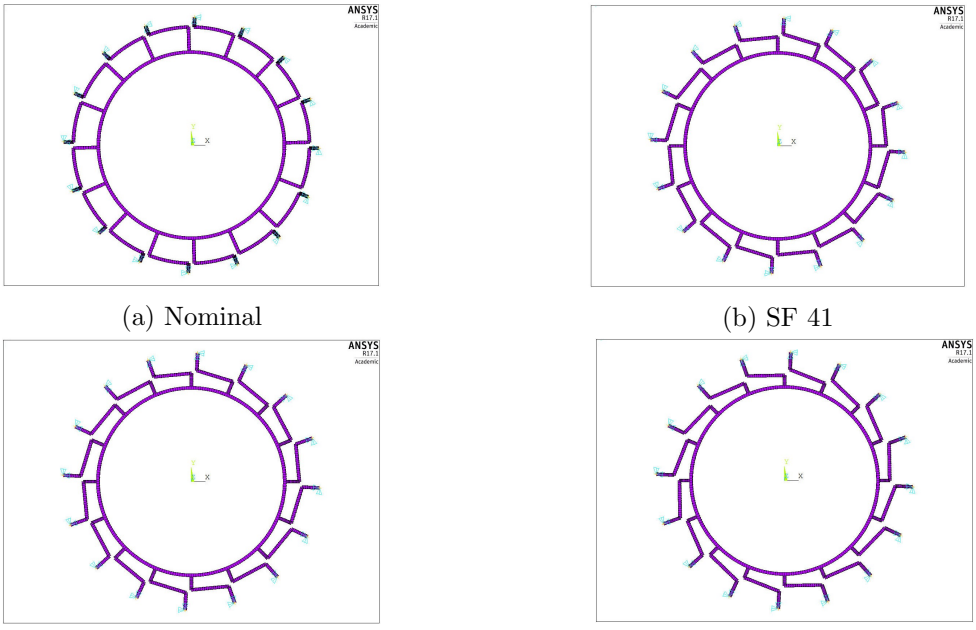



Figure 6.15: Diagram for nominal support and selected straight supports considered for FE verification.



(a) Nominal

(b) SF 41

(c) SG 105

(d) SB 20

Figure 6.16: Finite Element models for ring resonators having nominal supports and straight supports selected for FE verification.

| Geometry ID | $L_1$ [mm] | $L_3$ [mm] |
|---|---|---|
| SF 41 | 0.51 | 0.51 |
| SG 105 | 0.46 | 0.56 |
| SB 20 | 0.37 | 0.56 |

Table 6.1: Lengths of $L_1$ and $L_3$ for selected straight geometries considered for FE verification.

**Frequency backbone curves obtained using FE analysis**

The drive mode frequency backbone curves obtained using a FE analysis for nominal supports and straight supports SF 41, SG 105 and SB 20 are shown in Figure 6.17 and compared against those obtained using the mathematical model (i.e. equation (6.1)). In the plot, $\Delta f$ is the frequency variation from the natural resonance frequencies of the drive and sense $2\theta$ modes in Hertz. Numerical results refer to a Q-factor of 1000.

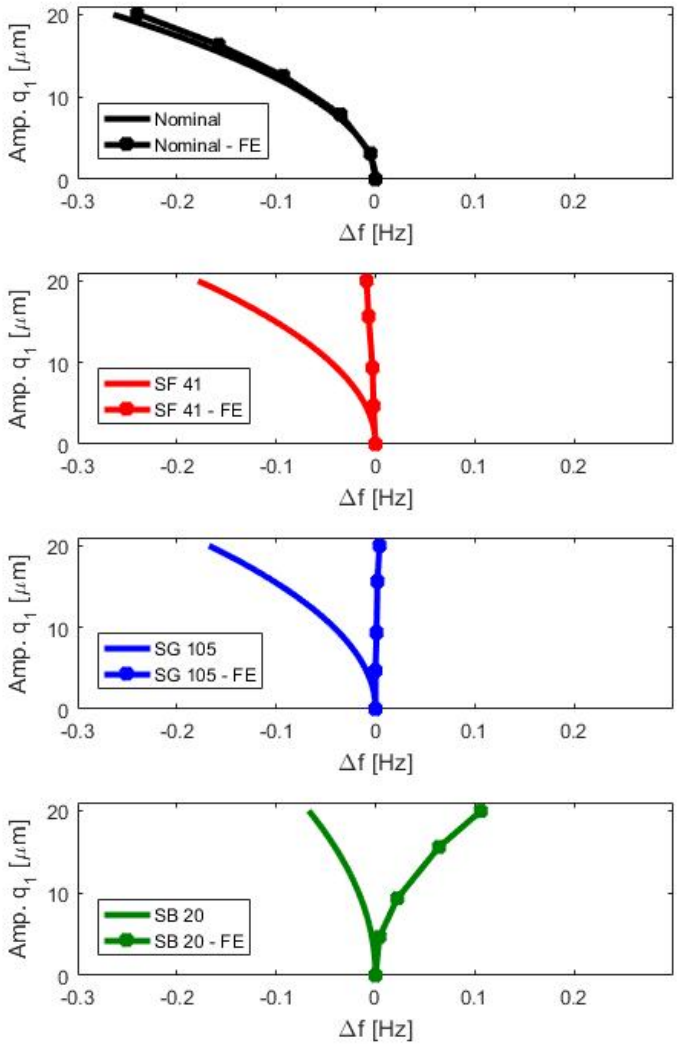



Figure 6.17: Drive mode frequency backbone curves obtained using mathematical model and FE analysis for ring-based resonators having nominal support and proposed straight supports. Q=1000.

**Accuracy of the mathematical model** Figure 6.17 indicates that the frequency backbone curves calculated using a FE analysis are more hardening than those obtained using the mathematical model, indicating limitations with accuracy of the mathematical model. As

already mentioned in Section 4.6, possible explanation for these inaccuracies are associated with the assumptions used to develop the mathematical model. Among these, the radial and tangential directions are assumed to be principal axes of stiffness for the supports. Table 6.2 indicates the frequency shift in Hertz obtained using the mathematical model and the FE analysis, the difference between the obtained values, and angle $\phi_{PA}$ between the principal axes of stiffness of the supports and the radial and tangential directions (calculated as described in Appendix A), for each selected straight support.

| Geometry ID | Math. [Hz] | FE [Hz] | Difference [Hz] | $\phi_{PA}$ |
|---|---|---|---|---|
| Nominal | -0.260 | -0.240 | 0.020 | $11.3^0$ |
| SF 41 | -0.178 | -0.009 | 0.169 | $11.9^0$ |
| SG 105 | -0.167 | 0.004 | 0.171 | $12.3^0$ |
| SB 20 | -0.067 | 0.105 | 0.172 | $14.7^0$ |

Table 6.2: Frequency shift in Hertz for drive amplitude of 20 $\mu$m obtained using the mathematical model ("Math."), the FE analysis ("FE"), and the difference between obtained values ("Difference"). Angle $\phi_{PA}$ calculated for selected straight supports is indicated.

From Table 6.2 it can be noted that the accuracy of the mathematical model decreases as angle $\phi_{PA}$ increases. This suggests that the mathematical model is less accurate for increasing $\phi_{PA}$ angles.

**Achievement of pseudo-linear drive mode frequency backbone curves** Figure 6.17 indicates that for a CVG having supports SG 105 and SF 41, the drive mode the frequency backbone curve obtained using the FE analyses is approximatively linear (or pseudo-linear). Table 6.3 indicates the percentage reduction of the absolute value of the frequency shift for selected straight supports compared to a CVG having nominal supports, obtained using the FE analyses for a drive amplitude of 20 $\mu$m.

| Geometry ID | % red. FE |
|---|---|
| SF 41 | 96% |
| SG 105 | 98% |
| SB 20 | 56% |

Table 6.3: Reduction of the frequency shift for selected straight supports compared to the nominal supports obtained using a FE analysis.

It is noted that supports SG 105 and SF 41 significantly reduce the frequency shift by 98% and 96%, respectively. Finite Element results demonstrate that support geometrical non-linearity can be used to linearise the frequency backbone curve for the drive mode. Hardening supports that neutralise the softening behaviour of the ring provide with a pseudo-linear frequency backbone curve for the drive mode and so reduce the dependency of the drive mode resonance frequency on the drive amplitude. For a CVG having supports SG 105 or SF 41, the drive mode responds in resonance to excitations having frequencies approx. equal to the natural frequency of the drive mode, also when the CVG operates at large amplitude vibration and ring and support geometrical non-linearity effects are significant. This simplifies the control system used to maintain the drive mode resonant and improves sensor performance.

**Use of the mathematical model to linearise the drive mode frequency backbone curve** The comparison between the drive frequency backbone curves obtained using the mathematical model and the FE analyses (see Figure 6.17) indicates that the frequency shift calculated using the mathematical model is not very accurate. However, the frequency backbone curves for supports SF 41 and SG 105 obtained using a FE analysis are pseudo-linear and significantly reduce the frequency shift compared to nominal supports (see Table 6.3). It is fundamental to highlight again that if the design investigation was based on a FE analysis only, the computational cost would be extremely high. In fact, it would be needed to

modify the support geometry, calculate the drive mode frequency backbone curve using a FE non-linear transient analysis and repeat this process until a support geometry that linearises the drive mode frequency backbone curve is found. In view of this, it can be concluded that the mathematical model aids identification of support geometries that have potential to linearise the drive mode frequency backbone curve of supported ring resonators, at very low computational cost. Once improved set of support geometries are identified using the mathematical model, FE analyses need to be performed to verify the drive mode frequency backbone curve obtained using the mathematical model, only for a selected (reduced) number of support geometries.

## 6.6 Summary and conclusions

In this Chapter, the mathematical model was used to investigate hardening support geometries that neutralise the softening behaviour of the ring. The support design investigation was presented for a CVG having 16 supports as previous chapters indicated that non-linear performance of ring-based CVGs are improved for numbers of supports that maintain the rotational symmetry. Two types of support geometries were considered i.e. arched supports and straight supports. The mathematical model was used to determine the drive mode frequency backbone curve so the frequency shift for large drive amplitudes.

It was shown that the arched supports considered cause the drive mode frequency backbone curve to be softening, and the frequency shift is not significantly reduced compared to nominal supports. In contrast, selected straight supports were found to be hardening and to linearise the drive mode frequency backbone curve.

Finite Element analyses were used to verify the drive frequency backbone curve for a number of selected straight supports for which the mathematical model predicts a pseudo-linear dynamic behaviour. Comparison between mathematical and FE results indicated limitations

with accuracy of the mathematical model, possibly due to assumptions used to develop the mathematical model that may not be accurate. However, FE results verified that the drive mode frequency backbone curve for selected straight supports is pseudo-linear, and demonstrated that the developed mathematical model can be used to guide design of supported ring resonators. Moreover, Finite Element results demonstrated that support non-linearity can be used to mitigate ring geometrical non-linearity, ensuring the drive mode resonance frequency of the resonator is approximatively equal to the linear resonance frequency even when the CVG undergoes large amplitude vibration.

# Chapter 7

# Conclusions and further work

## 7.1 Introduction

This thesis investigated the effects of ring and support structures geometrical non-linearity on high performance MEMS ring-based resonators used for inertial navigation systems. Non-linear drive and sense responses have been investigated by using a developed mathematical model including ring non-linear flexural vibration and support non-linear stiffness. The frequency backbone curve for the drive mode, the dependence of the drive mode dynamics on the drive axis location relative to the supports, and the zero-rate-output in the absence of angular rate have been verified using a Finite Element analysis. Support designs (support geometry and number of supports) were suggested to improve ring resonators performance at large amplitudes of vibration. This final Chapter summarises the work done and reviews the aims of the thesis. The main conclusions and contributions are recalled, and areas for further work are proposed.

## 7.2 Review of thesis aims and work done

This Section reviews the aims and objectives of the thesis presented in Chapter 1.

1. *Investigate the numbers of supports that maintain the rotational symmetry of ring-based resonators for any pair of $n\theta$ in-plane flexural modes of the ring in the linear regime.*
   Chapter 2 developed a mathematical model for modelling ring and $p$ supports for resonators operating in the $n\theta$ modes in the linear regime. The ring was modelled as a curved beam and the support was modelled using radial and tangential mass and linear spring elements. The model was used to determine the kinetic and potential energy expressions for ring and support structures. The obtained energies expressions were used to investigate the numbers of supports that maintain the rotational symmetry of the resonator in the linear regime.

2. *Investigate ring and support geometrical non-linearity effects on the rotational symmetry of supported ring-based resonators.*
   In Chapter 3, ring non-linear flexural vibration and support non-linear stiffness were included in the mathematical model developed in Chapter 2 to take account of ring and support geometrical non-linearity. The breathing mode of the ring was included in the ring mid-line deformation expressions, and the stiffness of the support was modelled using cubic non-linear radial and tangential springs. Ring and support kinetic and potential energy expressions were determined for ring resonators operating at large amplitudes of vibration and analysed to investigate the numbers of supports that maintain the rotational symmetry in the non-linear regime. The numbers of supports that maintain the rotational symmetry in the linear and non-linear regime were compared to investigate the influence of geometrical non-linearity on the ring resonator rotational symmetry.

3. *Develop the non-linear governing equations of motion for the drive and sense $n\theta$ modes for a ring resonator having p supports operating at large amplitudes of vibrations.*
   In Chapter 3 the mathematical model for modelling the non-linear supported ring resonator was used to develop the equations of motion governing the drive and sense

modes. The equations were determined using the Lagrange's equation in the drive and sense generalised coordinates, for the generic pair of $n\theta$ ring modes and number of supports $p$. The equations were developed to represent the drive and sense dynamics under practical operating conditions i.e. the drive mode is excited by harmonic external forces and the ring resonator rotates around the ring polar axis with constant angular rate, so that the sense mode is excited by the Coriolis force. The equations of motion were then analysed in detail for practical CVGs ring resonators operating in the $n = 2$ modes and supported by 8 and 16 supports.

4. *Investigate ring and support geometrical non-linearity effects on the drive and sense governing equations of motion.*

   Non-linear drive and sense governing equations of motion developed in Chapter 3 were compared against those in Chapter 2 for an equivalent linear ring resonator in which ring and support geometrical non-linearity is neglected, to highlight ring and support geometrical non-linearity effects on the drive and sense modes dynamics.

5. *Investigate the steady-state $2\theta$ drive response for a supported ring resonator when the ring is driven into large amplitudes of vibration, under practical operating conditions.*

   In Chapter 4 the averaging method was applied to the equation of motion governing the $2\theta$ drive mode (developed in Chapter 3) to investigate amplitude and phase of the drive response in steady-state, for ring resonators having 8 and 16 supports. The drive mode was assumed to be excited by harmonic external force. The frequency backbone curve for the drive mode was investigated based on a drive response having phase of 90 degrees relative to the applied external force.

6. *Investigate the steady-state $2\theta$ sense response for a supported ring resonator undergoing large drive amplitude of vibration, under practical operating conditions.*

   Similar to the drive response in Chapter 4, in Chapter 5 the averaging method was applied to the equation of motion governing the $2\theta$ sense mode (developed in Chapter

3) to investigate the in-phase and quadrature sense responses in steady-state, for ring resonators having 8 and 16 supports. Ring and support geometrical non-linearity effects on the sense response were investigated by comparing the non-linear sense response against that for an equivalent linear resonator in which geometrical non-linearity is neglected. The impact of non-linearity on sensor performance was investigated for symmetric and asymmetric ring resonators, and comparison were made.

7. *Investigate support designs that linearise the dynamic behaviour of resonators operating at large amplitudes.*

   In Chapter 6 the mathematical model was used to investigate support designs that linearise the dynamic behaviour of the drive mode at large amplitudes. The frequency backbone curve for the drive mode was investigated using the mathematical model, and verified using non-linear Finite Element analysis. Comparisons were made against the frequency backbone curve obtained for nominal supports, to investigate if proposed support designs reduce the frequency shift at large amplitudes. The accuracy of the results obtained using the mathematical model was discussed based on the comparison against Finite Element results.

## 7.3 Conclusions

Main conclusions of this work are summarised in the following points:

1. The rotational symmetry of the $n\theta$ modes of ring resonators operating in the linear regime is maintained when the number of regularly spaced supports $p$ is such that $\frac{2n}{p}$ is not an integer. Otherwise, the rotational symmetry is broken, and ring and support energy expressions are not invariant to the choice of drive and sense generalised coordinates. For practical CVGs operating in the $2\theta$ modes, 8 and 16 supports maintain the rotational symmetry in the linear regime.

2. When the ring is driven into large amplitudes of vibration, the rotational symmetry of ring resonators operating in the $n\theta$ modes is maintained when the number of regularly spaced supports $p$ is such that $\frac{mn}{p}$ is not an integer for $m = 1, ..., 6$. Ring and support geometrical non-linearity causes the rotational symmetry to break for some numbers of supports that maintain the symmetry in the linear regime. For practical CVGs operating in the $2\theta$ modes, 8 supports break the rotational symmetry of the ring resonator when the ring is driven into large amplitudes. In contrast, 16 supports maintain the rotational symmetry for large amplitudes of vibration.

3. Ring and support geometrical non-linearity causes the modal mass, stiffness and damping in drive and sense governing equations of motion to parametrically depend on non-linear terms in drive and sense generalised coordinates. In practice, drive response amplitude is much larger than the sense response, and dependency on non-linear terms involving the sense response can be neglected.

   If the rotational symmetry of the supported ring resonator is broken, drive and sense equations of motion depend on the position of the drive axis relative to the supports location, and have different system parts. Modes are coupled with each other in the absence of rotation and the sense mode is self excited by non-linear terms involving the drive response. These terms cause the sense response to be non-zero in the absence of rotation and produce zero-rate-output response.

   In contrast, if the rotational symmetry is maintained, drive and sense non-linear equations have identical system parts and are invariant to the drive axis angle. Modes are only coupled in the presence of rotation by the Coriolis force, and the zero-rate-output is negligible.

4. Ring and support geometrical non-linearity causes the drive mode resonance frequency to shift from the linear resonance frequency for large drive amplitudes of vibration. This frequency shift adversely affects the performance of ring-based gyroscopes that

normally operate at the drive mode resonance frequency. Whilst the ring structure is characterised by the known softening behaviour, the support structure significantly influences the dynamic behaviour of the drive mode, and the drive mode frequency backbone curve of supported ring resonators is softening or hardening depending on the support. If the rotational symmetry is broken, the drive mode frequency backbone curve varies depending on the drive mode axis location relative to the supports. In contrast, if the rotational symmetry is maintained, the frequency backbone curve is invariant to the drive axis angle.

5. Ring and support geometrical non-linearity causes the sense mode response to be amplified compared to the equivalent linear resonator in which geometrical non-linearity is neglected. This amplification is stronger for larger quality factors. For large drive amplitudes, geometrical non-linearity causes the largest sense response amplitude to occur at frequencies different than the drive mode pseudo-resonance frequencies, so sensor sensitivity is not maximised when the drive mode is excited into pseudo-resonance.
   If the rotational symmetry is broken, sense response at the drive mode pseudo-resonance frequencies has in-phase and quadrature components. If the angular rate is detected based on linear standard models, sensing errors degrade the quality of the rate measurement, and the sense response in the absence of angular rate is non-zero.
   In contrast, if rotational symmetry is maintained, the sense response at the drive mode pseudo-resonance frequency is in-phase relative to the drive response, and the sense response amplitude is the same as the equivalent linear resonator. A linear standard model can be used to accurately detect the applied angular rate, and the sense response is negligible in the absence of angular rate.

6. The frequency backbone curve for the drive mode can be linearised (or, pseudo-linearised) by using a hardening support structure that neutralises the softening behaviour of the ring. Selected straight support designs were found to pseudo-linearise the drive mode

frequency backbone curve and to mitigate geometrical non-linearity effects compared to nominal supports. Finite Element non-linear analyses indicated that the drive mode frequency backbone curve obtained using the mathematical model is not very accurate, but demonstrated that the mathematical model can be used to efficiently guide the investigation of improved support designs.

## 7.4 Contributions

Main contributions of this work to the knowledge of supported ring-based MEMS CVGs operating at large amplitude vibrations are summarised in the following.

- This work investigated the dynamics of the drive and sense modes including ring and support geometrical non-linearity. The non-linear drive and sense responses have been investigated to give an insight on the geometrical non-linearity effects which affect ring resonators performance when the ring is driven into large amplitudes of vibration. It was demonstrated that linear standard models cannot be used when the drive amplitude is large, and ring and support geometrical non-linearity need to be considered to accurately model the supported ring resonator dynamics.

- This thesis investigated the numbers of supports that maintain the rotational symmetry of supported ring resonators when the ring is driven into large amplitudes of vibrations, taking account of ring and support geometrical non-linearity. Use of numbers of supports that maintain the rotational symmetry are suggested in order to mitigate geometrical non-linearity effects and improve sensor performance. For ring resonators operating in the $2\theta$ modes, 16 supports have shown to provide improved performance compared to 8 supports.

- This work demonstrated that the dynamic behaviour of the drive mode can be linearised using hardening support structures that mitigate the softening behaviour of the ring.

This results was demonstrated using Finite Element non-linear transient analyses.

- This work developed a mathematical model that can be used to guide during support designs investigation. The proposed model can be used to develop the frequency backbone curve for the drive mode at a computational cost that is orders of magnitude lower compared to Finite Element non-linear analyses. Comparison against Finite Element results indicated that the results obtained using the mathematical model are not very accurate; however, mathematical results show similar characteristics to the Finite Element method. Finite Element analyses can be performed for a detailed quantification of the drive mode frequency backbone curve.

## 7.5 Further work

Further work is suggested in the following areas:

- Comparison between mathematical results and Finite Element results indicated limitations with accuracy of the mathematical model. It was discussed that inaccuracies may relate to assumptions considered for the mathematical model development. It is suggested to improve the accuracy of the mathematical model by:
  - Eliminating the assumption that the radial and tangential directions are principal axes of stiffness for the support.
  - Including higher stiffness coefficients to characterise the non-linear springs used to model the support non-linear stiffness.
  - Investigating the influence of the support structure on the modes of vibration of the supported ring resonator.
- The proposed mathematical model was developed under the assumption that the ring is perfect. In reality, fabrication imperfections are inevitable and the ring structure is not

perfect for practical devices. It would be interesting to extend the developed non-linear mathematical model by including the presence of small point mass imperfections on the ring mid-line, and compare the effect of imperfection with non-linearity.

# Bibliography


[1] C. Acar and A. Shkel, *MEMS vibratory gyroscopes: structural approaches to improve robustness*. Springer Science & Business Media, 2008.

[2] V. Apostolyuk, *Coriolis Vibratory Gyroscopes: Theory and Design*. Springer, 2015.

[3] M. N. Armenise, C. Ciminelli, F. Dell'Olio, and V. M. Passaro, *Advances in gyroscope technologies*. Springer Science & Business Media, 2010.

[4] S. Ghasemzade and F. Jamshidi, "Applications of inertial navigation systems in medical engineering," *Journal of biomedical physics & engineering*, vol. 8, no. 3, p. 325, 2018.

[5] P. M. Polunin and S. W. Shaw, "Self-induced parametric amplification in ring resonating gyroscopes," *International Journal of Non-Linear Mechanics*, vol. 94, pp. 300–308, 2017.

[6] X. Wang, W. Wu, B. Luo, Z. Fang, Y. Li, and Q. Jiang, "Force to rebalance control of hrg and suppression of its errors on the basis of fpga," *Sensors*, vol. 11, no. 12, pp. 11761–11773, 2011.

[7] Z. Hu and B. Gallacher, "A mode-matched force-rebalance control for a mems vibratory gyroscope," *Sensors and Actuators A: Physical*, vol. 273, pp. 1–11, 2018.

[8] Y. S. Hong, J. H. Lee, and S. H. Kim, "A laterally driven symmetric micro-resonator for gyroscopic applications," *Journal of Micromechanics and Microengineering*, vol. 10, no. 3, p. 452, 2000.

[9] S. H. Nitzan, V. Zega, M. Li, C. H. Ahn, A. Corigliano, T. W. Kenny, and D. A. Horsley, "Self-induced parametric amplification arising from nonlinear elastic coupling in a micromechanical resonating disk gyroscope," *Scientific reports*, vol. 5, p. 9036, 2015.

[10] S. E. Alper and T. Akin, "Symmetrical and decoupled nickel microgyroscope on insulating substrate," *Sensors and Actuators A: Physical*, vol. 115, no. 2-3, pp. 336–350, 2004.

[11] F. Ayazi and K. Najafi, "A harpss polysilicon vibrating ring gyroscope," *Journal of microelectromechanical systems*, vol. 10, no. 2, pp. 169–179, 2001.

[12] A. M. Shkel, "Type i and type ii micromachined vibratory gyroscopes," in *2006 IEEE/ION Position, Location, And Navigation Symposium, Colorado, USA*, pp. 586–593, IEEE, 2006.

[13] B. Chouvion, *Vibration transmission and support loss in MEMS sensors*. PhD thesis, The University of Nottingham, 2010.

[14] A. A. Trusov, A. Schofield, and A. Shkel, "Vacuum packaged silicon mems gyroscope with q-factor above 0.5 million," *Additional Papers and Presentations*, vol. 2010, no. DPC, pp. 001335–001359, 2010.

[15] P. Aggarwal, *MEMS-based integrated navigation*. Artech House, 2010.

[16] S. W. Yoon, S. Lee, and K. Najafi, "Vibration sensitivity analysis of mems vibratory ring gyroscopes," *Sensors and Actuators A: Physical*, vol. 171, no. 2, pp. 163–177, 2011.

[17] A. M. El-Sayed, M. Ghoneima, and M. A. Mahmoud, "Modeling of nonlinearities in vibratory ring gyroscopes," in *2013 Second International Japan-Egypt Conference on Electronics, Communications and Computers (JEC-ECC)*, pp. 52–57, IEEE, 2013.

[18] S. Sensing, "High performance mems gyroscopes for space-future roadmap," *9th esa round table on micro and nano technologies, Lausanne, Switzerland*, 2013.

[19] O. research. http://siliconsensing.com/technology/mems-gyroscopes.

[20] S. McWilliam, J. Ong, and C. Fox, "On the statistics of natural frequency splitting for rings with random mass imperfections," *Journal of sound and vibration*, vol. 279, no. 1-2, pp. 453–470, 2005.

[21] C. Fox, "A simple theory for the analysis and correction of frequency splitting in slightly imperfect rings," *Journal of Sound and Vibration*, vol. 142, no. 2, pp. 227–243, 1990.

[22] W. Soedel and H. Saunders, "Vibration of plates and shells," 1983.

[23] P. Bisegna and G. Caruso, "Frequency split and vibration localization in imperfect rings," *Journal of Sound and Vibration*, vol. 306, no. 3-5, pp. 691–711, 2007.

[24] W. Weaver Jr, S. P. Timoshenko, and D. H. Young, *Vibration problems in engineering*. John Wiley & Sons, 1990.

[25] R. Eley, C. Fox, and S. McWilliam, "Anisotropy effects on the vibration of circular rings made from crystalline silicon," *Journal of Sound and Vibration*, vol. 228, no. 1, pp. 11–35, 1999.

[26] J.-H. Weng, W.-H. Chieng, and J.-M. Lai, "Structural design and analysis of micromachined ring-type vibrating sensor of both yaw rate and linear acceleration," *Sensors and Actuators A: Physical*, vol. 117, no. 2, pp. 230–240, 2005.

[27] S. Sieberer, *In-plane shock response of capacitive MEMS ring rate sensors*. PhD thesis, University of Nottingham, 2014.

[28] D. Xia, C. Yu, and L. Kong, "The development of micromachined gyroscope structure and circuitry technology," *Sensors*, vol. 14, no. 1, pp. 1394–1473, 2014.

[29] G. Sérandour, *Non-linear dynamics of vibratory rate sensors*. PhD thesis, The University of Nottingham, 2005.

[30] Y.-C. Fung and E. E. Sechler, "Thin-shell structures: Theory, experiment, and design.," tech. rep., DTIC Document, 1974.

[31] D. A. Evensen, *Non-linear flexural vibrations of thin circular rings*. PhD thesis, California Institute of Technology, 1964.

[32] D. A. Evensen, "Nonlinear flexural vibrations of thin-walled circular cylinders," 1967.

[33] D. A. Evensen, "Nonlinear flexural vibrations of thin circular rings," *Journal of Applied Mechanics*, vol. 33, no. 3, pp. 553–560, 1966.

[34] G. Sérandour, C. Fox, and S. McWilliam, "Modelling geometric non-linearity in a mems resonator," in *Proceeding of the IX International Conference on Recent Advances in Structural Dynamics/RASD06, Southampton, England*, 2006.

[35] A. H. Nayfeh and D. T. Mook, *Nonlinear oscillations*. John Wiley & Sons, 2008.

[36] A. H. Nayfeh, *Perturbation methods*. John Wiley & Sons, 2008.

[37] Y. A. Mitropolsky and N. Van Dao, *Applied asymptotic methods in nonlinear oscillations*, vol. 55. Springer Science & Business Media, 2013.

[38] *ANSYS Mechanical APDL Structural Analysis Guide, ANSYS Inc. 275 Technology Drive Canonsburg PA 15317*. November 2013.

[39] W. Kim and J. Chung, "Free non-linear vibration of a rotating thin ring with the in-plane and out-of-plane motions," *Journal of Sound and Vibration*, vol. 258, no. 1, pp. 167–178, 2002.

[40] K. E. Atkinson, *An introduction to numerical analysis*. John wiley & sons, 2008.

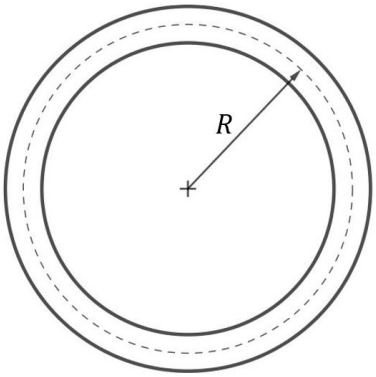
# Appendix A

# Geometrical data and FE model for the ring-based resonator

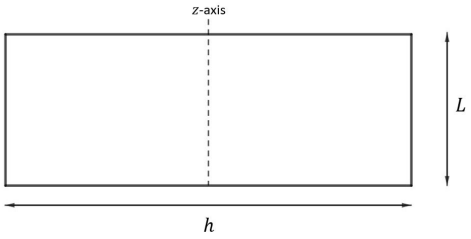
Chapters 4 and 5 showed numerical results for the drive and sense responses, respectively, obtained based on ring resonators having nominal supports. This Appendix provides with a description of the geometrical characteristics and material properties of ring and nominal support structures. The Finite Element (FE) model for the supported ring resonator developed using the commercial software package *ANSYS Parametric Design Language* (APDL) is described in this Appendix. The Finite Element model was used in Chapters 4, 5 and 6 to verify results obtained using the mathematical model. The procedure used to model the support inertia and non-linear stiffness in the mathematical model, introduced in Chapter 3, is described in detail. Mass and stiffness coefficients to model the nominal support are provided in this Appendix. Finally, the procedure used in Chapter 6 to determine angle $\phi_{PA}$ between the radial and tangential directions and the principal axes of stiffness of the support is described.

## A.1 Ring and nominal support dimensions

Figure A.1 illustrates a diagram for the ring structure; ring dimensions are provided in Table A.1.




(a) In-plane ring.



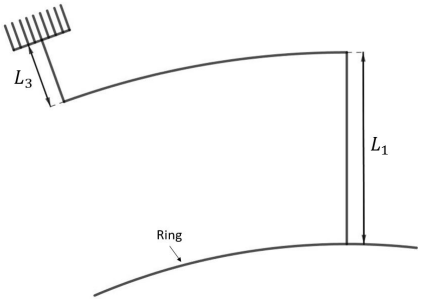

(b) Ring cross-section.

Figure A.1: Diagram for the ring structure.

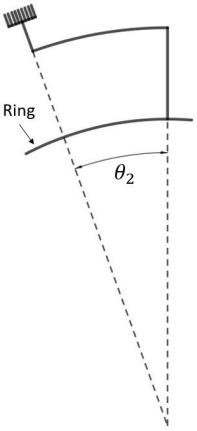
| **Ring geometrical data** | |
|---|---|
| $R$ | 3 mm |
| $L$ | 100 $\mu$m |
| $h$ | 125 $\mu$m |

Table A.1: Ring dimensions.

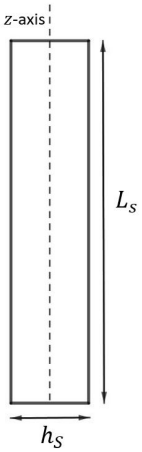
Figure A.2 shows a diagram for a single nominal arched support. Support dimensions can be found in Table A.2.




(a) In-plane support.




(b) Angle $\theta_2$.




(c) Support cross-section.

Figure A.2: Diagram for a single nominal arched support.

| Geometrical data for a nominal support | |
|---|---|
| $L_1$ | 0.8 mm |
| $L_3$ | 0.3 mm |
| $L_S$ | 100 $\mu$m |
| $h_S$ | 10 $\mu$m |
| $\theta_2$ | 20 deg. |

Table A.2: Geometrical data for an arched nominal support

Ring and support are made of isotropic silicon, having Young's modulus $E$ equal to 170 GPa and density $\rho$ of 2330 kg/m$^3$.

## A.2 Finite Element model for the supported ring resonator

Figures A.3 and A.4 show the FE models developed using the Finite Element software ANSYS to model ring resonators having 8 and 16 nominal supports, respectively. These models have been used to verify the results obtained using the mathematical model in Chapters 4, 5 and 6.

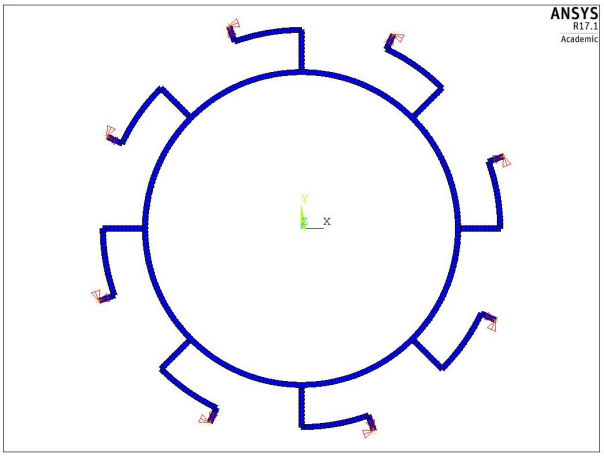



Figure A.3: FE model for the ring resonator having 8 nominal supports.

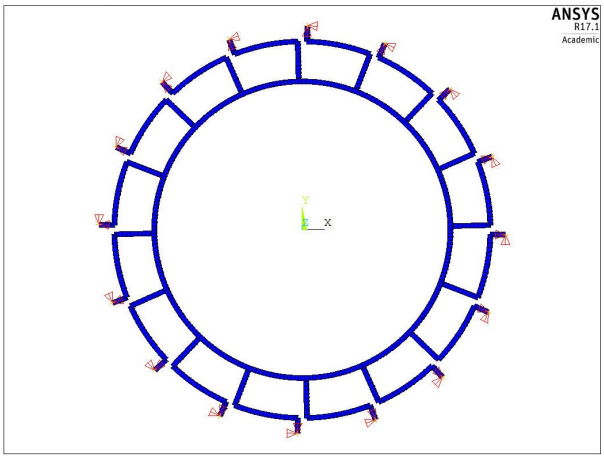



Figure A.4: FE model for the ring resonator having 16 nominal supports.

The ring-based resonator vibrates in the ring plane, so ring and support structures have been modelled using uni-axial beam elements BEAM3 that can translate in the ring plane and rotate around the $z$-axis orthogonal to the ring plane. Each support is attached to the ring by one end and fully clamped by the other end.

A mesh convergence analysis is conducted to determine the number of beam elements $N_R$ having identical length required to model the ring structure with sufficient accuracy. The length of each beam element is $\Delta l = \frac{2\pi R}{N_R}$. The proposed mesh convergence analysis is based on a FE modal analysis for the ring resonator having 16 supports, shown in Figure A.4. Figure A.5 shows the $2\theta$ modes natural frequency obtained by modelling the ring using numbers of beam elements $N_R$ indicated in abscissae.

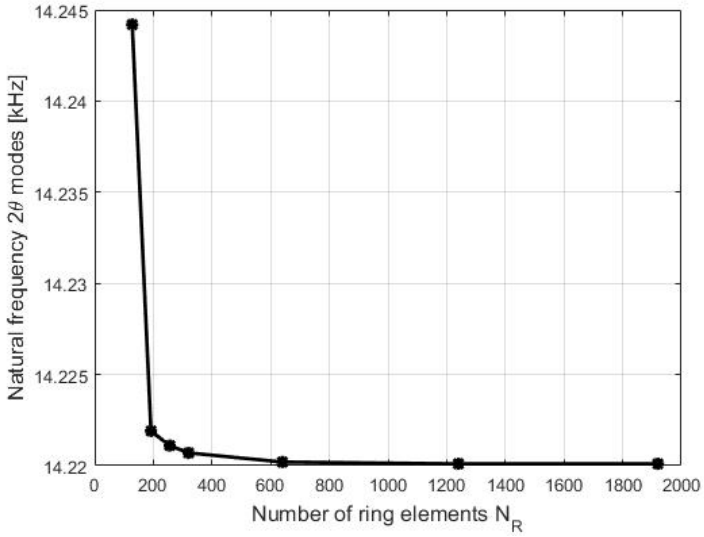



Figure A.5: Mesh convergence analysis based on a FE modal analysis.

Results indicate that for $N_R = 256$ the natural frequency of the $2\theta$ modes is larger than the convergence value by only 0.007%. Therefore, 256 beam elements have been used to model the ring structure, each beam element is long $\Delta l = \frac{2\pi R}{256}$. This same length has been used for support structure elements.

## A.3 Determination of the mass and stiffness coefficients to model the support

This Section describes the procedure used to determine the radial and tangential mass coefficients $m_r$ and $m_t$, the radial stiffness coefficients $k_{r_1}$, $k_{r_2}$ and $k_{r_3}$ and tangential stiffness coefficients $k_{r_1}$, $k_{r_2}$ and $k_{r_3}$ to model the inertia and stiffness of the support, as described in Chapter 3. The proposed procedure is based on a Finite Element analysis of a single support. The mathematical model was developed assuming that the $n\theta$ vibration of the ring is unaltered by the presence of the support. To take account of this assumption in the Finite Element model, the displacement of the ring-support attachment point is constrained to be

identical to that of the unsupported ring undergoing linear vibration at that angular position. For an unsupported ring, it can be shown that the in-plane rotation $\phi_z$ at circumferential coordinate $\theta$ can be expressed as [39]:

$$\phi_z(\theta) = \frac{1}{R}\frac{\partial u(\theta)}{\partial \theta} - \frac{v(\theta)}{R} \tag{A.1}$$

where $u(\theta)$ and $v(\theta)$ are the linear radial and tangential displacements (2.1) and (2.2). It can be shown that:

$$\frac{\partial u(\theta)}{\partial \theta} = n^2 v(\theta) \tag{A.2}$$

so the in-plane rotation $\phi_z(\theta)$ can be expressed as a function of the tangential displacement $v(\theta)$ at circumferential coordinate $\theta$ as:

$$\phi_z\left(\theta\right) = \frac{\left(n^2-1\right)v\left(\theta\right)}{R} \tag{A.3}$$

This relation is used in the Finite Element model to constrain the rotation around the $z$-axis of the support end attached to the ring, while the other end of the support is fully constrained.

The radial and tangential linear, quadratic and cubic stiffness coefficients to model the support stiffness are obtained by applying radial and tangential forces at the ring-support attachment point, respectively, and performing large-deflection FE static analyses to calculate the radial and tangential displacements caused by the applied forces. Under the assumption that the radial and tangential directions are principal axes of stiffness for the support, the tangential displacement caused by forces applied in the radial direction is constrained to be zero; similarly, the radial displacement following the application of tangential forces is set to zero. This is repeated by varying the magnitude of applied forces to calculate the non-linear force-deflection curves in the radial and tangential directions. The obtained force-displacement curves obtained using a Finite Element analysis are interpolated using cubic

fitting functions as shown in Figures A.6 and A.7 for the radial and tangential directions, respectively.

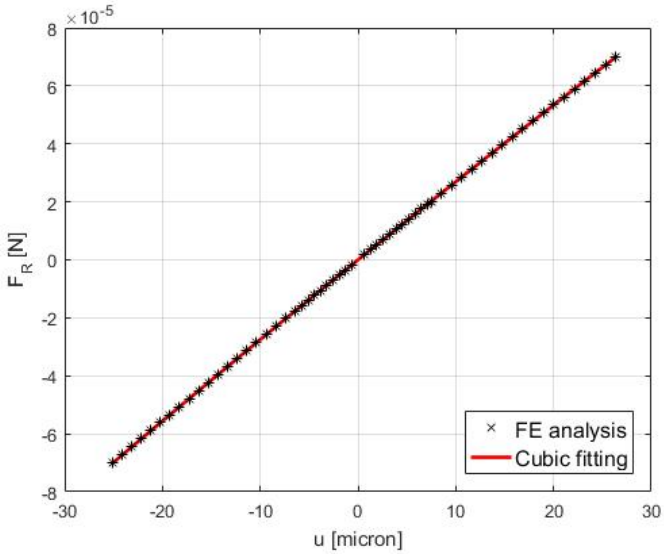



Figure A.6: Force-displacement relation in the radial direction.

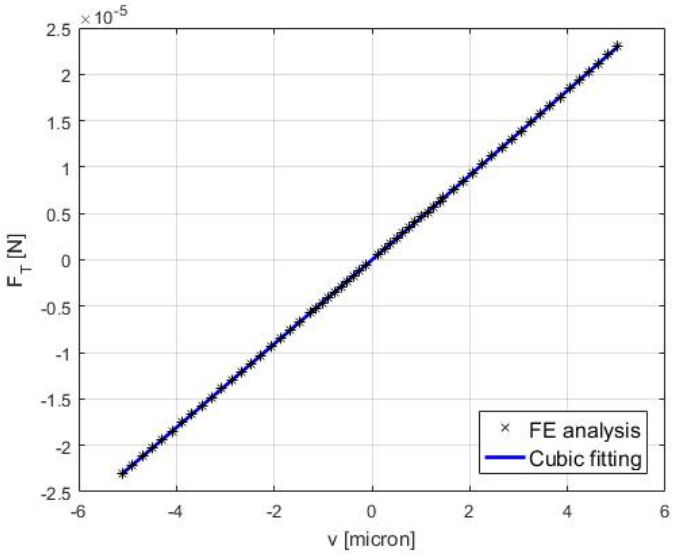



Figure A.7: Force-displacement relation in the tangential direction.

The linear, quadratic and cubic coefficients of the cubic fitting functions provide with the

linear, quadratic and cubic stiffness coefficients to model the support stiffness using cubic non-linear springs.

The radial and tangential mass coefficients to model the support inertia are obtained by applying harmonic radial and tangential forces at the ring-support attachment point. Similar to that described for the stiffness coefficients determination, tangential displacement caused by harmonic forces in the radial direction is set to zero, and the radial displacement caused by tangential forces is set to zero. The frequency $\omega$ of the radial and tangential harmonic forces matches the resonance frequency of the pair of $n\theta$ modes used in operation, in this example $n = 2$. FE harmonic response analyses are performed to obtain amplitudes and phases of the radial and tangential responses in steady-state. Mass coefficients $m_r$ and $m_t$ are calculated based on linear undamped equations of motion for radial and tangential displacements below:

$$m_r \ddot{u} + k_{r_1} u = F_r \cos \omega \tag{A.4}$$

$$m_t \ddot{v} + k_{t_1} v = F_t \cos \omega \tag{A.5}$$

where $u$ and $v$ are the radial and tangential displacements, respectively, and $F_r$ and $F_t$ the magnitudes of the applied radial and tangential harmonic forces.

Table A.3 provides the radial and tangential mass and stiffness coefficients obtained for the nominal support:

| Mass coefficients | | |
|---|---|---|
| $m_R$ | $3.07 \times 10^{-9}$ | kg |
| $m_T$ | $7.11 \times 10^{-10}$ | kg |
| **Stiffness coefficients** | | |
| $k_{r_1}$ | 2.72 | N/m |
| $k_{r_2}$ | $-2.76 \times 10^3$ | N/m$^2$ |
| $k_{r_3}$ | $4.82 \times 10^6$ | N/m$^3$ |
| $k_{t_1}$ | 4.54 | N/m |
| $k_{t_2}$ | $5.83 \times 10^3$ | N/m$^2$ |
| $k_{t_3}$ | $9.68 \times 10^6$ | N/m$^3$ |

Table A.3: Mass and stiffness coefficients to model a nominal support.

Mass and stiffness coefficients in Table A.3 are used in Chapters 4 and 5, respectively, to investigate the drive and sense responses associated with ring resonators having nominal supports using the developed mathematical model for the ring resonator.

## A.4 Principal axes of stiffness for the support

This Section describes the procedure used in Chapter 6 to determine angle $\phi_{PA}$ describing the orientation of the principal axes of stiffness for the straight supports, relative to the radial and tangential directions. Angle $\phi_{PA}$ is obtained by calculating the full support stiffness matrix $\mathbf{K_S^L}$ and using equation (2.19) given in Chapter 2.

Full stiffness matrix $\mathbf{K_S^L}$ is calculated using a Finite Element analysis of a single support. Radial and tangential forces $F_R$ and $F_T$ and momentum $M_Z$ around the $z$-axis are applied at the support end attached to the ring, and FE static analyses are performed to calculate the radial and tangential displacements $u(\theta)$, $v(\theta)$ and rotation $\phi_z(\theta)$ caused by the applied loads. The ring-support attachment point is free to move in both the radial and tangential

directions when the forces are applied, whilst the rotation around $z$-axis is assumed to be the same as the unsupported ring at that location and constrained to the tangential displacement as in equation (A.3). The displacements and rotation calculated using the FE static analysis are used in the equation below to calculate the full $3 \times 3$ stiffness matrix $\mathbf{K_S^{3x3}}$:

$$\mathbf{F} = \mathbf{K_S^{3x3}}\mathbf{u} \tag{A.6}$$

where $\mathbf{F} = [F_R \quad F_T \quad M_Z]^{\mathrm{T}}$ and $\mathbf{u} = \left[u(\theta) \quad v(\theta) \quad \frac{(n^2-1)v(\theta)}{R}\right]^{\mathrm{T}}$. No torsional springs are considered in the proposed support mathematical model, so the third row and the third column of $\mathbf{K_S^{3x3}}$ are neglected. The resulting matrix is the $2 \times 2$ stiffness matrix $\mathbf{K_S^L}$ that can be used in the eigenvalue problem (2.19) to determine angle $\phi_{PA}$.

# Appendix B

# Potential energy for a non-linear support structure

Section 3.3 in Chapter 3 developed analytical expressions for the kinetic and potential energies for $p$ non-linear supports. The potential energy associated with $p$ cubic non-linear springs in the radial and tangential directions was given by equation (3.22). In what follows, coefficients $V_{Cm}$, $V_{Sm}$ $(m = 1, ..., 6)$ respectively multiplied to $\cos mn\left(j\frac{2\pi}{p} - \alpha\right)$ and $\sin mn\left(j\frac{2\pi}{p} - \alpha\right)$ in equation (3.22) are provided.

$$\begin{aligned} V_{C1} = \left(Q_1^2 + Q_2^2\right) \Bigg\{ & -Q_1 \left(k_{r_1} + \frac{k_{t_1}}{4n^2}\right)\gamma + Q_1 \left[1 + 4\gamma^2 \left(Q_1^2 + Q_2^2\right)\right] \frac{k_{r_2}}{4} \\ & + Q_2 \left[2 + \gamma^2 \left(Q_1^2 + Q_2^2\right)\right] \frac{k_{t_2}}{8n^3} - Q_1 \left(Q_1^2 + Q_2^2\right)\gamma \left(\frac{3k_{r_3}}{4} + \frac{k_{t_3}}{8n^4}\right) \Bigg\} \end{aligned} \tag{B.1}$$

$$\begin{aligned} V_{S1} = \left(Q_1^2 + Q_2^2\right) \Bigg\{ & -Q_2 \left(k_{r_1} + \frac{k_{t_1}}{4n^2}\right)\gamma + Q_2 \left[1 + 4\gamma^2 \left(Q_1^2 + Q_2^2\right)\right] \frac{k_{r_2}}{4} \\ & - Q_1 \left[2 + \gamma^2 \left(Q_1^2 + Q_2^2\right)\right] \frac{k_{t_2}}{8n^3} - Q_2 \left(Q_1^2 + Q_2^2\right)\gamma \left(\frac{3k_{r_3}}{4} + \frac{k_{t_3}}{8n^4}\right) \Bigg\} \end{aligned} \tag{B.2}$$

$$\begin{aligned} V_{C2} = & \left(Q_1^2 - Q_2^2\right) \left(\frac{k_{r_1}}{4} - \frac{k_{t_1}}{4n^2}\right) - \left(Q_1^4 - Q_2^4\right) \Bigg\{ \frac{k_{r_2}}{2}\gamma - \frac{k_{r_3}}{8} \left[1 + 6\gamma^2 \left(Q_1^2 + Q_2^2\right)\right] \\ & + \frac{k_{t_3}}{64n^4} \left[8 + 3\gamma^2 \left(Q_1^2 + Q_2^2\right)\right] \Bigg\} - Q_1 Q_2 \left(Q_1^2 + Q_2^2\right) \frac{k_{t_2}}{2n^3}\gamma \end{aligned} \tag{B.3}$$

$$V_{S2} = Q_1 Q_2 \left( \frac{k_{r_1}}{2} - \frac{k_{t_1}}{2n^2} \right) - Q_1 Q_2 \left( Q_1^2 + Q_2^2 \right) \left\{ k_{r_2}\gamma - \frac{k_{r_3}}{4} \left[ 1 + 6\gamma^2 \left( Q_1^2 + Q_2^2 \right) \right] \right.$$
$$\left. + \frac{k_{t_3}}{32n^4} \left[ 8 + 3\gamma^2 \left( Q_1^2 + Q_2^2 \right) \right] \right\} + \left( Q_1^4 - Q_2^4 \right) \frac{k_{t_2}}{4n^3}\gamma \tag{B.4}$$

$$V_{C3} = Q_1 \left( Q_1^2 - 3Q_2^2 \right) \left[ \frac{k_{r_2}}{12} + \frac{k_{t_1}}{4n^2}\gamma - \left( Q_1^2 + Q_2^2 \right) \gamma \left( \frac{k_{r_3}}{4} - \frac{3k_{t_3}}{16n^4} \right) \right]$$
$$+ Q_2 \left( Q_2^2 - 3Q_1^2 \right) \frac{k_{t_2}}{48n^3} \left[ 4 - 3\gamma^2 \left( Q_1^2 + Q_2^2 \right) \right] \tag{B.5}$$

$$V_{S3} = Q_2 \left( 3Q_1^2 - Q_2^2 \right) \left[ \frac{k_{r_2}}{12} + \frac{k_{t_1}}{4n^2}\gamma - \left( Q_1^2 + Q_2^2 \right) \gamma \left( \frac{k_{r_3}}{4} - \frac{3k_{t_3}}{16n^4} \right) \right]$$
$$+ Q_1 \left( Q_1^2 - 3Q_2^2 \right) \frac{k_{t_2}}{48n^3} \left[ 4 - 3\gamma^2 \left( Q_1^2 + Q_2^2 \right) \right] \tag{B.6}$$

$$V_{C4} = Q_1 Q_2 \left( Q_1^2 - Q_2^2 \right) \frac{k_{t_2}}{2n^3}\gamma +$$
$$+ \left( Q_1^4 + Q_2^4 - 6Q_1^2 Q_2^2 \right) \left\{ -\frac{k_{t_1}}{16n^2}\gamma^2 + \frac{k_{r_3}}{32} + \frac{k_{t_3}}{32n^4} \left[ 1 - 3\gamma^2 \left( Q_1^2 + Q_2^2 \right) \right] \right\} \tag{B.7}$$

$$V_{S4} = - \left( Q_1^4 + Q_2^4 - 6Q_1^2 Q_2^2 \right) \frac{k_{t_2}}{8n^3}\gamma +$$
$$+ Q_1 Q_2 \left( Q_1^2 - Q_2^2 \right) \left\{ -\frac{k_{t_1}}{4n^2}\gamma^2 + \frac{k_{r_3}}{8} + \frac{k_{t_3}}{8n^4} \left[ 1 - 3\gamma^2 \left( Q_1^2 + Q_2^2 \right) \right] \right\} \tag{B.8}$$

$$V_{C5} = -Q_2 \left( Q_2^4 + 5Q_1^4 - 10Q_1^2 Q_2^2 \right) \frac{k_{t_2}}{16n^3}\gamma^2 - Q_1 \left( Q_1^4 + 5Q_2^4 - 10Q_1^2 Q_2^2 \right) \frac{k_{t_3}}{16n^4}\gamma \tag{B.9}$$

$$V_{S5} = Q_1 \left( Q_1^4 + 5Q_2^4 - 10Q_1^2 Q_2^2 \right) \frac{k_{t_2}}{16n^3}\gamma^2 - Q_2 \left( 5Q_1^4 + Q_2^4 - 10Q_1^2 Q_2^2 \right) \frac{k_{t_3}}{16n^4}\gamma \tag{B.10}$$

$$V_{C6} = \left( Q_1^6 - Q_2^6 + 15Q_1^2 Q_2^4 - 15Q_1^4 Q_2^2 \right) \frac{3k_{t_3}}{64n^4}\gamma^2 \tag{B.11}$$

$$V_{S6} = \left( 3Q_1^5 Q_2 + 3Q_1 Q_2^5 - 10Q_1^3 Q_2^3 \right) \frac{3k_{t_3}}{32n^4}\gamma^2 \tag{B.12}$$

These coefficients $V_{Cm}$, $V_{Sm}$ $(m = 1, ..., 6)$ are used in equation (3.22) to develop an analytical expression for the potential energy of $p$ non-linear supports.

# Appendix C

# Equations of motion for supported ring resonators operating at large amplitudes

Chapter 3 developed the equations of motion governing the dynamics of the drive and sense $n\theta$ modes when the ring is excited into large amplitude vibration, for ring resonator having $p$ identical supports uniformly spaced around the ring circumference. Section 3.4 indicated that drive and sense equations of motion can be obtained using Lagrange's equation (2.26), where the non-linear kinetic and potential energies of the ring $T_{ring}$ and $V_{ring}$ are given by (3.4) and (3.5), respectively, and the non-linear kinetic and potential energies of the support $T_S$ and $V_S$ are given by (3.9) and (3.22), respectively.

This Appendix shows the obtained equations of motion for drive and sense mode. Drive and sense equations are given by equations (C.1) and (C.2), respectively, in Section C.1. Equations are based on the excitation of the drive mode by harmonic external force having magnitude $F_D$ and frequency $\Omega$, and are expressed in terms of generalised coordinates $Q_1$

and $Q_2$. The modal mass and stiffness for the unsupported ring (i.e. $M_{ring}$ and $K_{ring}$) and for the supported ring resonator (i.e. $M_{res}$ and $K_{res}$) were given in Chapter 2 in equations (2.32), (2.33), (2.30) and (2.31), respectively.

As introduced in Section 3.4 in Chapter 3, for practical CVGs operation, the amplitude of the sense response is commonly much smaller than the amplitude of the drive response. Under these circumstances, non-linear terms in $Q_2$, $\dot{Q}_2$, $\ddot{Q}_2$ (and combinations) in equations (C.1) and (C.2) are considered to be small and neglected. Neglecting non-linear terms in $Q_2$, equations (C.1) and (C.2) reduce to equations (C.27) and (C.28), respectively, given in Section C.2. In Section 3.4, equations (C.27) and (C.28) were divided by $M_{res}$ and given in equations (3.25) and (3.26), respectively, expressed in terms of coefficients $\gamma_1, ..., \gamma_6$ given by (3.27)-(3.32). In Sections 3.4.1 and 3.4.2, equations (C.27) and (C.28) were specified for the case $n = 2$ and $p = 8$, and $n = 2$ and $p = 16$, respectively.

## C.1 Drive and sense mode governing equations

The governing equations for the drive and sense modes are given in (C.1) and (C.2), respectively.

$$
\begin{aligned}
&\ddot{Q}_1\left[M_{res}+\left(Q_1^2+Q_2^2\right)\left(\frac{M_{ring}}{(n^2+1)}\gamma^2+p\frac{m_t}{2n^2}\gamma^2\right)\right]+\\
&+\dot{Q}_1\left[M_{res}\frac{\omega_0}{Q}+\left(\dot{Q}_1Q_1+\dot{Q}_2Q_2\right)\left(\frac{2M_{ring}}{(n^2+1)}\gamma^2+2p\frac{m_t}{2n^2}\gamma^2\right)\right]+\\
&+Q_1\left\{K_{res}+\left(\dot{Q}_1^2+\dot{Q}_2^2\right)\left[\frac{\left(8n^2-1\right)M_{ring}}{(n^2+1)}\gamma^2+p\left(4m_r\gamma^2-\frac{m_t}{2n^2}\gamma^2\right)\right]+\right.\\
&+\left(\ddot{Q}_1Q_1+\ddot{Q}_2Q_2\right)\left(\frac{\left(8n^2\right)M_{ring}}{(n^2+1)}\gamma^2+p4m_r\gamma^2\right)+\left(Q_1^2+Q_2^2\right)^2p\left(\frac{9k_{t_3}}{16n^4}\gamma^2+\frac{9k_{r_3}}{2}\gamma^2\right)+\\
&\left.+\left(Q_1^2+Q_2^2\right)\left[\frac{4K_{ring}}{(n^4-2n^2+1)}\gamma^2+p\left(2k_{r_1}\gamma^2-2k_{r_2}\gamma+\frac{3k_{r_3}}{8}+\frac{k_{t_1}}{4n^2}\gamma^2+\frac{3k_{t_3}}{8n^4}\right)\right]\right\}+\\
&+\sum_{j=0}^{p-1}\left[C_1^D\cos n\left(j\frac{2\pi}{p}-\alpha\right)+S_1^D\sin n\left(j\frac{2\pi}{p}-\alpha\right)+C_2^D\cos 2n\left(j\frac{2\pi}{p}-\alpha\right)+\right.\\
&+S_2^D\sin 2n\left(j\frac{2\pi}{p}-\alpha\right)+C_3^D\cos 3n\left(j\frac{2\pi}{p}-\alpha\right)+S_3^D\sin 3n\left(j\frac{2\pi}{p}-\alpha\right)+\\
&+C_4^D\cos 4n\left(j\frac{2\pi}{p}-\alpha\right)+S_4^D\sin 4n\left(j\frac{2\pi}{p}-\alpha\right)+C_5^D\cos 5n\left(j\frac{2\pi}{p}-\alpha\right)+\\
&\left.+S_5^D\sin 5n\left(j\frac{2\pi}{p}-\alpha\right)+C_6^D\cos 6n\left(j\frac{2\pi}{p}-\alpha\right)+S_6^D\sin 6n\left(j\frac{2\pi}{p}-\alpha\right)\right]=\\
&=F_D\cos\Omega t+\frac{4nM_{ring}}{(n^2+1)}\Omega_z\dot{Q}_2
\end{aligned}
\tag{C.1}
$$

$$
\begin{aligned}
&\ddot{Q}_2\left[M_{res}+\left(Q_1^2+Q_2^2\right)\left(\frac{M_{ring}}{(n^2+1)}\gamma^2+p\frac{m_t}{2n^2}\gamma^2\right)\right]+\\
&+\dot{Q}_2\left[M_{res}\frac{\omega_0}{Q}+\left(\dot{Q}_1Q_1+\dot{Q}_2Q_2\right)\left(\frac{2M_{ring}}{(n^2+1)}\gamma^2+2p\frac{m_t}{2n^2}\gamma^2\right)\right]+\\
&+Q_2\left\{K_{res}+\left(\dot{Q}_1^2+\dot{Q}_2^2\right)\left[\frac{\left(8n^2-1\right)M_{ring}}{(n^2+1)}\gamma^2+p\left(4m_r\gamma^2-\frac{m_t}{2n^2}\gamma^2\right)\right]+\right.\\
&+\left(\ddot{Q}_1Q_1+\ddot{Q}_2Q_2\right)\left(\frac{\left(8n^2\right)M_{ring}}{(n^2+1)}\gamma^2+p4m_r\gamma^2\right)+\left(Q_1^2+Q_2^2\right)^2p\left(\frac{9k_{t_3}}{16n^4}\gamma^2+\frac{9k_{r_3}}{2}\gamma^2\right)+\\
&\left.+\left(Q_1^2+Q_2^2\right)\left[\frac{4K_{ring}}{(n^4-2n^2+1)}\gamma^2+p\left(2k_{r_1}\gamma^2-2k_{r_2}\gamma+\frac{3k_{r_3}}{8}+\frac{k_{t_1}}{4n^2}\gamma^2+\frac{3k_{t_3}}{8n^4}\right)\right]\right\}+\\
&+\sum_{j=0}^{p-1}\left[C_1^S\cos n\left(j\frac{2\pi}{p}-\alpha\right)+S_1^S\sin n\left(j\frac{2\pi}{p}-\alpha\right)+C_2^S\cos 2n\left(j\frac{2\pi}{p}-\alpha\right)+\right.\\
&+S_2^S\sin 2n\left(j\frac{2\pi}{p}-\alpha\right)+C_3^S\cos 3n\left(j\frac{2\pi}{p}-\alpha\right)+S_3^S\sin 3n\left(j\frac{2\pi}{p}-\alpha\right)+\\
&+C_4^S\cos 4n\left(j\frac{2\pi}{p}-\alpha\right)+S_4^S\sin 4n\left(j\frac{2\pi}{p}-\alpha\right)+C_5^S\cos 5n\left(j\frac{2\pi}{p}-\alpha\right)+\\
&\left.+S_5^S\sin 5n\left(j\frac{2\pi}{p}-\alpha\right)+C_6^S\cos 6n\left(j\frac{2\pi}{p}-\alpha\right)+S_6^S\sin 6n\left(j\frac{2\pi}{p}-\alpha\right)\right]=\\
&=-\frac{4nM_{ring}}{(n^2+1)}\Omega_z\dot{Q}_1
\end{aligned}
\tag{C.2}
$$

Coefficients $C_m^D$, $S_m^D$ $(m=1,...,6)$ for the drive equation (C.1) are:

$$
\begin{aligned}
C_1^D=&\ddot{Q}_1\left[Q_1\left(-4m_r\gamma-\frac{m_t}{n^2}\gamma\right)\right]+\dot{Q}_1\left[\dot{Q}_1\left(-2m_r\gamma-\frac{m_t}{2n^2}\gamma\right)\right]+\\
&+Q_1\left[Q_1\left(-\frac{3k_{t_1}}{4n^2}\gamma-3k_{r_1}\gamma+\frac{3k_{r_2}}{4}\right)+Q_2\left(\frac{k_{t_2}}{4n^3}\right)+Q_1^3\left(-\frac{5k_{t_3}}{8n^4}\gamma+5k_{r_2}\gamma^2-\frac{15k_{r_3}}{4}\gamma\right)+\right.\\
&\left.+Q_2^3\left(\frac{k_{t_2}}{2n^3}\gamma^2\right)\right]+\ddot{Q}_2\left[Q_2\left(-2m_r\gamma\right)\right]+\dot{Q}_2\left[\dot{Q}_2\left(-2m_r\gamma+\frac{m_t}{2n^2}\gamma\right)\right]+Q_2\left[Q_1\left(\frac{k_{t_2}}{4n^3}\right)+\right.\\
&\left.+Q_2\left(-\frac{k_{t_1}}{4n^2}\gamma-k_{r_1}\gamma+\frac{k_{r_2}}{4}\right)+Q_1^3\left(\frac{k_{t_2}}{2n^3}\gamma^2\right)+Q_2^3\left(-\frac{k_{t_3}}{8n^4}\gamma+k_{r_2}\gamma^2-\frac{3k_{r_3}}{4}\gamma\right)\right]+\\
&+Q_1^2Q_2^2\left(-\frac{3k_{t_3}}{4n^4}\gamma+6k_{r_2}\gamma^2-\frac{9}{2}k_{r_3}\gamma\right)
\end{aligned}
\tag{C.3}
$$

$$
\begin{aligned}
S_1^D =&\ddot{Q}_1\left[Q_2\left(-\frac{m_t}{n^2}\gamma\right)\right]+\dot{Q}_1\left[\dot{Q}_2\left(-\frac{m_t}{2n^2}\gamma\right)\right]+Q_1\left[Q_1\left(-\frac{3k_{t_2}}{4n^3}\right)+\right.\\
&+Q_2\left(-\frac{k_{t_1}}{4n^2}\gamma-k_{r_1}\gamma+\frac{k_{r_2}}{4}\right)+Q_1^3\left(-\frac{5k_{t_2}}{8n^3}\gamma^2\right)+Q_2^3\left(-\frac{k_{t_3}}{2n^4}\gamma+4k_{r_2}\gamma^2-3k_{r_3}\gamma\right)\Big]+\\
&+\ddot{Q}_2\left[Q_1\left(-2m_r\gamma\right)\right]+\dot{Q}_2\left[\dot{Q}_1\left(-\frac{m_t}{2n^2}\gamma\right)\right]+Q_2\left[Q_1\left(-\frac{k_{t_1}}{4n^2}\gamma-k_{r_1}\gamma+\frac{k_{r_2}}{4}\right)+\right.\\
&+Q_2\left(-\frac{k_{t_2}}{4n^3}\right)+Q_1^3\left(-\frac{k_{t_3}}{2n^4}\gamma+4k_{r_2}\gamma^2-3k_{r_3}\gamma\right)+Q_2^3\left(-\frac{k_{t_2}}{8n^3}\gamma^2\right)\Big]+\\
&+Q_1^2Q_2^2\left(-\frac{3k_{t_2}}{4n^3}\gamma^2\right)
\end{aligned}
\tag{C.4}
$$

$$
\begin{aligned}
C_2^D =&\ddot{Q}_1\left(\frac{m_r}{2}-\frac{m_t}{2n^2}\right)+Q_1\left[\left(-\frac{k_{t_1}}{2n^2}+\frac{k_{r_1}}{2}\right)+Q_1^2\left(-\frac{k_{t_3}}{2n^4}-2k_{r_2}\gamma+\frac{k_{r_3}}{2}\right)+\right.\\
&+Q_1^4\left(-\frac{9k_{t_3}}{32n^4}\gamma^2+\frac{9k_{r_3}}{2}\gamma^2\right)+Q_2^4\left(\frac{3k_{t_3}}{32n^4}\gamma^2-\frac{3k_{r_3}}{2}\gamma^2\right)+Q_1^2Q_2^2\left(-\frac{3k_{t_3}}{16n^4}\gamma^2+3k_{r_3}\gamma^2\right)\Big]+\\
&+Q_2\left[Q_1^2\left(-\frac{3k_{t_2}}{2n^3}\gamma\right)+Q_2^2\left(-\frac{k_{t_2}}{2n^3}\gamma\right)\right]
\end{aligned}
\tag{C.5}
$$

$$
\begin{aligned}
S_2^D =&\ddot{Q}_2\left(\frac{m_r}{2}-\frac{m_t}{2n^2}\right)+Q_1\left[Q_1^2\left(\frac{k_{t_2}}{n^3}\gamma\right)\right]+Q_2\left[\left(-\frac{k_{t_1}}{2n^2}+\frac{k_{r_1}}{2}\right)+\right.\\
&+Q_1^2\left(-\frac{3k_{t_3}}{4n^4}-3k_{r_2}\gamma+\frac{3k_{r_3}}{4}\right)+Q_2^2\left(-\frac{k_{t_3}}{4n^4}-k_{r_2}\gamma+\frac{k_{r_3}}{4}\right)+Q_1^4\left(-\frac{15k_{t_3}}{32n^4}\gamma^2+\frac{15k_{r_3}}{2}\gamma^2\right)+\\
&+Q_2^4\left(-\frac{3k_{t_3}}{32n^4}\gamma^2+\frac{3k_{r_3}}{2}\gamma^2\right)+Q_1^2Q_2^2\left(-\frac{9k_{t_3}}{16n^4}\gamma^2+9k_{r_3}\gamma^2\right)\Big]
\end{aligned}
\tag{C.6}
$$

$$
\begin{aligned}
C_3^D =&\ddot{Q}_1\left[Q_1\left(\frac{m_t}{n^2}\gamma\right)\right]+\dot{Q}_1\left[\dot{Q}_1\left(\frac{m_t}{2n^2}\gamma\right)\right]+Q_1\left[Q_1\left(\frac{3k_{t_1}}{4n^2}\gamma+\frac{k_{r_2}}{4}\right)+Q_2\left(-\frac{k_{t_2}}{4n^3}\right)+\right.\\
&\left.+Q_1^3\left(\frac{15k_{t_3}}{16n^4}\gamma-\frac{5k_{r_3}}{4}\gamma\right)+Q_2^3\left(\frac{k_{t_2}}{4n^3}\gamma^2\right)\right]+\ddot{Q}_2\left[Q_2\left(-\frac{m_t}{n^2}\gamma\right)\right]+\dot{Q}_2\left[\dot{Q}_2\left(-\frac{m_t}{2n^2}\gamma\right)\right]+\\
&+Q_2\left[Q_1\left(-\frac{k_{t_2}}{4n^3}\right)+Q_2\left(-\frac{3k_{t_1}}{4n^2}\gamma-\frac{k_{r_2}}{4}\right)+Q_1^3\left(\frac{3k_{t_2}}{4n^3}\gamma^2\right)+Q_2^3\left(-\frac{9k_{t_3}}{16n^4}\gamma+\frac{3k_{r_3}}{4}\gamma\right)\right]+\\
&+Q_1^2Q_2^2\left(-\frac{9k_{t_3}}{8n^4}\gamma+\frac{3k_{r_3}}{2}\gamma\right)
\end{aligned}
\tag{C.7}
$$

$$
\begin{aligned}
S_3^D =&\ddot{Q}_1\left[Q_2\left(\frac{m_t}{n^2}\gamma\right)\right]+\dot{Q}_1\left[\dot{Q}_2\left(\frac{m_t}{2n^2}\gamma\right)\right]+Q_1\left[Q_1\left(\frac{k_{t_2}}{4n^3}\right)+Q_2\left(\frac{3k_{t_1}}{4n^2}\gamma+\frac{k_{r_2}}{4}\right)+\right.\\
&\left.+Q_1^3\left(-\frac{5k_{t_2}}{16n^3}\gamma^2\right)+Q_2^3\left(\frac{3k_{t_3}}{4n^4}\gamma-k_{r_3}\gamma\right)\right]+\ddot{Q}_2\left[Q_1\left(\frac{m_t}{n^2}\gamma\right)\right]+\dot{Q}_2\left[\dot{Q}_1\left(\frac{m_t}{2n^2}\gamma\right)\right]+\\
&+Q_2\left[Q_1\left(\frac{3k_{t_1}}{4n^2}\gamma+\frac{k_{r_2}}{4}\right)+Q_2\left(-\frac{k_{t_2}}{4n^3}\right)+Q_1^3\left(\frac{9k_{t_3}}{4n^4}\gamma-3k_{r_3}\gamma\right)+Q_2^3\left(\frac{3k_{t_2}}{16n^3}\gamma^2\right)\right]+\\
&+Q_1^2Q_2^2\left(\frac{3k_{t_2}}{8n^3}\gamma^2\right)
\end{aligned}
\tag{C.8}
$$

$$
\begin{aligned}
C_4^D =&\ddot{Q}_1\left[Q_1^2\left(-\frac{m_t}{2n^2}\gamma^2\right)+Q_2^2\left(\frac{m_t}{2n^2}\gamma^2\right)\right]+Q_1\left[\dot{Q}_1^2\left(-\frac{m_t}{2n^2}\gamma^2\right)+\dot{Q}_2^2\left(\frac{m_t}{2n^2}\gamma^2\right)+\right.\\
&+Q_1^2\left(-\frac{k_{t_1}}{4n^2}\gamma^2+\frac{k_{t_3}}{8n^4}+\frac{k_{r_3}}{8}\right)+Q_2^2\left(\frac{3k_{t_1}}{4n^2}\gamma^2-\frac{3k_{t_3}}{8n^4}-\frac{3k_{r_3}}{8}\right)+Q_1^4\left(-\frac{9k_{t_3}}{16n^4}\gamma^2\right)+\\
&\left.+Q_2^4\left(\frac{15k_{t_3}}{16n^4}\gamma^2\right)+Q_1^2Q_2^2\left(\frac{15k_{t_3}}{8n^4}\gamma^2\right)\right]+\ddot{Q}_2\left[Q_1Q_2\left(\frac{m_t}{n^2}\gamma^2\right)\right]+\\
&+Q_2\left[\dot{Q}_1\dot{Q}_2\left(\frac{m_t}{n^2}\gamma^2\right)+Q_1^2\left(\frac{3k_{t_2}}{2n^3}\gamma\right)+Q_2^2\left(-\frac{k_{t_2}}{2n^3}\gamma\right)\right]
\end{aligned}
\tag{C.9}
$$

$$
\begin{aligned}
S_4^D =&\ddot{Q}_1\left[Q_1Q_2\left(-\frac{m_t}{n^2}\gamma^2\right)\right]+Q_1\left[\dot{Q}_1\dot{Q}_2\left(-\frac{m_t}{n^2}\gamma^2\right)+Q_1^2\left(-\frac{k_{t_2}}{2n^3}\gamma\right)+Q_2^2\left(\frac{3k_{t_2}}{2n^3}\gamma\right)\right]+\\
&+\ddot{Q}_2\left[Q_1^2\left(-\frac{m_t}{2n^2}\gamma^2\right)+Q_2^2\left(\frac{m_t}{2n^2}\gamma^2\right)\right]+Q_2\left[\dot{Q}_1^2\left(-\frac{m_t}{2n^2}\gamma^2\right)+\dot{Q}_2^2\left(\frac{m_t}{2n^2}\gamma^2\right)+\right.\\
&+Q_1^2\left(-\frac{3k_{t_1}}{4n^2}\gamma^2+\frac{3k_{t_3}}{8n^4}+\frac{3k_{r_3}}{8}\right)+Q_2^2\left(\frac{k_{t_1}}{4n^2}\gamma^2-\frac{k_{t_3}}{8n^4}-\frac{k_{r_3}}{8}\right)+\\
&\left.+Q_1^4\left(-\frac{15k_{t_3}}{8n^4}\gamma^2\right)+Q_2^4\left(\frac{3k_{t_3}}{8n^4}\gamma^2\right)\right]
\end{aligned}
\tag{C.10}
$$

$$
\begin{aligned}
C_5^D =&Q_1\left[Q_1^3\left(-\frac{5k_{t_3}}{16n^4}\gamma\right)+Q_2^3\left(\frac{5k_{t_2}}{4n^3}\gamma^2\right)\right]+Q_2\left[Q_1^3\left(-\frac{5k_{t_2}}{4n^3}\gamma^2\right)+Q_2^3\left(-\frac{5k_{t_3}}{16n^4}\gamma\right)\right]+\\
&+Q_1^2Q_2^2\left(\frac{15k_{t_3}}{8n^4}\gamma\right)
\end{aligned}
\tag{C.11}
$$

$$
\begin{aligned}
S_5^D =&Q_1\left[Q_1^3\left(\frac{5k_{t_2}}{16n^3}\gamma^2\right)+Q_2^3\left(\frac{5k_{t_3}}{4n^4}\gamma\right)\right]+Q_2\left[Q_1^3\left(-\frac{5k_{t_3}}{4n^4}\gamma\right)+Q_2^3\left(\frac{5k_{t_2}}{16n^3}\gamma^2\right)\right]+\\
&+Q_1^2Q_2^2\left(-\frac{15k_{t_2}}{8n^3}\gamma^2\right)
\end{aligned}
\tag{C.12}
$$

$$
C_6^D = Q_1\left[Q_1^4\left(\frac{9k_{t_3}}{32n^4}\gamma^2\right)+Q_2^4\left(\frac{45k_{t_3}}{32n^4}\gamma^2\right)+Q_1^2Q_2^2\left(-\frac{45k_{t_3}}{16n^4}\gamma^2\right)\right] \tag{C.13}
$$

$$
S_6^D = Q_2\left[Q_1^4\left(\frac{45k_{t_3}}{32n^4}\gamma^2\right)+Q_2^4\left(\frac{9k_{t_3}}{32n^4}\gamma^2\right)+Q_1^2Q_2^2\left(-\frac{45k_{t_3}}{16n^4}\gamma^2\right)\right] \tag{C.14}
$$

Coefficients $C_m^S$, $S_m^S$ $(m = 1, ..., 6)$ for the sense equation (C.2) are:

$$\begin{aligned}
C_1^S =&\ddot{Q}_2 \left[Q_1 \left(-\frac{m_t}{n^2}\gamma\right)\right] + \dot{Q}_2 \left[\dot{Q}_1 \left(-\frac{m_t}{2n^2}\gamma\right)\right] + \\
&+Q_2 \left[Q_1 \left(-\frac{k_{t_1}}{4n^2}\gamma - k_{r_1}\gamma + \frac{k_{r_2}}{4}\right) + Q_2 \left(\frac{3k_{t_2}}{4n^3}\right) + Q_1^3 \left(-\frac{k_{t_3}}{2n^4}\gamma + 4k_{r_2}\gamma^2 - 3k_{r_3}\gamma\right) + \right. \\
&\left. + Q_2^3 \left(\frac{5k_{t_2}}{8n^3}\gamma^2\right)\right] + \ddot{Q}_1 \left[Q_2 \left(-2m_r\gamma\right)\right] + \dot{Q}_1 \left[\dot{Q}_2 \left(-\frac{m_t}{2n^2}\gamma\right)\right] + Q_1 \left[Q_1 \left(\frac{k_{t_2}}{4n^3}\right) + \right. \\
&\left. + Q_2 \left(-\frac{k_{t_1}}{4n^2}\gamma - k_{r_1}\gamma + \frac{k_{r_2}}{4}\right) + Q_1^3 \left(\frac{k_{t_2}}{8n^3}\gamma^2\right) + Q_2^3 \left(-\frac{k_{t_3}}{2n^4}\gamma + 4k_{r_2}\gamma^2 - 3k_{r_3}\gamma\right)\right] + \\
&+Q_1^2 Q_2^2 \left(\frac{3k_{t_2}}{4n^3}\gamma^2\right)
\end{aligned} \tag{C.15}$$

$$\begin{aligned}
S_1^S =&\ddot{Q}_2 \left[Q_2 \left(-4m_r\gamma - \frac{m_t}{n^2}\gamma\right)\right] + \dot{Q}_2 \left[\dot{Q}_2 \left(-2m_r\gamma - \frac{m_t}{2n^2}\gamma\right)\right] + Q_2 \left[Q_1 \left(-\frac{k_{t_2}}{4n^3}\right) + \right. \\
&\left. + Q_2 \left(-\frac{3k_{t_1}}{4n^2}\gamma - 3k_{r_1}\gamma + \frac{3k_{r_2}}{4}\right) + Q_1^3 \left(-\frac{k_{t_2}}{2n^3}\gamma^2\right) + Q_2^3 \left(-\frac{5k_{t_3}}{8n^4}\gamma + 5k_{r_2}\gamma^2 - \frac{15k_{r_3}}{4}\gamma\right)\right] + \\
&+\ddot{Q}_1 \left[Q_1 \left(-2m_r\gamma\right)\right] + \dot{Q}_1 \left[\dot{Q}_1 \left(-2m_r\gamma + \frac{m_t}{2n^2}\gamma\right)\right] + Q_1 \left[Q_1 \left(-\frac{k_{t_1}}{4n^2}\gamma - k_{r_1}\gamma + \frac{k_{r_2}}{4}\right) + \right. \\
&\left. + Q_2 \left(-\frac{k_{t_2}}{4n^3}\right) + Q_1^3 \left(-\frac{k_{t_3}}{8n^4}\gamma + k_{r_2}\gamma^2 - \frac{3k_{r_3}}{4}\gamma\right) + Q_2^3 \left(-\frac{k_{t_2}}{2n^3}\gamma^2\right)\right] + \\
&+Q_1^2 Q_2^2 \left(-\frac{3k_{t_3}}{4n^4}\gamma + 6k_{r_2}\gamma^2 - \frac{9k_{r_3}}{2}\gamma\right)
\end{aligned} \tag{C.16}$$

$$\begin{aligned}
C_2^S =&\ddot{Q}_2 \left(-\frac{m_r}{2} + \frac{m_t}{2n^2}\right) + Q_2 \left[\left(\frac{k_{t_1}}{2n^2} - \frac{k_{r_1}}{2}\right) + Q_2^2 \left(\frac{k_{t_3}}{2n^4} + 2k_{r_2}\gamma - \frac{k_{r_3}}{2}\right) + \right. \\
&\left. + Q_1^4 \left(-\frac{3k_{t_3}}{32n^4}\gamma^2 + \frac{3k_{r_3}}{2}\gamma^2\right) + Q_2^4 \left(\frac{9k_{t_3}}{32n^4}\gamma^2 - \frac{9k_{r_3}}{2}\gamma^2\right) + Q_1^2 Q_2^2 \left(\frac{3k_{t_3}}{16n^4}\gamma^2 - 3k_{r_3}\gamma^2\right)\right] + \\
&+Q_1 \left[Q_1^2 \left(-\frac{k_{t_2}}{2n^3}\gamma\right) + Q_2^2 \left(-\frac{3k_{t_2}}{2n^3}\gamma\right)\right]
\end{aligned} \tag{C.17}$$

$$
\begin{aligned}
S_2^S =&\ddot{Q}_1\left(\frac{m_r}{2}-\frac{m_t}{2n^2}\right)+Q_2\left[Q_2^2\left(-\frac{k_{t_2}}{n^3}\gamma\right)\right]+Q_1\left[\left(-\frac{k_{t_1}}{2n^2}+\frac{k_{r_1}}{2}\right)+\right.\\
&+Q_1^2\left(-\frac{k_{t_3}}{4n^4}-k_{r_2}\gamma+\frac{k_{r_3}}{4}\right)+Q_2^2\left(-\frac{3k_{t_3}}{4n^4}-3k_{r_2}\gamma+\frac{3k_{r_3}}{4}\right)+Q_1^4\left(-\frac{3k_{t_3}}{32n^4}\gamma^2+\frac{3k_{r_3}}{2}\gamma^2\right)+\\
&\left.+Q_2^4\left(-\frac{15k_{t_3}}{32n^4}\gamma^2+\frac{15k_{r_3}}{2}\gamma^2\right)+Q_1^2Q_2^2\left(-\frac{9k_{t_3}}{16n^4}\gamma^2+9k_{r_3}\gamma^2\right)\right]
\end{aligned}
\tag{C.18}
$$

$$
\begin{aligned}
C_3^S =&\ddot{Q}_2\left[Q_1\left(-\frac{m_t}{n^2}\gamma\right)\right]+\dot{Q}_2\left[\dot{Q}_1\left(-\frac{m_t}{2n^2}\gamma\right)\right]+Q_2\left[Q_1\left(-\frac{3k_{t_1}}{4n^2}\gamma-\frac{k_{r_2}}{4}\right)+Q_2\left(\frac{k_{t_2}}{4n^3}\right)+\right.\\
&\left.+Q_1^3\left(-\frac{3k_{t_3}}{4n^4}\gamma+k_{r_3}\gamma\right)+Q_2^3\left(-\frac{5k_{t_2}}{16n^3}\gamma^2\right)\right]+\ddot{Q}_1\left[Q_2\left(-\frac{m_t}{n^2}\gamma\right)\right]+\dot{Q}_1\left[\dot{Q}_2\left(-\frac{m_t}{2n^2}\gamma\right)\right]+\\
&+Q_1\left[Q_1\left(-\frac{k_{t_2}}{4n^3}\right)+Q_2\left(-\frac{3k_{t_1}}{4n^2}\gamma-\frac{k_{r_2}}{4}\right)+Q_1^3\left(\frac{3k_{t_2}}{16n^3}\gamma^2\right)+Q_2^3\left(-\frac{9k_{t_3}}{4n^4}\gamma+3k_{r_3}\gamma\right)\right]+\\
&+Q_1^2Q_2^2\left(\frac{3k_{t_2}}{8n^3}\gamma^2\right)
\end{aligned}
\tag{C.19}
$$

$$
\begin{aligned}
S_3^S =&\ddot{Q}_2\left[Q_2\left(-\frac{m_t}{n^2}\gamma\right)\right]+\dot{Q}_2\left[\dot{Q}_2\left(-\frac{m_t}{2n^2}\gamma\right)\right]+Q_2\left[Q_1\left(-\frac{k_{t_2}}{4n^3}\right)+Q_2\left(-\frac{3k_{t_1}}{4n^2}\gamma-\frac{k_{r_2}}{4}\right)+\right.\\
&\left.+Q_1^3\left(\frac{k_{t_2}}{4n^3}\gamma^2\right)+Q_2^3\left(-\frac{15k_{t_3}}{16n^4}\gamma+\frac{5k_{r_3}}{4}\gamma\right)\right]+\ddot{Q}_1\left[Q_1\left(\frac{m_t}{n^2}\gamma\right)\right]+\dot{Q}_1\left[\dot{Q}_1\left(\frac{m_t}{2n^2}\gamma\right)\right]+\\
&+Q_1\left[Q_1\left(\frac{3k_{t_1}}{4n^2}\gamma+\frac{k_{r_2}}{4}\right)+Q_2\left(-\frac{k_{t_2}}{4n^3}\right)+Q_1^3\left(\frac{9k_{t_3}}{16n^4}\gamma-\frac{3k_{r_3}}{4}\gamma\right)+Q_2^3\left(\frac{3k_{t_2}}{4n^3}\gamma^2\right)\right]+\\
&+Q_1^2Q_2^2\left(\frac{9k_{t_3}}{8n^4}\gamma-\frac{3k_{r_3}}{2}\gamma\right)
\end{aligned}
\tag{C.20}
$$

$$
\begin{aligned}
C_4^S =&\ddot{Q}_2\left[Q_1^2\left(\frac{m_t}{2n^2}\gamma^2\right)+Q_2^2\left(-\frac{m_t}{2n^2}\gamma^2\right)\right]+Q_2\left[\dot{Q}_1^2\left(\frac{m_t}{2n^2}\gamma^2\right)+\dot{Q}_2^2\left(-\frac{m_t}{2n^2}\gamma^2\right)+\right.\\
&+Q_1^2\left(\frac{3k_{t_1}}{4n^2}\gamma^2-\frac{3k_{t_3}}{8n^4}-\frac{3k_{r_3}}{8}\right)+Q_2^2\left(-\frac{k_{t_1}}{4n^2}\gamma^2+\frac{k_{t_3}}{8n^4}+\frac{k_{r_3}}{8}\right)+Q_1^4\left(\frac{15k_{t_3}}{16n^4}\gamma^2\right)+\\
&\left.+Q_2^4\left(-\frac{9k_{t_3}}{16n^4}\gamma^2\right)+Q_1^2Q_2^2\left(\frac{15k_{t_3}}{8n^4}\gamma^2\right)\right]+\ddot{Q}_1\left[Q_1Q_2\left(\frac{m_t}{n^2}\gamma^2\right)\right]+\\
&+Q_1\left[\dot{Q}_1\dot{Q}_2\left(\frac{m_t}{n^2}\gamma^2\right)+Q_1^2\left(\frac{k_{t_2}}{2n^3}\gamma\right)+Q_2^2\left(-\frac{3k_{t_2}}{2n^3}\gamma\right)\right]
\end{aligned}
\tag{C.21}
$$

$$
\begin{aligned}
S_4^S =&\ddot{Q}_2\left[Q_1Q_2\left(\frac{m_t}{n^2}\gamma^2\right)\right]+Q_2\left[\dot{Q}_1\dot{Q}_2\left(\frac{m_t}{n^2}\gamma^2\right)+Q_1^2\left(\frac{3k_{t_2}}{2n^3}\gamma\right)+Q_2^2\left(-\frac{k_{t_2}}{2n^3}\gamma\right)\right]+\\
&+\ddot{Q}_1\left[Q_1^2\left(-\frac{m_t}{2n^2}\gamma^2\right)+Q_2^2\left(\frac{m_t}{2n^2}\gamma^2\right)\right]+Q_1\left[\dot{Q}_1^2\left(-\frac{m_t}{2n^2}\gamma^2\right)+\dot{Q}_2^2\left(\frac{m_t}{2n^2}\gamma^2\right)+\right.\\
&+Q_1^2\left(-\frac{k_{t_1}}{4n^2}\gamma^2+\frac{k_{t_3}}{8n^4}+\frac{k_{r_3}}{8}\right)+Q_2^2\left(\frac{3k_{t_1}}{4n^2}\gamma^2-\frac{3k_{t_3}}{8n^4}-\frac{3k_{r_3}}{8}\right)+\\
&\left.+Q_1^4\left(-\frac{3k_{t_3}}{8n^4}\gamma^2\right)+Q_2^4\left(\frac{15k_{t_3}}{8n^4}\gamma^2\right)\right]
\end{aligned}
\tag{C.22}
$$

$$
\begin{aligned}
C_5^S =&Q_2\left[Q_1^3\left(\frac{5k_{t_3}}{4n^4}\gamma\right)+Q_2^3\left(-\frac{5k_{t_2}}{16n^3}\gamma^2\right)\right]+Q_1\left[Q_1^3\left(-\frac{5k_{t_2}}{16n^3}\gamma^2\right)+Q_2^3\left(-\frac{5k_{t_3}}{4n^4}\gamma\right)\right]+\\
&+Q_1^2Q_2^2\left(\frac{15k_{t_2}}{8n^3}\gamma^2\right)
\end{aligned}
\tag{C.23}
$$

$$
\begin{aligned}
S_5^S =&Q_2\left[Q_1^3\left(-\frac{5k_{t_2}}{4n^3}\gamma^2\right)+Q_2^3\left(-\frac{5k_{t_3}}{16n^4}\gamma\right)\right]+Q_1\left[Q_1^3\left(-\frac{5k_{t_3}}{16n^4}\gamma\right)+Q_2^3\left(\frac{5k_{t_2}}{4n^3}\gamma^2\right)\right]+\\
&+Q_1^2Q_2^2\left(\frac{15k_{t_3}}{8n^4}\gamma\right)
\end{aligned}
\tag{C.24}
$$

$$
C_6^S = Q_2\left[Q_1^4\left(-\frac{45k_{t_3}}{32n^4}\gamma^2\right)+Q_2^4\left(-\frac{9k_{t_3}}{32n^4}\gamma^2\right)+Q_1^2Q_2^2\left(\frac{45k_{t_3}}{16n^4}\gamma^2\right)\right] \tag{C.25}
$$

$$S_6^S = Q_1 \left[ Q_1^4 \left( \frac{9k_{t_3}}{32n^4}\gamma^2 \right) + Q_2^4 \left( \frac{45k_{t_3}}{32n^4}\gamma^2 \right) + Q_1^2 Q_2^2 \left( -\frac{45k_{t_3}}{16n^4}\gamma^2 \right) \right] \tag{C.26}$$

In the next Section, drive and sense equations (C.1) and (C.2) are simplified for the case $Q_2 << Q_1$.

## C.2 Drive and sense equations for small sense response amplitudes

Under the assumption that the amplitude of the sense response is much smaller than the drive amplitude, all non-linear terms in $Q_2$, $\dot{Q}_2$, $\ddot{Q}_2$ (and combinations) in equations of motion for the drive and sense modes (C.1) and (C.2) are considered to be small and are neglected. Under these circumstances, the governing equations for the drive and sense modes (C.1) and (C.2) reduce to (C.27) and (C.28), respectively.

$$
\begin{aligned}
&\ddot{Q}_1\left[M_{res}+Q_1^2\left(\frac{M_{ring}}{(n^2+1)}\gamma^2+p\frac{m_t}{2n^2}\gamma^2\right)\right]+\\
&+\dot{Q}_1\left[M_{res}\frac{\omega_0}{Q}+\dot{Q}_1Q_1\left(\frac{2M_{ring}}{(n^2+1)}\gamma^2+2p\frac{m_t}{2n^2}\gamma^2\right)\right]+\\
&+Q_1\left\{K_{res}+\dot{Q}_1^2\left[\frac{\left(8n^2-1\right)M_{ring}}{(n^2+1)}\gamma^2+p\left(4m_r\gamma^2-\frac{m_t}{2n^2}\gamma^2\right)\right]+\right.\\
&+\ddot{Q}_1Q_1\left(\frac{\left(8n^2\right)M_{ring}}{(n^2+1)}\gamma^2+p4m_r\gamma^2\right)+Q_1^4p\left(\frac{9k_{t_3}}{16n^4}\gamma^2+\frac{9k_{r_3}}{2}\gamma^2\right)+\\
&\left.+Q_1^2\left[\frac{4K_{ring}}{(n^4-2n^2+1)}\gamma^2+p\left(2k_{r_1}\gamma^2-2k_{r_2}\gamma+\frac{3k_{r_3}}{8}+\frac{k_{t_1}}{4n^2}\gamma^2+\frac{3k_{t_3}}{8n^4}\right)\right]\right\}+\\
&+\sum_{j=0}^{p-1}\left[C_1^D\cos n\left(j\frac{2\pi}{p}-\alpha\right)+S_1^D\sin n\left(j\frac{2\pi}{p}-\alpha\right)+C_2^D\cos 2n\left(j\frac{2\pi}{p}-\alpha\right)+\right.\\
&+S_2^D\sin 2n\left(j\frac{2\pi}{p}-\alpha\right)+C_3^D\cos 3n\left(j\frac{2\pi}{p}-\alpha\right)+S_3^D\sin 3n\left(j\frac{2\pi}{p}-\alpha\right)+\\
&+C_4^D\cos 4n\left(j\frac{2\pi}{p}-\alpha\right)+S_4^D\sin 4n\left(j\frac{2\pi}{p}-\alpha\right)+C_5^D\cos 5n\left(j\frac{2\pi}{p}-\alpha\right)+\\
&\left.+S_5^D\sin 5n\left(j\frac{2\pi}{p}-\alpha\right)+C_6^D\cos 6n\left(j\frac{2\pi}{p}-\alpha\right)+S_6^D\sin 6n\left(j\frac{2\pi}{p}-\alpha\right)\right]=\\
&=F_D\cos\Omega t+\frac{4nM_{ring}}{(n^2+1)}\Omega_z\dot{Q}_2
\end{aligned}
\tag{C.27}
$$

$$
\begin{aligned}
&\ddot{Q}_2\left[M_{res}+Q_1^2\left(\frac{M_{ring}}{(n^2+1)}\gamma^2+p\frac{m_t}{2n^2}\gamma^2\right)\right]+\\
&+\dot{Q}_2\left[M_{res}\frac{\omega_0}{Q}+\dot{Q}_1Q_1\left(\frac{2M_{ring}}{(n^2+1)}\gamma^2+2p\frac{m_t}{2n^2}\gamma^2\right)\right]+\\
&+Q_2\left\{K_{res}+\dot{Q}_1^2\left[\frac{\left(8n^2-1\right)M_{ring}}{(n^2+1)}\gamma^2+p\left(4m_r\gamma^2-\frac{m_t}{2n^2}\gamma^2\right)\right]+\right.\\
&+\ddot{Q}_1Q_1\left(\frac{\left(8n^2\right)M_{ring}}{(n^2+1)}\gamma^2+p4m_r\gamma^2\right)+Q_1^4p\left(\frac{9k_{t_3}}{16n^4}\gamma^2+\frac{9k_{r_3}}{2}\gamma^2\right)+\\
&\left.+\ Q_1^2\left[\frac{4K_{ring}}{(n^4-2n^2+1)}\gamma^2+p\left(2k_{r_1}\gamma^2-2k_{r_2}\gamma+\frac{3k_{r_3}}{8}+\frac{k_{t_1}}{4n^2}\gamma^2+\frac{3k_{t_3}}{8n^4}\right)\right]\right\}+\\
&+\sum_{j=0}^{p-1}\left[C_1^S\cos n\left(j\frac{2\pi}{p}-\alpha\right)+S_1^S\sin n\left(j\frac{2\pi}{p}-\alpha\right)+C_2^S\cos 2n\left(j\frac{2\pi}{p}-\alpha\right)+\right.\\
&+S_2^S\sin 2n\left(j\frac{2\pi}{p}-\alpha\right)+C_3^S\cos 3n\left(j\frac{2\pi}{p}-\alpha\right)+S_3^S\sin 3n\left(j\frac{2\pi}{p}-\alpha\right)+\\
&+C_4^S\cos 4n\left(j\frac{2\pi}{p}-\alpha\right)+S_4^S\sin 4n\left(j\frac{2\pi}{p}-\alpha\right)+C_5^S\cos 5n\left(j\frac{2\pi}{p}-\alpha\right)+\\
&\left.+\ S_5^S\sin 5n\left(j\frac{2\pi}{p}-\alpha\right)+C_6^S\cos 6n\left(j\frac{2\pi}{p}-\alpha\right)+S_6^S\sin 6n\left(j\frac{2\pi}{p}-\alpha\right)\right]=\\
&=-\frac{4nM_{ring}}{(n^2+1)}\Omega_z\dot{Q}_1
\end{aligned}
\tag{C.28}
$$

Coefficients $C_m^D$, $S_m^D$ $(m=1,...,6)$ for the drive equation (C.27) are:

$$
\begin{aligned}
C_1^D=&\ddot{Q}_1\left[Q_1\left(-4m_r\gamma-\frac{m_t}{n^2}\gamma\right)\right]+\dot{Q}_1\left[\dot{Q}_1\left(-2m_r\gamma-\frac{m_t}{2n^2}\gamma\right)\right]+\\
&+Q_1\left[Q_1\left(-\frac{3k_{t_1}}{4n^2}\gamma-3k_{r_1}\gamma+\frac{3k_{r_2}}{4}\right)+Q_2\left(\frac{k_{t_2}}{4n^3}\right)+Q_1^3\left(-\frac{5k_{t_3}}{8n^4}\gamma+5k_{r_2}\gamma^2-\frac{15k_{r_3}}{4}\gamma\right)\right]+\\
&+Q_2\left[Q_1\left(\frac{k_{t_2}}{4n^3}\right)+Q_1^3\left(\frac{k_{t_2}}{2n^3}\gamma^2\right)\right]
\end{aligned}
\tag{C.29}
$$

$$
\begin{aligned}
S_1^D =&\ddot{Q}_1\left[Q_2\left(-\frac{m_t}{n^2}\gamma\right)\right]+\dot{Q}_1\left[\dot{Q}_2\left(-\frac{m_t}{2n^2}\gamma\right)\right]+\\
&+Q_1\left[Q_1\left(-\frac{3k_{t_2}}{4n^3}\right)+Q_2\left(-\frac{k_{t_1}}{4n^2}\gamma-k_{r_1}\gamma+\frac{k_{r_2}}{4}\right)+Q_1^3\left(-\frac{5k_{t_2}}{8n^3}\gamma^2\right)\right]+\ddot{Q}_2\left[Q_1\left(-2m_r\gamma\right)\right]+\\
&+\dot{Q}_2\left[\dot{Q}_1\left(-\frac{m_t}{2n^2}\gamma\right)\right]+Q_2\left[Q_1\left(-\frac{k_{t_1}}{4n^2}\gamma-k_{r_1}\gamma+\frac{k_{r_2}}{4}\right)+Q_1^3\left(-\frac{k_{t_3}}{2n^4}\gamma+4k_{r_2}\gamma^2-3k_{r_3}\gamma\right)\right]
\end{aligned}
\tag{C.30}
$$

$$
\begin{aligned}
C_2^D =&\ddot{Q}_1\left(\frac{m_r}{2}-\frac{m_t}{2n^2}\right)+Q_1\left[\left(-\frac{k_{t_1}}{2n^2}+\frac{k_{r_1}}{2}\right)+Q_1^2\left(-\frac{k_{t_3}}{2n^4}-2k_{r_2}\gamma+\frac{k_{r_3}}{2}\right)+\right.\\
&\left.+Q_1^4\left(-\frac{9k_{t_3}}{32n^4}\gamma^2+\frac{9k_{r_3}}{2}\gamma^2\right)\right]+Q_2\left[Q_1^2\left(-\frac{3k_{t_2}}{2n^3}\gamma\right)\right]
\end{aligned}
\tag{C.31}
$$

$$
\begin{aligned}
S_2^D =&\ddot{Q}_2\left(\frac{m_r}{2}-\frac{m_t}{2n^2}\right)+Q_1\left[Q_1^2\left(\frac{k_{t_2}}{n^3}\gamma\right)\right]+\\
&+Q_2\left[\left(-\frac{k_{t_1}}{2n^2}+\frac{k_{r_1}}{2}\right)+Q_1^2\left(-\frac{3k_{t_3}}{4n^4}-3k_{r_2}\gamma+\frac{3k_{r_3}}{4}\right)+Q_1^4\left(-\frac{15k_{t_3}}{32n^4}\gamma^2+\frac{15k_{r_3}}{2}\gamma^2\right)\right]
\end{aligned}
\tag{C.32}
$$

$$
\begin{aligned}
C_3^D =&\ddot{Q}_1\left[Q_1\left(\frac{m_t}{n^2}\gamma\right)\right]+\dot{Q}_1\left[\dot{Q}_1\left(\frac{m_t}{2n^2}\gamma\right)\right]+\\
&+Q_1\left[Q_1\left(\frac{3k_{t_1}}{4n^2}\gamma+\frac{k_{r_2}}{4}\right)+Q_2\left(-\frac{k_{t_2}}{4n^3}\right)+Q_1^3\left(\frac{15k_{t_3}}{16n^4}\gamma-\frac{5k_{r_3}}{4}\gamma\right)\right]+\\
&+Q_2\left[Q_1\left(-\frac{k_{t_2}}{4n^3}\right)+Q_1^3\left(\frac{3k_{t_2}}{4n^3}\gamma^2\right)\right]
\end{aligned}
\tag{C.33}
$$

$$
\begin{aligned}
S_3^D =&\ddot{Q}_1\left[Q_2\left(\frac{m_t}{n^2}\gamma\right)\right]+\dot{Q}_1\left[\dot{Q}_2\left(\frac{m_t}{2n^2}\gamma\right)\right]+\\
&+Q_1\left[Q_1\left(\frac{k_{t_2}}{4n^3}\right)+Q_2\left(\frac{3k_{t_1}}{4n^2}\gamma+\frac{k_{r_2}}{4}\right)+Q_1^3\left(-\frac{5k_{t_2}}{16n^3}\gamma^2\right)\right]+\\
&+\ddot{Q}_2\left[Q_1\left(\frac{m_t}{n^2}\gamma\right)\right]+\dot{Q}_2\left[\dot{Q}_1\left(\frac{m_t}{2n^2}\gamma\right)\right]+Q_2\left[Q_1\left(\frac{3k_{t_1}}{4n^2}\gamma+\frac{k_{r_2}}{4}\right)+Q_1^3\left(\frac{9k_{t_3}}{4n^4}\gamma-3k_{r_3}\gamma\right)\right]
\end{aligned}
\tag{C.34}
$$

$$\begin{aligned} C_4^D =& \ddot{Q}_1 \left[ Q_1^2 \left( -\frac{m_t}{2n^2}\gamma^2 \right) \right] + Q_2 \left[ Q_1^2 \left( \frac{3k_{t_2}}{2n^3}\gamma \right) \right] + \\ &+ Q_1 \left[ \dot{Q}_1^2 \left( -\frac{m_t}{2n^2}\gamma^2 \right) + Q_1^2 \left( -\frac{k_{t_1}}{4n^2}\gamma^2 + \frac{k_{t_3}}{8n^4} + \frac{k_{r_3}}{8} \right) + Q_1^4 \left( -\frac{9k_{t_3}}{16n^4}\gamma^2 \right) \right] \end{aligned} \tag{C.35}$$

$$\begin{aligned} S_4^D =& \ddot{Q}_1 \left[ Q_1 Q_2 \left( -\frac{m_t}{n^2}\gamma^2 \right) \right] + Q_1 \left[ \dot{Q}_1 \dot{Q}_2 \left( -\frac{m_t}{n^2}\gamma^2 \right) + Q_1^2 \left( -\frac{k_{t_2}}{2n^3}\gamma \right) \right] + \ddot{Q}_2 \left[ Q_1^2 \left( -\frac{m_t}{2n^2}\gamma^2 \right) \right] + \\ &+ Q_2 \left[ \dot{Q}_1^2 \left( -\frac{m_t}{2n^2}\gamma^2 \right) + Q_1^2 \left( -\frac{3k_{t_1}}{4n^2}\gamma^2 + \frac{3k_{t_3}}{8n^4} + \frac{3k_{r_3}}{8} \right) + Q_1^4 \left( -\frac{15k_{t_3}}{8n^4}\gamma^2 \right) \right] \end{aligned} \tag{C.36}$$

$$C_5^D = Q_1 \left[ Q_1^3 \left( -\frac{5k_{t_3}}{16n^4}\gamma \right) \right] + Q_2 \left[ Q_1^3 \left( -\frac{5k_{t_2}}{4n^3}\gamma^2 \right) \right] \tag{C.37}$$

$$S_5^D = Q_1 \left[ Q_1^3 \left( \frac{5k_{t_2}}{16n^3}\gamma^2 \right) \right] + Q_2 \left[ Q_1^3 \left( -\frac{5k_{t_3}}{4n^4}\gamma \right) \right] \tag{C.38}$$

$$C_6^D = Q_1 \left[ Q_1^4 \left( \frac{9k_{t_3}}{32n^4}\gamma^2 \right) \right] \tag{C.39}$$

$$S_6^D = Q_2 \left[ Q_1^4 \left( \frac{45k_{t_3}}{32n^4}\gamma^2 \right) \right] \tag{C.40}$$

Coefficients $C_m^S$, $S_m^S$ $(m = 1, ..., 6)$ for the sense equation (C.28) are:

$$\begin{aligned} C_1^S =& \ddot{Q}_2 \left[ Q_1 \left( -\frac{m_t}{n^2}\gamma \right) \right] + \dot{Q}_2 \left[ \dot{Q}_1 \left( -\frac{m_t}{2n^2}\gamma \right) \right] + \ddot{Q}_1 \left[ Q_2 \left( -2m_r\gamma \right) \right] + \dot{Q}_1 \left[ \dot{Q}_2 \left( -\frac{m_t}{2n^2}\gamma \right) \right] + \\ &+ Q_2 \left[ Q_1 \left( -\frac{k_{t_1}}{4n^2}\gamma - k_{r_1}\gamma + \frac{k_{r_2}}{4} \right) + Q_1^3 \left( -\frac{k_{t_3}}{2n^4}\gamma + 4k_{r_2}\gamma^2 - 3k_{r_3}\gamma \right) \right] + \\ &+ Q_1 \left[ Q_1 \left( \frac{k_{t_2}}{4n^3} \right) + Q_2 \left( -\frac{k_{t_1}}{4n^2}\gamma - k_{r_1}\gamma + \frac{k_{r_2}}{4} \right) + Q_1^3 \left( \frac{k_{t_2}}{8n^3}\gamma^2 \right) \right] \end{aligned} \tag{C.41}$$

$$\begin{aligned} S_1^S =& Q_2 \left[ Q_1 \left( -\frac{k_{t_2}}{4n^3} \right) + Q_1^3 \left( -\frac{k_{t_2}}{2n^3}\gamma^2 \right) \right] + \ddot{Q}_1 \left[ Q_1 \left( -2m_r\gamma \right) \right] + \dot{Q}_1 \left[ \dot{Q}_1 \left( -2m_r\gamma + \frac{m_t}{2n^2}\gamma \right) \right] + \\ &+ Q_1 \left[ Q_1 \left( -\frac{k_{t_1}}{4n^2}\gamma - k_{r_1}\gamma + \frac{k_{r_2}}{4} \right) + Q_2 \left( -\frac{k_{t_2}}{4n^3} \right) + Q_1^3 \left( -\frac{k_{t_3}}{8n^4}\gamma + k_{r_2}\gamma^2 - \frac{3k_{r_3}}{4}\gamma \right) \right] \end{aligned} \tag{C.42}$$

$$\begin{aligned} C_2^S =& \ddot{Q}_2 \left( -\frac{m_r}{2} + \frac{m_t}{2n^2} \right) + Q_1 \left[ Q_1^2 \left( -\frac{k_{t_2}}{2n^3}\gamma \right) \right] + \\ &+ Q_2 \left[ \left( \frac{k_{t_1}}{2n^2} - \frac{k_{r_1}}{2} \right) + Q_1^4 \left( -\frac{3k_{t_3}}{32n^4}\gamma^2 + \frac{3k_{r_3}}{2}\gamma^2 \right) \right] \end{aligned} \tag{C.43}$$

$$\begin{aligned} S_2^S =& \ddot{Q}_1 \left( \frac{m_r}{2} - \frac{m_t}{2n^2} \right) + Q_1 \left[ \left( -\frac{k_{t_1}}{2n^2} + \frac{k_{r_1}}{2} \right) + Q_1^2 \left( -\frac{k_{t_3}}{4n^4} - k_{r_2}\gamma + \frac{k_{r_3}}{4} \right) + \right. \\ &\left. + Q_1^4 \left( -\frac{3k_{t_3}}{32n^4}\gamma^2 + \frac{3k_{r_3}}{2}\gamma^2 \right) \right] \end{aligned} \tag{C.44}$$

$$\begin{aligned} C_3^S =& \ddot{Q}_2 \left[ Q_1 \left( -\frac{m_t}{n^2}\gamma \right) \right] + \dot{Q}_2 \left[ \dot{Q}_1 \left( -\frac{m_t}{2n^2}\gamma \right) \right] + \ddot{Q}_1 \left[ Q_2 \left( -\frac{m_t}{n^2}\gamma \right) \right] + \dot{Q}_1 \left[ \dot{Q}_2 \left( -\frac{m_t}{2n^2}\gamma \right) \right] + \\ &+ Q_2 \left[ Q_1 \left( -\frac{3k_{t_1}}{4n^2}\gamma - \frac{k_{r_2}}{4} \right) + Q_1^3 \left( -\frac{3k_{t_3}}{4n^4}\gamma + k_{r_3}\gamma \right) \right] + \\ &+ Q_1 \left[ Q_1 \left( -\frac{k_{t_2}}{4n^3} \right) + Q_2 \left( -\frac{3k_{t_1}}{4n^2}\gamma - \frac{k_{r_2}}{4} \right) + Q_1^3 \left( \frac{3k_{t_2}}{16n^3}\gamma^2 \right) \right] \end{aligned} \tag{C.45}$$

$$\begin{aligned} S_3^S =& Q_2\left[Q_1\left(-\frac{k_{t_2}}{4n^3}\right)+Q_1^3\left(\frac{k_{t_2}}{4n^3}\gamma^2\right)\right]+\ddot{Q}_1\left[Q_1\left(\frac{m_t}{n^2}\gamma\right)\right]+\dot{Q}_1\left[\dot{Q}_1\left(\frac{m_t}{2n^2}\gamma\right)\right]+ \\ &+Q_1\left[Q_1\left(\frac{3k_{t_1}}{4n^2}\gamma+\frac{k_{r_2}}{4}\right)+Q_2\left(-\frac{k_{t_2}}{4n^3}\right)+Q_1^3\left(\frac{9k_{t_3}}{16n^4}\gamma-\frac{3k_{r_3}}{4}\gamma\right)\right] \end{aligned} \tag{C.46}$$

$$\begin{aligned} C_4^S =& \ddot{Q}_2\left[Q_1^2\left(\frac{m_t}{2n^2}\gamma^2\right)\right]+Q_2\left[\dot{Q}_1^2\left(\frac{m_t}{2n^2}\gamma^2\right)+Q_1^2\left(\frac{3k_{t_1}}{4n^2}\gamma^2-\frac{3k_{t_3}}{8n^4}-\frac{3k_{r_3}}{8}\right)+Q_1^4\left(\frac{15k_{t_3}}{16n^4}\gamma^2\right)\right] \\ &+\ddot{Q}_1\left[Q_1Q_2\left(\frac{m_t}{n^2}\gamma^2\right)\right]+Q_1\left[\dot{Q}_1\dot{Q}_2\left(\frac{m_t}{n^2}\gamma^2\right)+Q_1^2\left(\frac{k_{t_2}}{2n^3}\gamma\right)\right] \end{aligned} \tag{C.47}$$

$$\begin{aligned} S_4^S =& Q_2\left[Q_1^2\left(\frac{3k_{t_2}}{2n^3}\gamma\right)\right]+\ddot{Q}_1\left[Q_1^2\left(-\frac{m_t}{2n^2}\gamma^2\right)\right] \\ &+Q_1\left[\dot{Q}_1^2\left(-\frac{m_t}{2n^2}\gamma^2\right)+Q_1^2\left(-\frac{k_{t_1}}{4n^2}\gamma^2+\frac{k_{t_3}}{8n^4}+\frac{k_{r_3}}{8}\right)+Q_1^4\left(-\frac{3k_{t_3}}{8n^4}\gamma^2\right)\right] \end{aligned} \tag{C.48}$$

$$C_5^S = Q_2\left[Q_1^3\left(\frac{5k_{t_3}}{4n^4}\gamma\right)\right]+Q_1\left[Q_1^3\left(-\frac{5k_{t_2}}{16n^3}\gamma^2\right)\right] \tag{C.49}$$

$$S_5^S = Q_2\left[Q_1^3\left(-\frac{5k_{t_2}}{4n^3}\gamma^2\right)\right]+Q_1\left[Q_1^3\left(-\frac{5k_{t_3}}{16n^4}\gamma\right)\right] \tag{C.50}$$

$$C_6^S = Q_2\left[Q_1^4\left(-\frac{45k_{t_3}}{32n^4}\gamma^2\right)\right] \tag{C.51}$$

$$S_6^S = Q_1\left[Q_1^4\left(\frac{9k_{t_3}}{32n^4}\gamma^2\right)\right] \tag{C.52}$$

Equations (C.27) and (C.28) have been specified in Section 3.4.1 for the case $n = 2$ and $p = 8$, and in Section 3.4.1 for $n = 2$ and $p = 16$.

# Appendix D

# Validation using Runge-Kutta method

In Chapters 4 and 5 the averaging method was used to investigate the drive and sense responses, respectively, for ring resonators operating at large drive amplitudes under practical operating conditions. For ring resonators having 8 supports, the averaging method was applied based on drive and sense governing equations (3.45) and (3.46) given in Section 3.4.1. Equations (3.45) and (3.46) were obtained from equations (3.43) and (3.44), respectively, by neglecting the backwards coupling from the sense response to the drive response, and by neglecting higher powers of $Q_1$ than the cubic. The obtained drive and sense frequency response curves for ring resonators having 8 nominal supports were shown in Section 4.4.2 and Section 5.3, respectively.

In this Appendix, the frequency response curves for the drive and sense modes are obtained using the fourth-order Runge-Kutta numerical time-integration scheme based on equations (3.43) and (3.44). The results obtained using the averaging method are verified by comparing the frequency response curves obtained using the averaging method against those obtained using the Runge-Kutta method.

## D.1 Runge-Kutta time-integration method to determine the drive and sense responses

The Runge-Kutta time-integration scheme is an iterative method to approximate the solution of ordinary differential equations [40]. Given initial values for $Q_1$, $Q_2$, $\dot{Q}_1$ and $\dot{Q}_2$ at $t = t_0$, and rearranging the drive and sense equations to express $\ddot{Q}_1$ and $\ddot{Q}_2$ as functions of time, $Q_1$, $Q_2$, $\dot{Q}_1$ and $\dot{Q}_2$, the Runge-Kutta method determines the radial anti-node amplitudes $Q_1$ and $Q_2$ (and their first order time derivatives) at the time $t_n = t_0 + n\Delta t$ where $\Delta t$ is the time step considered for the numerical method.

Time step $\Delta t$ needs to ensure that the obtained solution is sufficiently accurate. It can be shown that $\Delta t = \frac{1}{60 f_0}$ (where $f_0$ is the natural frequency for the $2\theta$ modes of the supported ring resonator considered) ensures the obtained drive and sense responses are accurate. The drive and sense responses are considered to be in steady-state when the difference between the peak values of two consecutive cycles is within 0.01%. The amplitudes and phases of the steady-state drive and sense responses to the applied external harmonic force are used to develop the drive and sense frequency response curves.

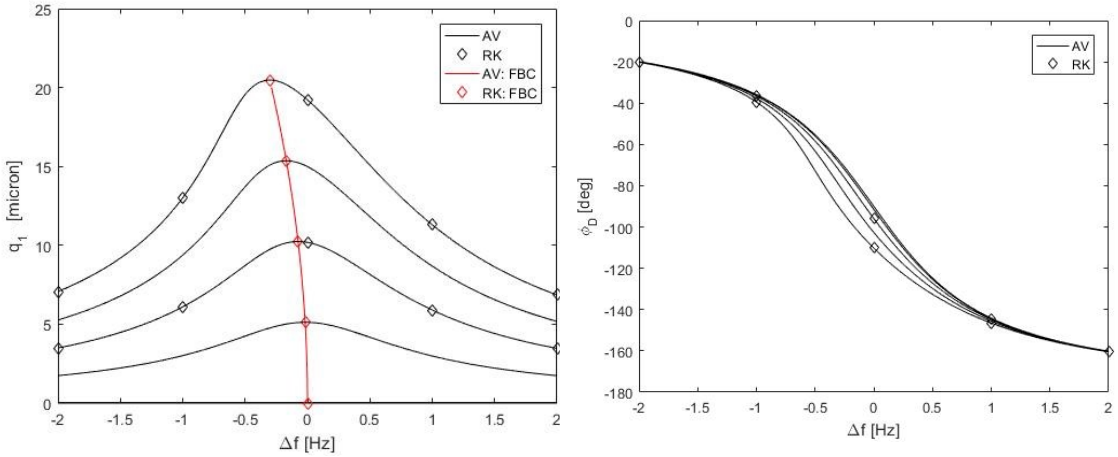
## D.2 Runge-Kutta method ad averaging method compared

Figures D.1 and D.2 respectively show the frequency response curves for the drive and sense modes obtained using the averaging method and the Runge-Kutta method for the ring resonator having 8 nominal supports shown in Figure 4.1a. The drive response amplitude and phase relative to the applied force are $q_1$ and $\phi_D$, respectively. The sense response amplitude and phase relative to the drive response are $q_2$ and $\phi_{SD}$, respectively.

The frequency response curves for the drive mode are obtained using the averaging method as described in Section 4.4.1. The drive response amplitude is obtained by solving equation (4.22) and the drive response phase is given by (4.26). The frequency backbone curve for the

drive mode is obtained using equation (4.27). The frequency response curves for the sense mode are obtained using the averaging method as described in Section 5.3.1, using equations (5.13) and (5.14).

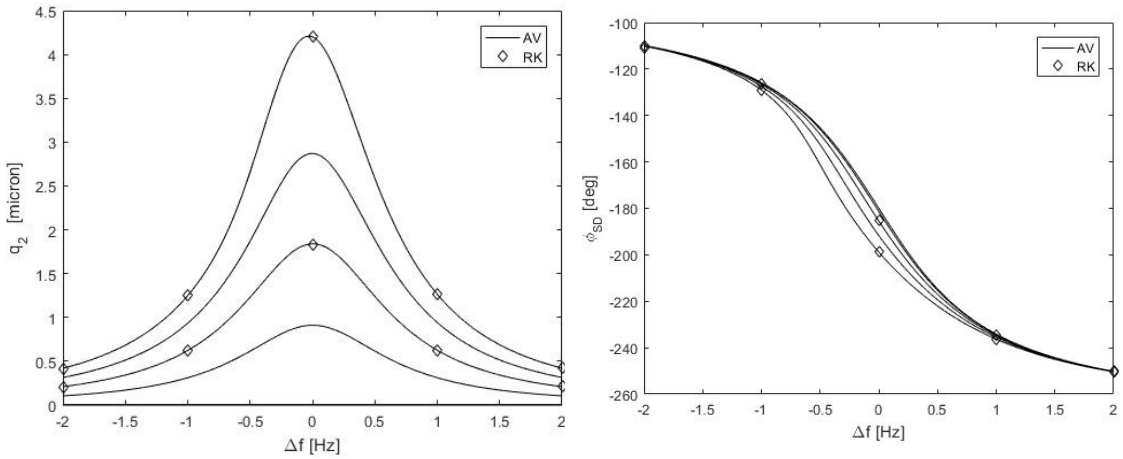
Drive and sense responses (amplitude and phase) are obtained applying the Runge-Kutta method to equations (3.43) and (3.44) as described in Section D.1, for applied driving harmonic force having frequencies $f_0$, $f_0 \pm 1$ Hz and $f_0 \pm 2$ Hz, where $f_0$ is the linear resonance frequency of drive and sense $2\theta$ modes. Results are shown for two levels of magnitude of the applied force. Drive mode pseudo-resonance frequencies are calculated using the Runge-Kutta method for four levels of drive response amplitudes, based on a drive response having a phase of 90° degrees relative to the applied force.




(a) Amplitude.

(b) Phase.

Figure D.1: Drive mode frequency response curves and frequency backbone curve obtained using averaging method (AV) and the Runge-Kutta method (RK) for the ring resonator having 8 nominal supports. Q=10000. $\alpha = 22.5°$.




(a) Amplitude.

(b) Phase.

Figure D.2: Sense mode frequency response curves obtained using averaging method (AV) and the Runge-Kutta method (RK) for the ring resonator having 8 nominal supports. Q=10000. $\alpha = 22.5°$.

Comparison between the frequency response curves obtained using the averaging method and the Runge-Kutta time-integration method shows that the results obtained using both methods are in good agreement. This demonstrates the validity of the assumptions made for the application of the averaging method in Chapters 4 and 5 i.e. for the range of drive response amplitudes considered in this work, the backwards coupling from the sense response to the drive response and higher powers of $Q_1$ than the cubic have negligible effect on the drive and sense dynamics and can be safely neglected.